DEPARTAMENT DE FÍSICA ATÒMICA MOLECULAR I NUCLEAR

VNIVERSITAT Ŏ ID VALÈNCIA

(ESTUDI GENERAL)

Sensitivity to Diffuse Fluxes and Energy Spectrum Reconstruction in the ANTARES Neutrino Telescope

PhD THESIS

JUAN DE DIOS ZORNOZA GÓMEZ

January 2005

D. JUAN ZÚÑIGA ROMÁN, Profesor Titular de la Universidad de Valencia,

CERTIFICA :

Que la presente memoria, **Sensitivity to Diffuse Fluxes and Energy Spectrum Reconstruction in the ANTARES Neutrino Telescope**, ha sido realizada bajo su dirección en el Departamento de Física Atómica, Molecular y Nuclear de la Universitat de València por D. Juan de Dios Zornoza Gómez y constituye su Tesis Doctoral, que presenta para optar al grado de Doctor en Física.

Y para que conste, en cumplimiento de la legislación vigente, firmo el presente Certificado en Paterna a 11 de Enero de 2005.

Fdo.: Juan Zúñiga Román

Visto bueno del Director del Depto.: D. Ramón Cases Ruiz

A mi esposa

Agradecimientos

Quiero dar las gracias en primer lugar a mi director de tesis, Juan Zúñiga, por su apoyo durante estos años. A través de él entré en el proyecto ANTARES y desde entonces ha mantenido su confianza en mí. Ha sido siempre un tutor cercano y dispuesto a ayudar, enriqueciendo extraordinariamente esta tesis. Me considero muy afortunado por haber trabajado con él.

También deseo agradecer al director del proyecto, Juan José Hernández, la oportunidad de colaborar en este grupo, así como el tiempo y el esfuerzo dedicado a mi trabajo, que le han valido mi admiración y respeto. Sus acertados comentarios han sido una guía muy útil.

La ayuda de Emiliano Carmona desde que llegué a ANTARES la considero fundamental. Decir que ha sido una fuente inagotable de colaboración es resumir una larguísima lista de consejos que han hecho mucho más fructífero mi trabajo. Además, esta ayuda siempre ha ido acompañada de amabilidad y simpatía, haciendo de él un perfecto compañero y amigo.

Quiero también manisfestar mi gratitud hacia Teresa Montaruli, responsable del Grupo de Astrofísica de ANTARES, por apoyarme dentro de la colaboración. Veo su incansable labor como un ejemplo de cómo el prestigio se consigue con mucho y buen trabajo.

Otros miembros de la colaboración, como Jürgen Brunner, Alain Romeyer, Luciano Moscoso o Igor Sokalski por citar sólo algunos, han contruibuido apreciablemente con sus consejos y sugerencias, que desde aquí agradezco.

Doy las gracias a Juanan su ayuda contra los ordenadores, demostrándome que siempre se puede aprender mucho también de los que son algo más jóvenes. Pero sobre todo, le agradezco su compañía y su amistad.

También tengo que dar las gracias a Víctor, a Diego y a Paco, con quienes siempre ha habido una buena camaradería. Y por supuesto no quiero olvidarme de Sergio, con quien he pasado muy buenos ratos.

Gracias también a la gente del IFIC, con un recuerdo especial para Asun. También tengo que resaltar la ayuda que he recibido de personas como Javier, Amparo, Rosario o Tere y del grupo del GRID.

También he encontrado aquí buenos amigos como Santi, Arantza, Pablo, Luis, Belén y muchos más, que se han sumado a otros como Gustavo, Jose, Esteban, César o Jose Enrique. A todos ellos he de darles las gracias por hacer que el IFIC no sólo sea un lugar de trabajo.

Y gracias a mis padres y a mi hermano. Han sido los primeros en darme su apoyo y en valorar mi trabajo. A ellos les debo mucho de lo que soy y me es difícil resumir en unas líneas toda mi gratitud.

Finalmente quiero dar las gracias a Ana, porque no ha dudado nunca en apoyarme. Siempre ha estado dispuesta a prestarme toda su ayuda y ni ella se imagina cúan valiosa ha sido. Su confianza en mí ha sido fundamental y me anima a seguir hacia adelante.

Muchas otras personas me han ayudado durante este tiempo y me es imposible nombrarlas a todas. En todo caso, que lean en estas palabra mi agradecimiento y mi recuerdo.

"–Los sucesos lo dirán, Sancho -respondió don Quijote-,
que el tiempo, descubridor de todas las cosas,
no se deja ninguna que no la saque a la luz del sol,
aunque esté escondida en los senos de la tierra."
Don Quijote de la Mancha, Capítulo XXV (2ª parte).

Contents

Sensibilidad a flujos difusos y deconvolución de espectros de energía en el telescopio de neutrinos ANTARES

Introducción

Astronomía de neutrinos

El comienzo de la Astronomía de neutrinos, aunque reciente, promete ser un fructífero campo experimental en la observación del Cosmos. Actualmente, la más importante fuente de información sobre los fenómenos astrofísicos la constituyen los fotones y los rayos cósmicos. La Astronomía de fotones empezó mediante la detección de la luz visible, pero ha ido ampliando el rango del espectro electromagnético utilizado: ondas de radio, infrarrojo, rayos X, rayos gamma...Los rayos cósmicos también han aportado gran cantidad de información sobre la composición del Universo y otros procesos cósmicos desde que fueron descubiertos por V. Hess a principios de siglo. Las observaciones realizadas hasta ahora con fotones y rayos cósmicos han respondido a muchas cuestiones de gran interés científico, pero a su vez han planteado otras, como el origen de las partículas más energéticas que vienen desde el espacio.

Por otro lado, existen limitaciones en estos mensajeros que dificultan el estudio de las zonas más alejadas o más densas del Universo. El handicap para los fotones es su interacción con fotones de baja energía del fondo cósmico de radiación y con la materia. Los fotones con una energía de unos cuantos centenares de TeV no pueden viajar desde el centro de la Galaxia hasta la Tierra (8.5 kpc). Existe un inconveniente similar para los protones, ya que también interaccionan con el fondo de radiación de microondas, lo que limita su recorrido a unos 100 Mpc para energías $E_p \sim 10^{20}$ eV (efecto GZK). Para energías más bajas, la información direccional se pierde debido a los campos magnéticos.

Los neutrones, aunque son neutros y por tanto no se desvían por los campos magnéticos, tienen una vida media corta, lo que limita críticamente su alcance. Incluso a muy altas energías (EeV), apenas pueden recorrer la distancia que nos separa

del centro de la Galaxia.

Por lo tanto, para llegar más lejos en la observación del Universo, necesitamos una sonda que sea neutra, estable y que interaccione débilmente. Los neutrinos reúnen todas estas condiciones. Sin embargo, el hecho de que sólo interaccionen débilmente es también la razón por la cual no se han usado en Astronomía hasta muy recientemente.
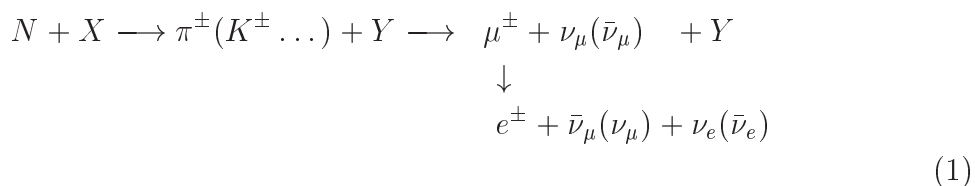
El primer experimento que detectó neutrinos provenientes de una fuente astrofísica fue el experimento de R. Davis en 1969, quien además observó por primera vez un déficit (respecto a lo predicho por el Modelo Estándar del Sol) en el número de neutrinos solares que incidían en un tanque con 400.000 litros de percloretileno. Este resultado abriría lo que ha sido y sigue siendo materia de estudio de gran número de experimentos: las oscilaciones de neutrinos.

Por otro lado, el primer ejemplo de detección de neutrinos originados fuera del Sistema Solar fue la explosión de la supernova SN1987A, en la Gran Nube de Magallanes, que fue observada simultáneamente por Kamiokande e IMB.

Los neutrinos detectados en estos experimentos son de baja energía. Para observar neutrinos de más alta energía y de fuentes más lejanas necesitamos un método experimental distinto, ya que los flujos predichos son mucho más pequeños. Por tanto, es necesario un volumen de detección mucho mayor. En 1960 M. A. Markov propuso construir una matriz tridimensional de fotomultiplicadores bajo el agua o el hielo. Así se puede detectar la luz Cherenkov emitida por los muones relativistas producidos en la interacción de los neutrinos con el medio circundante.

Fuentes de neutrinos

El principal mecanismo de producción de neutrinos es la interacción de un nucleón de alta energía con un blanco (que puede ser materia o radiación electromagnética) y la posterior desintegración de los piones (u otros mesones más pesados, como kaones) a muones. A su vez, la desintegración de estos muones también produce neutrinos.

$$
\begin{aligned}
N + X \longrightarrow \pi^{\pm}(K^{\pm}\dots) + Y \longrightarrow \quad & \mu^{\pm} + \nu_{\mu}(\bar{\nu}_{\mu}) \quad + Y \\
& \downarrow \\
& e^{\pm} + \bar{\nu}_{\mu}(\nu_{\mu}) + \nu_{e}(\bar{\nu}_{e})
\end{aligned}
\tag{1}
$$

La atmósfera terrestre es una fuente segura de neutrinos producidos en la interacción de los rayos cósmicos con los núcleos. A su vez, es también el fondo para la detección de señales cósmicas. Hay que distinguir entre dos tipos de neutrinos atmosféricos: los neutrinos convencionales, provenientes de la desintegración de los piones y los kaones y los neutrinos *prompt* producidos en las desintegraciones de los mesones *charmed* (D, $\Lambda\dots$).

En cuanto a las fuentes astrofísicas, podemos destacar los diversos candidatos:

- **Explosiones de Rayos Gamma:** Estos fenónemos son, durante unos segundos, los más energéticos del Universo ($\sim 10^{51} - 10^{54}$ erg/s). Se caracterizan por una breve explosión de rayos gamma, a menudo seguida de emisión de rayos X, visible y de radio. El modelo más aceptado para explicar estas explosiones asume que el núcleo de una estrella supermasiva colapsa y resulta en una supernova fallida.

- **Galaxias de Núcleo Activo:** Esta clasificación incluye varios tipos de objetos (Seyfert I y II, cuásares, radio galaxias, blazars...) En el modelo unificado, estas fuentes son el mismo tipo de objeto visto desde perspectivas distintas. Si se comprueba que las AGNs emiten neutrinos, se apoyarían los mecanismos de aceleración hadrónicos.

- **Microcuásares:** Estos objetos comparten muchas características morfológicas con los cuásares, pero a escala galáctica. Aunque todavía no hay consenso para explicar el "motor" central de la fuente, se piensa que consisten en un objeto compacto hacia el cual se acreta materia procedente de su estrella compañera.

Otras fuentes astrofísicas que podrían emitir flujos detectables de neutrinos son las explosiones de supernovas, los pleriones, los remanentes de supernovas, los púlsares, los sistemas binarios con una estrella de neutrones o las magnetoestrellas.

Además, hay que mencionar otras posibles fuentes como la desintegración del neutralino (uno de los candidatos a constituir la materia oscura), la interacción de neutrinos de muy alta energía con neutrinos primordiales o la desintegración de partículas superpesadas con masa en la escala GUT.

A partir de los flujos de rayos gamma (ϕ_γ) y de rayos cósmicos (ϕ_{CR}) observados en la Tierra y de ciertas hipótesis relativas a los modelos de producción, se pueden establecer límites superiores al flujo de neutrinos (ϕ_ν) esperado:

$$\int \phi_\gamma(E_\gamma)dE_\gamma \simeq 2 \int \phi_\nu(E_\nu)dE_\nu \tag{2}$$

$$\phi_\nu(E_\nu) \le \phi_{CR}(E_{CR} = f^{-1}E_\nu) \cdot K \cdot O_n \cdot P \tag{3}$$

donde f es la fracción de energía liberada en neutrinos respecto a la de neutrones y los factores K, O_n y P tienen en cuenta los efectos cinemáticos, de opacidad de las fuentes a neutrones y de propagación de los rayos cósmicos, respectivamente.

A partir de hipótesis ligeramente distintas, se han establecido dos límites teóricos al flujo de neutrinos:

$$E_\nu^2 \frac{d\phi}{dE_\nu} < 4.5 \times 10^{-8} \text{ GeVcm}^{-2}\text{s}^{-1}\text{sr}^{-1} \quad (\text{Waxman} - \text{Bahcall}) \tag{4}$$

$$E_\nu^2 \frac{d\phi}{dE_\nu} < 2 \times 10^{-6} \text{ GeVcm}^{-2}\text{s}^{-1}\text{sr}^{-1} \quad (\text{Mannheim} - \text{Protheroe} - \text{Rachen}) \tag{5}$$

RESUMEN

4

Estos límites se reducen en un factor dos cuando se tienen que en cuenta las oscilaciones, ya que la relación entre los flujos de neutrinos pasa de ser $\nu_e : \nu_\mu : \nu_\tau \sim$ 1:2:0 en la fuente a 1:1:1 en la Tierra.

El telescopio de neutrinos ANTARES

La colaboración ANTARES tiene por objetivo demostrar la viabilidad de un telescopio de neutrinos en el fondo del mar. Estará situado a 2500 m de profundidad en el mar Mediterráneo y a una distancia de 40 km de la costa de Tolón. El principio de funcionamiento está basado en la detección de los fotones Cherenkov inducidos por el muon producido en la interacción por corriente cargada de un neutrino con un nucleón de la roca o el agua que rodea el detector.

Los 900 fotomultiplicadores del detector están distribuidos en tripletes a lo largo de 12 líneas de 450 m de longitud. La conexión entre la base en la costa y las líneas se realiza mediante un cable electro-óptico, que sirve para la transmisión de datos y para suministrar el alto voltaje.

Pese a que los flujos esperados disminuyen exponencialmente con la energía del neutrino, este hecho está parcialmente compensado por el aumento de la sección eficaz de interacción y del alcance del muon con la energía.

Existen dos tipos de fondo físico en estos detectores. Por un lado, los muones producidos por los rayos cósmicos en la atmósfera. Para evitar este fondo se consideran únicamente las trazas ascendentes, ya que los muones atmosféricos no pueden atravesar la Tierra. Sin embargo, una pequeña fracción de los muones atmosféricos descendentes pueden ser reconstruidos como ascendentes, de manera que es necesario además construir el detector a gran profundidad, para que el agua sobre él atenúe el flujo de muones. Por otro lado, los neutrinos ascendentes producidos por los rayos cósmicos en la atmósfera son una fuente irreducible de fondo. Solamente pueden ser discriminados buscando acumulaciones en declinación y ascensión recta o en base a los diferentes índices espectrales que se esperan para las fuentes astrofísicas ($\phi \sim E_\nu^{-2}$) y los neutrinos atmosféricos ($\phi \sim E_\nu^{-3.7}$).

Los primeros trabajos de la colaboración ANTARES han estado dedicados a investigación y desarrollo del proyecto. Entre las medidas más relevantes hay que destacar la determinación de los parámetros ópticos del agua (longitud de dispersión y de absorción), la tasa de potasio-40 y de bioluminiscencia y el nivel de sedimentación sobre los elementos del detector. Estos resultados se han obtenido mediante el despliegue de diversas líneas, lo cual además ha permitido verificar el diseño y los componentes del detector en condiciones reales. Por ejemplo, mediante la llamada "Línea 5" se pudo comprobar el sistema de posicionamiento acústico y se detectaron muones atmoféricos descendentes. Aún más relevante ha sido la instalación y conexión de una línea prototipo que reproduce una versión reducida (un quinto) de la versión final de las líneas.

El plan para el futuro inmediato es desplegar una línea mecánica completa en marzo de 2005. La primera línea del detector será sumergida en agosto del mismo año y el

telescopio estará completamente instalado en febrero de 2007.

Objetivos

El objetivo de este trabajo incluye varias cuestiones relacionadas con la reconstrucción de la energía. Como se ha apuntado previamente, este es un aspecto clave del detector, ya que los flujos producidos por fuentes no localizadas espacialmente sólo pueden ser discriminados frente al fondo de neutrinos atmosféricos mediante criterios basados en la energía.

Además de desarrollar un algoritmo para reconstruir la energía de los muones, es necesario cuantificar la capacidad ("sensibilidad") de ANTARES para detectar señales astrofísicas por encima del fondo de neutrinos atmosféricos. Este parámetro permite comparar distintos experimentos, así como estimar qué modelos teóricos pueden ser descartados si no se observa señal.

Otro aspecto importante a investigar es la deconvolución de los espectros energéticos. En principio, el espectro se puede obtener a partir de la energía reconstruida individualmente para cada suceso. Sin embargo, el hecho de que el flujo de neutrinos sigue una ley de potencias de rápido decrecimiento, unido a la gran dispersión en la deposición de la energía de los muones en el detector, hacen que sea necesario usar métodos alternativos basados en las técnicas de deconvolución.

Algoritmo para la reconstrucción de la energía

En general, la energía de los neutrinos no es accesible debido a que la señal en el detector es producida fundamentalmente por el muon, el cual sólo se lleva una fracción de la energía del neutrino. Esta fracción fluctúa y depende de la energía. Únicamente en aquellos sucesos en los que se detecta la cascada hadrónica se puede estimar el resto de la energía del neutrino del suceso.

La determinación de la energía del muon tampoco es una tarea sencilla por varias razones. En primer lugar, si el vértice de interacción está lejos del detector, el muon producido pierde parte de su energía antes de llegar al "can", que es el volumen donde los fotones Cherenkov emitidos pueden ser detectados antes de ser absorbidos en el agua. Por tanto, sólo se puede medir la energía que los muones tienen cuando están lo suficientemente cerca como para que la luz Cherenkov no sea absorbida en el agua.

El algoritmo de reconstrucción está basado en la dependencia de la pérdida de energía del muon ($\Delta E_\mu/\Delta x$) con la energía del muon. Esta pérdida se debe a varios procesos: ionización, producción de pares, radiación de frenado e interacciones fotonucleares.

La ionización es el factor dominante a bajas energías ($E_\mu \leq 600$ GeV). La dependencia de este proceso con la energía es muy suave, y por tanto apenas permite reconstruir la energía del muon en este rango.

Por encima de la energía crítica, definida como aquella para la cual las pérdidas

por ionización sólo contribuyen con la mitad del total, $\Delta E_\mu / \Delta x$ crece linealmente con la energía. El proceso dominante en todo el rango de interés es la producción de pares (básicamente $e^+ e^-$), aunque también es muy significativa la contribución de la radiación de frenado. El efecto de las interacciones nucleares es aproximadamente cinco veces menor. Sin embargo, estos procesos "radiativos" presentan un gran carácter estocástico, por lo que se producen grandes fluctuaciones suceso a suceso en la deposición de energía de los muones, lo que limita inevitablemente la resolución energética del detector.

El estimador utilizado para la reconstrucción de la energía se define como:

$$ x = N_{hits} \left(\frac{\Sigma_i A_{hit}}{\Sigma_i A_{MIM}} - 1 \right) \tag{6} $$

donde N_{hits} es el número total de *hits* con una diferencia temporal respecto al tiempo directo (el de los fotones que no han sufrido dispersión) menor de 4 ns, A_{hit} es la amplitud medida por cada fotomultiplicador y A_{MIM} es la amplitud que el fotomultiplicador habría registrado si el muon tuviera una energía tal que se pueda considerar de mínima ionización. La razón de comparar la suma de las amplitudes medidas con las amplitudes MIM es reducir las fluctuaciones debidas a la dependencia con la posición y el ángulo de la traza relativos al detector. Además, y también para limitar las fluctuaciones del estimador, se definen dos versiones de este, incluyendo sólo los *hits* que cumplen $0.1 < \frac{A_{hit}}{A_{MIM}} < 100$ (estimador de baja energía, x_{low}) o $10 < \frac{A_{hit}}{A_{MIM}} < 1000$ (estimador de alta energía, x_{high}).

Una vez definido el estimador se puede parametrizar la relación entre este y la energía del muon. Se han usado diferentes parametrizaciones polinómicas obteniéndose los mejores resultados para el caso lineal.

Cálculo de la sensibilidad a flujos difusos

Como se ha mencionado anteriormente, la sensibilidad permite cuantificar la capacidad del detector para distinguir una señal sobre el fondo de neutrinos atmosféricos. El límite superior para un espectro de flujo predicho $\phi(E)$ a un determinado nivel de confianza CL es $\Phi(E)_{CL} = \Phi(E) \ \mu_{CL}(n_{obs}, n_{bg})/n_s$, donde n_{obs} es el número de sucesos observados; n_{bg}, el fondo esperado, y n_s, la señal esperada.

Con el fin de evitar introducir un sesgo cuando se elige el valor óptimo en la variable usada para hacer la discriminación, este se ha de determinar sin utilizar información observacional. Por ello se calcula un límite promedio que tiene en cuenta todos los posibles números de sucesos observados de acuerdo con su probabilidad de Poisson:

$$ \bar{\mu}_{CL}(n_{bg}) = \sum_{n_{obs}=0}^{\infty} \mu_{CL}(n_{obs}, n_{bg}) \frac{(n_{bg})^{n_{obs}} e^{-n_{bg}}}{n_{obs}!} \tag{7} $$

De esta manera, el límite no depende del número de sucesos observados. El valor óptimo como umbral para discriminar los neutrinos atmosféricos será aquel que mini-

mice el llamado "Factor de Rechazo de Modelos" (MRF, por sus siglas en inglés) y por tanto, el límite promedio en el flujo:

$$\bar{\Phi}(E)_{90} = \Phi(E) \; \frac{\bar{\mu}_{90}(n_{obs}, n_{bg})}{n_s} \tag{8}$$

La variable que se use para hacer esta discriminación ha de tener una dependencia lo más lineal posible con la energía y una baja dispersión. En este análisis se han estudiado dos posibilidades:

- La energía reconstruida del muon.

- El número total de hits con un tiempo de llegada $|t - t_{directo}| < 4$ ns.

Una vez elegida la mejor variable y el valor umbral para el corte de acuerdo con los criterios antes mencionados, se ha de analizar la influencia de las distintas fuentes de errores sistemáticos. Hay que distinguir entre dos tipos de efectos:

- Incertidumbre en el fondo predicho, donde se incluyen tanto las predicciones de neutrinos atmosféricos convencionales como la componente de los neutrinos *prompt*.

- Efectos sistemáticos en la eficiencia de detección. En este caso se incluyen las incertidumbres en los parámetros del agua y se tienen en cuenta otros efectos como la simulación de la propagación de los neutrinos y los muones.

Tests estadísticos

Un método alternativo para la comparación de las distintas predicciones de señal y neutrinos *prompt* son los tests estadísticos como el de Kolmogorov-Smirnov o el de Pearson. De esta manera se puede calcular la probabilidad de que una cierta distribución sea compatible con la hipótesis asumida (diferentes modelos de señal y de neutrinos *prompt*).

Deconvolución de espectros de energía

En principio, el espectro de energía de los neutrinos (o de los muones producidos por ellos) puede ser reconstruido usando la energía de cada suceso. Sin embargo, este método no es el más eficiente en nuestro caso. Por un lado, el flujo de neutrinos atmosféricos sigue una ley de potencias con una rápida disminución del número de sucesos con la energía. Además, la dispersión en la energía depositada en el detector es muy alta, debido a la naturaleza estocástica de los procesos de pérdida de energía de los muones. La combinación de ambos factores provoca un exceso de sucesos para energías intermedias y altas.

Por lo tanto, el enfoque correcto para este problema son las técnicas de deconvolución de espectros. Estas técnicas se basan en el hecho de que la distribución

medida (que puede ser la energía reconstruida u otra variable relacionada con ella) es el resultado de la convolución del espectro de energías verdadero por una función respuesta del detector, que se puede expresar mediante una matriz calculada mediante Monte Carlo. Se han estudiado dos métodos para hacer esta deconvolución. El primero consiste en la descomposición en valores de singulares de la matriz respuesta (SVD, por *Singular Value Decomposition*). El segundo es un método iterativo basado en el teorema de Bayes.

Discusión de los resultados

Reconstrucción de la energía

Usando el estimador x_{low}, definido anteriormente, se han obtenido los resultados que se muestran en la figura 1. El valor medio de la distribución de $\log_{10} E_{rec}^{\mu}/E_{gen}^{\mu}$ para energías intermedias (desde 500 GeV hasta 1 PeV) es estable en torno a cero (dentro de un margen de 0.2). Para energías más bajas, la dependencia de $\Delta E_{\mu}/\Delta x$ con la energía del muon es casi plana, lo que hace difícil la reconstrucción en este rango. A energías más altas hay una desviación que tiende a subestimar la energía del muon. Por esta razón, para sucesos muy energéticos se puede usar el estimador x_{high}, que presenta un mejor comportamiento. Por otro lado, la anchura de estas distribuciones es 0.4-0.5 a bajas energías ($E < 30$ TeV) y 0.2-0.3 a energías más altas, lo que supone un factor 2-3 en la energía del muon.
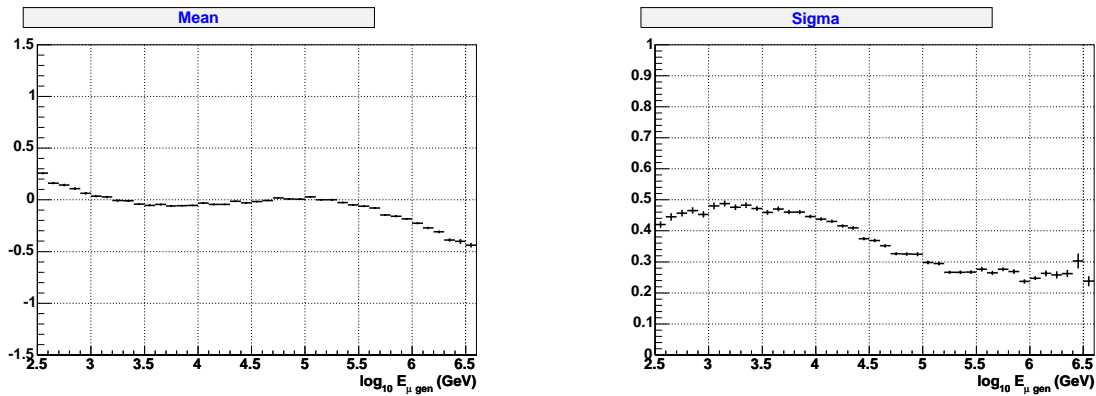

Figure 1: Dependencia con la energía de la media (izquierda) y la desviación estándar (derecha) del ajuste de la distribución de $\log_{10} E_{\mu}^{rec}/E_{\mu}^{gen}$ a una función Gaussiana.

Cortes de selección

El primer paso en el análisis es determinar qué criterios de selección se han de usar para eliminar el fondo de muones atmosféricos. Como se ha mencionado, estos muones,

producidos por los rayos cósmicos en la atmósfera se eliminan casi en su totalidad al seleccionar únicamente trazas ascendentes. Sin embargo, una pequeña fracción de ellos sobrevive a esta condición, debido a los errores en la reconstrucción (especialmente vulnerable a los multimuones, es decir, aquellos muones que han sido producidos en la misma cascada y por tanto con direcciones paralelas y correlacionadas temporalmente). Para estudiar el efecto de estos muones se han utilizado diversas muestras producidas para este propósito por la colaboración ANTARES. La muestra principal contiene primarios cuyas energías van desde 20 TeV hasta 3 EeV, equivalentes a un tiempo de adquisición de datos de entre ∼1 día hasta ∼1 año, dependiendo del rango de energía. Como base para los cortes de selección o de calidad (*Quality cuts*) se han utilizado los definidos para la estrategia de reconstrucción de trazas de Carmona, que usan el error en el ajuste de los parámetros de la traza, así como el ángulo entre el ajuste definitivo y un ajuste previo y una variable definida específicamente para eliminar las trazas "fantasma" debidas a la simetría del efecto Cherenkov. Sin embargo, unos pocos sucesos sobreviven a ellos, de manera que se han estudiado diferentes criterios para eliminar totalmente este fondo de muones atmosféricos. El conjunto final de criterios de selección adoptados en este análisis se denomina *Level* 2.

La tabla 1 muestra el número de sucesos por año después de aplicar distintos niveles de selección. Como se puede ver en la tabla, además de rechazar completamente los muones atmosféricos de la muestra se consigue disminuir un 17% el número de neutrinos atmosféricos respecto a los cortes de selección estándares de la estrategia Carmona. El número de sucesos de señal (usando el límite Waxman-Bahcall) sólo se reduce un 7%.

Nivel de selección	Muones atmosféricos (año^{-1})	Neutrinos atmosféricos (año^{-1})	Señal (año^{-1})
Reconstruidos	7.8×10^6	6120	26
Reconstruidos hacia arriba	6.1×10^6	6080	26
Carmona Quality	1170	1800	13
Level 2	0	1510	12

Table 1: Comparación del número de sucesos por año que pasan distintos criterios de selección.

Sensibilidad a flujos difusos de neutrinos de alta energía

El fondo de neutrinos atmosféricos no puede ser eliminado simplemente con cortes en la calidad de la reconstrucción de la traza porque son también sucesos producidos por neutrinos. Para el caso de búsqueda de fuentes puntuales se han de buscar acumulaciones de sucesos con una probabilidad suficientemente baja de haber sido producidos por fondo. En cambio, cuando se busca un exceso de señal de flujos difusos (es decir, el flujo integrado producido por todas las fuentes que no pueden ser resueltas

espacialmente) solamente se puede usar como criterio de discriminación el hecho de que las fuentes emiten con un índice espectral menor que el esperado para el fondo de neutrinos atmosféricos. Por ello se espera que a altas energías (> 10 TeV) el espectro medido esté dominado por los neutrinos astrofísicos. Sin embargo, hay que tener en cuenta que es también a partir de esas energías cuando se espera que los neutrinos *prompt* empiecen a ser relevantes.

Siguiendo el método descrito en el apartado anterior se ha calculado el Factor de Rechazo de Modelos usando la energía reconstruida y el número total de *hits* del suceso. También se ha calculado el MRF usando la energía verdadera como valor de referencia. En la tabla 2 se muestran estos resultados. Se ha comprobado que la mejor variable para hacer esta discriminación es el número de *hits*.

1 año					
Variable	MRF (FC)	MRF (Neyman)	Corte óptimo	Fondo	Señal
Energía verdadera	1.17	0.96	2.2×10^4 (GeV)	3.6	4.0
Energía reconstruida	2.56	2.09	7.9×10^4 (GeV)	4.6	2.0
Número de *hits*	1.72	1.40	287	4.6	2.9

Table 2: Factor de la Rechazo de Modelos para distintas variables. En la primera columna el MRF se obtiene de manera que el límite superior se calcula utilizando el método Feldman-Cousins. En la siguiente columna se usa el método frecuentista de Neyman. También se indica el valor de corte óptimo y el número de sucesos de señal (límite Waxman-Bahcall) y de fondo esperados por encima de dicho umbral tras un año de toma de datos.

El MRF obtenido para Waxman-Bahcall se traduce en un límite para flujos difusos de $E^2\Phi_{90} < 7.7 \times 10^{-8}$ GeV cm^{-2} s^{-1} sr^{-1} tras un año, según el método Feldman-Cousins. En tres años, este límite se reduce en un factor dos. También se ha calculado el MRF para el límite de Mannheim-Protheroe-Rachen y para otros modelos de señal. Estos valores son aproximadamente un 20% más bajos que los del anterior cálculo realizado en la colaboración ANTARES para el límite de flujos difusos. Esta mejora se explica parcialmente porque el detector usado en este análisis tiene dos líneas más (aunque el mismo número de fotomultiplicadores). Otras diferencias importantes, además de la variable usada para hacer la discriminación de los neutrinos atmosféricos, son la estrategia de reconstrucción de trazas y la muestra de muones atmosféricos, con una mayor cantidad de sucesos.

Como se ha explicado anteriormente, existen varias fuentes de errores sistemáticos en este cálculo. En primer lugar, la incertidumbre en la normalización del flujo de neutrinos convencionales se estima en un 25-30%, principalmente debido a la incertidumbre en el flujo de primarios y en las secciones eficaces de interacción a alta energía. Por otro lado, hay que añadir la incertidumbre debida a los neutrinos *prompt* (25%), que son dominantes a altas energías. En cuanto a las incertidumbres en la eficiencia de detección, cabe destacar las debidas al modelo de agua. Otros errores sistemáticos como

los de la propagación de los neutrinos y los muones, o la tasa de potasio-40 se estima que tienen un efector menor. Cuando se incluyen estas fuentes de errores en el cálculo de la sensibilidad, el límite superior tras un (tres) año en el flujo difuso de neutrinos es $E^2\Phi_{90} < 9.0 \times 10^{-8}$ GeV cm^{-2} s^{-1} sr^{-1} ($E^2\Phi_{90} < 4.3 \times 10^{-8}$ GeV cm^{-2} s^{-1} sr^{-1}), es decir un 15% mayor.

Comparación de modelos mediante tests estadísticos

Se han comparado las distribuciones esperadas para el estimador x_{low} para diferentes modelos de neutrinos atmosféricos con y sin contribución de señal o de neutrinos *prompt*, considerando los siguientes casos:

- Neutrinos atmosféricos convencionales: modelos Bartol y Fluka.

- Neutrinos atmosféricos *prompt*: modelo QGSM, en las versiones que predicen un número máximo y mínimo de neutrinos.

- Señal: límites de Waxman-Bahcall y de Mannheim-Protheroe-Rachen.

El procedimiento llevado a cabo para comparar las distribuciones esperadas es el siguiente. Para cada una de la hipótesis anteriores se generan las correspondientes distribuciones del estimador x_{low} incluyendo las fluctuaciones poissonianas. Entonces comparamos dicha distribución con el espectro original y con la predicción de Bartol. Dado que las fluctuaciones estadísticas hacen que los resultados cambien de un *run* a otro, generamos 1000 experimentos de un año y tres años y obtenemos el porcentaje de experimentos en los que la probabilidad del estadístico analizado (Kolmogorov-Smirnov y Pearson) es mayor del 5% y del 50%, como se indica en la tabla 3. Los resultados muestran que, salvo para los modelos más optimistas, las diferencias no son lo suficientemente significativas como para ser concluyentes. Sin embargo, el poder de discriminación al cabo de tres años es bastante mejor.

Deconvolución de espectros de energía

Para estudiar las prestaciones de los métodos de deconvolución que se han estudiado, se ha reconstruido la distribución del estimador x_{low} de los muones ascendentes.

En el caso del método SVD, el primer paso es generar la matriz respuesta. Esta matriz es generada usando tres espectros distintos, con el fin de demostrar que el método es poco sensible a esta elección. En principio, bastaría con invertir la matriz respuesta para calcular el espectro verdadero. Sin embargo, las fluctuaciones estadísticas en la distribución medida dan lugar a soluciones altamente oscilantes carentes de sentido físico. Una de las ventajas del método SVD es que permite identificar los términos que contribuyen en mayor medida a dichas oscilaciones. El siguiente paso consiste en añadir un término de regularización para atenuar estas oscilaciones. Para elegir el valor

P>0.05				
	Pearson		**Kolmogorov-Smirnov**	
Modelo	Verdadero (%)	Bartol (%)	Verdadero (%)	Bartol(%)
Bartol	95	95	95	95
Fluka	94	90	96	95
$QGSM_{op}$	92	32	93	58
$QGSM_{pe}$	93	85	95	90
WB	95	30	94	90
MPR	94	0	95	0
0.1·MPR	95	29	94	71

P>0.50				
	Pearson		**Kolmogorov-Smirnov**	
Modelo	Verdadero (%)	Bartol (%)	Verdadero (%)	Bartol (%)
Bartol	50	50	51	51
Fluka	51	45	51	48
$QGSM_{op}$	49	06	50	11
$QGSM_{pe}$	54	32	50	42
WB	50	06	51	42
MPR	48	0	51	0
0.1·MPR	48	4	48	19

Table 3: Porcentaje de experimentos en los que la probabilidad de los estadísticos de los tests de Kolmogorov-Smirnov y de Pearson es mayor que 0.05 (arriba) y 0.50 (abajo) cuando la distribución medida de $\log_{10} X_{low}$ se compara con la original y con la de Bartol, tras tres años de toma de datos.

óptimo que modula este término se ha usado la curva que relaciona la contribución de la solución regularizada con el correspondiente residuo. La figura 2 muestra los resultados para uno de los casos estudiados.
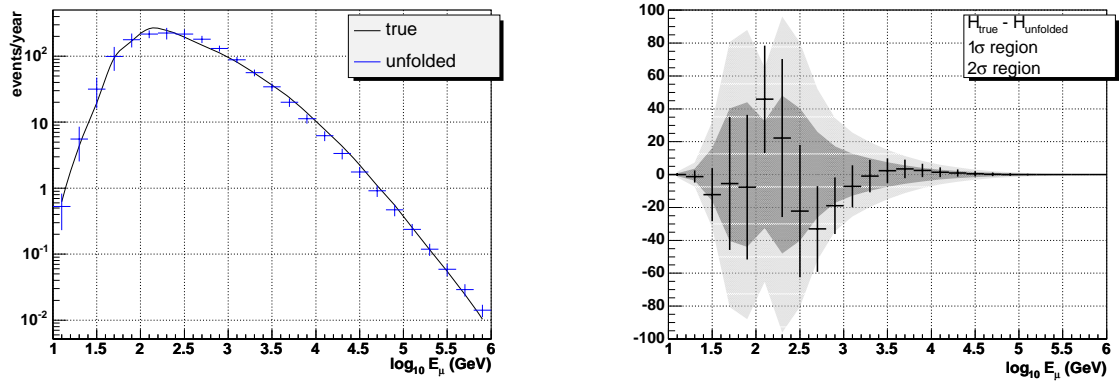

Figure 2: Resultados de la deconvolución para uno de los casos estudiados. Izquierda: espectros verdadero (línea continua negra) y deconvolucionado (barras azules). Derecha: diferencia entre el espectro verdadero y el deconvolucionado. Las regiones de 1σ y 2σ están también indicadas como referencia.

En el caso del método iterativo, es necesario asumir una distribución inicial, de manera que tras varias iteraciones, el espectro resultante ha de converger al verdadero. Sin embargo, las fluctuaciones estadísticas impiden esta convergencia, por lo que el proceso se detiene tras un número fijo de iteraciones. Los estudios realizados para varios modelos muestran que el número óptimo es $n_{it}=3$.

Ambos métodos muestran, en general, buen comportamiento. Sin embargo, consideramos más recomendable el método SVD, ya que la calidad de la reconstrucción suele ser ligeramente mejor y no depende de un número determinado de iteraciones.

Conclusiones

El telescopio ANTARES abrirá la ventana de la Astrofísica de neutrinos del Hemisferio Sur. Muchos de los objetos astrofísicos más interesantes (galaxias de núcleo activo, explosiones de rayos gamma, microcuásares...) se espera que emitan flujos de neutrinos de alta energía, de manera que detectores como ANTARES tendrán un destacado papel en los próximos años. Otros objetivos de interés para ANTARES son la búsqueda de materia oscura y las oscilaciones de neutrinos. Tras varios años de intensos estudios de los aspectos técnicos del proyecto, de los parámetros ambientales del emplazamiento y de las prestaciones del telescopio, la adquisición de datos comenzará en 2005. El objetivo de esta tesis ha estado enfocado hacia aspectos relacionados con la "calorimetría" del detector, como la reconstrucción de la energía, la sensibilidad a flujos difusos de neutrinos de alta energía y la deconvolución de espectros de energía.

- **Reconstrucción de la energía**

  – Se han considerado varias parametrizaciones de la relación entre la energía verdadera del muon y el estimador. Los mejores resultados se obtienen con el ajustes a una línea recta.

  – Otros polinomios de mayor grado también se han considerado, pero hay una fracción de sucesos que no pueden ser reconstruidos, ya que quedan por debajo del mínimo (bajas energías) o por encima del máximo (altas energías) de la parábola o la función cúbica.

  – A energías intermedias, se obtiene una buena relación entre la energía reconstruida y la generada. El valor medio de la distribución de $\log_{10} E_{rec}^{\mu}/E_{gen}^{\mu}$ está en torno a cero (± 0.2) para energías intermedias (500 GeV-1 PeV).

  – El valor de la anchura de la distribución $\log_{10} E_{rec}^{\mu}/E_{gen}^{\mu}$ decrece con la energía desde 0.45 (a 500 GeV) hasta 0.25 (a 1 PeV). Esto implica un factor 2-3 en la resolución energética.

  – A energías por debajo de la energía crítica, la relación entre el estimador y la energía del muon se desvía de una línea recta debido a que $(\Delta E_{\mu}/\Delta x)$, dominado por la ionización, es casi independiente de la energía. A altas energías, el estimador se satura, de manera que la energía se subestima ligeramente (0.25 a 1 PeV).

  – La dependencia de estos resultados con factores geométricos también ha sido estudiada. Entre otras conclusiones se ha encontrado una ligera tendencia a sobreestimar (subestimar) la energía de los sucesos más lejanos (cercanos) al detector. Además, la energía de los muones verticales ($\cos\theta > 0.8$) también es levemente sobreestimada (~ 0.1).

- **Sensibilidad a flujos difusos**

  – Al nivel de la estadística simulada, todo el fondo de muones atmosféricos es rechazado por los criterios de selección que se han usado.

  – La pérdida de sucesos de señal respecto a los cortes de calidad estándares de la estrategia de Carmona es menor del 7%, mientras que se mejora en un 17% el rechazo del fondo de neutrinos atmosféricos.

  – Se han estudiado dos variables para hacer el corte final que separa la señal del fondo de neutrinos atmosféricos: la energía reconstruida y el número total de *hits* del suceso. Estas opciones se han comparado minimizando el denominado Factor de Rechazo de Modelos.

  – El mejor MRF usando la energía reconstruida es, para una señal en el límite Waxman-Bahcall, 2.56 (FC) con un corte en 7.9×10^4 GeV. Utilizando el número total de *hits* se obtiene un resultado mejor: MRF=1.72, con un corte en 287 *hits*. Estos valores se pueden comparar con el obtenido usando la energía verdadera: MRF=1.17.

- El límite calculado para una señal en el límite Waxman-Bahcall es $E^2\Phi_{90} < 7.7 \times 10^{-8}$ GeV cm^{-2} s^{-1} sr^{-1} tras un año de toma de datos. El límite para tres años es $E^2\Phi_{90} < 3.8 \times 10^{-8}$ GeV cm^{-2} s^{-1} sr^{-1}.

- Cuando se incluyen los errores sistemáticos debidos a las incertidumbres en la normalización del fondo de neutrinos atmosféricos convencionales, el modelo de neutrinos *prompt*, las propiedades ópticas de agua y otros factores menores, el límite es $E^2\Phi_{90} < 9.0 \times 10^{-8}$ GeV cm^{-2} s^{-1} sr^{-1} para un año y $E^2\Phi_{90} < 4.3 \times 10^{-8}$ GeV cm^{-2} s^{-1} sr^{-1}.

- Estos valores son un 20% menor que los obtenidos en el anterior análisis realizado en la colaboración ANTARES. Parte de esta mejora se explica por hecho de que el detector usado en este análisis es la versión actual de 12 líneas (en lugar de 10), aunque el número de fotomultiplicadores es el mismo. Otra diferencia importante, aparte de la variable usada para la discriminación del fondo de neutrinos atmosféricos y la estrategia de reconstrucción de trazas, es la nueva muestra Monte Carlo de muones atmosféricos que se ha utilizado, más significativa estadísticamente.

- La sensibilidad calculada para ANTARES tras un año de toma de datos es un factor tres mejor que el valor actualmente establecido por AMANDA.

También se ha utilizado el test de Kolmogorov-Smirnov y el de Pearson para comparar las distribuciones del estimador x_{low} generadas incluyendo la presencia de señal o de una componente de neutrinos *prompt*, con una distribución generada únicamente con neutrinos atmosféricos convencionales. Los resultados muestran que esta comparación es poco concluyente para un año de adquisición, pero mejoran de manera apreciable en tres años.

- **Deconvolución de espectros**

  - Se han estudiado dos métodos de deconvolución. El primero de ellos se basa en la descomposición en valores singulares de la matriz respuesta y el segundo es un método iterativo basado en el teorema de Bayes.

  - Se ha probado que el algoritmo SVD reconstruye correctamente el espectro, incluso si la matriz respuesta ha sido generada con una función distinta de la distribución a medir.

  - El método iterativo basado en el teorema de Bayes es más sensible a incertidumbres en la forma de la distribución inicial, aunque la reconstrucción es también aceptable.

  - Mediante el algoritmo SVD se ha podido reconstruir simplificadamente el flujo atmosférico de muones y de neutrinos.

Preface

The observation of the outside Universe has historically been a source of knowledge. The first instrument for such observation was the bare eye, but the objects seen in this way were just the tip of a cosmic iceberg. When Galileo turned his telescope on the night sky in 1609, a giant step was taken towards a better knowledge of the Universe. But this was just the beginning. We know now that the visible radiation is just a small region of the electromagnetic spectrum. In the last century, scientists have developed instruments to detect radio-waves, infrared radiation, X-rays, gamma rays... which have provided a large amount of information about many of the most relevant questions concerning the Cosmos. In addition to the electromagnetic radiation, the role played by the detection of cosmic rays has also been fundamental. They were the first signal which pointed out that our list of the basic elements of matter was incomplete.

Nowadays, the observation of the most energetic cosmic rays and photons represents again a major challenge, since the question about their origin is still open. However, both photons and cosmic rays have limitations to study the very far or dense regions of the Universe.

The handicap for photons is their interaction with low energy photons of the cosmic background radiation and with matter. Photons with energy of a few hundred TeV cannot travel from the center of the Galaxy to the Earth (8.5 kpc).

There is a similar limitation with protons, since they also interact with the cosmic microwave background, what limits their range to <100 Mpc for $E_p \sim 10^{20}$ eV. For lower energies, the directional information is lost due to magnetic fields.

Neutrons, although neutral and thus not deflected by magnetic fields, have a short lifetime that limits severely their range. Even at very high energies (EeV), they hardly could reach us from the Galactic Center.

Thus, in order to go further in the observation of the Universe, we would need a probe which should be neutral, stable and weakly interacting. A candidate which fulfills all these conditions is the neutrino.

Neutrinos can travel distances much longer than protons or photons because they only interact weakly. However, this is also the reason why they have not been used in Astronomy until very recently. Large detectors are needed to compensate the low interaction cross section. A possible way to detect these neutrinos was proposed by Markov in 1960 [1]. Neutrinos would interact *via* charged current with one of the nucleons of the surrounding medium, and would produce a muon, which would emit Cherenkov photons in the water or ice, to be detected by photomultipliers. Given the

low cross section of the νN interaction and the predicted fluxes, the size of the detector should be of the order of $\sim$km^3 [2].

The first results from AMANDA [3] and BAIKAL [4] encourage the interest of this idea, since they have shown its feasibility in the ice and lake water environments, respectively. The ANTARES collaboration aims to prove that a neutrino telescope can be built in the sea, since this environment has some advantages with respect to lake water or antarctic ice. The project is integrated by scientists (astronomers, particle physicists, oceanographers...) of France, Italy, the Netherlands, Germany, Spain, the United Kingdom, and Russia. It is meant to be a first step towards a km^3 neutrino observatory in the North Hemisphere.

The aim of this work is to study one of the most relevant characteristics of this experiment, the energy reconstruction as well as some related topics. In particular, this study has focused on the high-energy neutrino diffuse flux, i.e. the total integrated flux produced by spatially unresolved cosmic sources in the whole sky. As it will be explained later, the discrimination between this cosmic signal flux and the atmospheric neutrino background can only be made on the basis of the neutrino energy. The performance of the detector to make such discrimination is called sensitivity and is an important parameter to compare with other experiments. In addition, another interesting subject, the capability of the detector to reconstruct the energy spectra, has also been tackled.

The structure of this work is as follows. First, a general overview of neutrino astronomy (Chapter 1) and the ANTARES detector (Chapter 2) are given. Then, the Montecarlo simulation tools are explained in Chapter 3. The energy reconstruction procedure is described in Chapter 4. The calculation of the sensitivity to diffuse fluxes is shown in Chapter 5. In this chapter, a comparison based on fit-of-goodness tests is also presented. Finally, Chapter 6 is devoted to the deconvolution of energy spectra.

Chapter 1

High-energy neutrino astronomy

The onset of Neutrino Astronomy is very recent. In this chapter we will review briefly the main milestones which have led scientists to believe that neutrinos can be a powerful tool to study the Universe. The expected neutrino background and sources will be described and an explanation of the upper bounds for diffuse fluxes will be given.

1.1 Introduction

The hypothesis of the existence of neutrinos was put forward by W. E. Pauli in 1930 in order to explain the continuous energy spectrum of the beta decay. Several physicists, including N. H. D. Bohr, had proposed the violation of the energy conservation principle. However, even giving up this solid principle, the violation of the angular momentum could not be explained. The suggestion of Pauli that an electrically neutral particle[1] would be also produced in the beta decay implied, however that it would be very hard to detect.

It took more than twenty years to demonstrate experimentally the existence of neutrinos. By that time, the observation of charged particles in several meson decays had given additional support to the idea of Pauli but the confirmation came in 1956, when C. L. Cowan and F. Reines [5] detected some neutrinos produced in the Hanford nuclear reactor. Indeed, they saw the anti-neutrinos produced by beta decay. A small fraction of these anti-neutrinos interacted as initiators of the inverse-beta decay reaction:

$$\bar{\nu}_e + p \to n + e^+ \tag{1.1}$$

The signature of this reaction is given by the two photons produced by the annihilation of the positron and the photon emitted after by the excited nucleus of cadmium which had absorbed the neutron.

---

[1]The name proposed by Pauli was "neutron", but this was latter reserved for the heavy component of the nucleus. The term neutrino was coined by Fermi.

The confirmation of the existence of the neutrino solved an important question, but soon, other puzzles arose. R. Davis [6] measured in 1969 a significant disagreement between the detected number of neutrinos produced in a tank with 400,000 liters of perchlorethylene and the theoretical prediction according to the Standard Solar Model. Many explanations tried to justify this discrepancy. Some of them involved a change in the solar model and others demanded new particle physics. At the end, it has been proved that the solution concerns the nature of the neutrino. There are three flavours of neutrinos and each flavour can oscillate from one type to another, as suggested by B. Pontecorvo in 1957 [7].

In the experiment of R. Davis, the signal consisted in the formation of radioactive ^{37}Ar, which was extracted later, so directional information was lost. This changed with Kamiokande, a large pool of pure water surrounded by 1,000 photomultipliers, which measured the Cherenkov cone produced by electrons and muons induced by neutrinos. This experiment detected, together with IMB [8], the burst of neutrinos produced in the supernova 1987A. In 1988, the Kamiokande collaboration confirmed the deficit of electron neutrinos coming from the Sun. The upgrading of this experiment is SuperKamiokande [9], with 11,146 photomultipliers, which provided much more accurate data on the electron neutrino deficit. The best explanation of the observed difference between downward and upward fluxes was neutrino oscillation.

The last piece of information to confirm the oscillations of neutrinos was given in 2002 by the Sudbury Neutrino Observatory (SNO) [10]. This experiment, basically a 100 ton heavy water target surrounded by PMTs, allowed to determine separately the fluxes of solar electron neutrinos and of all active flavours. It was seen that the latter flux agrees perfectly with the solar model computations for the electron neutrinos and a ν_e deficit was still observed, confirming the neutrino flavour transition for the first time.

Other relevant experiments to measure neutrino parameters can be mentioned. The KamLAND experiment [11] detects electron anti-neutrinos emitted by nuclear power reactors within few hundred kilometers. In the K2K project [12], a neutrino beam produced at the KEK proton synchrotron is sent towards Superkamiokande (250 km away). Two long baseline experiments are also planned: NuMi, a neutrino beam from Fermilab to the MINOS [13] detector located at the Soudan mine, and CNGS, a neutrino beam from CERN to Gran Sasso, where two experiments, ICARUS [14] and OPERA [15] have been proposed. Experiments where the neutrinos will be used as astrophysics tool will be described in the next chapter.

This brief introduction only summarizes the past and current activity in the neutrino experiment field, but shows the key role which neutrinos play in experimental particle physics.

1.2 High-energy cosmic rays

In this section we will review the most important properties about cosmic rays, which are intimately linked to neutrino astronomy, since some of the hints about the existence of high-energy neutrinos are given by the studies on cosmic rays.

Cosmic rays were discovered by V. Hess in 1912 [16]. He used a gold leaf electroscope as radiation counter on a balloon flight and measured the amount of radiation as the balloon climbed[2]. Contrary to what was expected, the level of radiation increased with altitude, showing that some kind of radiation is entering the atmosphere from the space. This is why he gave the name of "cosmic radiation" to this new phenomenon.

1.2.1 Composition

The composition of cosmic rays has been measured by several experiments on ground, balloons and space satellites. It has been seen that most cosmic rays are protons (90% of nuclei). There is also a small fraction of heavier nuclei (mainly alpha particles: 9% of the total). When compared with the solar system, both compositions are similar, with some relevant differences. Firstly, nuclei with Z>1 are much more abundant in cosmic rays (which is not well understood yet). Secondly, there are two groups of elements (Li-Be-B and Sc-Ti-V-Cr-Mn) which are many orders of magnitude more abundant in cosmic rays than in the Solar System due to the collisions of carbon and oxygen (for the first group) and of iron (for the second group) in the interstellar medium. Apart from a few ($\sim 0.1\%$) anti-protons, no anti-nuclei have been observed [17].

1.2.2 Energy spectrum

One of the most striking features of the cosmic rays is that it expands along many decades of energy, from 10^9 eV up to above 10^{20} eV. The energy spectrum follows a power law, which breaks in two points[3]:

$$\frac{dN}{dE} \propto E^{-\gamma}; \ \gamma = \begin{cases} 2.7 & \text{for } 10^{10} \text{ eV} < E \leq 5 \times 10^{15} \text{ eV} \\ 3.0 & \text{for } 5 \times 10^{15} \text{ eV} < E \leq 3 \times 10^{18} \text{ eV} \\ \sim 2.7 & \text{for } E > 3 \times 10^{18} \text{ eV} \end{cases} \tag{1.2}$$

This means a fast decrease with energy. The flux falls from 1 particle/cm^2 per second at $E = 10^9$ eV to 1 particle/km^2 per century at $E = 10^{20}$ eV. Figure 1.1 shows the measured spectrum of cosmic rays.

---

[2]Hess showed himself as a real physics adventurer climbing 5300 m without oxygen to perform this experiment.

[3]There is some evidence that a second knee at 3×10^{17} eV could exist, where the spectrum appears to dip [18]. However, this evidence is still limited.

For energies lower than 100 MeV, cosmic rays are not energetic enough to arrive at the Earth due to the solar wind shielding. Above $\sim$10 GeV per charge unit of the particle the effect of solar wind becomes negligible.

The Galactic magnetic field, which is about 6×10^{-6} G, has also a relevant effect on cosmic rays. This magnetic field determines a radius of gyration (Larmor radius), proportional to the energy to charge ratio. For protons of 3×10^{18} eV, the Larmor radius is larger than the thickness of the Galactic disk, so protons with energy larger than this value cannot originate in the Galaxy. They should have an extragalactic origin. A change in the chemical composition towards lighter elements at that point has also been measured.

Above 6×10^{19} eV, the flux should vanish due to the theoretically predicted Greisen-Zatsepin-Kuz'min (GZK) cut-off [19, 20] caused by the photo-interaction of protons with the 2.7 K primordial background radiation. However, whether this prediction is fulfilled is controversial. Some experiments, like the fluorescence detector HiRes [21] support it, whereas the ground array detector AGASA [22] has observed 8 events above the GZK cut-off.

1.2.3 Origin of cosmic rays

The origin of cosmic rays is a key issue for neutrino astronomy, since high energy neutrinos are associated to the production of cosmic rays in some scenarios. One of the difficulties in the determination of the origin of cosmic rays comes from the fact that charged particles are deviated by the Galactic and extra-Galactic magnetic fields. The bending angle of a particle in a magnetic field is given by

$$\theta(rad) \sim L(kpc) \cdot Z \frac{B(\mu G)}{E(EeV)} \tag{1.3}$$

where L is the travelled distance; Z, the charge; B, the magnetic field, and E, the particle energy.

The most accepted scenario to understand how the cosmic rays are accelerated is the Fermi mechanism [23,24], since it explains very naturally the observed power-law energy spectrum. Although it was proposed to explain the particle acceleration in supernovas, it can be applied to many other cataclysmic astrophysical objects. Let us consider the scenario of a supernova explosion which has produced a moving magnetized plasma. The underlying idea of Fermi mechanism is to transfer macroscopic kinetic energy from this plasma to individual charged particles. If we assume that the accelerated particle crosses the acceleration region several times increasing its energy by an amount proportional to its energy ($\Delta E = \xi E$), the particle energy after n encounters will be

$$E_n = E_o(1 + \xi)^n \tag{1.4}$$

where E_o is the initial energy of the particle. It can be shown [25] that the number of particles with energy larger that E follows a power law
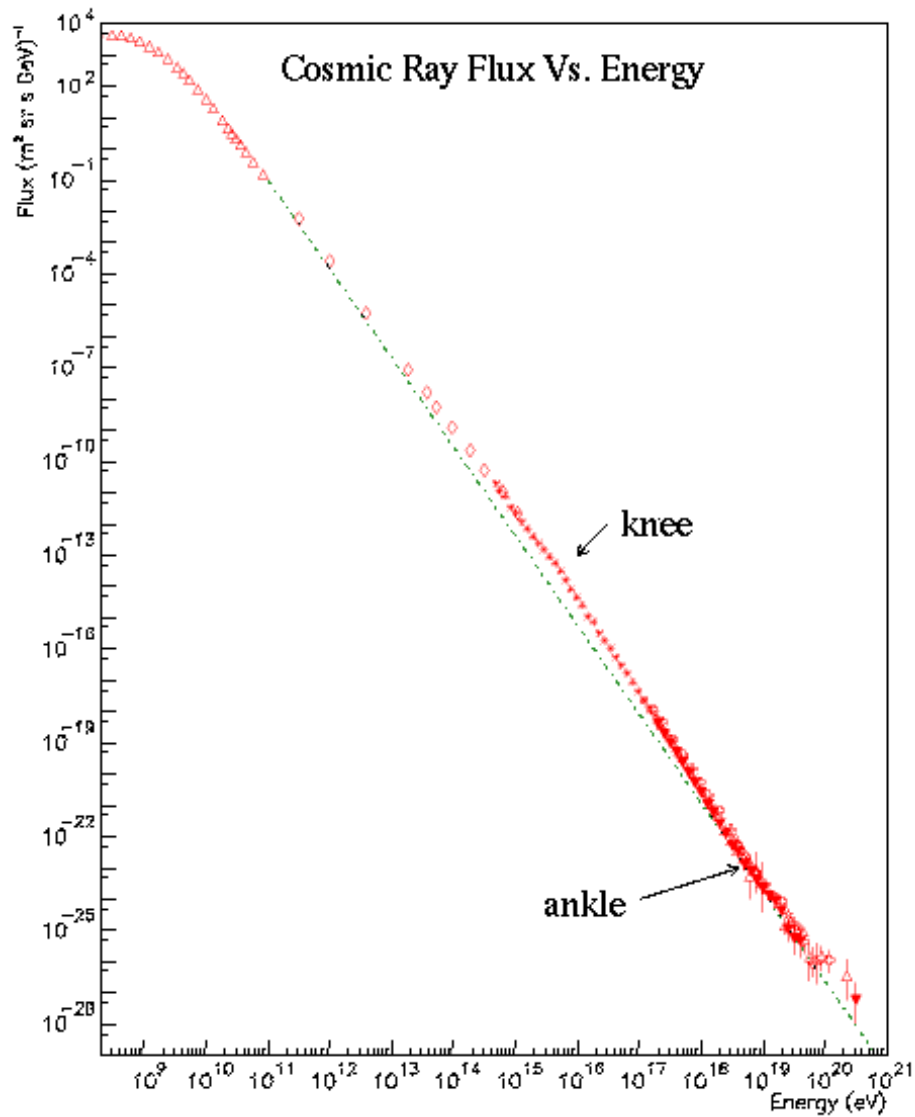
Figure 1.1: Cosmic ray spectrum. Although it spans a wide range of energies, the shape can be described by a power law whose spectral index changes in two points: the *knee*, at 5×10^{15} eV and the *ankle*, at 3×10^{18} eV.

$$N(> E) \propto \frac{1}{P_{esc}} \left(\frac{E}{E_o} \right)^{-\gamma} \qquad (1.5)$$

where P_{esc} is the probability of the particle to escape from the acceleration region after each encounter.

The original idea of Fermi assumed that the particle enters in a moving, magnetized cloud of plasma and "scatters" elastically on the irregularities in the magnetic field. After several interactions, the average motion of the particle is the same as the motion of the gas cloud (see figure 1.2, left). The average gain in energy is

$$\frac{\langle \Delta E \rangle}{E} \sim \frac{4}{3} \beta^2 \qquad (1.6)$$

This is called the second order Fermi acceleration mechanism since the net average gain in energy is proportional to the square of β, the velocity of the plasma cloud.

In 1977, a slightly different version of the mechanism was proposed [26, 27]. It is illustrated in figure 1.2 (right). In this case, the particle does not enter into a cloud but goes back and forth between the two sides of a shock-wave front. The average energy increase is

$$\frac{\langle \Delta E \rangle}{E} \sim \frac{4}{3} \beta \qquad (1.7)$$

where now β is the relative velocity of the shocked plasma flow.

Note that the key difference between both cases is that for gas clouds, the average scattered angle is isotropic in the rest frame of the moving cloud, while this is not the case for a plane shock. In other words, the particle in the first case can go out in every direction but in the second case it goes out "upstream".

The Fermi mechanism is supposed to occur in supernova explosions, which would mean the bulk of cosmic rays in the Galaxy. The maximum energy that can be reached in this phenomenon is ~ 100 TeV. During the travel of these accelerated cosmic rays through the Galaxy, they can interact and produce gamma-rays (from neutral pion decay), positrons, neutrons, anti-protons and neutrinos.

There is no much consensus about how particles are accelerated to energies beyond the knee. One possibility could be the effect of a new accelerator, such as pulsars, but the fact that the predicted flux has to match in the knee is a problem. Other possibility could be a decrease of the acceleration efficiency in those theories which appeal to supernova shocks racing through stellar winds. The acceleration between the expanding shells and shocks of different supernovae could also explain this feature.

Concerning the region between the ankle and the GZK-cutoff, the most plausible sources are pulsars (in particular magnetars, i.e. pulsars with very high magnetic fields) and gamma-ray bursts. These sources will be described in more detail later, since they are also high-energy neutrino candidate sources.

Beyond the GZK-cutoff, challenging difficulties arise since no astrophysical sources which could account for such high energetic particles seem to exist nearby. For this
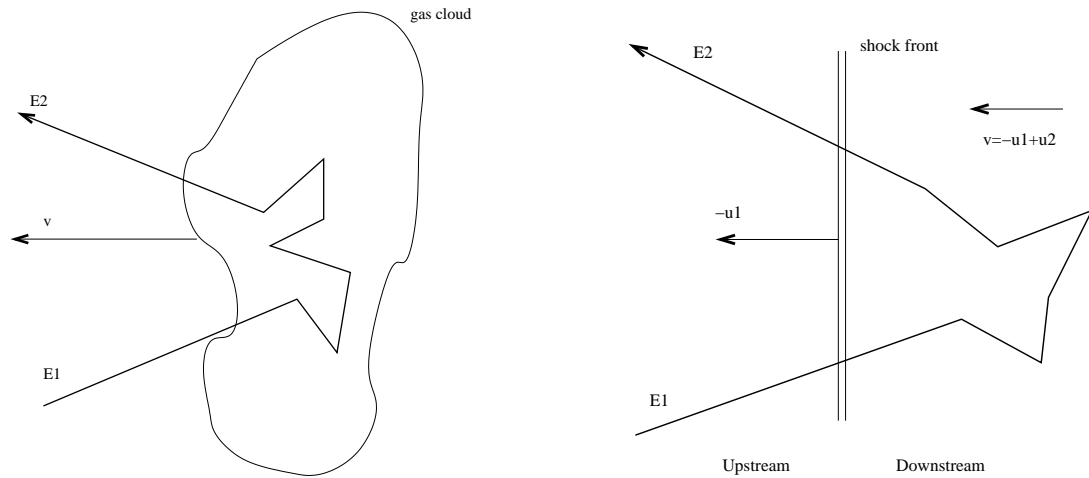
Figure 1.2: Left: Second order Fermi acceleration mechanism, produced by a moving magnetized cloud. Right: First order Fermi acceleration mechanism, produced by a shock front. The initial energy of the particle is E1. After several scatters, it exits with energy E2.

reason, more exotic models have been developed, such as the decay of topological defects (strongly constrained by observations), decay of primordial black holes or the violation of Lorentz invariance.

1.3   High energy photons

Gamma-ray astronomy is also deeply linked with neutrino astronomy. Most of the cosmic γ-rays form a random background, produced by the interaction of cosmic rays with the interstellar gas. However, the EGRET detector on the Compton Gamma-Ray Observatory has showed the existence of point-like gamma-rays sources, which has opened the question of how these high energy photons are produced.

There are mainly two possibilities to produce such gamma-rays: on the one hand the leptonic mechanisms (synchrotron radiation, *bremsstrahlung* and inverse Compton scattering), and on the other hand the hadronic mechanism, which assumes that the photons are produced by the decay of neutral pions. The latter possibility implies that in addition to neutral pions, charged pions should also be produced. In this case, a flux of high energy neutrinos would also be emitted. For this reason, the sources which emit high energy photons will be described in this section.

Figure 1.3 shows the sky plot of the EGRET sources emitting above 100 MeV. It can be seen that apart from objects like active galactic nuclei or pulsars, most of the other sources have not been identified. Nowadays, there are three satellite projects which will continue the work of EGRET: AMS [28], Agile [29] and GLAST [30].

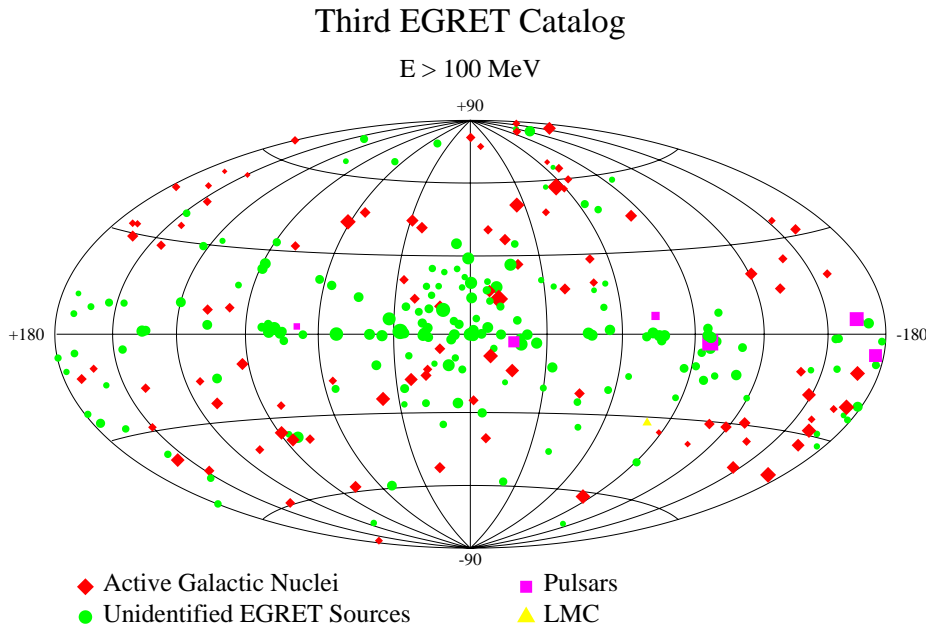Since the gamma-ray fluxes for higher energies (above few tens of GeV) are very

Figure 1.3: Third EGRET catalog. γ-ray sources emitting above 100 MeV are shown.
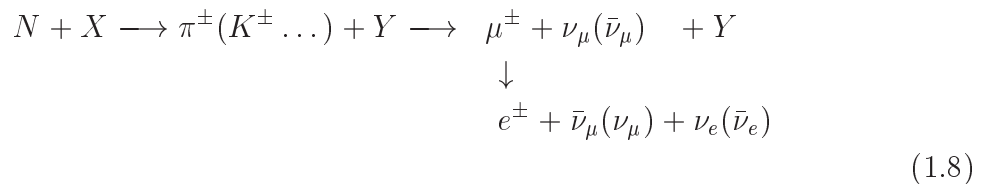
low and the acceptance of satellites is too small, ground-based detectors are needed to observe these energies. Photons in the TeV range will produce an electron-positron pair in the upper atmosphere. These particles will in turn emit high energy photons by *bremsstrahlung*, which will convert into new electron-positron pairs giving rise to an electromagnetic shower. The electrons and the positrons will eventually also produce Cherenkov photons, which can be detected at ground level by means of telescopes which collect the light towards photomultipliers. In this way, the direction and energy information of the primary photon can be obtained. This technique was proved to be successful by several experiments (Whipple [31], HEGRA [32], CANGAROO [33] and CAT [34]). At present, four ground experiments have already started to take data: HESS [35], VERITAS [36], CANGAROO-II [37] and MAGIC [38].

Very recent results support the idea that the TeV photons emitted by some sources are produced by hadronic mechanisms and therefore the existence of high energy neutrino sources. Firstly, the CANGAROO collaboration has reported the observation of a spectrum of RX J1713.7 3946 which is perfectly compatible with a neutral pion decay origin and which cannot be easily explained by electromagnetic mechanisms [39]. However, this conclusion is still controversial [40]. On the other hand, the HESS collaboration has pointed out that the energy spectrum of Sgr A* seems to follow a power-law with spectral index 2.20$\pm$0.09$\pm$0.15 [41], which would not be compatible with an inverse Compton origin since magnetic fields are very low in this region. Although these explanations have to be confirmed, they encourage the observation of

high energy neutrinos. Both J1713.7 3946 and Sgr A* will be visible for ANTARES.

1.4 Neutrino production

Neutrinos are expected to be produced as a product of the interaction of high energy nucleons with matter or radiation:

$$
\begin{aligned}
N + X \longrightarrow \pi^{\pm}(K^{\pm}\dots) + Y \longrightarrow \quad & \mu^{\pm} + \nu_{\mu}(\bar{\nu}_{\mu}) \quad + Y \\
& \downarrow \\
& e^{\pm} + \bar{\nu}_{\mu}(\nu_{\mu}) + \nu_{e}(\bar{\nu}_{e})
\end{aligned}
\tag{1.8}
$$

The target for these interactions are protons and photons, in cosmic sources, or protons and neutrons, in the atmosphere. The energy distribution of the target and the proton beam determines the spectrum of the neutrino energy. In dilute targets (like typical cosmic accelerators), all secondaries decay in flight, so the neutrino spectrum is very similar to the proton primary spectrum ($\gamma \sim 2.2$). On the other hand, the atmosphere is a much more dense target, so the meson interaction competes with decay and the spectrum steepens ($\gamma \sim 3.7$). Finally, the Galaxy intestellar medium represents a third scenario, since it is dilute enough to allow free decay, but protons leak in an energy-dependent way, so the neutrino spectrum is intermediate ($\gamma \sim 2.9$).

1.5 Neutrino background

An important question for neutrino astronomy is related to the possible sources of neutrino background, which indeed constitute the guaranteed sources of neutrinos.

1.5.1 Atmospheric neutrinos

Atmospheric neutrinos are yielded by cosmic rays when they penetrate the Earth's atmosphere. Their energy spectrum expands from a few MeVs to the energies of the most energetic cosmic rays. Therefore, they represent an unavoidable source of background for extraterrestrial neutrinos. They are produced in the decay of pions and other mesons and, to a lesser degree, in muon decays.

The atmospheric neutrino production is characterized by the competition between the decay and interaction of the parent meson. When the meson decay length equals the interaction length in the atmosphere both processes are balanced and the meson energy is called the critical energy. This energy depends on the target density and on the type of meson, being $\epsilon_{\pi^{\pm}}$=115 GeV for pions, $\epsilon_{K^{\pm}}$=850 GeV for kaons and $\epsilon_{D^{\pm}}$=4×10^7 GeV for D-charmed mesons. Below the critical energy, decay dominates over interaction and the neutrino spectrum follows the primary spectrum. For energies

higher than the critical enegy, the decay probability falls and the spectrum for the decay products steepens by about one power of the energy.

Neutrinos from charmed mesons are not affected by this competition between decay and interaction since due to their lifetime charmed mesons always decay in the atmosphere and, therefore, follow the original primary spectrum.

The neutrino flux coming from pions and kaons is called conventional and dominates the atmospheric flux from GeV to PeV energies. Neutrinos from charmed mesons are called prompt neutrinos because of their instantaneous decay. The energy where this prompt neutrino component starts to dominate is expected to be between 20 TeV to 1 PeV, depending on the model. Since the spectral index is similar to the one expected from extraterrestrial sources, prompt neutrinos are a very important and serious background.

The neutrino and muon spectra are directly related [42]. Above 10 GeV and up to 100 TeV, the atmospheric muon neutrino flux (ν_μ and $\bar{\nu}_\mu$) can be described by

$$\frac{d^2\Phi_{\nu_\mu}}{dE_{\nu_\mu}d\Omega} \simeq 0.0286 E_\nu^{-2.7} \left(\frac{1}{1 + \frac{6.0 E_\nu cos\theta^*}{115 \text{GeV}}} + \frac{0.213}{1 + \frac{1.44 E_\nu cos\theta^*}{850 \text{GeV}}} \right) \text{cm}^{-2}\text{s}^{-1}\text{sr}^{-1}\text{GeV}^{-1} \quad (1.9)$$

and the cosmic-ray muon flux (μ and $\bar{\mu}$) by

$$\frac{d^2\Phi_{\mu}}{dE_{\mu}d\Omega} \simeq 0.185 E_\mu^{-2.78} \left(\frac{1}{1 + \frac{1.1 E_\mu cos\theta^*}{115 \text{GeV}}} + \frac{0.054}{1 + \frac{1.1 E_\mu cos\theta^*}{850 \text{GeV}}} \right) \text{cm}^{-2}\text{s}^{-1}\text{sr}^{-1}\text{GeV}^{-1} \quad (1.10)$$

where, θ^* is the zenith angle at production. It relates to the zenith angle at the detector by $\sin\theta^* = \sin\theta \ (R_e - D)/(R_e + h)$, where R_e is the Earth radius; D, the detector depth and h, the production altitude.

The atmospheric flux follows a power law with spectral index 2.7 for energies below 100 GeV, where it steepens to 3.7 up to 1 PeV. The uncertainty in the flux normalization is around 25-30% [43, 44] for conventional neutrinos at TeV energies, whereas the spectrum shape is known with a 5% precision. The prompt neutrino contribution follows a spectral index of 2.7 and is known with an order of magnitude precision.

Another relevant characteristic of the atmospheric neutrino is the angular distribution. It has been observed that the flux is higher in the horizontal direction ("secant effect"), due to the fact that the horizontal pions and kaons which are produced in the higher part of the atmosphere have greater chances to decay in these less dense regions. The higher the energy, the stronger the effect.

1.5.2   Neutrinos from the Sun

The neutrinos produced by the Sun are of low energy ($E < 20$ MeV). However, the impact of cosmic rays on the solar atmosphere can create high energy neutrinos in a similar way as it occurs in the Earth's atmosphere. Most of the mesons are produced

in low density regions so the spectral shape is similar to the primary spectrum. Monte Carlo calculations show that only for energies above 10 TeV the neutrino flux from the Sun exceeds significantly the atmospheric flux in an aperture of one-square degree [45]. The expected rate is about 17 events per year above 100 TeV in a km^3 detector.

1.5.3 Neutrinos from the Galactic Disk

The Galactic Disk is also expected to be a source of high-energy neutrinos. These neutrinos are produced by the hadronic interactions of cosmic rays with the interstellar medium. As it has been explained, the neutrino spectrum from the secondary mesons is somewhat steeper ($\gamma \sim 2.9$) than the cosmic ray spectrum, because of the leakage energy-dependence. On the other hand, it is not as steep as the atmospheric neutrino spectrum, so the background coming from the Galactic Disk could be larger at high energies than the rate produced by conventional atmospheric neutrinos. The Galactic Centre surpasses the atmospheric background above 250 TeV, with a flux of $\sim$160 neutrinos per year and km^2 in an aperture of 5 square degrees.

1.6 Astrophysical sources

Many kinds of sources have been suggested to be high energy neutrino emitters. We review the most relevant ones, classified as galactic or extragalactic.

1.6.1 Galactic sources

The requirement on luminosity for Galactic sources is much lower than for extra-galactic objects due to the smaller distance scales. Moreover, the ANTARES location will allow to observe the Galactic Centre, where a higher density of interesting sources is expected. Among those which can produce the largest rates, we can mention (see [46] for an extensive review) the following:

- **Supernova explosions**

  The supernova are prodigious sources of gamma-rays and neutrinos at nuclear energies, which are too small to be detected by high-energy neutrino telescopes. However, and in spite of the low expected rate (2-4 per century), significant fluxes of high-energy neutrinos can be produced during the short period after the explosion. Moreover, these events would arrive in a short time window, which makes their detection easier. Different scenarios can be considered. Firstly, in the shock waves created by type II supernovae, protons could be accelerated above 10 TeV, so that up to 100 events could be detected in a km^2 detector (for a supernova at 10 kpc) [47]. Supernova remnants (SNR) containing pulsars are also canditates to neutrino emitters. Different calculations [48, 49] predict a pulsar formation rate around 0.5-5 per century. Several models exist to describe

the production of high energy neutrinos. Protheroe et al. [50] assume that heavy ions, mainly ^{56}Fe are accelerated along open magnetic field lines into the pulsar magnetosphere. Neutrons produced after the photodisintegration of these ions will interact with the dense SNR shell giving rise to gamma-rays and neutrino signals (few events in a km^2 detector). In the Beall and Bednarek model [51], neutrinos are produced in collisions of nuclei with the radiation filling the cavity below the hot expanding supernova remnant envelope. Nagataki [52] considers the production of neutrinos by the hadrons which have been thermalized in the inner shock and interact between themselves inside the pulsar wind nebula.

- **Plerions**

Supernova remnants with a centre-filled morphology are called plerions. They constitute around 10% of the SNRs, being the Crab Nebula the youngest and most energetic observed. It is believed that the emission spectrum (radio, optical and X-ray bands) is due to synchrotron radiation. It is likely that hadrons contribute in a significant fraction.

Depending on the theoretical model, the predicted neutrino rate varies from 1 event/year·km^2 [53] to 4-14 event/year·km^2 from the Crab nebula [54], which is expected to be the strongest source.

- **Shell-type supernova remnants**

Spherical supernova remnants are also a promising candidate for neutrino astronomy. As it has been mentioned in section 1.3, the CANGAROO Cherenkov telescope has reported the observation of γ-rays in the TeV range from the SNR RX J1713.7-3946 (see figure 1.4). They found that the observed spectrum can be explained better by assuming that gamma-rays are the products of π° decays in pp collisions rather than with leptonic mechanisms.

Assuming that all charged pions decay close to the supernova and that the shape of the neutrino spectrum follows the input proton spectrum, the associated neutrino spectrum flux is given by

$$\frac{dN_\nu}{dE_\nu} = 4.14 \times 10^{-4} \left(\frac{E_\nu}{1 GeV} \right)^{-2} \quad (E_\nu < 10^4 GeV) \tag{1.11}$$

If the hadronic origin of these gamma-rays is confirmed, neutrino rates of the order of $\sim$40 km^{-2}yr^{-1} could be expected, according to Alvarez-Muniz & Halzen [55].

- **Pulsars in high density regions**

Pulsars are likely to be formed in star-rich regions. In this high density regions the typical magnetic fields are of the order of $10^{-5} - 10^{-4}$ G, so particles accelerated by pulsars can be trapped and produce high energy neutrinos. The Galactic Centre extended region, with a total mass of $\sim 10^6 M_\odot$, and a density of 10^2 cm^{-3}
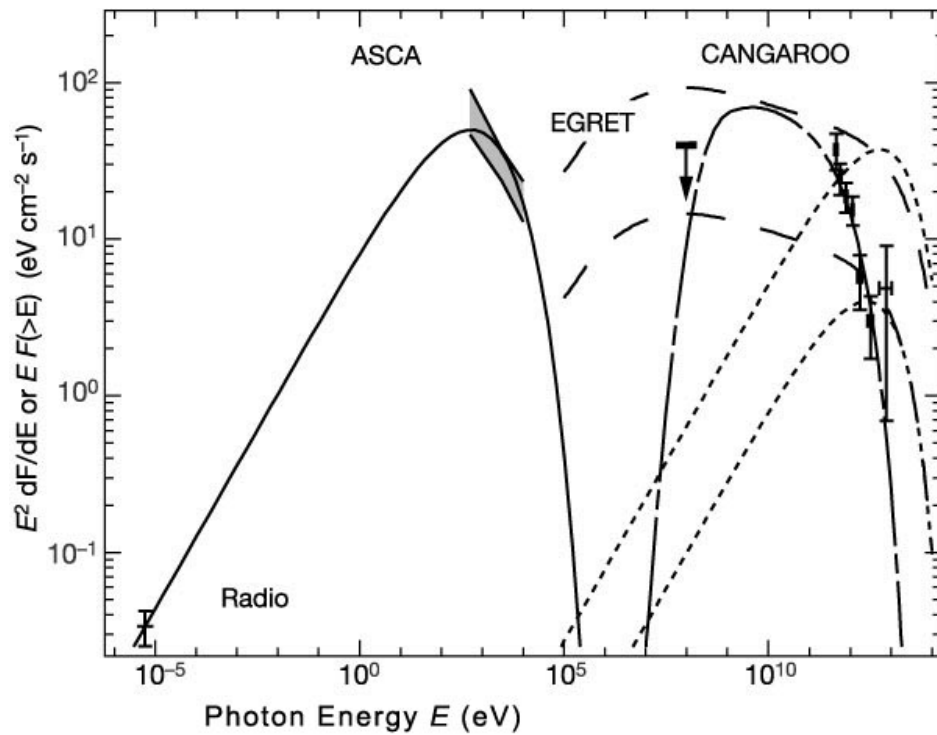
Figure 1.4: Multi-band emission from RX J1713.7-3946. Emission models are also shown: synchrotron emission (solid line), inverse Compton emission (dotted lines), bremsstrahlung (dashed lines) and emission from neutral pion decay (short-long dashed line). Inverse Compton emission and *bremsstrahlung* are plotted for two cases: 3 μG (upper curves) and 10 μG (lower curves) [39].

fulfills the previous requirements. Estimations predict [56] several (2-10) muon neutrinos per year in a km^3 detector.

- **Neutron stars in binary systems**

  Binary systems containing a neutron star are likely to produce detectable rates of high energy neutrinos. One of the possible mechanisms considers a system formed by a fast rotating pulsar and a massive stellar companion. Some of the nuclei accelerated by the pulsar will suffer photodisintegration in the thermal radiation field of its companion. The nuclei which survive to the photodisintegration can also produce neutrinos when they fall on the massive star.

- **Microquasars**

  Microquasars are one of the most promising Galactic candidates for neutrino astronomy. These objects are a sort of reduced version of a quasar. They are strong X-ray sources with lobes emitting in radio and IR. As indicated in the schematic view shown in figure 1.5, a microquasar consists of a compact object (black hole or neutron star) towards which a companion star is accreting matter. An important fraction of this energy is liberated in the jets, which produces intense radio and IR flares. There are indications that these jets are relativistic ($\Gamma \sim 2$ have been measured in some sources, but it could be much larger in other cases). Time correlations between the X-ray and the synchrotron emission have also been observed, which points to a relationship between accretion and jet activity.

  Concerning the jet content, there is no consensus about whether it is leptonic or hadronic. The detection of TeV neutrinos from microquasars would imply a baryonic content. These TeV neutrinos are predicted, for instance, in the Levinson and Waxman model [58], where they assume that the energy content of the jets in transient sources (e.g. V4641Sgr) is dominated by electron-proton plasma. In this model, an important fraction of the energy dissipates (for instance by internal collisionless shocks) and accelerates protons and electrons. A significant fraction of the proton energy (12%-25%) is converted into muon neutrinos with a flat spectrum in the 1-100 TeV range. Several neutrinos would be detected during a typical outburst from a source at 10 kpc (over a negligible background, since the duration of the event takes a few hours).

  Persistent sources can also produce detectable event rates in ANTARES, as shown in figure 1.6. Among the most promising sources GX339$-$4 and SS433 can be mentioned (see [59] for further details).

  Another mechanism for neutrino production in microquasars containing early-type stars has been proposed by Romero et al. [60]. In this model, the relativistic hadrons accelerated in the jet can also interact with the dense matter of the massive star wind. Fluxes a factor 3 larger than the atmospheric background have been predicted.
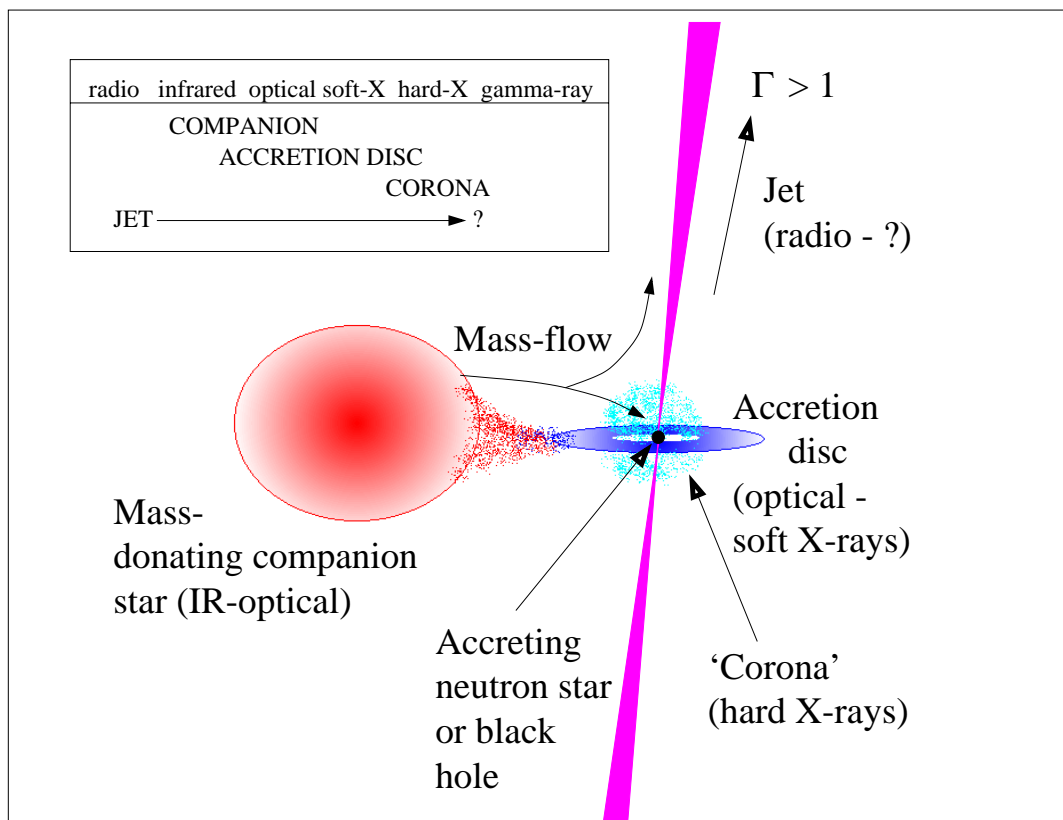
Figure 1.5: Schematic view of a microquasar. The matter lost by the companion star forms a fast-spinning accretion disk. The typical size of the accretion disk is $\sim 10^3$ km. The length of the jets is of the order of light years. From [57].
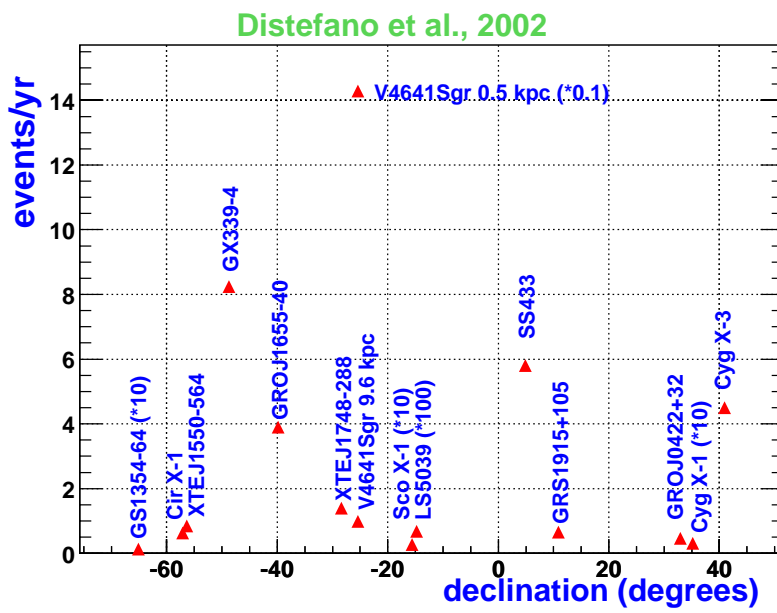
Figure 1.6: Event rates in ANTARES for several microquasars, assuming the hadronic mechanism [61]. The most interesting objects for ANTARES are GX339−4 and SS433. The two predictions for the transient microquasar V4641Sgr correspond to a small (0.5 kpc) or a large distance (9.6 kpc). The atmospheric neutrino background is of the order of 0.5 in one degree around the source.

- **Magnetars**

  Magnetars are isolated neutron stars characterized by surface dipole magnetic fields much larger than in ordinary pulsars ($\sim 10^{15}$ G). X-rays and particle emission are powered not only by pulsar rotation but also by the decaying magnetic field. This gives rise to internal heating and seismic activitiy that shakes the inducing particle acceleration in the magnetosphere.

  Zhang et al. have proposed that these protons could gain energy enough to produce mesons via $p\gamma$ interactions [62]. The expected rate from SGR1900+14, one of the most promising sources coud be 1.5-13($0.1/\Delta\Omega_\nu$) km^{-2} year^{-1}, where $\Delta\Omega_\nu$ is the beaming angle. It has to be noticed that rates are very dependent on the relative beam angle.

1.6.2 Extragalactic sources

Some extragalactic objects are interesting candidates for neutrino astronomy. Even if they are very distant, these objects are so violent that can be observed from the Earth.

- **Gamma-ray bursters**

  Gamma-ray burts (GRBs) were discovered in the late 60's by military satellites which aimed to detect banned atomic bomb tests. These phenomena are characterized by a brief explosion of gamma-rays, often followed by X-ray, optical and radio emission. The luminosity of such events is enormous, typically $\sim 10^{51} - 10^{54}$ erg/s, released during seconds (indeed, there are two peaks in the duration distribution, about 2 and 20 seconds). Although during a brief period, they are the most powerful objects in the Universe. It exists an increasing consensus about the cosmological nature of these events. Redshifts larger than 4 have been measured [63]. From BATSE observations (see figure 1.7), it has been estimated that there is one burst per galaxy per million years. This rate could be larger if GRBs are beamed, as it is suspected.

  There is not a single model to describe these spectacular events. The most accepted description is the *fireball* model, which assumes that matter moving at relativistic speed powered by radiation pressure collides with other material in the vicinity. The progenitor behind GRBs is still an open question, although there are several suggestions. In the "collapsar" scenario, the core of a super-massive star collapses and results in a failed supernova [64]. Another possibility is the merging of two compact objects (neutron star or neutron star-black hole binaries) which would generate a black hole surrounded by debris. The accretion of this debris into the black hole would generate the observed fireball [65]. The fireball would be generated from the star binding energy released in the contraction. More exotic scenarios assume that a seed of primordial strange matter could trigger a chain reaction which would convert a neutron star into a strange star [66]. As a
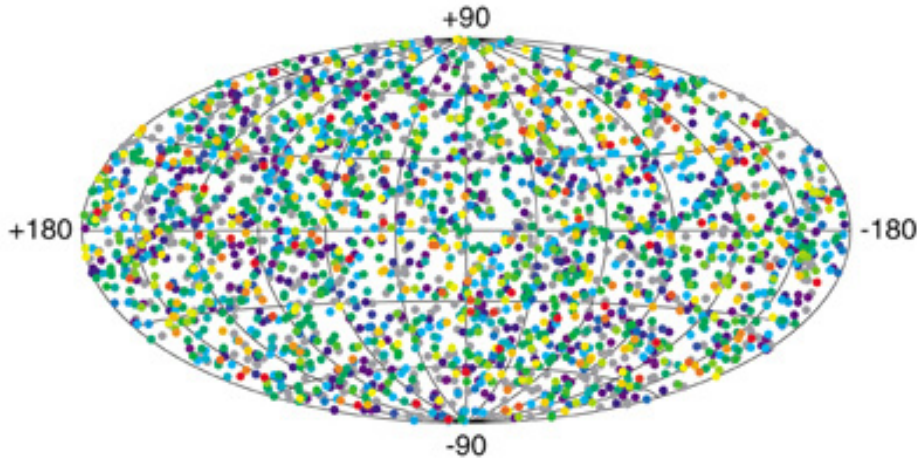
Figure 1.7: Skymap with the locations of a total of 2704 Gamma-Ray Bursts recorded by the Burst and Transient Source Experiment (BATSE) during its nine-year mission. Source: NASA.

result from this conversion, a big amount of energy is released. Maybe there is more than one gamma-ray generator, as it is hinted by the bimodal distribution of the GRB duration.

Concerning neutrino production, there are many stages in the GRB formation that can yield neutrinos. The most relevant mechanism for the high energy neutrino telescopes is due to the interaction of the accelerated protons with fireball photons giving rise to TeV-EeV neutrinos through pion decay. If it is assumed that the highest energy cosmic rays are produced by GRBs, a flux of neutrinos detectable in a km^3 is expected.

- **Active galactic nuclei**

  The classification of Active Galactic Nuclei (AGNs) includes several kinds of objects: Seyferts I and II, quasars, radio galaxies, blazars and others. Although their observational properties seem different, the standard model of AGNs suggests that all of them are the same kind of astrophysical source viewed from different relative angles. In figure 1.9 a scheme of the unified model can be seen. According to this model, a super-massive black hole (10^6-10^8 solar masses) constitutes the nucleus of the host galaxy and large amounts of matter accretes towards it. Although their maximum luminosity is lower than that of GRBs, they radiate over much longer periods of time. The typical spectrum in the MeV-GeV region shows an spectral index $\gamma = 2.2$, according to the EGRET observations.

  Neutrino telescopes can determine the acceleration mechanism in AGNs. If the hadronic mechanism plays an important role in the acceleration process, a detectable rate of neutrinos can be produced. Blazars are a subset of particular
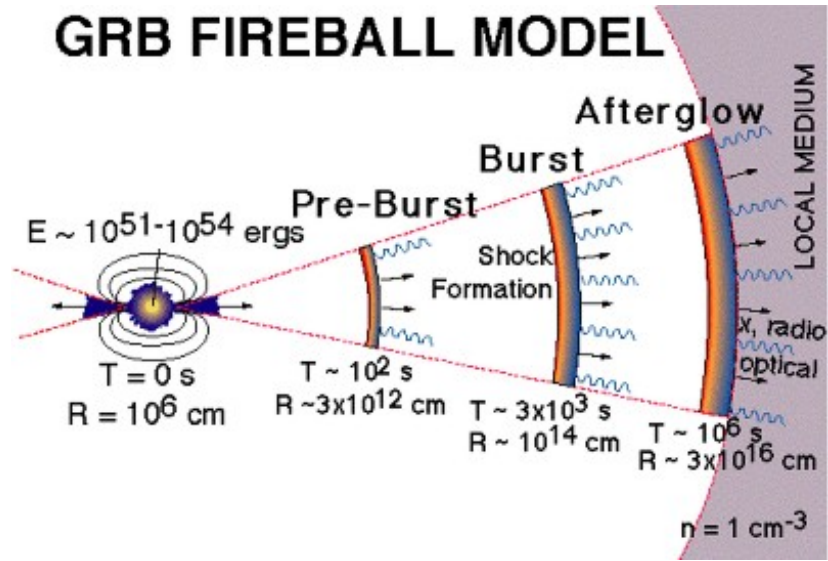
Figure 1.8: The fireball model assumes that the gamma-rays and the afterglow are produced by material moving at relativistic speeds ($\Gamma \sim 300$) which interacts with the surrounding medium. Source: NASA
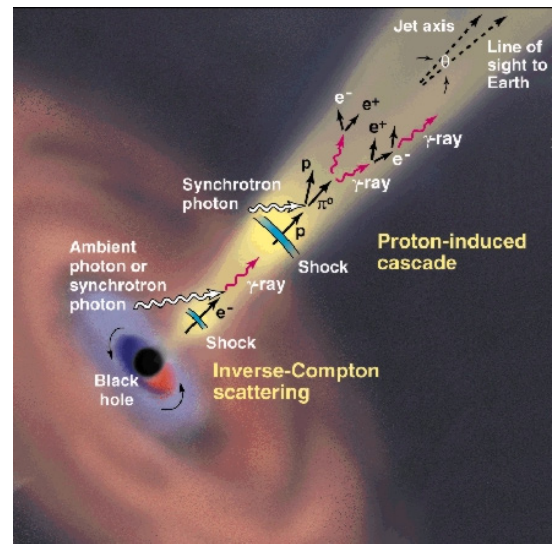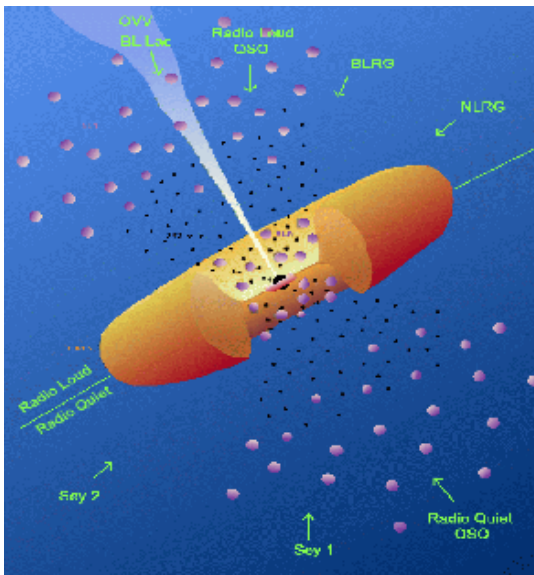
Figure 1.9: Left: AGN unified model. Depending of the observer point of view, the AGN is seen with different characteristics. Right: Acceleration mechanisms (hadronic and leptonic) inside an AGN jet.

interest in neutrino astronomy since they can be the source of the highest energy gamma-rays. In the standard AGN model, a blazar is an active galaxy with one of its jets pointing towards us. Two peaks are observed in the blazar spectrum. The first one, in the IR to X-ray region, is due to synchrotron radiation emitted by accelerated electrons. The peak in the MeV-GeV region is more controversial. In the leptonic models [67], it is explained by inverse Compton scattering of synchrotron and ambient photons by the electrons. In the hadronic models [68,69], these photons are produced by the interaction of accelerated protons with gas or ambient radiation. The observed gamma rays would come from the decay of the neutral pions produced in these interactions. From the estimates of the density of the blazar population, it has been calculated that the total flux due to this kind of sources could produce between tens to hundreds muon neutrino events per year and km^2 [70].

1.7 Other neutrino sources

- **Propagation of cosmic rays**

  It has been suggested that cosmic rays may produce high energy neutrinos during their propagation. Possible targets for such production are the microwave background or the hydrogen in the Galactic plane. Z-bursts produced by the interacion of ultra-high energy neutrinos with relic neutrinos $\nu + \nu_{bg} \rightarrow Z$ are another related phenomenon [71].

- **Dark matter**

  There is large evidence that dark matter exists (galactic rotation curves, gravitational lensing, redshift space distortions...) However, there is no consensus about its nature and many different candidates exist. The direct search experiments usually try to observe the recoil of the nuclei when dark matter scatters off the detector material. Additionally, indirect search experiments have been also proposed to observe the products of the annihilation of dark matter (gamma-rays, positrons, anti-protons, neutrinos). Both approaches are complementary, since they cover different regions of the parameter space.

  One of the most solid candidates to constitute the non-baryonic dark matter is the lightest supersymmetric particle (LSP). Supersymmetric models assume that a spontaneously broken symmetry between bosons and fermions exists. This symmetry is characterized by the R-parity ($R = (-1)^{3B+L+2S}$), where B, L and S are the baryon and lepton number and the spin of the particle. It takes the value +1 for Standard Model particles and -1 for supersymmetric particles. In this scenario, the LSP would be stable. Many of the variants of this theory suppose that the LSP is the lightest neutralino.

  Neutralinos should accumulate in the centre of the Sun, Earth and the Galactic Centre, due to gravitational interactions. They collide with the matter of these

objects, slow down and "fall". Their annhilation would generate high-energy neutrinos [72], which could be detectable by neutrino telescopes ($E_{th} \sim 50$ GeV). One of the advantages of looking for neutrinos instead of gamma-rays, positrons or anti-protons is that this method does not depend so much on the dark matter distribution.

- **Top-down models**

    The so-called top-down models assume that the highest-energy cosmic rays are produced by the decay of super-heavy particles with GUT-scale masses. The list of candidates includes monopoles, cosmic strings, primordial black holes, etc. These models usually predict a large content of gamma-rays in the annihilation or disintegration. Since observational data seem to indicate that protons, and not gamma rays, dominate the very high energy cosmic spectrum, these top-down models are disfavoured. However, there is still room for some detectable neutrino rates. These neutrinos can be produced in several ways. Firstly, after the semi-leptonic decay of bottom and charm quarks. Secondly, from the pions produced in the hadronic cascades. Thirdly, in the semi-leptonic decay of the $W^{\pm}$ bosons produced in the top quark decay. Depending on the parameters, tens to thousand events per year could be generated in a km^2 detector above an energy threshold of 1 PeV [70].

1.8 Diffuse neutrino fluxes and upper bounds

The most direct way to find evidences of the high energy neutrino sources described in the previous sections is to search for clusters pointing to individual sources. Even though some expected fluxes are promising for the ANTARES location, the possibilities to detect point-like sources are remote in detectors smaller than one km^3. An alternative way to prove the existence of high energy neutrino sources is the measurement of the cumulative flux coming from unresolved cosmic sources in the whole sky. This is known as the diffuse neutrino flux and the main topic of this work is the study of the ANTARES sensitivity to detect it. Since there is no directional information, the only way to detect diffuse neutrinos is looking for an excess of high energy events in the energy spectrum. Diffuse sources have a much harder spectrum than the atmospheric neutrino background (see section 1.4).

The observations of the diffuse fluxes of gamma-rays and cosmic rays have been used to set theoretical upper bounds on the diffuse neutrino flux. It is believed that most of the non-thermal radiation is originated in extragalactic sources. In the case of proton acceleration, high-energy gamma-rays would be produced by the decay of neutral pions. As it has been mentioned, neutrinos will be produced in parallel from the decay of charged pions and will escape from the source without further interactions. However, high-energy photons will develop electromagnetic cascades when interacting with the intergalactic radiation field, so most of the photon energy will be released in

the 1 MeV$-$ 100 GeV range. Therefore, the observable neutrino flux is limited by the bolometric observed gamma-ray flux, being the integrated energy of these particles the same, within a factor two depending on branching ratios and kinematics at production.

The diffuse gamma-ray background spectrum above 30 MeV measured by EGRET is [73]

$$E^2 I_E(E) = (1.37 \pm 0.06) \times 10^{-6} E^{-(0.1 \pm 0.03)} \text{ GeVcm}^{-2}\text{s}^{-1}\text{sr}^{-1} \qquad (1.12)$$

so the upper theoretical bound of the neutrino flux can be estimated to be of the order of 10^{-6} cm^{-2} s^{-1} sr^{-1} GeV.

If nucleons escape from the cosmic source, a similar bound can be derived from the observed extragalactic cosmic ray flux. Cosmic ray protons are magnetically confined at the source so that the Fermi acceleration mechanism can take place. But neutrons produced in $p\ \gamma \to n\pi^+$ collisions can escape from optically thin sources and decay into cosmic protons outside the magnetic field of the host accelerator.

Some additional factors have to be taken into account before establishing a relationship between the fluxes. These are the production kinematics, the opacity of the source to neutrons and the effect of propagation. The resulting expression is

$$\phi_\nu(E_\nu) \le \phi_{CR}(E_{CR} = f^{-1}E_\nu) \cdot K \cdot O_n \cdot P \qquad (1.13)$$

The factor f takes into account the fraction of energy released in neutrinos with respect to the energy released by neutrons. The value of f ranges from 0.01 to 0.05 and it is determined by the interaction kinematics. The kinematics factor K, calculated from simulations [74], ranges from 0.2 to 1, depending on the mean CMF energy. The opacity O_n of the source to neutrons is determined by the photon density, which can limit the neutron propagation by $n\gamma$ interactions. It strongly depends on the particular choice of the source. Finally, the propagation term for non-evolving sources is not well known, since it has a strong dependence on the poorly-known magnetic fields in the Universe. However, reasonable values could be [75]:

$$P \begin{cases} \sim 1 & \text{for } E_{CR} \le 10^{17} \text{ eV} \\ \sim 3 & \text{for } E \sim 10^{19} \text{ eV} \\ \gtrsim 100 & \text{for } E_{CR} > 10^{20} \text{ eV} \end{cases} \qquad (1.14)$$

For evolving sources the value at $E_{CR} \gtrsim 10^{19}$ eV would be a factor 5 larger.

There is some controversy about how to use these relationships to constrain the neutrino flux limit. We will describe briefly two of the most relevant predictions.

1.8.1 Waxman-Bahcall upper bound

The upper bound proposed by Waxman and Bahcall (WB98) [76] takes the cosmic-ray observations at $E_{CR} \sim 10^{19}$ eV to constrain the neutrino flux. This bound is about 1-2 orders of magnitude lower than the limit given by the extragalactic MeV-GeV gamma-ray background.

Several hypothesis are made to derive this prediction. It is assumed that neutrinos are produced in the interactions of protons with ambient photons or matter. The sources are transparent to high energy neutrons ($E_n \sim 10^{19}$ eV) and the cosmic rays of 10^{19} eV produced by these sources are not deflected by magnetic fields. Finally, in order to extend the validity of the bound to other energies, the authors assume that the spectral shape up to the GZK-cutoff is $dN/dE \propto E^{-2}$, as typically expected from Fermi acceleration.

The limit that they obtain for evolving sources is

$$E_\nu^2 \frac{d\phi}{dE_\nu} < 4.5 \times 10^{-8} \text{ GeVcm}^{-2}\text{s}^{-1}\text{sr}^{-1} \tag{1.15}$$

Some authors have argued [75] that this limit is not as model-independent as Waxman and Bahcall claim. In particular, it does not seem straigthforward that the spectral index should be $\gamma = 2$ because larger values are also possible.

1.8.2   Mannheim-Protheroe-Rachen upper bound

The upper bound proposed by Mannheim et al. (MPR98) [77] not only uses the spectrum of cosmic rays observed in the Earth as a constraint, but also the observed gamma-ray diffuse flux. Two kinds of sources (which are assumed to follow a cosmological distribution) are considered: opaque and transparent to neutrons. Intermediate cases would give intermediate limits.

The limit for sources opaque to neutrons is

$$E_\nu^2 \frac{d\phi}{dE_\nu} < 2 \times 10^{-6} \text{ GeVcm}^{-2}\text{s}^{-1}\text{sr}^{-1} \tag{1.16}$$

The limit of $E_\nu^2 d\phi/dE_\nu$ for transparent sources decreases from the previous values at $E_\nu \sim 10^6$ GeV to the value set by Waxman and Bahcall at $E_\nu \sim 10^9$ GeV. Above this energy, the limit increases again due to the scarce observational information. Both bounds are compared in Figure 1.10.

1.9   The neutrino oscillation influence

The fluxes shown in the previous sections do not include the effect of neutrino oscillations. In the case of neutrinos produced by pion decay, which is the most natural production mechanism in astrophysical objects, the ratio for electron, muon and tau neutrinos at the source is $\nu_e : \nu_\mu : \nu_\tau \sim 1 : 2 : 0$. Due to the long distances between the source and the Earth, the flavors of the arriving neutrinos will be completely mixed $\nu_e : \nu_\mu : \nu_\tau \sim 1 : 1 : 1$. This implies a reduction of a factor two in the predicted fluxes which should be considered when interpreting the analysis results. Nevertheless, this effect is not so negative at very high energies, since electron and tau neutrinos can be also observed.
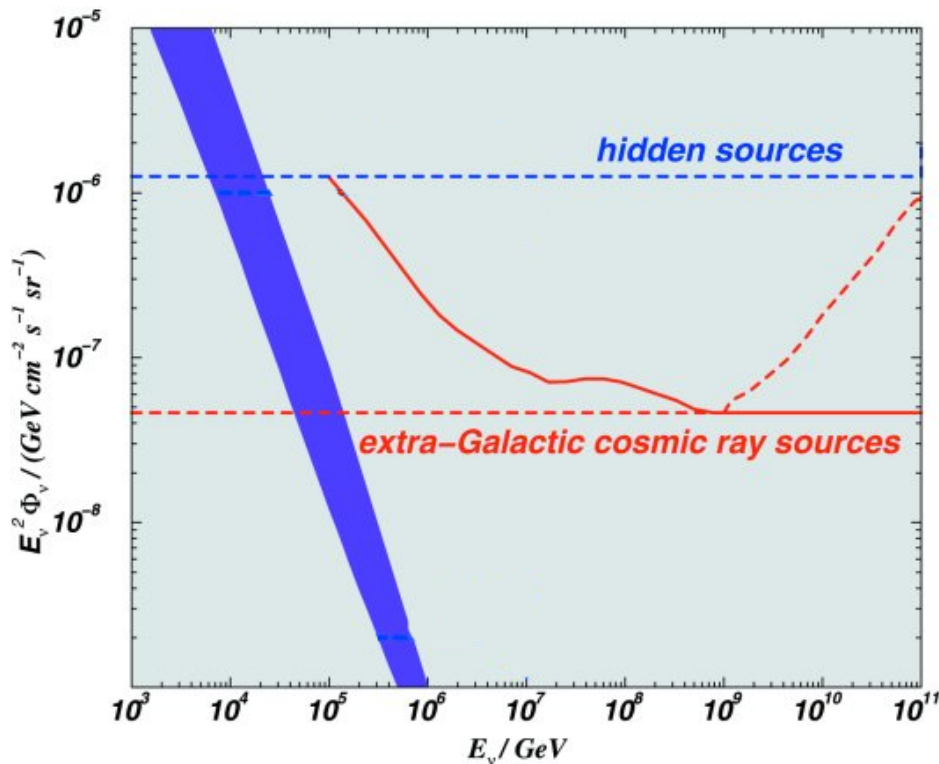
Figure 1.10: The upper blue (red) line shows the Mannheim-Protheroe-Rachen upper bound for thick (transparent) sources. The bottom red line is the Waxman-Bahcall limit. Both limits agree at $E_\nu \sim 10^9$ GeV, where the cosmic-rays sources are thought to be extragalactic. For lower energies, the uncertainty in the Galactic background increases the limit above the E^{-2} Waxman-Bahcall bound (flat curve in this plot). For higher energies, the cosmic ray flux is not well constrained due to the scarcity of data. From [78].

Chapter 2

The ANTARES neutrino telescope

This chapter is devoted to the operation techniques of neutrino telescopes in general and of ANTARES in particular. First, the detection principle is explained and then a detailed description of the ANTARES telescope is given, with a review of the tests already performed and the plans for the future. The status and results of other neutrino telescopes will be also shown.

2.1 Detection principle

The detection of high energy neutrinos is severely constrained by the fact that the expected fluxes and the neutrino interaction cross-section are very low. Therefore, very large detectors ($\sim$ GTon) are needed. Underground detectors would be too small, so the use of large volumes of sea/lake water or antarctic ice was proposed by M. A. Markov in 1960 [1]. The basic idea is to build a matrix of light detectors inside a medium in which high energy muons (or other leptons) produced by the charged current interaction of cosmic neutrinos:

$$
\begin{aligned}
\nu_l + N &\longrightarrow l^- + X \\
\bar{\nu}_l + N &\longrightarrow l^+ + X
\end{aligned}
\tag{2.1}
$$

would emit Cherenkov light.

At high energies (> 10 TeV), the muon and the neutrino tracks are almost collinear. The angle between them can be approximated by

$$
\langle \theta_{\mu\nu} \rangle = \frac{0.64°}{(E_\nu/\text{TeV})^{0.56}}
\tag{2.2}
$$

which justifies the name of neutrino "telescopes", since sub-degree accuracies can be achieved in such detectors.

The cross section of the neutrino deep inelastic charged current for $\nu_l + N \rightarrow l^- + X$ is given by [79]

$$\frac{d^2\sigma_{\nu N}}{dxdy} = \frac{2G_F^2 m_N E_\nu}{\pi} \frac{M_W^4}{(Q^2 + M_W^2)^2} \left[xq(x, Q^2) + x(1-y)^2 \bar{q}(x, Q^2) \right] \tag{2.3}$$

where G_F is the Fermi constant, m_N and M_W are the nucleon and W-boson masses, Q^2 is the square of the momentum transfer between the neutrino and the lepton and $q(x, Q^2)$ and $\bar{q}(x, Q^2)$ are the parton distributions for quarks and anti-quarks. The Feymann-Bjorken scale variables are given by

$$x = Q^2/2m_N(E_\nu - E_l) \tag{2.4}$$

and

$$y = (E_\nu - E_l)/E_\nu \tag{2.5}$$

Figure 2.1 shows the cross-section dependence with energy. At low and intermediate energies ($E_\nu << M_W^2/2m_N \approx 5\,\mathrm{TeV}$), the cross-section grows linearly with the neutrino energy as [80]

$$\sigma_{\nu N} = (0.677 \pm 0.014) \times 10^{-38} \left(\frac{E_\nu}{1\,\mathrm{GeV}} \right) \quad cm^2 \tag{2.6}$$

$$\sigma_{\bar{\nu} N} = (0.334 \pm 0.008) \times 10^{-38} \left(\frac{E_\nu}{1\,\mathrm{GeV}} \right) \quad cm^2 \tag{2.7}$$

At higher energies ($E_\nu \gg M_W^2/2m_N \approx 5\,\mathrm{TeV}$), the cross-section is dominated by the behaviour of the structure functions at small x. Since there are not data to constrain the structure functions at very small x, a 10% uncertainty is estimated on the total cross section at $E_\nu \sim 100\,\mathrm{PeV}$ [81]. From 10^{16} eV to 10^{21} eV, it can be approximated as [79]

$$\sigma_{\nu N} \simeq 5.53 \times 10^{-36} \left(\frac{E_\nu}{1\,\mathrm{GeV}} \right)^{0.363} \quad cm^2 \tag{2.8}$$

$$\sigma_{\bar{\nu} N} \simeq 5.52 \times 10^{-36} \left(\frac{E_\nu}{1\,\mathrm{GeV}} \right)^{0.363} \quad cm^2 \tag{2.9}$$

The increase of the interaction cross-section with the neutrino energy enlarges the effective volume of the detector. This effect is enhanced by the fact that the muon range also increases with the energy ($\sim$1 km at 300 GeV and $\sim$25 km at 1 PeV). However, at very high energies ($>$1 PeV), the Earth becomes opaque to the neutrinos, so the effective volume decreases.

The muon produced in the charged-current interaction will lose its energy due to ionization and radiative processes (*bremstralhung*, pair production and photonuclear interactions). At low energies ($\lesssim 500$ GeV), losses are dominated by ionization, whereas
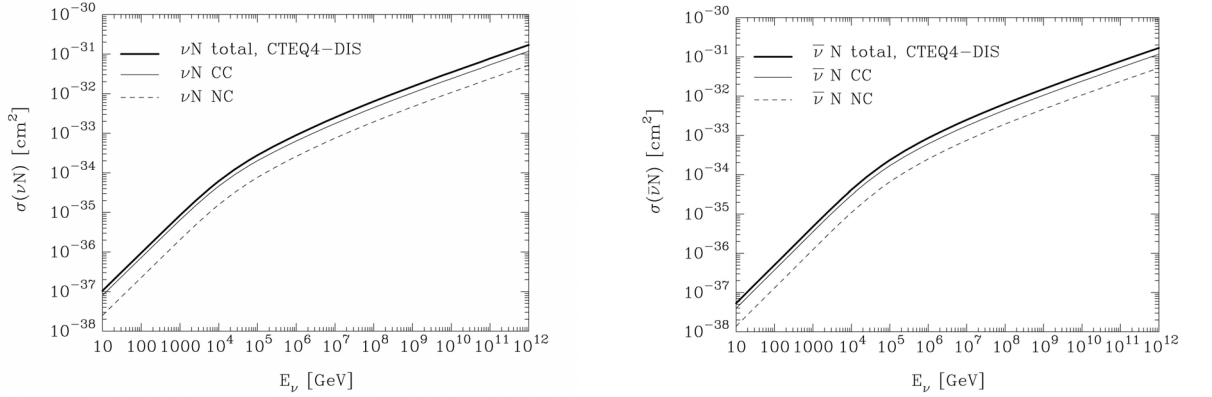
Figure 2.1: Cross-section of the νN (left) and the $\bar{\nu} N$ (right) interactions, calculated with the CTEQ4-DIS parton distributions.

above this energy, the radiative losses are more important. This will be discussed in more detail in chapter 4.

The muon and the charged secondaries will induce Cherenkov radiation, since they are relativistic particles moving faster than light in water. The emission angle is given by:

$$\cos \theta_C = \frac{1}{\beta n} \tag{2.10}$$

where β is the particle speed and n is the refractive index of water ($n = 1.346$ in the ANTARES site). Since these particles move at relativistic velocities, $\beta \simeq 1$ the emission angle is independent of the speed ($\theta_C = 42.2°$). Some smearing in the Cherenkov cone is produced due to the scattering of the light in water and to the fact that the trajectories of the secondaries are not exactly collinear.

The spectral distribution of the Cherenkov emission can be described by the following formula, which gives the number of photons N of wavelength λ induced by a particle of charge z travelling at speed β in a medium of refractive index n:

$$\frac{d^2 N}{dx d\lambda} = \frac{2\pi \alpha z^2}{\lambda^2} \left(1 - \frac{1}{n^2 \beta^2} \right) \tag{2.11}$$

Consequently, the spectrum is dominated by blue and ultraviolet light [1]. In order to be able to detect the light, transparent media are needed. As we have mentioned, given the low cross-section of these interactions, a huge detector is needed, so the location of Cherenkov neutrino telescopes is restricted to lakes, oceans or antarctic ice, which

---

[1]Since the largest absorption length in water/ice corresponds to blue light, this is the dominant transmitted wavelength.

are naturally available targets. In order to shield the detector against the atmospheric muon background from cosmic rays, it has to be built as deep as possible.

Apart from muon tracks, cascades produced by electron and tau neutrinos can also be used as a detection signature. The interaction of an electron neutrino within the sea water produces a hadronic shower and an electron, which in turn gives rise to an electromagnetic shower. The shower length (along which 95% of the initial energy is deposited) is of the order of [82]:

$$L_{em}(m) \sim 2 \log_{10} \left(\frac{E_{em}}{110 \text{ MeV}} \right) \tag{2.12}$$

$$L_{had}(m) \sim 1.5 \log_{10} \left(\frac{E_{had}}{22 \text{ MeV}} \right) \tag{2.13}$$

As it is shown, the length of cascades increases only as the logarithm of the energy. The typical cascade length is 5-10 m and the diameter is $\sim$10 cm. In figure 2.2 the signatures of a muon track event and a cascade event are compared. Given the low granularity of neutrino telescopes, the Cherenkov light from electromagnetic and hadronic cascades is seen as a brilliant sphere. This makes the effective volume smaller, since only contained or very nearby cascades will be detected. Moreover, the angular resolution is poorer than in the case of muon tracks. However, there are some advantages: better energy resolution, lower background and better sensitivity to neutrinos from all directions. Another interesting feature of cascade events is that they allow to look for neutrino oscillation studying the ratio of cascades to muon neutrino events. Other processes, like the elastic neutrino scattering do not produce useful signatures in this kind of detectors.

The case of the tau neutrino is somewhat more complex. The CC interaction between a tau neutrino and a nucleon produces a hadronic shower and a τ lepton. The signature depends on the tau decay length ($\langle L_\tau \rangle \sim 4.9 \frac{E_\tau}{100 \ TeV} \ m$), the position of the interaction point with respect to the detector and the tau decay mode. In general, the visible output looks like an electron neutrino event (or a muon track, if this is the decay mode of the τ). However, a very clear signature called double bang is also possible. At very high energies, the decay of the τ lepton can produce a second hadronic cascade hundred metres away that could be distinguished from the first one. Unfortunately, given the tau neutrino fluxes at very high energies and the size of ANTARES, these events would be extremely rare, even though they would be background-free events.

2.1.1 Physical background

There are two kinds of physical background in the ANTARES detector. First, the neutrinos produced by cosmic rays in the atmosphere, as it has been explained in the previous chapter. This background is very dangerous because the quality of the track reconstruction cannot be used to reject them. The only rejection criterion is based,
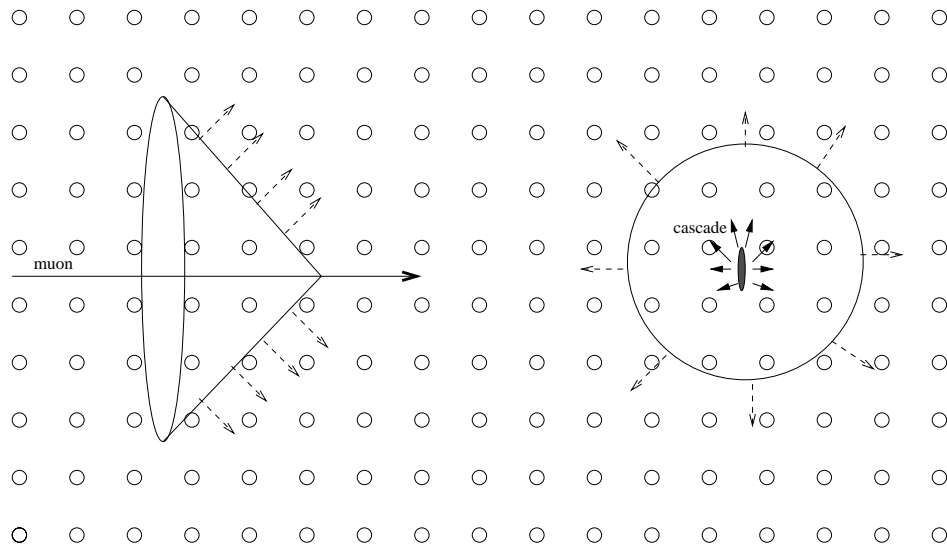
Figure 2.2: Schematic comparison between the signature of a muon track (left) and a cascade event (right).

as we have mentioned, on the different spectral index predicted for the atmospheric neutrino background and the cosmic signals.

Secondly, cosmic rays also produce muons which can be misinterpreted as muons induced by astrophysical neutrinos. In principle, these muons can be rejected by accepting only up-going events, since the Earth filters all the muons produced in the opposite side. However, the enormous background of atmospheric muons makes this task difficult, in particular because of the multi-muons, which are bundles of parallel muons produced in the same cascade, which can be mis-reconstructed as up-going events. In order to reduce this background, the detector has to be built as deep as possible, so that the water above absorbs a large fraction of these atmospheric muons. Figure 2.3 compares the zenith distribution of these two kinds of background: the muons induced by atmospheric neutrinos and the atmospheric muons.

2.2 The ANTARES detector

The aim of the ANTARES (Astronomy with a Neutrino Telescope and Abyss environmental RESearch) collaboration is to build an undersea neutrino telescope in the Mediterranean sea. Extensive R&D studies have been carried out during the first years (1996-1999), with the deployment of several autonomous lines devoted to the characterization of the ANTARES site and the validation of the sea operation procedures. The acoustic positioning system was tested with a demonstrator line ("Line 5"), immersed from November 1999 to June 2000, which also allowed to measure the atmospheric muon zenith distribution. The construction of the detector started in 2001. The first
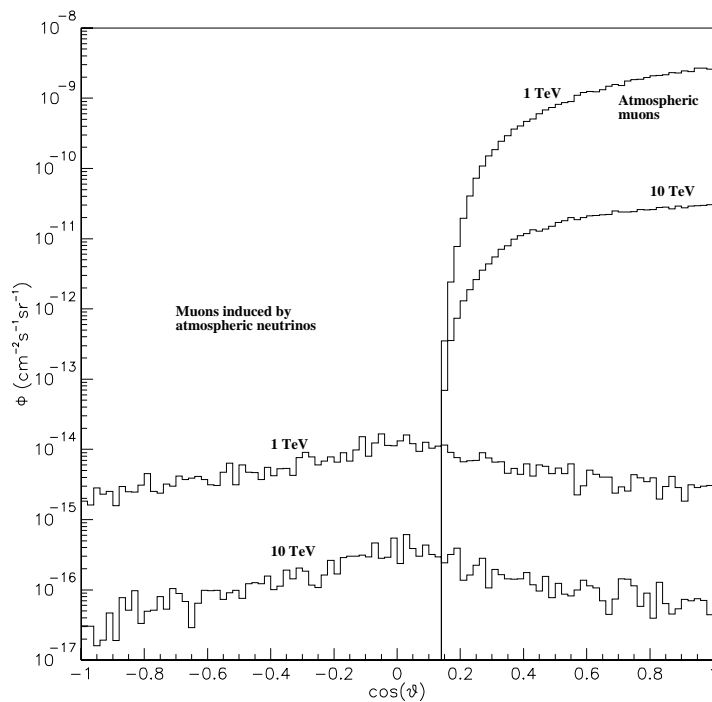
Figure 2.3: Physical background at 2300 m deep. On the one hand, the muons induced by the atmospheric neutrinos. The maximum at $\cos\theta=0$ ("secant effect") is due to the fact that horizontal pions have a larger probability to decay. On the other hand, the atmospheric muons. The up-going atmospheric muons are filtered by the Earth.

elements which have been built and installed are the electro-optical cable, the junction box, the Prototype Sector Line (PSL) and the Mini-Instrumentation Line (MIL), which will be described in the following sections.

2.2.1 Layout

The ANTARES detector will consist of a tridimensional array of large photomultipliers to detect the Cherenkov light induced by charged particles when crossing the sea water. Figure 2.4 shows a schematic view of the detector. It consists of 12 lines separated 60-75 m from each other. Each line is equipped with 75 optical modules (OMs), grouped in triplets, on 25 storeys, with a vertical distance of 14.5 m. The lines are held vertically taut by buoys.

The main criteria to establish the geometry of the detector has been to ensure the largest possible area in the 1–100 TeV range, since the astrophysical sources, which are the main scientific goal of the experiment, are expected to produce a low number of detectable events. The photomultipliers point 45° downwards and are set in triplets in order to make the rejection of optical background easier.
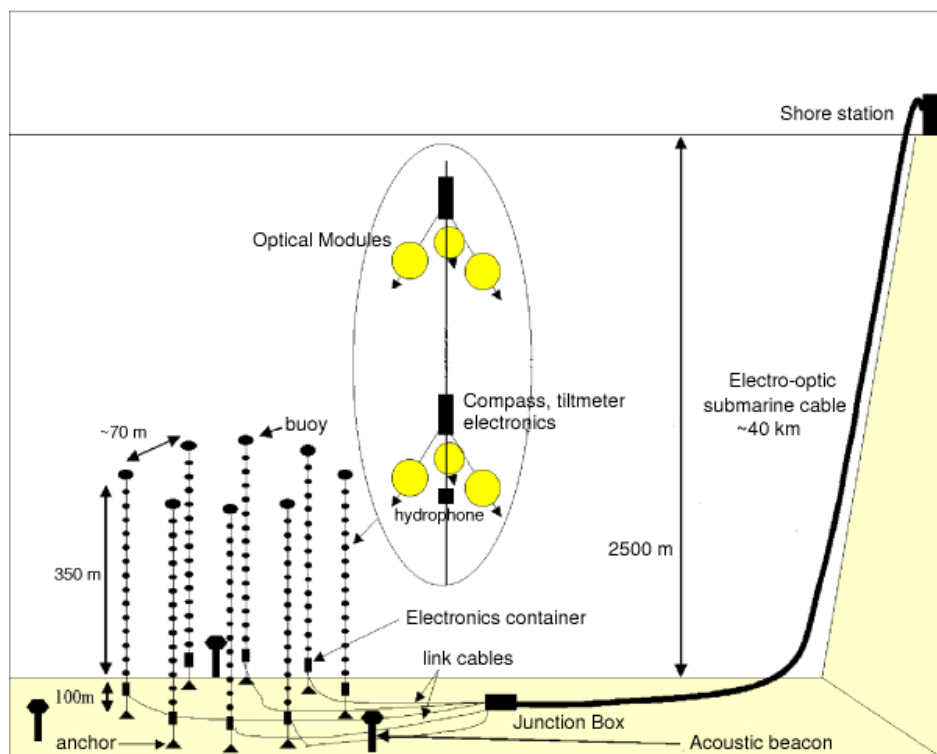
Figure 2.4: Schematic view of the ANTARES detector. It consists of 900 photomultipliers set along 12 lines, which are connected to shore by an electro-optical cable. The PMTs point 45° downwards. A system of compasses, tiltmeters and hydrophones allows to monitor the position of the detector elements.

In the following, we review the characteristics of the main detector elements.

- **Optical modules**

  The optical module [83] is the basic element of the ANTARES detector. It consists of a pressure-resistant glass sphere which houses the photomultiplier and the associated electronics (see figure 2.5).
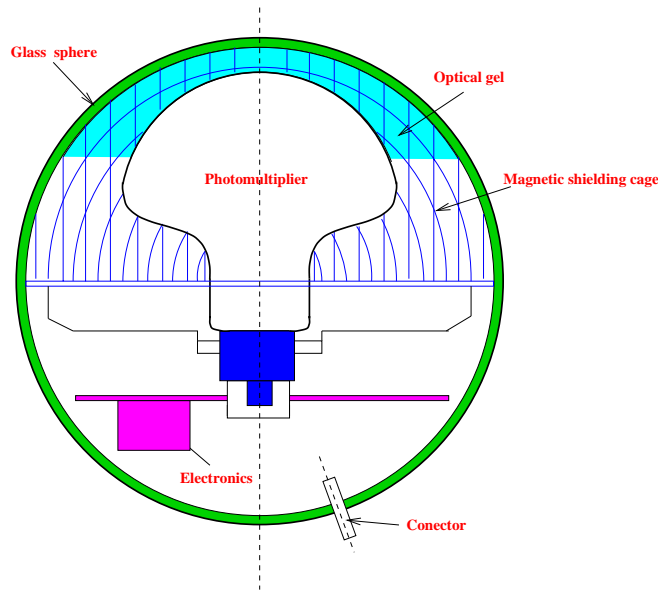
Figure 2.5: Distribution of elements within an optical module.

The studies performed by the collaboration [84] lead to the selection of the 10" Hamamatsu R7081-20 model. The transit time spread, a key parameter to guarantee a good angular resolution is 3 ns (FWHM) and its effective area is 450 cm^2.

The high-pressure glass sphere is required to stand up to 260 bars during normal operation and 700 bars in qualification tests. It has an external diameter of 43 cm and a thickness of 1.5 cm, with a transmission better than 95%. A black paint in the lower hemisphere reduces inner reflections.

In order to ensure a good optical coupling between the sphere and the photomultiplier, an optical glue (SilGel 612 A/B) is used. It also serves to fix mechanically the position of the PMT.

Finally, a μ-metal cage protects the photomultiplier against the Earth's magnetic field, which is expected to be uniform, pointing downwards at 23° from the vertical and with an intensity of about 44 μT.

Another important element inside the optical module is the LED system used for PMT internal calibration, specially transit time calibration.

- **Lines**

  Each detector line contains 25 storeys, i.e. 75 optical modules (see figure 2.6). From the electronics point of view, the basic unit of a line is the sector, which includes 5 storeys and a Main Local Control Module (MLCM). The String Control Module (SCM) houses the electronics concerning the Slow Control, clock, and instruments for acoustic positioning and sea property measurements. The total length is 450 m (including 100 non-active meters in the bottom part to avoid dust from the seabed). Moreover, several calibration and monitoring devices are also included:

  -**Positioning calibration:** in order to guarantee a good precision in the determination of the position of the optical modules, a calibration system based on tiltmeters, compasses and hydrophones is installed. The position of each hydrophone is obtained by triangulation from the travel times between the hydrophone and each fixed emitter at the bottom of each line. An accuracy of $\sim$5 cm has been measured. The shape of the line can also be reconstructed from the measurements of all acoustic reception hydrophones and from all tiltmeters and compasses. The tiltmeters and compasses also allow to obtain the OM orientation.

  -**Timing calibration:** two kinds of optical beacons are used to perform the detector relative calibration. Firstly, a set of four LED beacons will be set along each line. Each LED beacon (see figure 2.7, left) consists of a pressure-resistant glass cylinder containing 36 LEDs. These LEDs (λ=470 nm) are distributed in six faces fixed to an hexagonal structure, which allow to illuminate several storeys of the adjacent lines with an adjustable light output ($5 \times 10^6 - 8 \times 10^7$ photons per LED). The electronics of each face allows to fire simultaneously either 1, 4 or all 6 LEDs, which gives a factor $\sim$100 in the amount of light emitted per pulse by each beacon. The LED rise-time (10% to 90%) is between 1.8 ns and 2.0 ns, with a FWHM between 4.5 ns and 6.5 ns. In addition to the LED calibration system, a laser beacon (figure 2.7, right) will be located at the base of some lines. It consists of a Nd-YAG laser which emits $\sim$1μJ per pulse at a wavelength of emission of 532 nm (green light), which will illuminate several lines with one pulse. The pulse width (FWHM) is 0.8 ns [85].

- **Storeys**

  As it has been mentioned, the photomultipliers are grouped in triplets (storeys), looking 45° downwards (see figure 2.8).

  The signal digitization is not performed inside the Optical Module but in the Local Control Module (LCM)[2], by means of a specific integrated circuit called "Analogue Ring Sampler" (ARS). Only pulses exceeding a given threshold (L0

---

[2]There is one LCM per PMT triplet.

1 **string** (or line)
= **5** assembled sectors
+ Buoy + EMC + BSS

1 sector = **5** storeys

1 storey =
3 OM + MLCM/LCM

Total length ~ 460 m
Buoy to top storey ~ 10 m
5 sectors = **25** floors ~ 348 m
BSS to bottom storey ~ 100 m

Buoy

Electromechanical
cables (EMC)

LCM

LCM

LCM

14.5 m
between
storeys

MLCM

LCM

100m
to 1st
Storey

SCM/SPM   BSS

Interconnecting Link cables (IL)

Shore Station

Shore link
(~ 4 km)

Power Hut

MEOC Cable to
shore (~50 km)

Junction
Box JB

(not to scale)

Figure 2.6: Schematic view of a line of the ANTARES detector. The basic unit from the electronics point of view is the sector, which includes five storeys. The Local Control Module (LCM) contains the storey electronics (readout, power, trigger, DAQ, slow control and clock). One of the LCMs in each sector is the Master Local Control Module (MLCM), with an Ethernet switch, a bidirectional concentrator and a DWDM board.
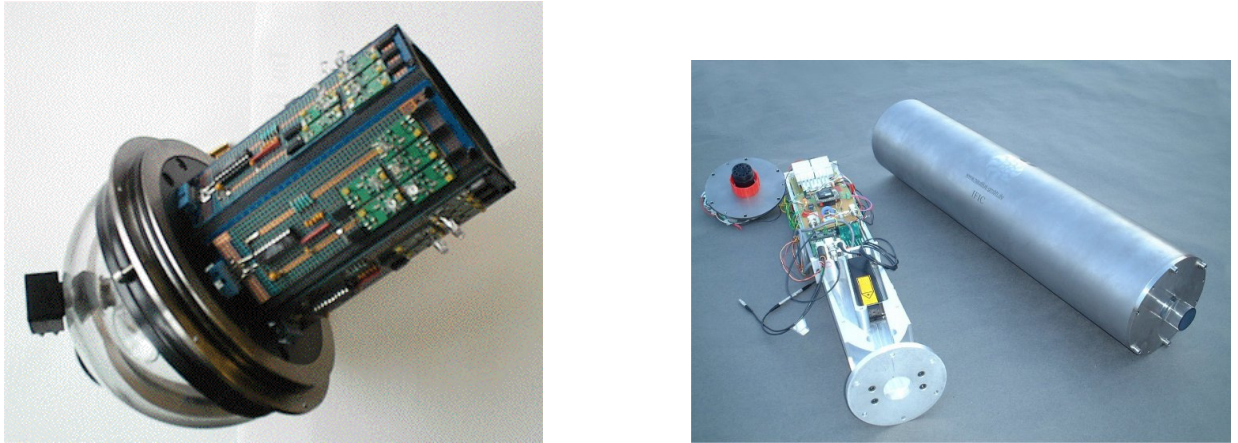
Figure 2.7: Optical beacon (left) and laser beacon (right) used in the timing ANTARES calibration.
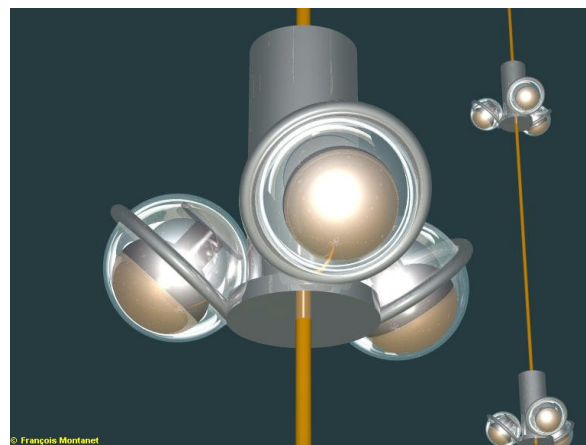
Figure 2.8: Schematic view of a storey.

trigger) are integrated and their waveform sampled to determine if they are processed as Single Photoelectron (SPE) or Waveform (WF). The Time-to-Voltage Converter (TVC) gives an analogue signal proportional to the time elapsed since the last signal of the external reference clock (20 MHz) to the instant when the pulse crossed the L0 threshold. In order to reduce the dead-time introduced by the ARS digitalization, each PMT can be read out by two ARSs. Another function of the ARS is to supply the HV to the PMT base.

- **Junction box and electro-optical cable**

  The junction box (JB) receives power from the shore station via an electro-optical cable and distributes it to the lines. The clock and control signals are also distributed by the JB. The data from the different lines is collected in the JB. The internal elements are protected from the sea pressure by a titanium, egg-shape structure. In order to provide stability on the seabed, this structure is housed in a parallelepiped frame (see figure 2.9).
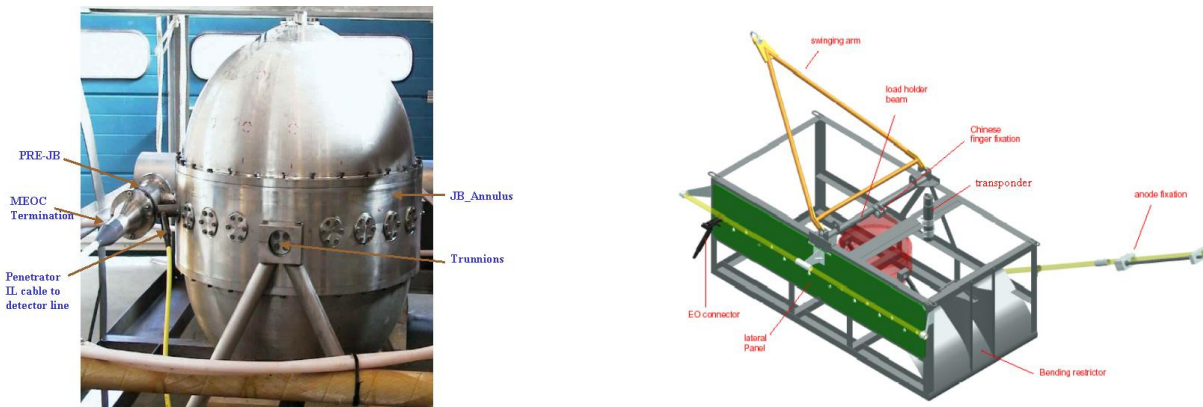
Figure 2.9: Left: Picture of the JB container. Right: Schematic view of the JB frame with the JB container.

  The electro-optical cable provides power and data link between the JB and the shore station. It contains an internal steel tube and 48 optical fibers. The cable is protected and insulated by a set of external layers of copper and steel. The total diameter is 58 mm.

  The optical-cable and the junction box were deployed in October 2001 and December 2002, respectively.

2.3   Site evaluation

The ANTARES detector will be deployed in the Mediterranean Sea (42°50'N, 6°10'E), near the French southern coast, at 2500 m deep. The distance to La Seyne

sur Mer, where the shore station is located, is 40 km. This location ensures a 3.5π sr sky coverage, including the Galactic Centre during 67% of the time.
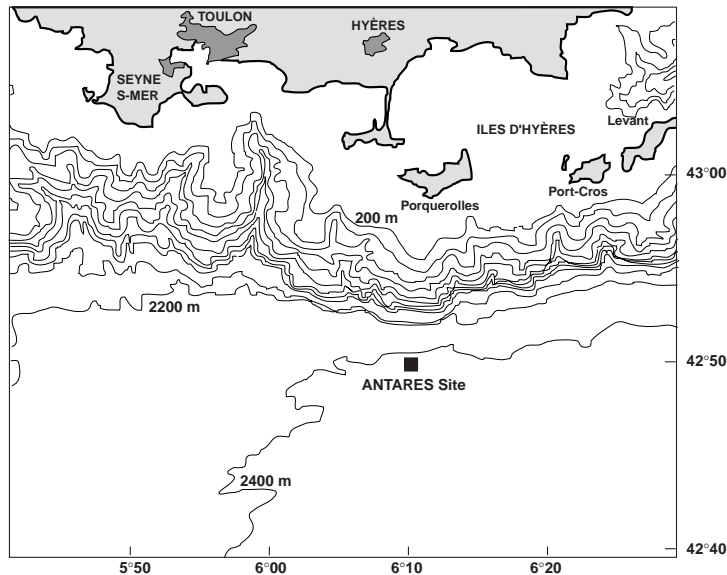
Figure 2.10: Map of the ANTARES site. The detector will be located at 2500 m deep, 40 kilometers away from the shore station.

Since the collaboration started the site evaluation phase, an extensive measurement program has been carried out. This section reviews the most relevant results, which concern water optical properties, optical background, sedimentation and biofouling.

2.3.1 Water optical properties

The photon propagation can be described measuring the following parameters:

- the absorption length λ_{abs}

- the scattering length λ_{scat}

- the volume scattering function $\beta(\theta, \lambda)$, which represents the probability that photons are scattered out of a beam through an angle θ.

The absorption length is a critical parameter to set the distance between lines, and therefore, the effective volume of the detector. The scattering length and the scattering function affect the angular resolution for $E_\nu \gtrsim 10$ TeV. In practice, it is common to summarize the effect of scattering by means of the effective scattering length, which is defined as:

$$\lambda_{scat}^{eff} = \frac{\lambda_{scatt}}{1 - \langle \cos\theta \rangle} \tag{2.14}$$

where $\langle \cos\theta \rangle$ is the average value of the scattering angle.

The combination of the absorption and the (effective) scattering length allows us to define the (effective) attenuation length as:

$$\frac{1}{\lambda_{att}^{(eff)}} = \frac{1}{\lambda_{abs}} + \frac{1}{\lambda_{scat}^{(eff)}} \tag{2.15}$$

Between 1997 and 2000, several tests were performed to measure these quantities for blue and ultraviolet light [86]. The experimental setup used to measure the attenuation length consisted of a rigid structure and a collimated and continuous LED source located at a variable distance from an Optical Module. The intensity of the source was adjusted so as to yield a constant current on the PMT. The emitted and detected intensities are related by:

$$I_{PMT} \propto \frac{\Phi_{LED}}{D^2} \times \exp\left(-\frac{D}{\lambda_{att}^{eff}}\right) \tag{2.16}$$

and the measured value for the effective attenuation length[3] at $\lambda = 466$ nm is:

$$\lambda_{att}^{eff}(\text{collimated}) = 41 \pm 1_{\text{stat}} \pm 1_{\text{syst}} \ (\text{m}) \tag{2.17}$$

Since this result includes the effect of scattering and absorption, complementary measurements were needed to separate both contributions. The photon arrival time distributions (see figure 2.11) are widened by the effect of scattering, so an isotropic pulsed LED was used to illuminate a PMT at two different distances (24 and 44 m). The effective scattering length can be extracted from a fit to the arrival time distributions.

The measured values of the attenuation, absorption and scattering lengths are shown in table 2.1.

Wavelengh	λ_{att}^{eff} (m)	λ_{abs} (m)	λ_{scat}^{eff} (m)
466 nm (blue)	$46.4 \pm 1.9 \pm 2$	$49.3 \pm 0.3 \pm 2$	$301 \pm 3 \pm 27$
370 nm (ultraviolet)	$26.0 \pm 0.5 \pm 1$	$28.9 \pm 0.1 \pm 1$	$133 \pm 3 \pm 12$

Table 2.1: Measured optical properties of the water. These values correspond to the measurements performed in June 2000. The first error is statistical and the second systematic. Equation 2.15 does not hold for the values of the table because the value of λ_{att}^{eff} and those of λ_{abs} and λ_{scat}^{eff} were derived from different methods.

---

[3]The collimation of the source prevents a direct comparison with the value given in table 2.1
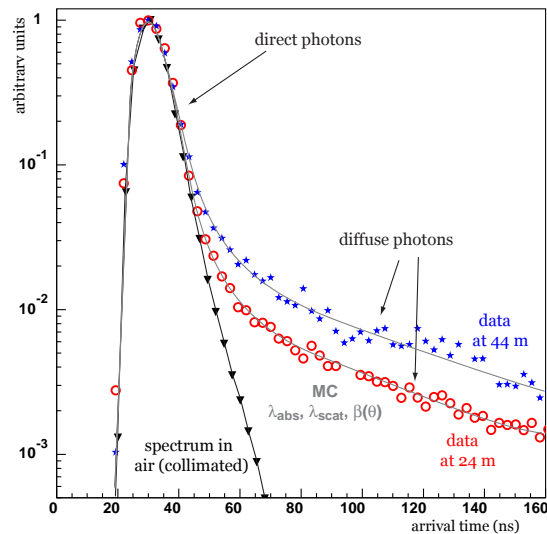
Figure 2.11: Photon time arrival distributions for several distances to the PMT. The distributions are normalized. The widening of the distributions is due to the scattering.

2.3.2 Optical background

The optical background is not produced by physical events, but it has an environmental origin [87]. Figure 2.12 shows a typical time dependence of the counting rate measured by one of the OMs of the PSL (described in section 2.4). Two components can be distinguished. First, there is a continuous baseline of ~60 kHz (for a 10" PMT) which is due to two factors. On the one hand, there is a contribution of the β-decay of the ^{40}K isotope present in sea water. The emitted electron can achieve a maximum energy of 1.3 MeV, enough to produce Cherenkov emission. On the other hand, bioluminiscence activity from bacteria colonies also contributes to the continous baseline. This contribution depends on the data taking period.

Second, there is a discontinuous component characterized by rapid (~ 1 s) flashes of light which increases the counting rate up to tens of Mhz. These bursts have also an organic origin.

Figure 2.13 shows the base rate and the burst fraction measured by the PSL for the whole period of data taking. Large variations in the optical background were observed.

2.3.3 Biofouling and sedimentation

In the sea water, the detector elements will be exposed to the adherence of bacteria (biofouling) and particle sedimentation, which will reduce the light transmission in the surface of the photomultipliers and the optical beacons. The effect of bioufouling and sedimentation on the ANTARES optical modules have been measured [88]. The experimental setup (see figure 2.14) consists of an Optical Module containing PIN diodes which are illuminated by the LEDs contained in a glass sphere located at a
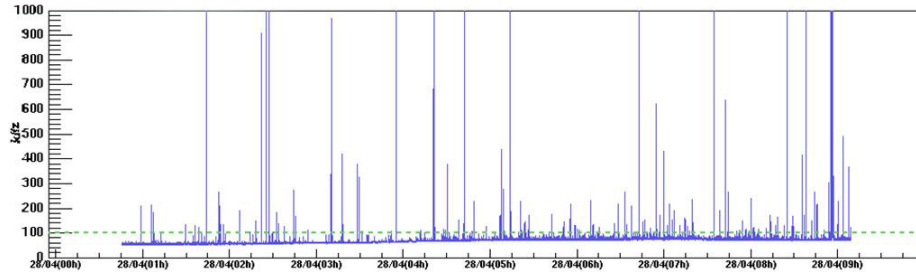
Figure 2.12: ANTARES optical background. Count rate measured by one of the OMs of the Prototype Sector Line. There is a continuous component (due to ^{40}K and bioluminiscence) and light bursts produced by living organisms.
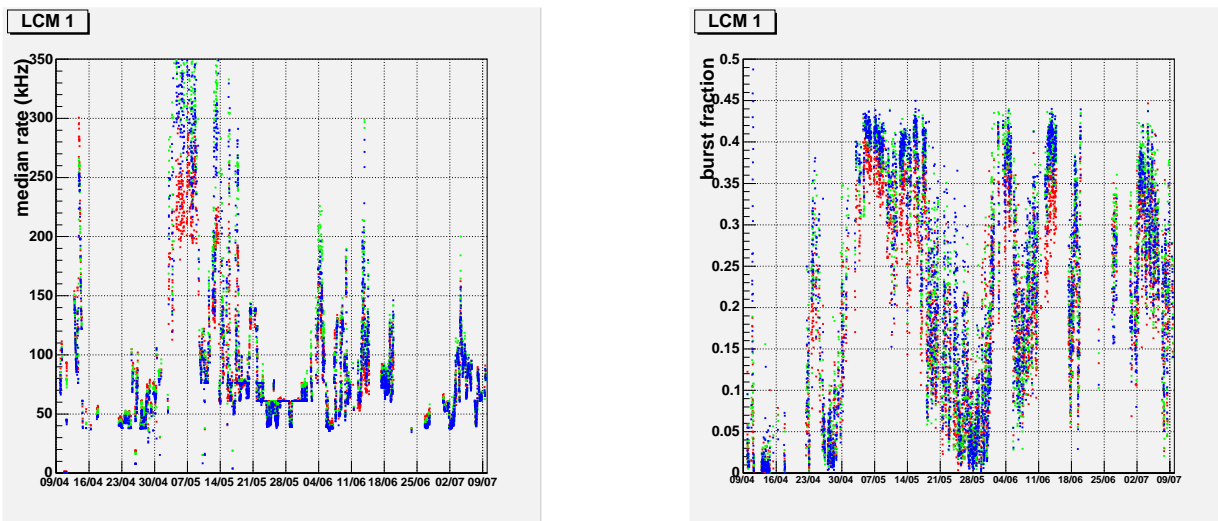
Figure 2.13: Left: Base rate (defined as the median value of the rate distribution in a time slice of 15 minutes) as a function of time. Right: Burst fraction (defined as the fraction of time, in a time slice of 15 minutes, during which the rate is 20% larger than the base rate) as a function of time. Both plots correspond to three months of data taking).

distance of 2.5 m.
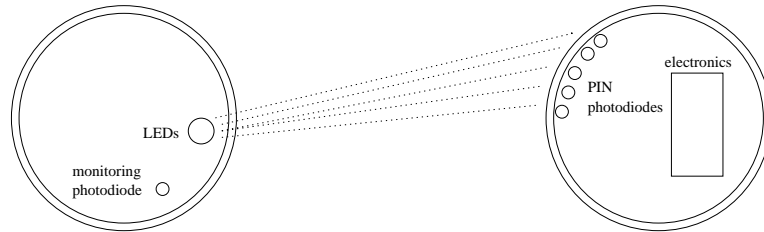
Figure 2.14: Experimental setup used to measure loss of transparency in the Optical Module. The spheres were separated by a distance of 2.5 m.

After 250 days of operation, the loss of transparency in the equatorial region of the OM dropped only ~1.6% and then saturated (see figure 2.15). These results imply that sedimentation would not be a major problem with the actual detector geometry since the PMTs are pointing 45° downwards. The effect of sedimentation has been also taken into account in the design of the LED and laser beacons. In both devices light is emitted through vertical surfaces.
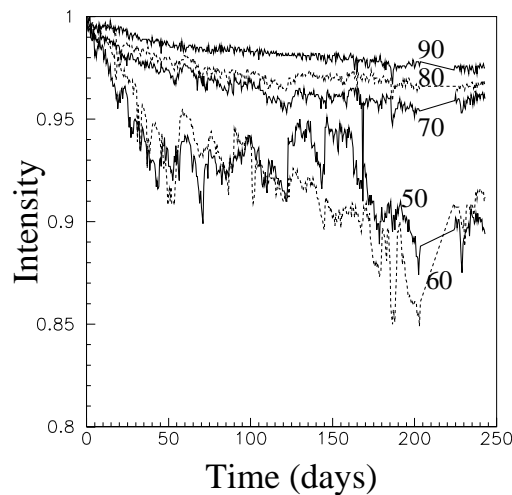
Figure 2.15: Results of sedimentation and biofouling tests. The loss of transparency from the top to the equator of an Optical Module has been measured. After almost one year, transmission only drops ~1.6% and then saturates for equatorial positions.

2.4   Milestones and construction status

The following list reviews the major milestones reached by the ANTARES collaboration:

- 1996-1999: Site evaluation studies. The main results of this programme have been already presented in the previous section.

- November 99 - June 2000: The Demonstrator Line was deployed. It consisted of a 350 m long line equiped with 7 PMTs. Inmersed at 1200 m deep, it allowed to check the acoustic positioning system and the measurement of the first atmospheric muons. The feasibility of the deployment of a long mechanical structure was shown.

- March 2001: A sea-bed study was performed by means of the Cyana submarine to evalute the obstacle average density. Only one "big" object per ha was found, which is low enough given the accuracy reached for deployment (~ 5 m).

- October 2001: The main electro-optical cable was deployed.

- December 2002: The Junction Box and the Prototype Sector Line (PSL) were deployed (see figure 2.16). The PSL is a reduced (one fifth) version of a complete line, which represents the basic unit of the detector. Apart from the 15 PMTs, it contained a LED beacon, a sound velocimeter, a pressure sensor, hydrophones and an acoustic transceiver.

- February 2003: Deployment of the Mini-Instrumentation Line (MIL) (figure 2.16). This line contained several devices for time calibration (a laser and LED beacons), triangulation (hydrophones and acoustic transceiver) and monitoring of the environmental parameters (a seismometer, a sound velocimeter, a pressure sensor and a conductivity-temperature-density meter).

- March 2003: The PSL and the MIL were connected to the Junction Box by the manned submarine "Nautile". The lines allowed to test a "mini-detector" in realistic conditions. This test validated the detector design and the deployment and connection procedures. This operations also revealed some problems: one of the optical fibres of the PSL and the MIL was broken (and thus the accuracy in the timing calibration was only $\sim$1 ms, instead of $\sim$1 ns), and there was a leak in an electronic container of the MIL. Both problems have been understood and corrected for the future.

The immediate future plan is to deploy a complete mechanical test line ("Line_Zero") with 25 storeys in early 2005. Among other things, this line aims to check the optical fibre transmission and the mechanical soundness of the different components. In addition to the Line_Zero, an improved version of the Mini-Instrumentation Line will be also deployed by March 2005. The first detector line will be inmersed in August 2005 and the complete detector will be installed by February 2007.
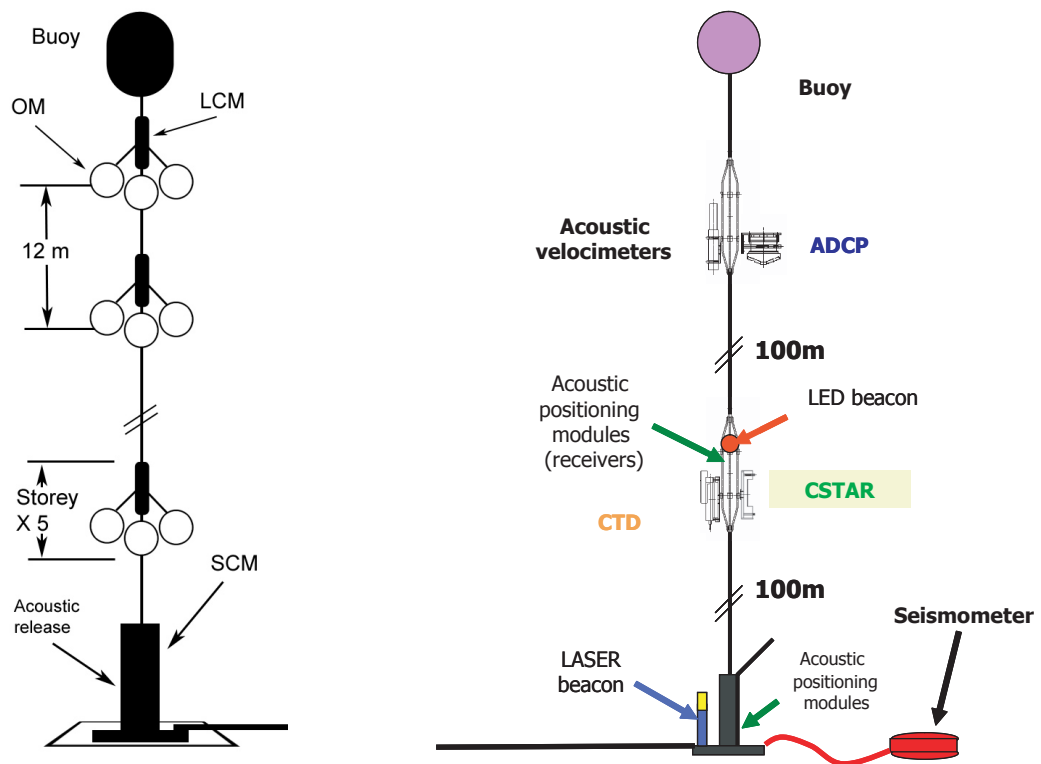
Figure 2.16: Left: Prototype Sector Line (PSL), which represents a fifth of a complete line. Right: Mini-Instrumentation Line (MIL), with calibration and monitoring devices.

2.5   Other neutrino telescopes

Although Neutrino Astronomy is a young field, it has become a very active experimental activity. In this section we review the most relevant experiments and results in high energy neutrino telescopes.

- **DUMAND**

  DUMAND was the first project for a Cherenkov neutrino telescope [89]. It started in 1975 in Hawaii and was cancelled in 1995. The technical studies performed during this period have been very useful for later experiments.

- **BAIKAL**

  BAIKAL is the first demonstration of the feasibility of underwater neutrino telescopes. It is located 1100 m deep at the Lake Baikal (Russia). They have made the first atmospheric neutrino detection underwater. The present detector (NT-200), which consists of 192 15" PMTs on eight strings, will be upgraded by three sparsed instrumented outer lines [90].

- **AMANDA**

  The AMANDA detector, located at the South Pole, uses the Antarctic ice as target. The present version, AMANDA-II, consists of 677 PMTs on 19 lines, most between 1500 m and 2000 m. The scientific impact of this experiment is very wide. Among the most important results the new limits on diffuse ν_μ fluxes can be mentioned [91]:

$$E^2 \Phi_{\nu_\mu}(E) < 2.6 \times 10^{-7} \ \text{GeV cm}^{-2} \ \text{s}^{-1} \ \text{sr}^{-1} \quad (100 \text{ TeV} < E_\nu < 300 \text{ TeV}) \tag{2.18}$$

  The limit obtained using cascades events is:

$$E^2 \Phi_{all \ \nu}(E) < 8.6 \times 10^{-7} \ \text{GeV cm}^{-2} \ \text{s}^{-1} \ \text{sr}^{-1} \quad (50 \text{ TeV} < E_\nu < 5 \text{ PeV})$$

$$E^2 \Phi_{all \ \nu}(E) < 0.99 \times 10^{-6} \ \text{GeV cm}^{-2} \ \text{s}^{-1} \ \text{sr}^{-1} \quad (1 \text{ PeV} < E_\nu < 3 \text{ EeV}) \tag{2.19}$$

  where a $\nu_e : \nu_\mu : \nu_\tau = 1{:}1{:}1$ flavour mixing has been assumed. The latter limit is obtained from the almost horizontal events, since up-going neutrinos are absorbed by the Earth at such high energies.

  On the other hand, a neutrino sky mapping has been made (see figure 2.17). No point-like source has been found [91], which allows also to set a limit in the flux:

$$\Phi_\nu^{lim}(E) \approx 1.3 \times 10^{-8} \ \text{cm}^{-2} \ \text{s}^{-1} \tag{2.20}$$

They have also constrained the WIMP allowed parameter space. All these results show the great scientific potential of this kind of projects and encourages the continuation of the work in two ways: increasing the effective volume to being sensible to astrophysical sources and building an equivalent detector in the North Hemisphere to achieve complete coverage of the sky.
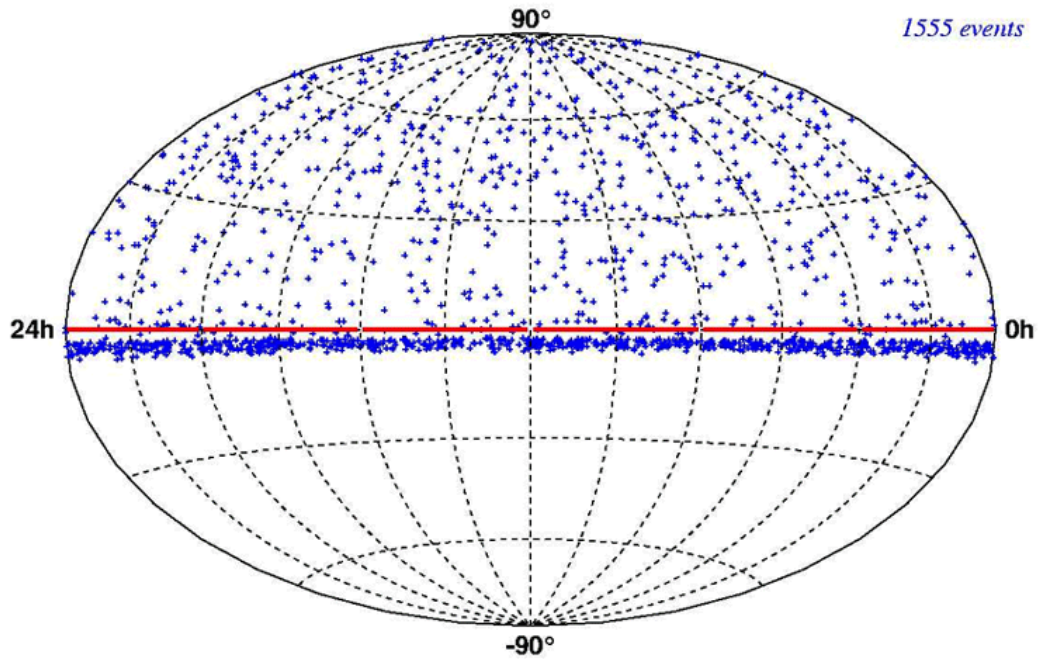
Figure 2.17: AMANDA-II sky plot of neutrino events (equatorial coordinates). The angular dimension of a search bin is 6×6 square degrees. The thick band of events below the horizon is produced by the atmospheric muon background. Above a declination of 5 degrees the muon background contamination is lower than 3%
.

- **IceCube**

  The ICECUBE project will be the first km^3 neutrino telescope, which is the natural size of neutrino telescopes. It is based on the AMANDA experience, and will deploy 4800 10" PMTs on 80 vertical lines (see figure 2.18). Moreover, important upgrades in the electronics have been included. The sensitivity of the full detector after one year is expected to be two orders of magnitude better than present experiments.

  The first four lines are expected to be installed in 2005 and the whole detector installation is foreseen in 2010. An additional detector, IceTop, will be set in the surface for atmospheric muon veto and calibration.
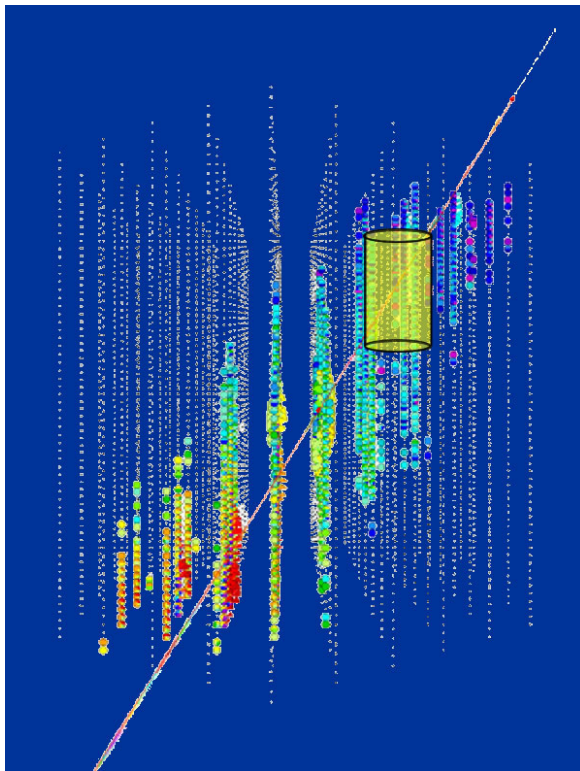
Figure 2.18: Comparison of ICECUBE and AMANDA (yellow cylinder) sizes. The effective area of ICECUBE will allow a major improvement of the reconstruction accuracy and the detected rates. (From D. Rianto / NSF)

- **NESTOR**

  The NESTOR collaboration [92] aims to deploy a tower of 12 floors, each of them with 12 PMTs. The site evaluation program has shown an extraordinary quality in the water transparency, due to the large depth (4000 m) which is available near the Greek coast.

- **NEMO**

  The NEMO collaboration [93] has performed extensive environmental measurements at Capo Passero, 70 km away of the coast of Sicily at 3500 m deep. The analysis performed show low rate of sedimentation and biofouling and good water properties. The present work includes prototype studies for a km^3 detector, which would consist of an array of towers, formed by a sequence of storeys, each of them supporting four optical sensors (two on each end).

- **The Mediterranean cubic kilometre detector**

  As it has been mentioned, next step in the high energy astronomy effort should be the construction of a cubic kilometre detector in the Northern Hemisphere, following the experience of the three Mediterranean projects. Due to the large scale of such detector, it would be necessary to concentrate this effort in a single detector in the Mediterranean Sea. This project has been submitted for financial support to the FP6 EU programme.

- **Other high energy neutrino detectors**

  Complementary experimental techniques are necessary to extend the search of astrophysical neutrinos to higher energies. For instance, hydrophones will be installed in some Cherenkov telescopes like ANTARES, ICECUBE or NESTOR to detect the acoustic wave produced by high energy particle cascades. In other experiments, the radio wave produced by the electromagnetic showers originated by high energy electron neutrinos will be used. For example, ANITA will deploy radio antennas in balloons in the South Pole and GLUE will search for radio emission produced by extremely high energy neutrinos and cosmic rays passing through the lunar limb. Finally, air showers will be used in the AUGER project (a combination of water Cherenkov tanks and fluorescence detectors) and the satellites OWL and EUSO.

Table 2.2 compares the characteristics of the Cherenkov telescopes with other experimental techniques to detect high energy neutrinos.

Radiation	Medium	$E_\nu threshold$	Att. length
Cherenkov	Filtered H_2O	GeV	100 m
	Natural lake	GeV	$\sim$ 20 m
	Deep ocean	GeV	$\sim$ 40 m
	Polar ice	GeV	$\sim$ 20 m
Cherenkov radio	Polar ice	>5 PeV	$\sim$ 1 km
	Moon	>100 EeV	
	Salt	>PeV	$\sim$ 1 km
Acoustic	Water	>1 PeV	$\sim$ 5 km
	Ice	>PeV	$\sim$ 1 km
EAS particles	Air	10 PeV	1 km
N_2 fluorescence	Air	EeV	10 km
EAS radar	Air	>EeV	$\sim$100 km

Table 2.2: Comparison of the characteristics of different experimental techniques to detect high energy neutrinos [94].

Chapter 3

Monte Carlo simulation and reconstruction tools

The purpose of this chapter is twofold. On the one hand, we will present the software Monte Carlo tools which have been used in this work. These programs have been developed by the ANTARES collaboration and include all the physical processes relevant for the detection. The different simulation steps: generation, propagation and reconstruction will be described. Moreover, large Monte Carlo samples of background and signal events have been produced and their characteristics will also be presented in this chapter.

3.1 Monte Carlo tools

As indicated in figure 3.1, the main steps in the Monte Carlo simulation chain are the generation of events, the track propagation simulating the Cherenkov light emission and the simulation of the detector response. Subsequently, the reconstruction of the track and the energy of the events is carried out.

3.1.1 Physics generators

For the analysis performed in this study, two kinds of physical events have to be generated: down-going muons to simulate the atmospheric muon background and neutrino events to simulate both the cosmic signal and the atmospheric neutrino background.

Neutrinos

Several programs have been developed in the ANTARES collaboration for the generation of events. For this analysis, the package we have used is GENHEN [95]. It includes the possibility of simulating both the neutral current and charged current interaction of any of the three neutrino flavours. The energy spectrum and the zenith
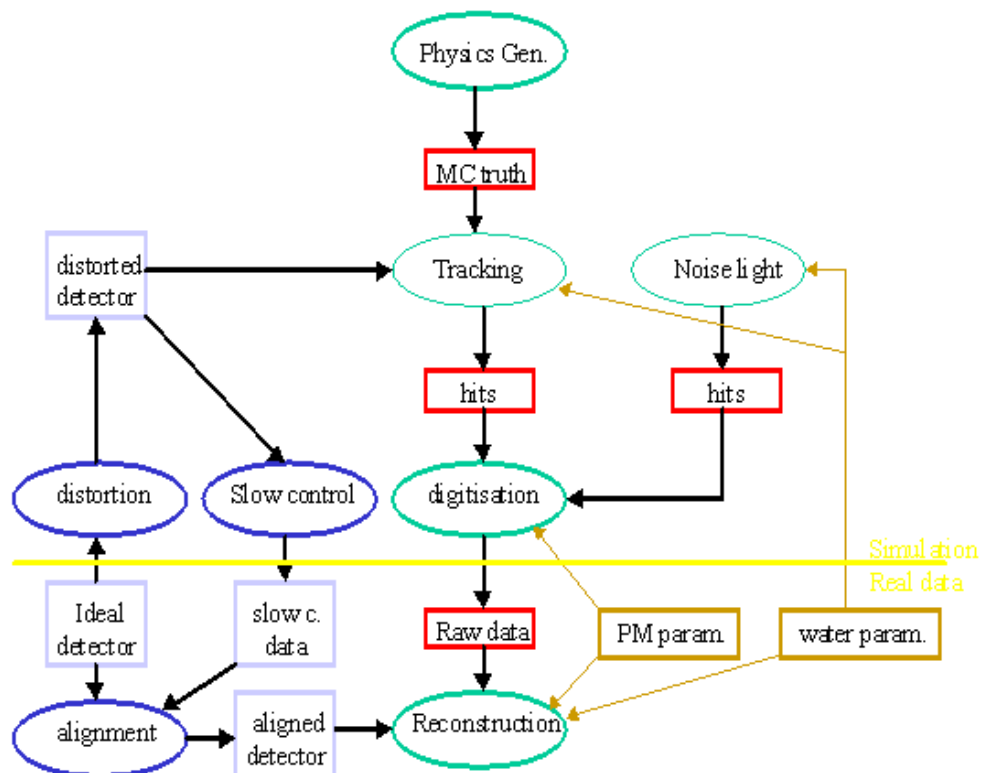
Figure 3.1: After generating the events (neutrinos or atmospheric muons), the corresponding muon tracks are generated. These muons are propagated and their Cherenkov emission simulated. Once the light input in the detector is calculated, the response of the detector is simulated. This information will be used to reconstruct the track and the energy of the muon.

angular region of generation are also inputs of the program. After selecting the energy and the zenith angle, the type of target nucleon and the vertex position are chosen.

A large cylindrical "can" is defined around the instrumented volume. This can determines the surrounding region where the Cherenkov light is generated in the Monte Carlo. The radius and the vertical length of the can are those of the instrumented volume cylinder increased by roughly three attenuation lengths (see figure 3.2). If the generated neutrino vertex is inside the can, all final particles produced in the interaction will be stored to calculate their Cherenkov light output. On the contrary, if the vertex is outside the can, only the muon is propagated up to the can surface, since the Cherenkov light produced by the rest of the particles will not reach the instrumented volume.
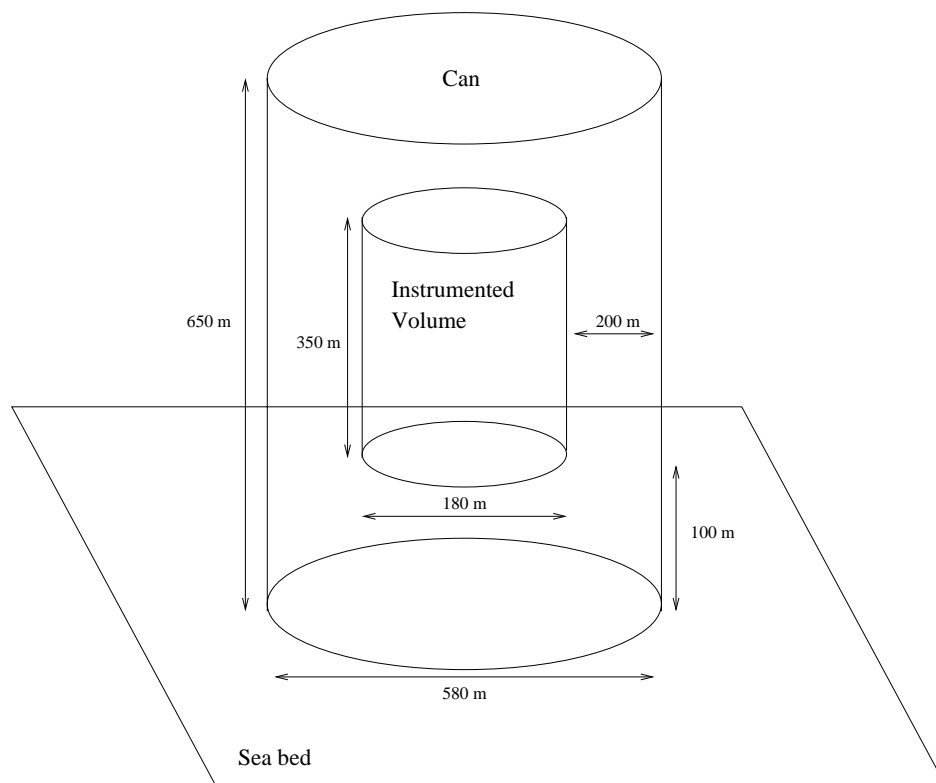
Figure 3.2: The can is built by extending the instrumented volume by three attenuation lengths. If the vertex is outside the can, only the muon is propagated up to the can surface, since the Cherenkov light produced by the rest of the particles would not reach the detector.

In the case of the ν_e and ν_τ CC interactions and ν_μ NC interactions, the interaction vertex is calculated inside the "can" volume, since external events would not give a detectable signal. For the ν_μ CC interactions, the large muon range allows to extend the generation volume beyond the geometric volume of the detector. The size of the generation volume is given by the muon range associated to the highest neutrino energy generated.

The program used to simulate the neutrino interaction is LEPTO [96], with the CTEQ6 structure functions [81]. For the hadronisation, PHYTIA/JETSET [97] is used. The simulation of τ interactions is carried out by TAUOLA [98], which includes the τ polarization. The muon propagation is made by MUSIC [99] and MUM [100]. Both packages take into account all the energy loss processes up to the highest energies. MUSIC includes also the multiple scattering (which is negligible for ANTARES but could have some effect in km^3 detectors).

As it has been said, the generation is made according to an input energy spectrum. In order to use the same sample for different spectra, the generation weight is used. As it is indicated later, it is convenient to generate with a hard spectral index, typically $\gamma = 1.4$. In this way, we can produce statistically significant samples at high energies in a reasonable time.

The generation weight that is used to calculate the detected number of events for a given spectral index γ is given by:

$$w_i = V \cdot I_\theta \cdot I_E \cdot E^\gamma \cdot \sigma(E) \cdot \rho N_A \cdot P_{Earth}(E, \theta) \tag{3.1}$$

where:

- V: Generation volume

- I_θ: Angular phase space factor. For a generation uniform in
  $\cos \theta$ and ϕ between θ_{min} and θ_{max}, $I_\theta = 2\pi(\cos \theta_{max} - \cos \theta_{min})$.

- I_E: Energy phase space factor. If $\gamma \neq 1$, $I_E = (E_{max}^{1-\gamma} - E_{min}^{1-\gamma})/(1 - \gamma)$. If $\gamma = 1$, $I_E = \ln(E_{max}/E_{min})$

- E^γ: Factor that takes into account the generation spectral index.

- $\sigma(E)$: Total neutrino-cross section of the charged current neutrino interaction.

- ρN_A: Total number of target nucleons per unit volume (ρ is the target density and N_A, Avogadro's number.)

- $P_{Earth}(E, \theta)$: The probability of neutrinos to penetrate the Earth.

The rate of detected neutrinos for a given flux is then given by:

$$R = \frac{1}{N} \sum_{i=1}^{N} w_i \frac{d\Phi(E, \theta, \phi)}{dEd\Omega} \tag{3.2}$$

where N is the total number of generated events.

Atmospheric muons

The approach used for atmospheric muons presents some differences with respect to the neutrino generation. Although the flux of muons at the detector level can be parameterized, it would not take into account the possibility of detecting two or more events at the same time. These events, called multi-muons, are very dangerous, since they can be easily mis-reconstructed as up-going events. For this reason, a full simulation has been performed. Two codes have been used: the CORSIKA [101] and the HEMAS [102] packages.

The primary energy spectrum used in these simulations ranges from ~1 TeV to ~100 PeV. Primaries with lower energies will not produce detectable muons at a depth of 2500 m. The packages used for the hadronic shower are QGSJET [103] in CORSIKA and DPMJET [104] in HEMAS.

The next step is to propagate the HEMAS and CORSIKA muon events from the sea level down to the ANTARES depth. A threshold of 500 GeV at sea level is applied since muons below this energy will not reach the detector. As in the case of the neutrino event, the muon propagation is done with MUSIC and MUM.

3.1.2 Muon propagation in water

The particle simulation inside the can volume is done by the KM3 [105] and GEASIM [106] packages. Both programs simulate the muon propagation in water including the production of Cherenkov light for the muon itself and secondary particles. GEASIM, based on GEANT 3.21, performs a full tracking simulation of all particles as they go through the detector. The number of detected Cherenkov photons is computed by means of an analytical function taken into account the light absorption. However, photon scattering is not assumed.

The approach followed in KM3 presents some differences. The muon propagation is done in one-meter steps using a modified version of the MUSIC package. In case the muon energy loss surpasses a critical threshold (0.3 GeV), electro-magnetic showers are randomly generated. Cherenkov photons are then sampled from photon tables containing the average photon field produced by the muons and the electro-magnetic showers. These tables have been created previously and parameterize the amount and arrival times of Cherenkov light detected by individual PMTs. The effect of the photon scattering is included in the simulation but light from hadronic shower is not.

Since light scattering is a key aspect in the angular resolution, we have performed the track simulation with KM3 and then, the contribution of the hadronic cascade calculated with GEASIM is added.

The KM3 program simulates the Cherenkov light in three steps. First, the GEN package generates the photon field produced by track muons and secondary showers. The water volume is divided in spherical shells of different radii centered at the track segment source. Cherenkov photons are tracked individually through the water until absorption takes place or photons leave the can volume. At each shell boundary,

the position, direction and arrival time of every photon are recorded. Then, the HIT program translates all this information into photoelectron probabilities and arrival time distributions which are stored in large photon tables as previously mentioned. Photon probabilities are computed taking into account the optical properties of the sea water at the ANTARES site, the relative orientation of the PMTs, the quantum efficiency of the PMTs and the glass sphere and silicon gel trasmission (see figure 3.3). The GEN and HIT programs are run once only to build the Optical Module hit probability tables. The KM3MC program takes as input the detector description and uses the photon tables to calculate the number of photoelectros produced in each PMT and their arrival time. The transit time spread of the PMTs and the electronics (a simplified version of the ARS simulation) are also taken into account. The background due to ^{40}K has been also simulated.

3.1.3   Water model

Light scattering in water distorts the spatial and timing distributions of the Cherenkov cone. Light scattering takes place when randomly distributed optical inhomogeneities in the medium (scattering centres) produce random changes in the direction of light. In seawater, the scattering centres are density fluctuations originated by random molecular motion (molecular scattering), and organic and inorganic suspended particles (scattering by particles).

On the other hand, suspended particles which are large in comparison with the light wavelength tend to scatter light mainly in the forward direction, that is, at small angles with respect to the direction of the incident light. Therefore, the phase function from particle scattering is strongly peaked in the forward direction. Two models have been used to describe the scattering produced by particles, called thereafter "Medsea" and "Global".

Mediterranean sea model: Medsea

The analytical formula most commonly used to describe the asymmetric scattering is the Henyey-Greenstein (HG) function [107]. Measurements made in the Mediterranean sea (Ref. [108] p.106) can be well approximated by the linear combination of two Henyey-Greenstein phase functions [109]:

$$\tilde{\beta}_{HG}(g, \theta) = \frac{1}{4\pi} \frac{1 - g^2}{(1 + g^2 - 2g\cos\theta)^{3/2}} \tag{3.3}$$

where g is the average of the cosine of the scattering angle, $\langle \cos\theta \rangle$.

Global

Instead of using an analytical approximation, this model is based on a linear combination of two terms depending on the population of scattering centres [110]. The first
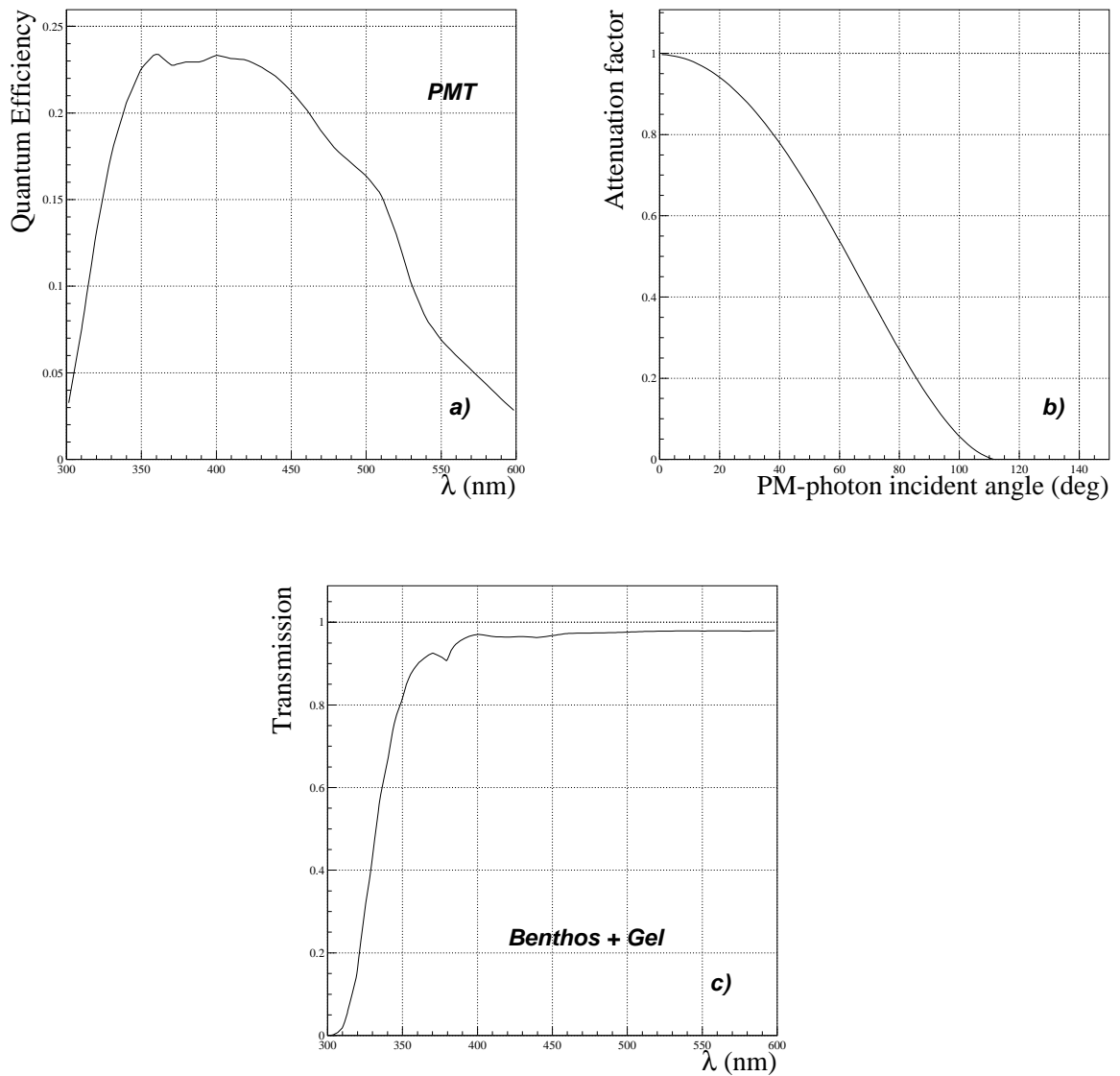
Figure 3.3: Experimental results of OM parameters included in the simulation: a) quantum efficiency of the photomultiplier, b) light attenuation factor in the pressure-resistant sphere, c) transmission of the glass sphere and the silicone gel.

term is related to the molecular scattering. The second term takes into account scattering by particles. In this case, following the approach of Mobley (Ref [108] p.111), the phase function is obtained as the average of three-particle phase functions measured by Petzold [111] in different waters: turbid, coastal and clear water. The uniform shape of the angular dependence for different kind of waters makes the definition of a typical particle phase function, $\tilde{\beta}_{part}(g, \theta)$, reasonable.

In figure 3.4, a comparison between the different approaches is presented.
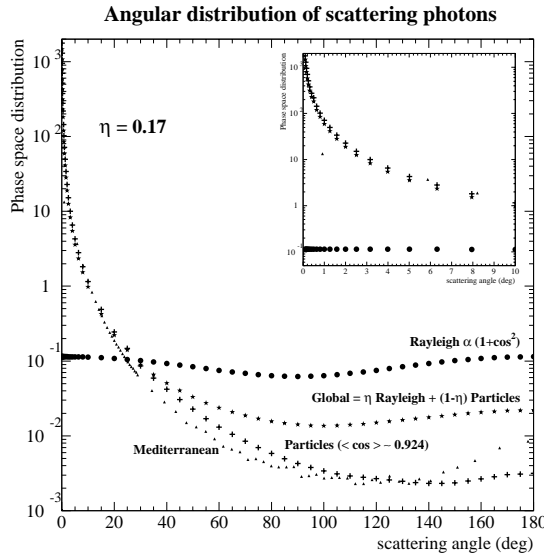
Figure 3.4: Comparison between the scattering phase function of the models **Medsea** and **Global**. **Rayleigh** and **Particle** distributions are also shown. See [112] for more details.

3.1.4   Detector generation

The generation of the detector is performed by GENDET [113,114]. This program allows the generation of several geometries and can provide the positions of all the elements of a typical line (OM, LCM, PMT, tiltmeter, hydrophone, etc.) Moreover, misalignments due to the action of horizontal currents can be introduced, as well as other kinds of offsets: time delays in the LCMs, twists in the lines, time and efficiency differences in the OMs, etc. Figure 3.5 shows the layout of the 12-line detector.

3.1.5   Track reconstruction

Several approaches have been developed in the ANTARES collaboration in order to reconstruct the direction and the energy of the muon. The energy reconstruction, which is one of the subjects of this work, will be described in detail in the next chapter.
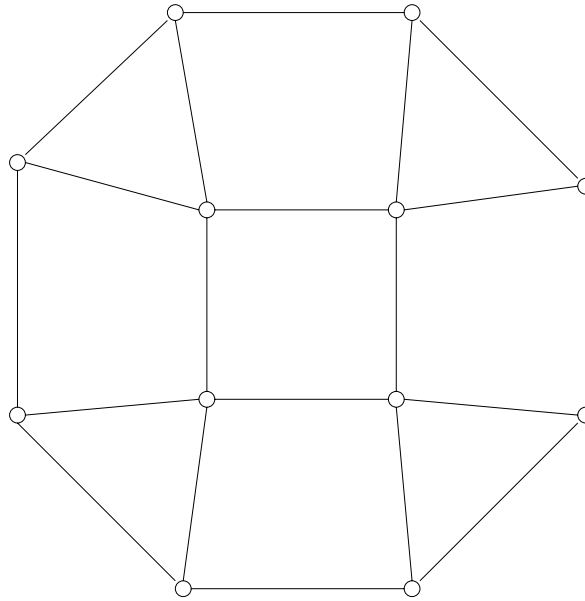
Figure 3.5: Layout of the 12-line detector.

Concerning the track reconstruction, the frame program is RECO [115–117] written in C++ and based on an older FORTRAN program called POSIDONIA. Four different reconstruction strategies can be used:

- **Standard strategy:** The standard strategy is based on the arrival times of the Cherenkov photons emitted by the muons. Direct photons are those which have not undergone scattering. The corresponding arrival time is given by

$$\tilde{t}_i = t_0 + (L_i + r_i \tan \theta_C)/c \tag{3.4}$$

  where $\tilde{t}_i$ is the direct time, t_0 is the time when the muon was at a certain reference position (taken by convention in ANTARES to be the plane perpendicular to the track which contains the center of the detector), L_i is the distance between the reference position and the point of closest approach to the optical module, r_i is the minimum distance between the muon track and the optical module and θ_C is the Cherenkov angle (see figure 3.6).

  However, not all the photons fit this relationship. First, scattered photons will undergo some delay. Moreover, the photons produced by the electromagnetic and hadronic cascades will also arrive at different times. Finally, photons from optical background (^{40}K and bioluminiscence) will arrive randomly.

  Monte Carlo simulation is used to compute the distribution of the difference between the actual time t_i and the direct time $\tilde{t}_i$. This estimated distribution is used as an average probability density function to assign a probability for a hit
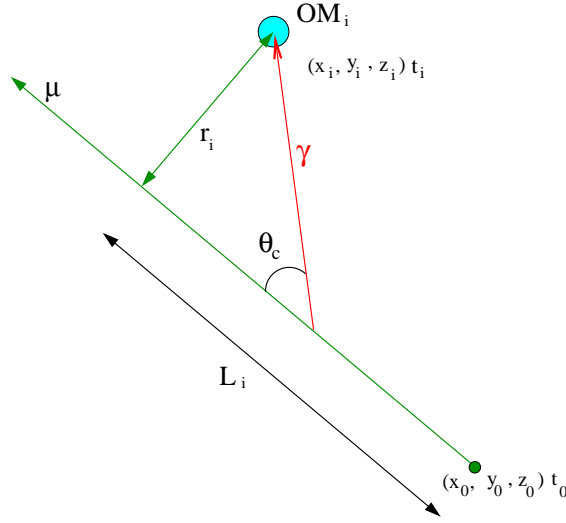
Figure 3.6: Magnitudes used in the arrival time definition.

to come from a track. Track reconstruction is based on the maximization of a likelihood function using the previous Monte Carlo pdf.

- **Carmona Strategy**: The Carmona strategy [118] improves greatly the re-sults of the Standard Strategy by using the geometrical relationships between the Cherenkov hits and the corresponding track as a consequence of the fixed Cherenkov angle. In equation 3.4, the dependence on t_0 can be avoided combin-ing two hits and calculating $\Delta r_{ij} = r_i - r_j$:

$$\Delta r_{ij} = \frac{c\Delta t_{ij} - \Delta L_{ij}}{\tan\theta_c} \quad (3.5)$$

As explained in [119, 120], this allows to reconstruct the x and y variables, which set the crossing point of the track, and the value of t_0. This method uses the Standard Strategy ouput as a first guess, and then improves iteratively the re-sult. Figure 3.7 shows the angular resolution and the effective area. The latter parameter is the size of a 100%-efficient surface that observes the same number of neutrinos than the detector

$$A^\nu_{eff}(E_\nu, \theta_\nu, \phi_\nu) = \frac{N_{sel}(E_\nu, \theta_\nu, \phi_\nu)}{N_{gen}(E_\nu, \theta_\nu, \phi_\nu)} \times V_{gen} \times (\rho N_A) \times \sigma(E_\nu) \times P_{Earth}(E_\nu, \theta_\nu) \quad (3.6)$$

where N_{sel} is the number of selected events after applying the selection cuts; N_{gen}, the number of events in the generated neutrino flux, and V_{gen}, the generation vol-ume. The other factors refer to the propagation: ρ is the average Earth's density,

$\sigma(E_\nu)$ is the neutrino interaction cross-section and $P_{Earth}(E_\nu, \theta_\nu)$ is the probability that a neutrino with energy E_ν and zenith angle θ_ν reach the interaction point.

- **Aart Strategy:** This algorithm [121] consists of a chain of fit procedures which estimate the track with increasing accuracy. As in the Standard Strategy, the maximization of the likelihood is used. The angular resolution of this strategy is similar to Carmona's results.

- **Single Line Strategy:** This strategy only uses the hits of one string. It is useful when only one line is deployed or for low energy events, which could only illuminate one string.

3.2 Monte Carlo samples

In this section, the characteristics of the Monte Carlo samples used in the analysis are described. As mentioned, two different types of MC events are used: neutrino events and atmospheric muons.

3.2.1 Neutrino events

For neutrino events (i.e. atmospheric neutrinos and cosmic signal), mainly two samples have been used. On the one hand, a sample with 2.5×10^{11} neutrinos and 1.5×10^{11} anti-neutrinos (sample I), generated at Valencia. On the other hand, a sample with 10^{12} neutrinos and 10^{12} anti-neutrinos (sample II), generated at Bari and Valencia. Table 3.1 shows a summary of the main characteristics of both samples. The most relevant difference is that in the first case the hadronic cascade simulation is not included, while in the second sample it has been taken into account.

In both cases, neutrinos and anti-neutrinos are generated with an angular distribution isotropic in 2π (up-going events) and with an energy spectrum $E^{-1.4}$. As it was explained in the previous section, proper weights can be calculated to transform this spectrum into another one. Fluxes for different atmospheric and signal neutrino models are computed with the INFLUX package [122]. The neutrino energy ranges from 10^2 to 10^8 GeV in sample I and from 10^2 to 10^7 GeV in sample II. The electronics simulation includes 2 ARS per OM, with a 25 ns integration gate and 250 ns of dead time. Light propagation is simulated using group velocity. Finally, the detector geometry corresponds to the 10 string layout in sample I (see appendix A for more details on this detector) and the 12 string detector in sample II, both with 900 photomultipliers in total.
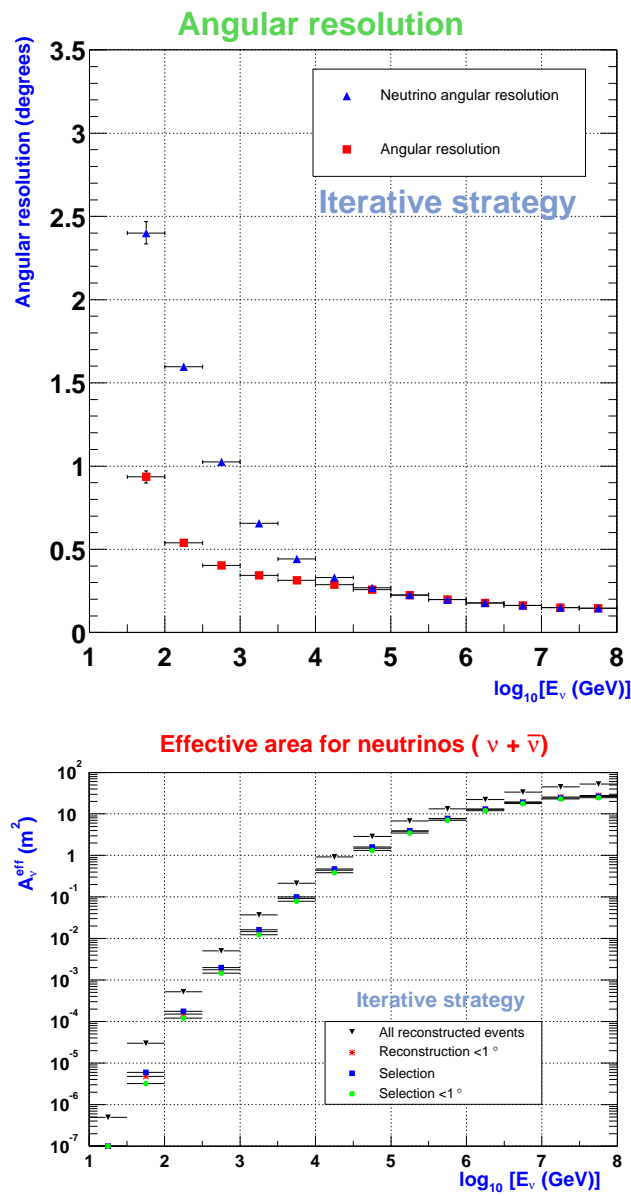
Figure 3.7: Neutrino and muon angular resolution (top) and effective area for $\nu + \bar{\nu}$ (bottom) using the Carmona strategy as a function of the neutrino energy.

Sample	Event Generation	Detector	Propagation	Reconstruction
I	GENNEU v5r1 $2.5 \cdot 10^{11} \ \nu + 1.5 \cdot 10^{11} \ \bar{\nu}$ upgoing, isotropic $E^{-1.4}$ [10^2-10^8 GeV]	GENDET v1r2 10 lines	KM3 v2r0 partic-0.0075 v_{group} used	RECO v4r2 Carmona Strategy
II	GENHEN v5r6 $10^{12} \ \nu + 10^{12} \ \bar{\nu}$ upgoing, isotropic $E^{-1.4}$ [10^2-10^7 GeV]	GENDET v1r2 12 lines	KM3 v2r1 GEASIM v4r8 partic-0.0075 v_{group} used hadronic shower	RECO v4r3 Carmona Strategy

Table 3.1: Characteristics of the samples of neutrino events and versions of the programs used to generate them.

3.2.2 Atmospheric muons

As it has been explained in section 3.1.1, atmospheric muon simulation requires a different treatment. In order to have the largest statistical significance available, several atmospheric muon samples have been used.

Most of the detailed results shown in this work correspond to the sample generated at Bologna with HEMAS [123]. The model used to describe the cosmic ray primary energy spectrum is a simplified version of the Hörandel model [124]. In this version, only elements with A≤56 are considered (above A=56 the fluxes are much lower), grouped in five cases (p, He, Li-F, Ne-Cr and Mn-Fe). Figure 3.8 shows the energy spectra for these groups. The flux of each element is given by

$$\frac{d\Phi_Z}{dE_0}(E_0) = \Phi_Z^0 E_0^{\gamma_Z} \left[1 + \left(\frac{E_0}{\hat{E}_z} \right)^{\epsilon_c} \right]^{(\gamma_c - \gamma_Z)/\epsilon_c} \tag{3.7}$$

where Φ_Z^0, γ_Z and $\hat{E}_z$ are the absolute flux at 1 TeV/nucleus, the spectral index and the cut-off energy, respectively. The values for each group are given in table 3.2. This table also shows γ_c, the hypothetical slope beyond the knee and ϵ_c, which accounts for the smoothness of the transition from the first to the second power-law.

The main characteristics of this sample are summarized in table 3.3. Primary events are generated with zenith angles ranging from 0° to 85°. Zenith angles greater than 85° are not simulated because neutrino-induced muons dominate at such large angles at the ANTARES depth. For angles $0° < \theta < 60°$, the atmosphere can be considered as a flat disc where the air density decreases with height, but for greater angles, the Earth's curvature has been taken into account.

An important point to consider concerning the atmospheric muon sample is its equivalent data taking time. It depends on the energy since the sample has been

	γ_Z	$\Phi_Z^0 \; (m^2 \; sr \; s \; TeV)^{-1}$	$\hat{E}_z$ (GeV)
p	-2.71	$8.73 \cdot 10^{-2}$	$4.5 \cdot 10^6$
He	-2.64	$5.71 \cdot 10^{-2}$	$9.00 \cdot 10^6$
Li-F	-2.68	$3.24 \cdot 10^{-2}$	$3.06 \cdot 10^7$
Ne-Cr	-2.67	$3.16 \cdot 10^{-2}$	$6.48 \cdot 10^7$
Mn-Fe	-2.58	$2.18 \cdot 10^{-2}$	$1.17 \cdot 10^8$

γ_C	ϵ_c
-4.7	1.87

Table 3.2: Numerical values used in the atmospheric muon generation [123].

generated with a low spectral index in order to increase the statistics at high energies. Therefore, a global time for the whole sample cannot be defined. Details of the values of the equivalent time are presented in [123]. Typical values (see table 3.4) range from ∼1 day for low energies (∼100 TeV) to ∼1 year for high energies (∼ 1 EeV). The fact that statistics at intermediate (and low) energies are not of the order of years enhances the importance of establishing stringent selection cuts to guarantee full downgoing cosmic rejection.
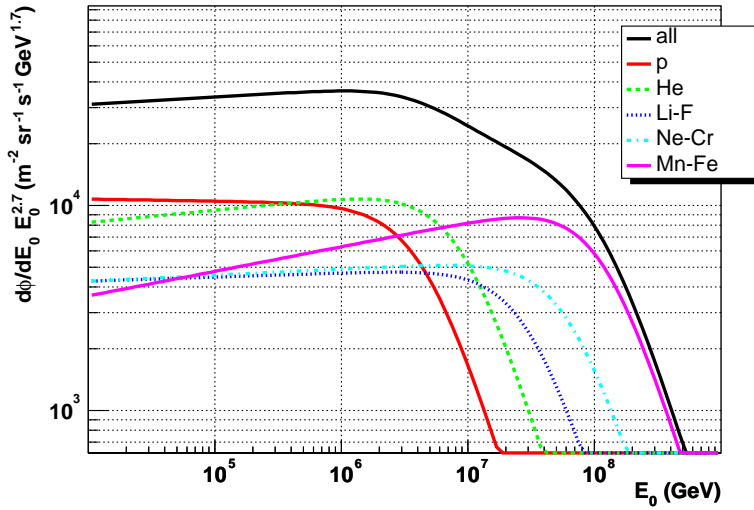
Figure 3.8: Differential energy spectra for the five groups considered in the cosmic ray simulation.

Other atmospheric muon samples have been used for cross-checks. A sample of 3.367×10^8 primaries generated with GEM using the Okada parameterization has been tested. These files are equivalent to 8.9 days of data taking in a detector as ANTARES.

Moreover, a sample of 4.0×10^7 multimuons in the range $0° < \theta < 70°$, produced

Event generation	HEMAS	5 mass groups (p, He, Li-F, Ne-Cr and Mn-Fe) from 20 to $2 \cdot 10^6$ TeV
Detector	GENDET v1r2	12 lines
Propagation	MUSIC KM3 v2r1	partic-0.0075
Reconstruction	RECO v4r3	Carmona strategy

Table 3.3: Main characteristics of the Bologna atmospheric muon sample. The reconstruction was redone using the Carmona strategy.

θ bin	$0° < \theta < 60°$					$0° < \theta < 60°$				
Energy bin	1	2	3	4	5	1	2	3	4	5
p	1.51	0.75	1.35	15.70	174	1.38	5.05	5.29	57	668
He	1.35	0.98	2.98	38.57	602	1.09	6.63	9.00	142	$2.2 \cdot 10^3$
Li-F	2.00	1.48	2.42	50.88	979	1.83	7.25	7.12	154	$2.9 \cdot 10^3$
Ne-Cr	1.90	0.81	1.36	30.17	549	1.60	4.81	4.63	81	$2.1 \cdot 10^3$
Mn-Fe	1.86	0.38	0.45	5.68	59	1.71	1.85	0.87	8.1	207

Table 3.4: Equivalent data taking time in days of the Bologna sample. The energy bins are given by the following limits: 20 TeV - 200 TeV - 2 PeV - 20 PeV - 200 PeV - 2 EeV [123].

by primaries with energies exceeding 200 TeV has also been used. This sample is equivalent to 9 days of data taking time.

Chapter 4

Energy reconstruction

The reconstruction of the neutrino energy is not an easy task. In general, the neutrino energy can not be measured directly since only an unknown fraction of its energy goes to the muon. For contained events, where the hadronic shower develops inside the detector volume, an estimation of the total neutrino energy can be made, but these are low energy events and represent a small fraction of the total detected events. On the other hand, only part of the muon energy at the vertex interaction is visible at the detector due to the energy losses produced outside the can. Nevertheless, there is a correlation between the neutrino energy and the muon energy which can be used to estimate the former.

In the first part of this chapter we review the muon energy loss processes and topics related to the muon propagation as the muon effective range, energy loss distributions, etc. In section 4.3, we explain a method which takes into account the dependence of the muon energy loss with the muon energy to estimate the latter and present the results. Finally, a calculation of the neutrino energy is made, although it has to be considered as a first estimation which could be useful especially for high energy events.

4.1   Muon energy loss

In order to reconstruct the muon energy, the muon energy loss is used, because the higher its energy, the higher the energy loss along its track. The total energy loss by unit of length can be written as

$$\frac{dE}{dx} = \frac{dE}{dx}\bigg|_I + \frac{dE}{dx}\bigg|_p + \frac{dE}{dx}\bigg|_b + \frac{dE}{dx}\bigg|_{pn} \tag{4.1}$$

where the subscripts I, p, b and pn refer to the energy losses due to ionization (including δ-ray production and excitation processes), pair production, *bremsstrahlung* and photo-nuclear interactions, respectively. The previous formula can be parameterized as

$$-\left\langle \frac{dE}{dx} \right\rangle = \alpha(E) + \beta(E) \cdot E \qquad (4.2)$$

There is an almost constant term, $\alpha(E)$, due to ionization and a term which grows linearly with the energy with slope $\beta(E)$ accounting for radiative losses. In water, $\alpha \simeq 2.67 \cdot 10^{-3}$ GeV g^{-1} cm^2 and $\beta \simeq 3.40 \cdot 10^{-6}$ g^{-1} cm^2 (for 30 GeV$< E_\mu <$35 TeV) [125]. As a first approximation, they can be considered as energy independent. Figure 4.1 shows the dependence of the energy loss due to each interaction on the muon energy.

The energy loss dependence due to ionization is weak, whereas the losses caused by radiative process grow linearly with the energy. For this reason, this method is only valid when radiative process dominate, i.e. above the critical energy ($\sim$600 GeV in water, $\sim$500 GeV in rock), defined as $\epsilon_c = \alpha/\beta$. Nevertheless, the stochastic nature of the radiative losses makes very difficult the muon energy reconstruction and limits unavoidably the accuracy of the results.
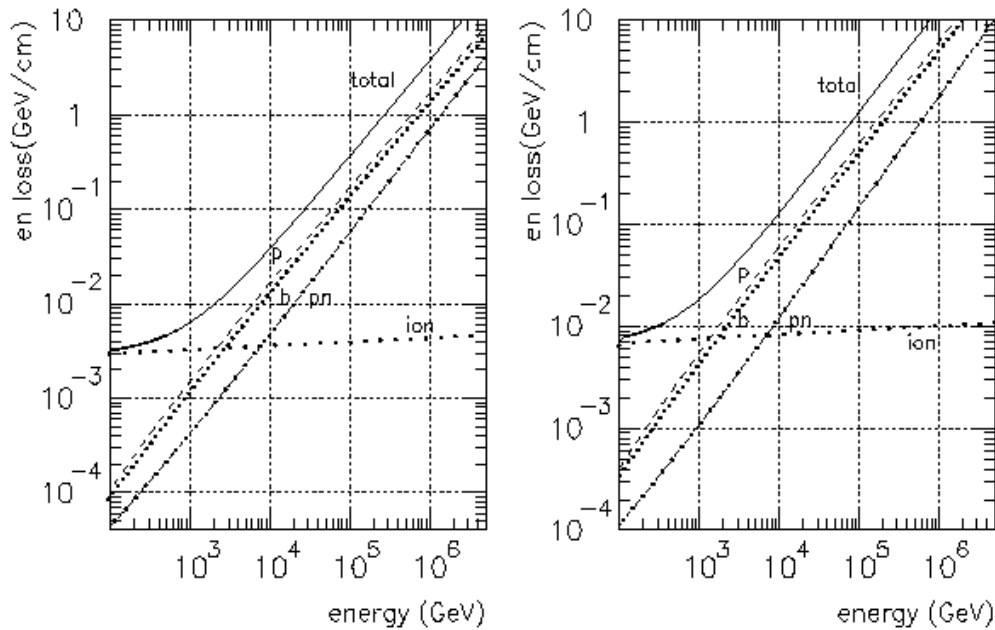
Figure 4.1: Energy loss of a muon in water (left) and standard rock (right) [126]: p, pair production; b, *bremsstrahlung*; pn, photo-nuclear interactions; ion, ionization.

In the following sections, a brief description of the energy loss processes is shown. A more detailed description can be found in [126].

4.1.1 Ionization

Muons traversing matter produce atomic excitations and ionizations. If the electrons stripped off are very energetic, they are called δ-rays. Ionization is the dominant process of muon energy loss at low energies (< 1 TeV). When the incident muon velocity is larger than the orbital velocity of electrons ($\sim Z\alpha c$), the mean energy loss is given by the Bethe-Bloch formula

$$-\frac{1}{\rho}\frac{dE}{dx} = K\frac{Z}{A\beta^2}\left[\frac{1}{2}\ln\left(\frac{2m_e(\gamma^2-1)}{I(Z)^2}T_{max}\right) - \beta^2 - \frac{\delta}{2}\right] \tag{4.3}$$

where

$$T_{max} = \frac{2m_e(\gamma^2-1)}{1+2\gamma\frac{m_e}{m_\mu}+\left(\frac{m_e}{m_\mu}\right)^2} \tag{4.4}$$

is the maximum kinetic energy that can be transferred to a free electron in a single collision, $K = 4\pi N_A r_e^2 m_e c^2$, $I(Z)$ is the mean ionization potential of the medium and δ is a correction to take into account the density effect.

4.1.2 Pair production

The dominant energy loss process for muons with energy above $\sim$1 TeV is the electron pair production[1] (see figure 4.2). The differential cross section of this process can be approximated as

$$\frac{d\sigma(E,v,\rho)}{dvd\rho} = \frac{2}{3\pi}(Z\alpha r_e)^2\frac{1-v}{v}\left(\Phi_e + \frac{m_e^2}{m_\mu^2}\Phi_\mu\right) \tag{4.5}$$

where $v = (\epsilon_+ + \epsilon_-)/E$ is the energy fraction transferred to the pair, $\rho = (\epsilon_+ - \epsilon_-)/E$ is the asymmetry coefficient and the functions Φ_e and Φ_μ correspond to different QED diagrams and contain atomic and nuclear corrections.

4.1.3 Bremsstrahlung

Bremsstrahlung is the process by which charged particles emit radiation in the presence of an electromagnetic field giving rise to a deceleration. Concerning muon propagation in a dense medium, this deceleration is produced by the electromagnetic interaction with the nuclei and electrons of surrounding atoms. The general formula for the cross section of this process can be expressed as

$$\sigma = \sigma_{el} + \Delta\sigma_a^{in} + \Delta\sigma_n^{in} \tag{4.6}$$

---

[1]The contribution of $\mu\bar{\mu}$ pair production to the energy loss is negligible below 10 TeV (less than 0.01% of the total energy loss [127]).

Figure 4.2: Feynman diagrams of the pair production process.

where σ_{el} is the elastic cross section for *bremsstrahlung* on the Coulomb centre with corrections accounting for the alteration of the Coulomb field by atomic and nuclear charge distributions and $\Delta\sigma_{a,n}^{in}$ are the contributions of additional inelastic processes involving changes in the electronic and nuclear structure of the final state (see figures 4.3 and 4.4). Numerically, the elastic cross section can be expressed as

$$\sigma_{el}(E, v) = \frac{\alpha}{v} \left(2Z \frac{m_e}{m_\mu} r_e \right)^2 \left(\frac{4}{3} - \frac{4}{3}v + v^2 \right) \Phi(\delta) \tag{4.7}$$

$$\Phi(\delta) = \ln \left(\frac{\frac{B m_\mu}{m_e} Z^{-1/3}}{1 + \frac{B\sqrt{e}}{m_e}\delta Z^{-1/3}} \right) - \Delta\sigma_n^{el}(\delta) \tag{4.8}$$

where v is the fraction of energy transferred to the outgoing photon, δ is the minimal momentum transfer $(\delta \simeq \frac{m_\mu^2 v}{2E(1-v)})$ and B is a constant $(B = 189)$.

The contribution of the inelastic processes is lower, although not negligible, especially at high values of v. The nuclear inelastic correction is roughly one order of magnitude larger than the atomic contribution.

4.1.4 Photo-nuclear interactions

The photo-nuclear interaction consists in the interaction of a muon with an atomic nucleus *via* the exchange of a virtual photon (see figure 4.5). The calculation of the cross section for the inelastic scattering of a lepton on a nucleus requires to integrate over Q^2 the γ-nucleus cross section, multiplied by some kinematic factors. This can be approximated by:

Figure 4.3: Feynman diagrams of the *bremsstrahlung* process on nucleus.
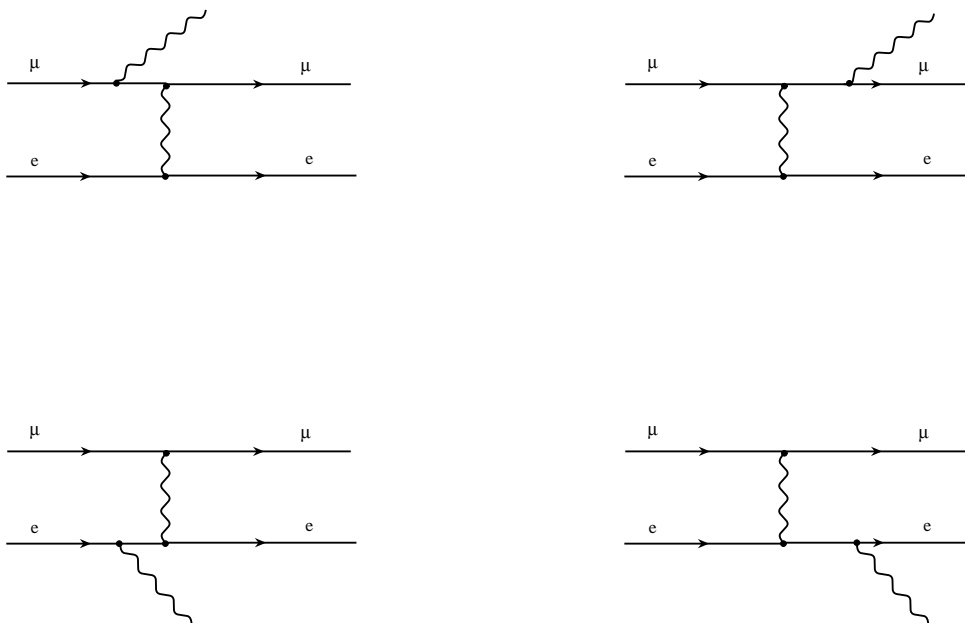
Figure 4.4: Feynman diagrams of the *bremsstrahlung* process on atomic electrons.

$$\frac{d\sigma}{dv} = \frac{\alpha}{2\pi} A\sigma_{\gamma N} v \left\{ 0.75 G(x) \left[\kappa \ln\left(1 + \frac{m_1^2}{t} \right) - \frac{\kappa m_1^2}{m_1^2 + t} - \frac{2m_\mu^2}{t} \right] + \right.$$

$$+ 0.25 \left[\kappa \ln\left(1 + \frac{m_2^2}{t} \right) - \frac{2m_\mu^2}{t} \right] +$$

$$\left. + \frac{m_\mu^2}{2t} \left[0.75 G(x) \frac{m_1^2}{m_1^2 + t} + 0.25 \frac{m_2^2}{t} \ln\left(1 + \frac{t}{m_2^2} \right) \right] \right\} \quad (4.9)$$

with $G(x) = \frac{3}{x^3}(x^2/2 - 1 + e^{-x}(1+x))$ (where $x \simeq 0.00282 A^{1/3}\sigma_{\gamma N}$), $\kappa = 1 - 2/v + 2/v^2$, $m_1^2 = 0.54$ GeV^2 and $m_2^2 = 1.8$ GeV^2.
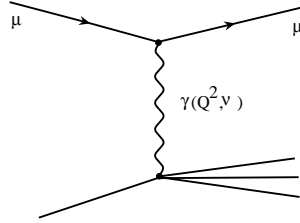
Figure 4.5: Feynman diagrams of the photo-nuclear interactions.

4.2   Muon range and energy loss distributions

The energy losses explained in the previous section limit the propagation distance of the muons. Figure 4.6 shows the muon survival probabilities P_{surv} versus the propagation distance for several energies. Three different codes are compared: MUM, MUSIC and PROPMU (see chapter 3). It can be seen that there are no significant differences between MUM and MUSIC, but for PROPMU the survival probability is higher up to 30 TeV and lower above this energy. This survival probability allows us to define the effective muon range R_{eff} above a given energy threshold E_μ^{min}, which is an average range taking into account stochastic losses [128]:

$$R_{eff}(E_\mu; E_\mu^{min}) = \int_0^\infty P_{surv}(E_\mu; E_\mu^{min}, X) dX \quad (4.10)$$

It is also interesting to plot the distribution of the energy loss, since its large fluctuations limit intrinsically the energy resolution of the detector. In order to study these distributions, several samples (for energies ranging from 100 GeV to 10 PeV)
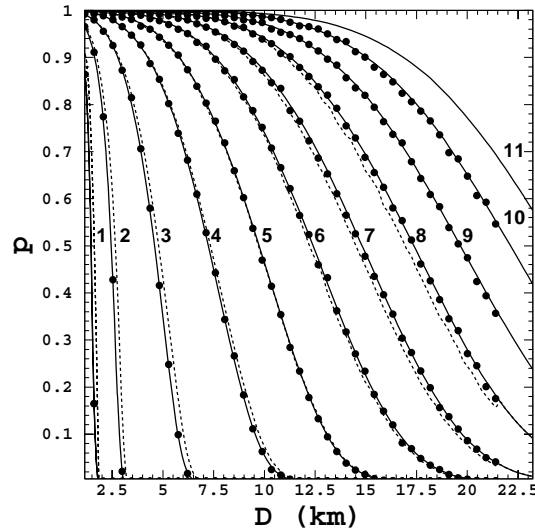
Figure 4.6: Dependence of the survival probabilities on the propagation distance in water propagated with MUM (solid lines), PROPMU (dashed lines) and MUSIC (circles) for different energies (from left to right: 500 GeV, 1 TeV, 3 TeV, 10 TeV, 30 TeV, 100 TeV, 300 TeV, 1 PeV, 3 PeV, 10 PeV, 30 PeV. From [129].)

containing 10^7 muons passing through a thin layer of sea water or rock have been generated. Figures 4.7 and 4.8 shows the energy loss distributions in sea water and rock, respectively [130]. It can be seen that radiative processes produce a long tail in the energy loss distributions which makes difficult the muon energy reconstruction.

4.3 Muon energy reconstruction

The reconstruction of the muon energy is based on a method proposed by F. Hubaut [131] (see also [132]). The signal amplitude in the photomulitiplier is proportional to the number of hits, i.e., it is proportional to the muon energy loss. Therefore, we can compare the signal actually seen in the detector with the signal produced by a minimum ionizing muon (MIM):

$$\sum A_{hit} \propto -\left\langle \frac{dE}{dx} \right\rangle = \alpha + \beta E_\mu \qquad (4.11)$$

$$\sum A_{MIM} \propto -\left\langle \frac{dE}{dx} \right\rangle_{MIM} = \alpha \qquad (4.12)$$

where A_{hit} is the signal amplitude in each PMT and A_{MIM} is the amplitude that a minimum ionizing muon along the same track would have produced in such PMT.
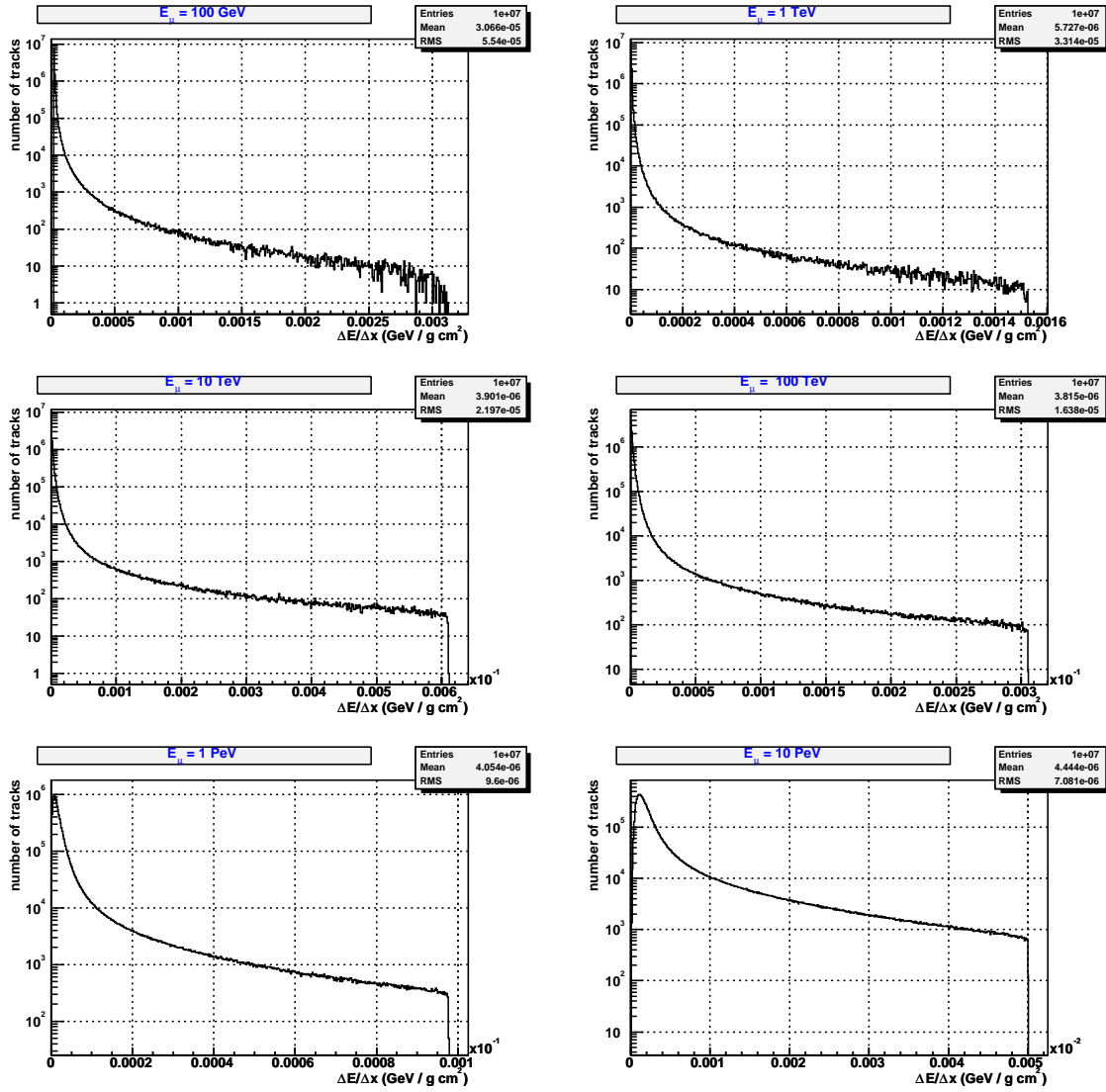
Figure 4.7: Distribution of muon energy loss for samples of 10^7 muons propagated with MUM in sea water.
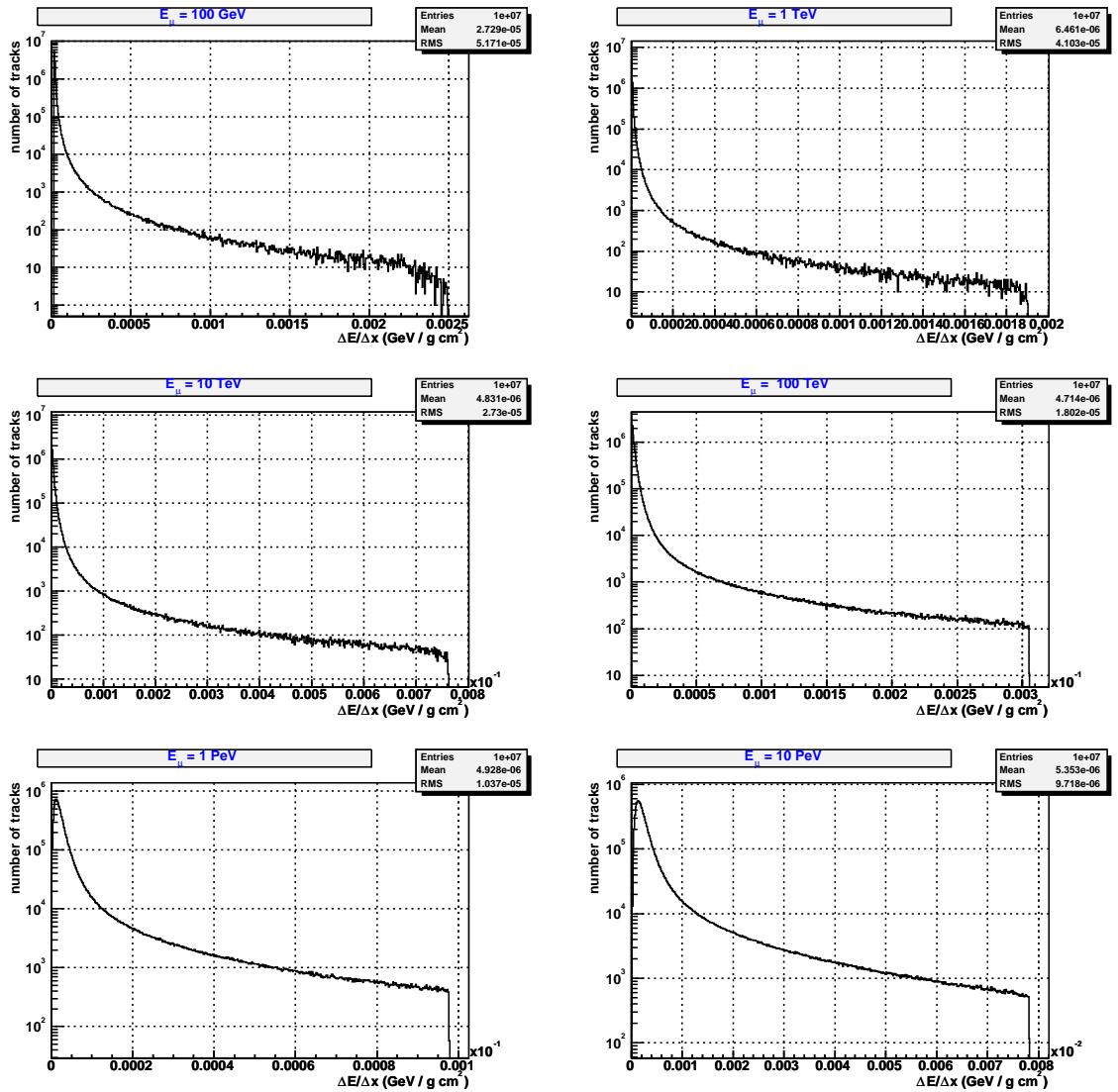
Figure 4.8: Distribution of muon energy loss for samples of 10^7 muons propagated with MUM in standard rock.

Therefore, the ratio between both is

$$\frac{\sum A_{hit}}{\sum A_{MIM}} \propto 1 + \frac{E_\mu}{\epsilon_c} \tag{4.13}$$

so the muon energy is proportional to

$$E_\mu \propto \left(\frac{\Sigma_i A_{hit}}{\Sigma_i A_{MIM}} - 1 \right) \tag{4.14}$$

The final estimator x is defined as

$$x = N_{hits} \left(\frac{\Sigma_i A_{hit}}{\Sigma_i A_{MIM}} - 1 \right) \tag{4.15}$$

where N_{hits} is the number of hits produced by the track. The factor N_{hits} has been proved empirically useful to enhance the energy dependence. Only hits in a $|\Delta t| < 4$ ns time window, i.e, the Cherenkov photons produced by the muon and its secondaries, are included.

The advantage of this algorithm is that, by comparing the effect produced by the muon with the effect produced by a minimum ionization muon, the influence on the distance and the PMT orientation is minimized.

It is also useful to define two versions of such estimator, to separate high energy and low energy events, since it reduces the estimator fluctuations:

- low energy estimator, x_{low}: i runs for all the hits having $0.1 < \frac{A_{hit}}{A_{MIM}} < 100$

- high energy estimator, x_{high}: i runs for all the hits having $10 < \frac{A_{hit}}{A_{MIM}} < 1000$

Figures 4.9 and 4.10 show the relationship between the muon energy and the estimators (x_{low} or x_{high}) [2]. This relationship can be parameterized and different functions have been tried, as discussed below. Table 4.1 shows the values of the parameters of the fit to a straight line:

$$\log_{10} E_\mu = p_0 + p_1 \log_{10} x \tag{4.16}$$

For energies greater that 1 TeV, the value of the low energy estimator grows with the muon energy, as desired. However, the reconstruction at low energies (<1 TeV) is complicated mainly for two reasons. First, below the critical energy, the energy loss is dominated by ionization, weakly dependent on the muon energy. Furthermore, there is also the effect of the hadronic shower, which increases the light seen in the detector (i.e. the value of x_{low}) for many events. This light has not been produced by the muon, so does not fit the light output predicted by equation 4.1. At very high energies, there is a saturation effect, caused by the definition of the low energy estimator (which

---

[2]All the results presented in this chapter have been obtained with the neutrino sample II and using the quality cuts defined in chapter 5.
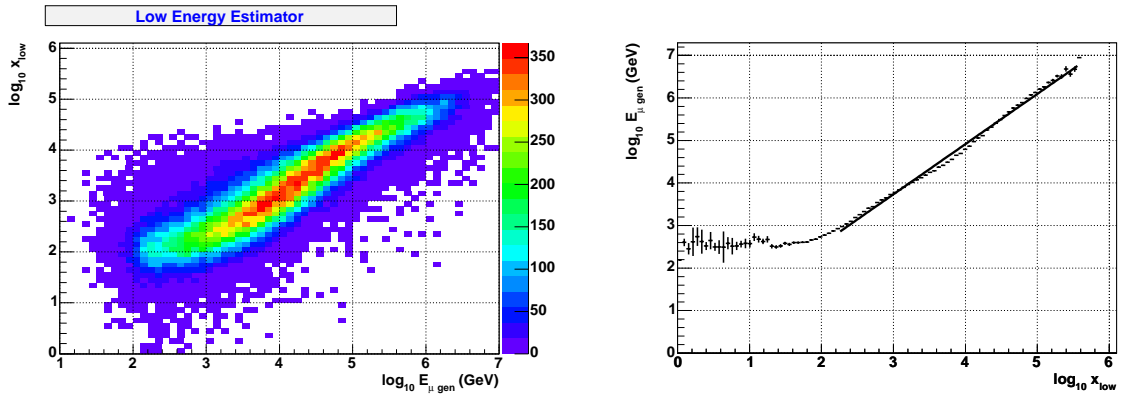
Figure 4.9: Left: Low energy estimator distribution on the muon energy. Right: Parametrisation of the dependence of the muon energy on x_{low}.

includes only hits for which $0.1 < \frac{A_{hit}}{A_{MIM}} < 100$). Based on these facts, a parabolic parameterization was tried, in order to avoid the overestimation (at low energies) and the underestimation (at high energies). However, this was not finally used since events with a x_{low} value below (above) the minimum (maximum) of the parabola cannot be reconstructed, what introduces an important bias in the energy estimation.
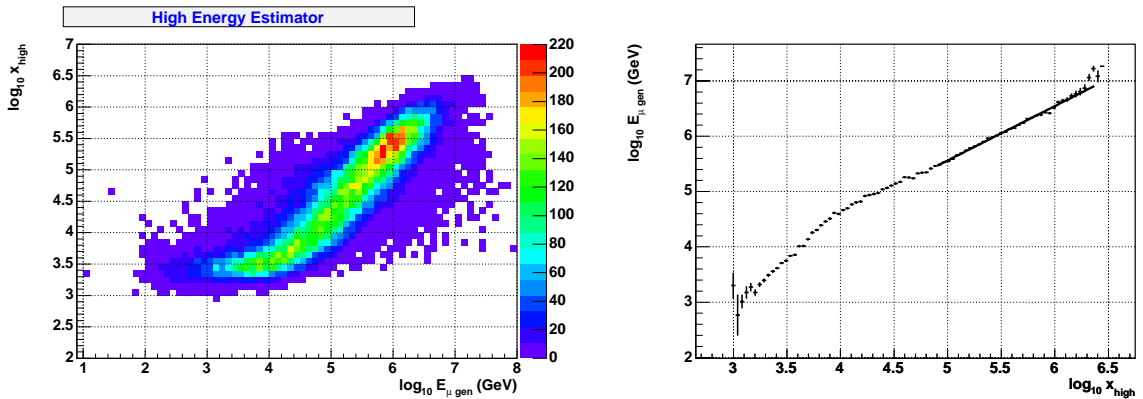
Figure 4.10: Left: High energy estimator distribution on the muon energy. Right: Parameterization of the dependence of the muon energy on x_{high}.

The high energy estimator extends the range of applicability of the method to higher energies. In this case, the saturation effect at high energies is not appreciated. On the other hand, this high energy estimator is not useful for intermediate and low energy events, because the response is not linear. The kind of analysis and the energy range will determine which estimator is more appropriate.

	Low energy	High energy
p_0	0.20	0.65
p_1	1.19	0.98

Table 4.1: Low and high energy parameters from the linear fit of the estimators on muon energy.

The relationship between the generated and the reconstructed energy using the low energy estimator parameterization is shown in figure 4.11.
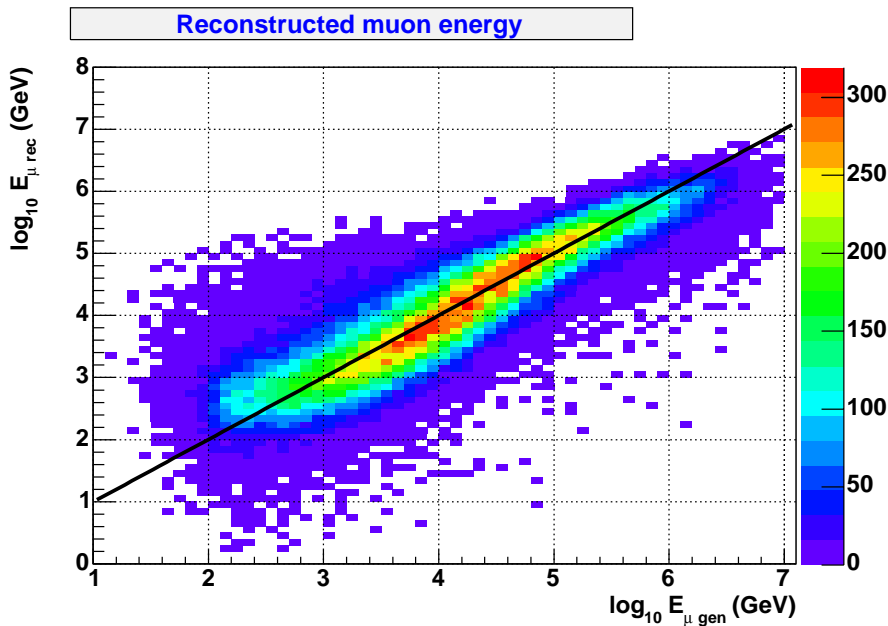
Figure 4.11: Comparison between the reconstructed and generated muon energy. The line $E_\mu^{rec} = E_\mu^{gen}$ is also drawn for reference. The low energy estimator has been used.

Although the dispersion in the results is large, due to the stochastic nature of the energy loss processes, the general behavior of the distribution seems to follow, as desired, the $E_\mu^{rec} = E_\mu^{gen}$ line.

The accuracy of the reconstruction can be better seen in figure 4.12, where the mean and the standard deviation of a Gaussian fit to the distribution of $\log_{10} E_{rec}^\mu / E_{gen}^\mu$ as a function of the true muon energy are shown. Of course, the closer to zero the mean and the narrower the standard deviation, the better.

Several comments can be made from the previous plot. Firstly, the value of the mean from 500 GeV up to almost 1 PeV is quite stable around zero (± 0.2). At higher energies, there is a deviation which tends to underestimate the energy. For this reason, future analysis devoted to energy reconstruction of very high energy events should be
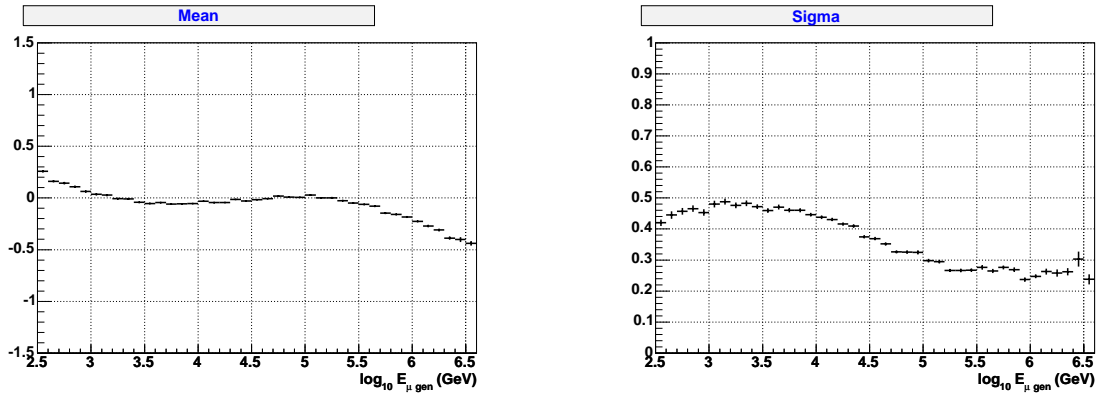
Figure 4.12: Mean (left) and standard deviation (right) of a Gaussian fit of the $\log_{10} E_\mu^{rec}/E_\mu^{gen}$ distribution as a function of the muon energy, using the low energy estimator.

based on the high energy estimator. This allows to improve the value of the mean beyond 1 PeV, as shown in figure 4.13.
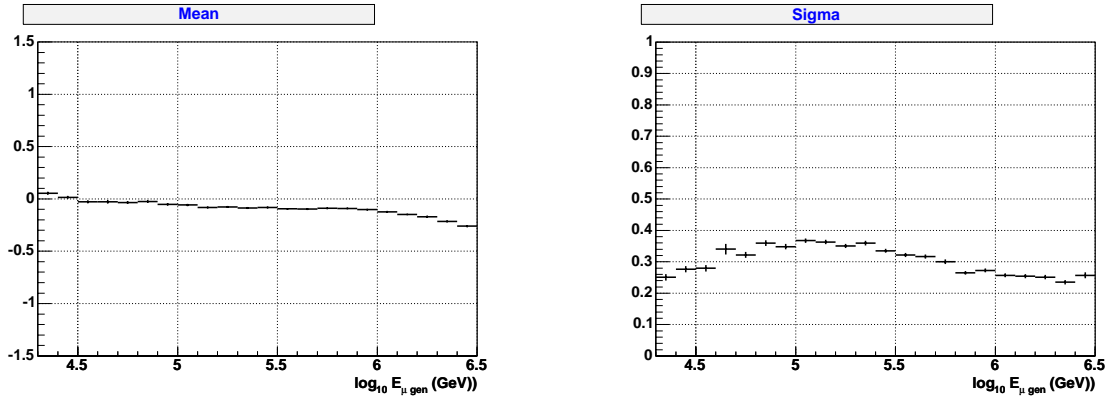
Figure 4.13: Mean (left) and standard deviation (right) of a Gaussian fit of the $\log_{10} E_\mu^{rec}/E_\mu^{gen}$ distribution as a function of the muon energy, using the high energy estimator.

Regarding the width of the $\log_{10} E_\mu^{rec}/E_\mu^{gen}$ distributions, there are also two different regions. For energies below $10^{4.5}$ GeV the resolution lies in the range 0.4 to 0.5, which means a factor 2.5-3 of accuracy in the reconstructed energy. Above $10^{4.5}$ GeV the sigma of the $\log_{10} E_\mu^{rec}/E_\mu^{gen}$ distribution is around 0.25, i.e. a factor two.

For the resolution using the high energy estimator, a similar tendency is seen. Below $10^{5.5}$ GeV, the standard deviation is ~ 0.35 and decrease to ~ 0.25 for higher energies.

Figure 4.14 shows the $\log_{10} E_\mu^{rec}/E_\mu^{gen}$ distributions for different muon energies. It

is verified that the shape of these distributions is approximately Gaussian, with only small asymmetries at very low or very high energies.
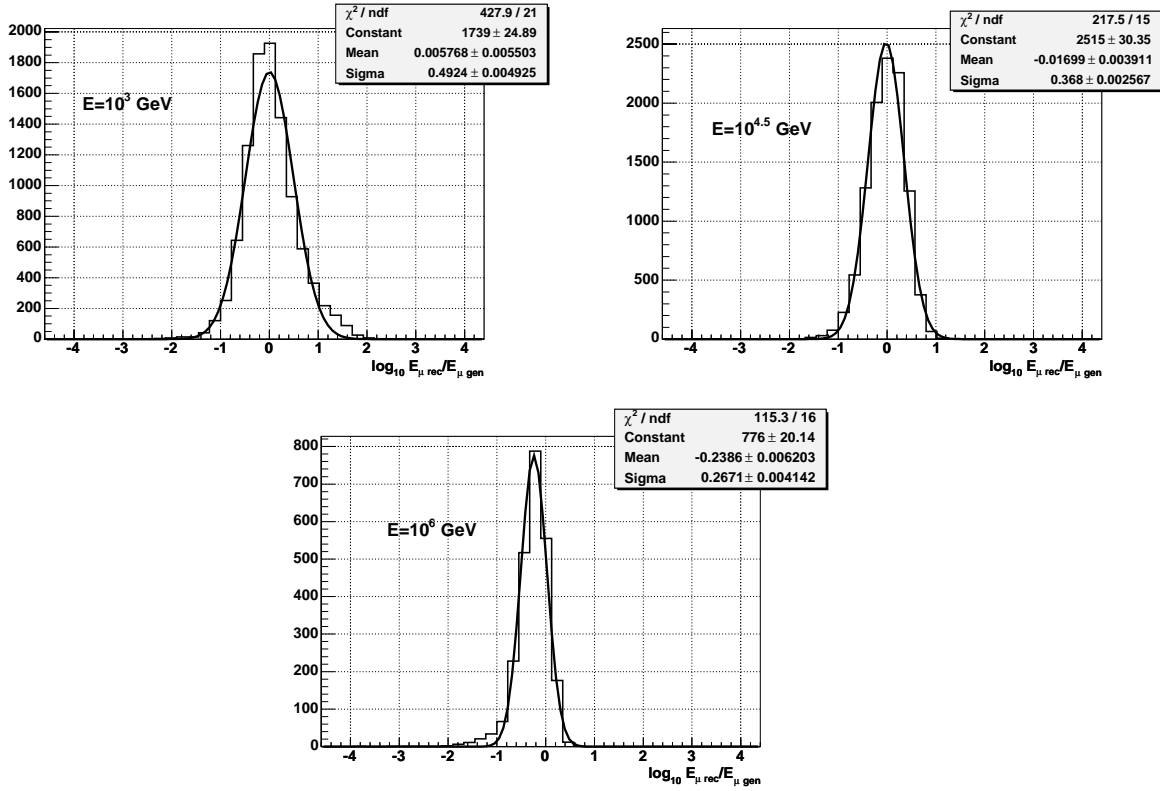
Figure 4.14: Distributions of $\log_{10} E_\mu^{rec}/E_\mu^{gen}$ at several muon energies.

It is also interesting to plot the mean and the sigma of $\log_{10} \ E_{rec}^\mu/E_{gen}^\mu$ with respect to the reconstructed energy (see figure 4.15). These plots will be used to estimate how much we can rely on the results of the energy of any reconstructed event (since in real life we will not have the true energy).

4.4   Dependence on geometrical factors

In this section we present a study of the dependence of the muon energy reconstruction on the distance to the centre of the detector, the zenith and azimuth angles and the angular resolution. In all the cases, the reconstructed energy is estimated from the low energy estimator.
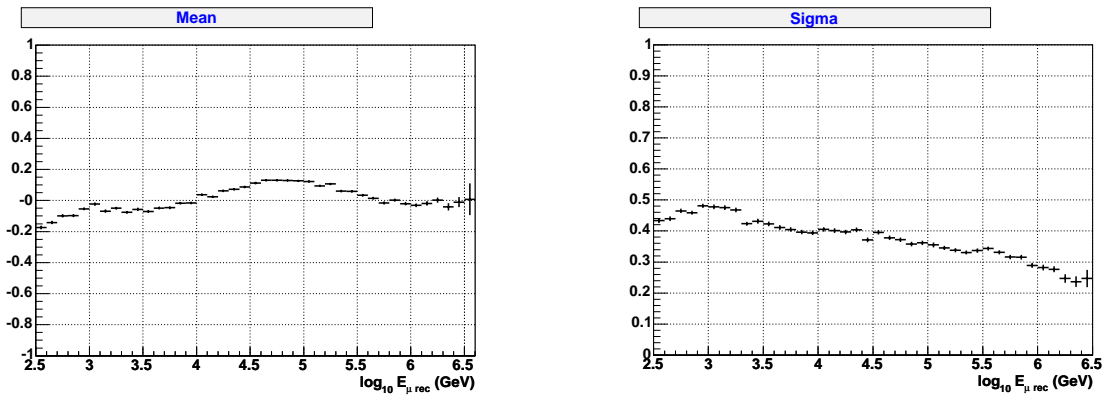
Figure 4.15: Mean (left) and standard deviation (right) of a Gaussian fit of the $\log_{10} E_\mu^{rec}/E_\mu^{gen}$ distribution as a function of the reconstructed muon energy.

4.4.1   Distance to the detector

Figures 4.16 and 4.17 show the dependence of the mean and the standard deviation of the $\log_{10} E_\mu^{rec}/E_\mu^{gen}$ distribution on the distance to the centre of the detector. A plot with two different energy regimes (low and high energies) is also shown to search for correlations with energy. In the case of the mean, it can be seen that there is a stronger effect on the mean value at high energies. With regard to the standard deviation, its decrease with distance could be due to the fact that only those tracks which loss sufficient energy pass the selection cuts.
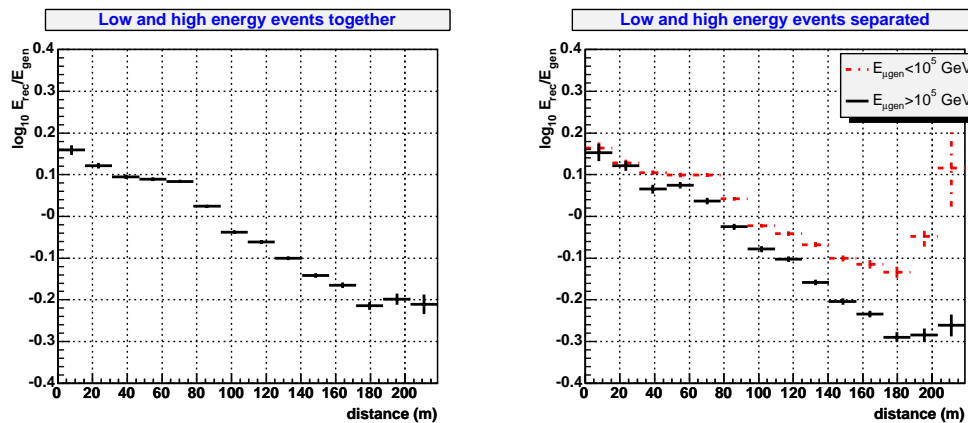
Figure 4.16: Dependence of the mean of the $\log_{10} E_\mu^{rec}/E_\mu^{gen}$ distribution on the distance from the track to the detector.
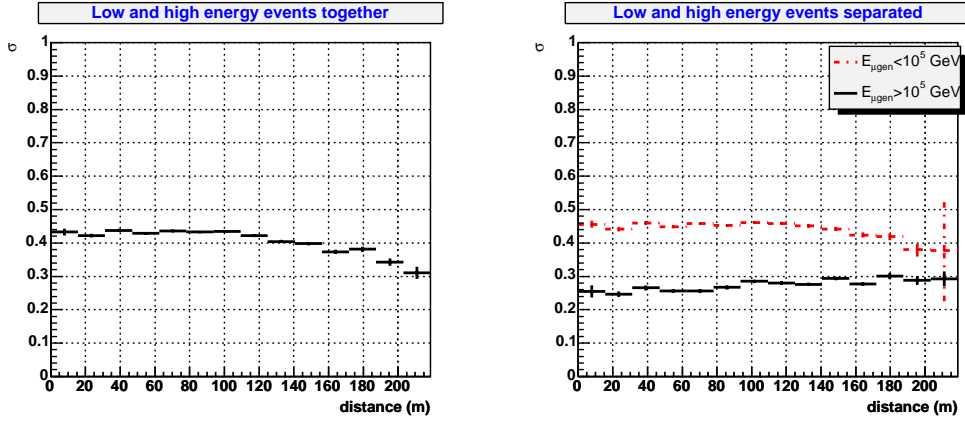
**Figure 4.17:** Dependence of the standard deviation of the $\log_{10} E_\mu^{rec}/E_\mu^{gen}$ distribution on the distance from the track to the detector.

4.4.2   Zenith angle

The dependence of the mean and the standard deviation of the $\log_{10} E_\mu^{rec}/E_\mu^{gen}$ distribution on the zenith angle is shown in figures 4.18 and 4.19. There is a small underestimation for horizontal muons while below 45° the energy is overestimated. This behavior is more pronounced in the low energy regime. The standard deviation is greater for low energies, as expected.
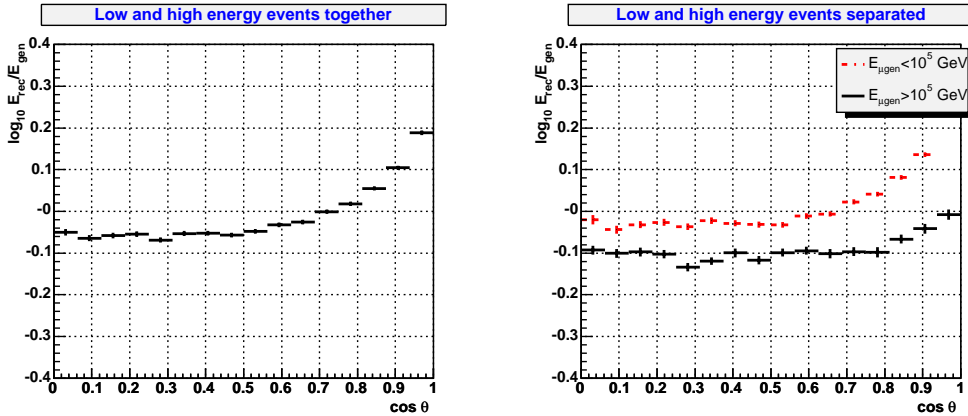
Figure 4.18: Dependence of the mean of the $\log_{10} E_\mu^{rec}/E_\mu^{gen}$ distribution on the track zenith angle.
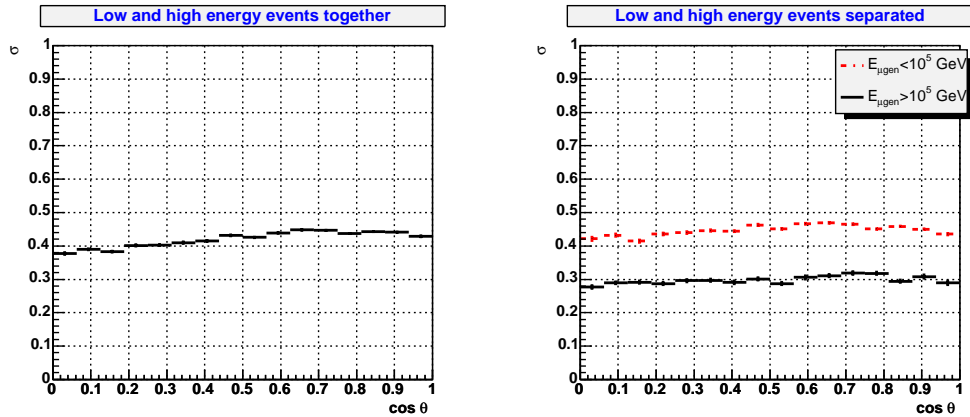
Figure 4.19: Dependence of the standard deviation of the $\log_{10} E_\mu^{rec}/E_\mu^{gen}$ distribution on the track zenith angle.

4.4.3   Azimuth angle

The dependence of $\log_{10} E_\mu^{rec}/E_\mu^{gen}$ on the azimuth angle is small. However, there is a tiny $45°$ modulation for the mean value due to the detector layout in the horizontal plane (there are eight peaks in that distribution because of the octagonal symmetry of the detector). This is more evident in the low energy regime. Figures 4.20 and 4.21 show these results.
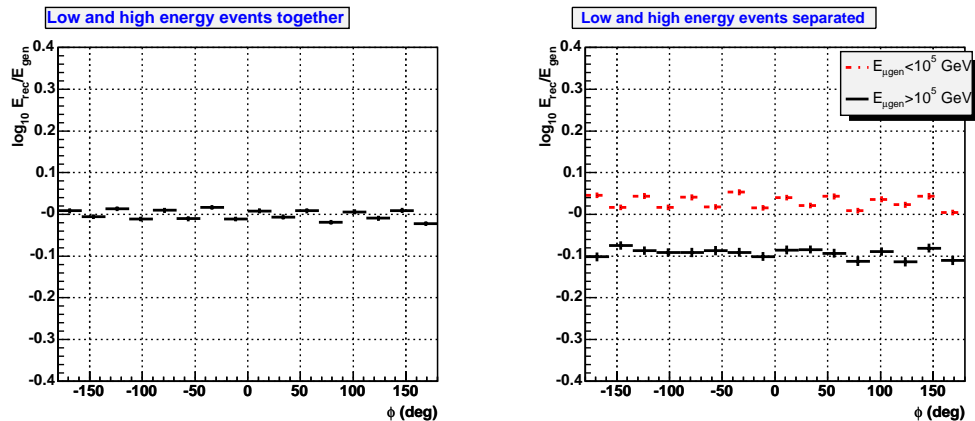
Figure 4.20: Dependence of the mean of the $\log_{10} E_\mu^{rec}/E_\mu^{gen}$ distribution on the track azimuth angle.
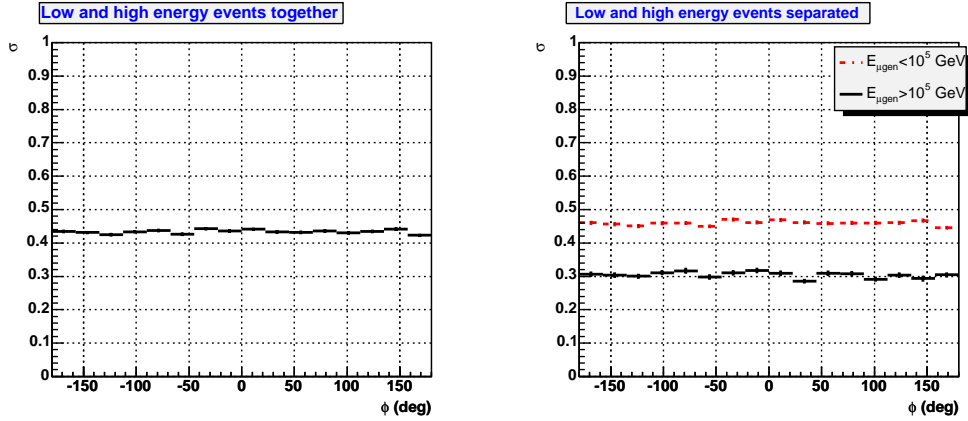
Figure 4.21: Dependence of the standard deviation of the $\log_{10} E_\mu^{rec}/E_\mu^{gen}$ distribution on the track azimuth angle.

4.4.4   Angular resolution

Finally we also consider the effect of misreconstruction of the muon track in the energy resolution. As explained, one of the ingredients involved in the energy reconstruction algorithm is the amplitude which the PMT would measure if the muon was a MIM. Since these amplitudes are computed using the reconstructed track, the reconstruction algorithm will be very sensitive to the angular resolution. Figures 4.22 and 4.23 show this effect. As expected, the largest deviations from zero occur when the track is not well reconstructed. Fortunately, bad reconstructed events are only a small fraction (see figure 4.24), since the track reconstruction performance is good. The best values of the mean and the standard deviation are obtained for accurately reconstructed tracks.
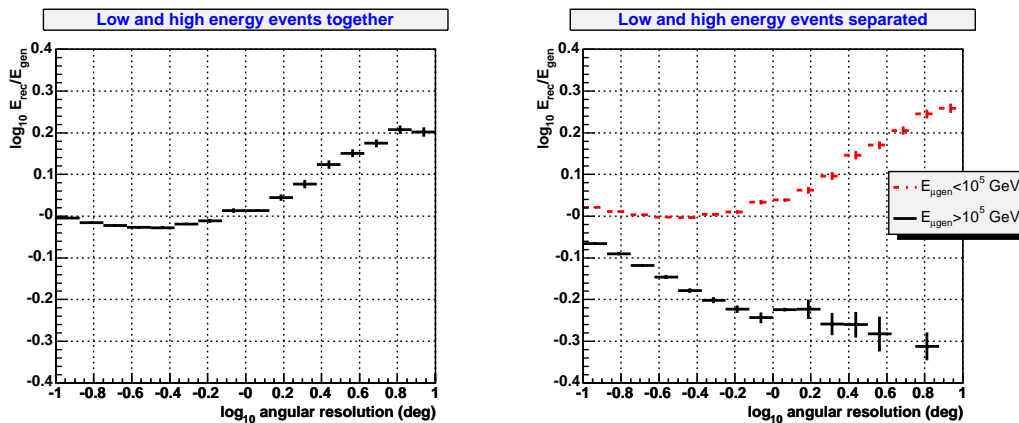
Figure 4.22: Dependence of the mean of the $\log_{10} E_\mu^{rec}/E_\mu^{gen}$ distribution on the angular resolution.
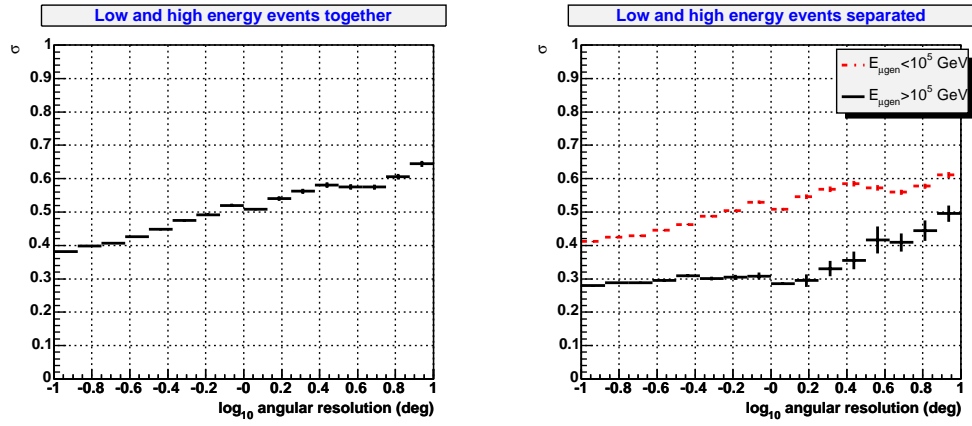
Figure 4.23: Dependence of the standard deviation of the $\log_{10} E_\mu^{rec}/E_\mu^{gen}$ distribution on the angular resolution.
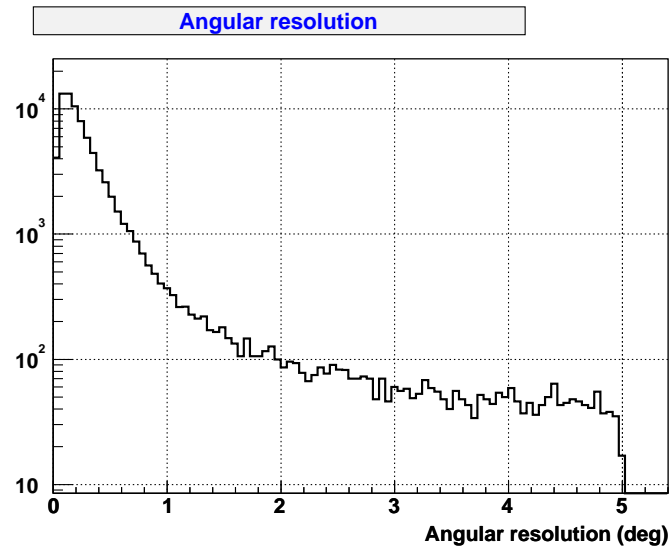
Figure 4.24: Distribution of the angular resolution for the selected events.

4.5   Neutrino energy reconstruction

The neutrino energy can be also reconstructed using a similar approach. However, two remarks have to be made. First, at high energies only the muon energy is seen in the detector. Second, we can only estimate the energy of the muon when it enters the can volume (if the interaction vertex is in the can, we consider the initial muon energy), since the light produced before will not reach the detector. Although these considerations make energy reconstruction more difficult, the neutrino energy can be estimated from the light output in the detector by Monte Carlo studies. In figure 4.25, the relationship between the neutrino energy and the energy of the muon when it enters the can is shown. The ratio between the muon energy when entering the can and the neutrino energy versus the neutrino energy is shown in figure 4.26. At high energies, most of the detected muons are produced far from the detector, so they have lost an important fraction of their energy when they arrive at the detector.
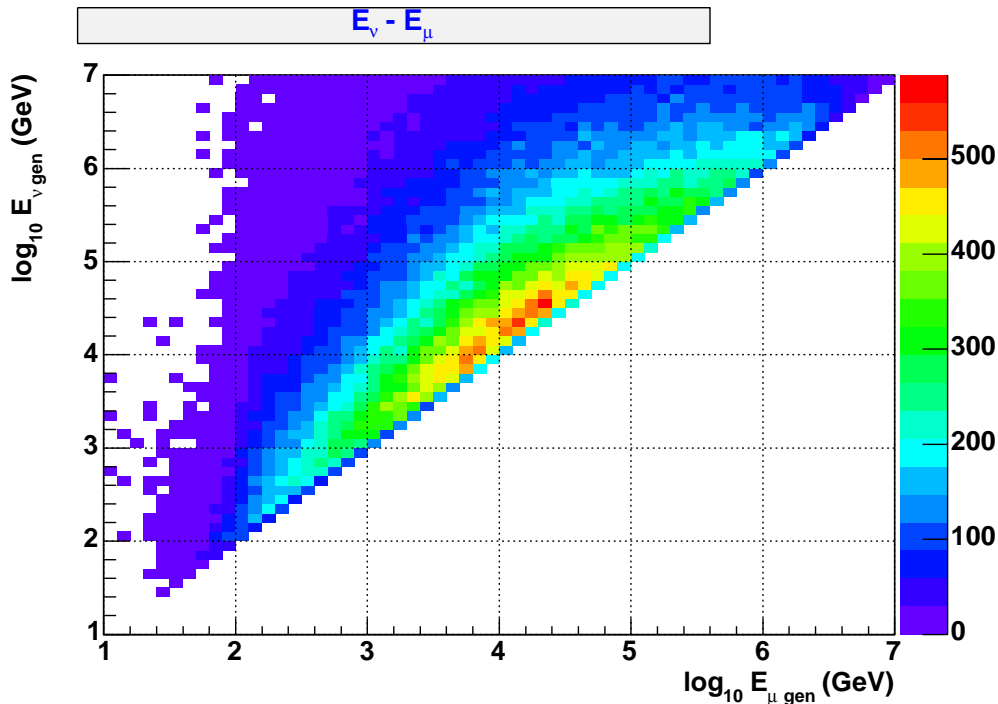
Figure 4.25: Relationship between the neutrino energy and the muon energy when it enters in the can.

In figure 4.27, E_ν distributions for different values of the muon energy are shown. The shape of these distributions suggests a fit to a Landau distribution, taking the peak position as the most likely value for the neutrino energy. When this is done for every $\log_{10} E_\mu$ slice in the E_ν-E_μ distribution, we can parameterize this relationship (see figure 4.28).
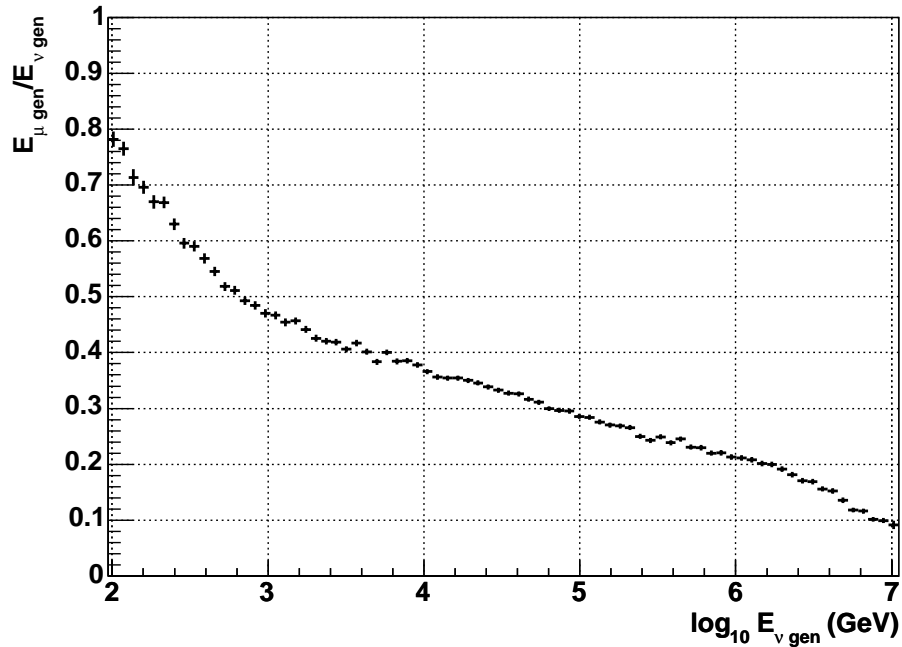
Figure 4.26: Average ratio between the energy of the muon when it enters the can and the neutrino energy. The mean fraction of the muon at the can decreases because the mean distance from the production vertex to the detector increases, so the muons loss part of their energy before entering the can.
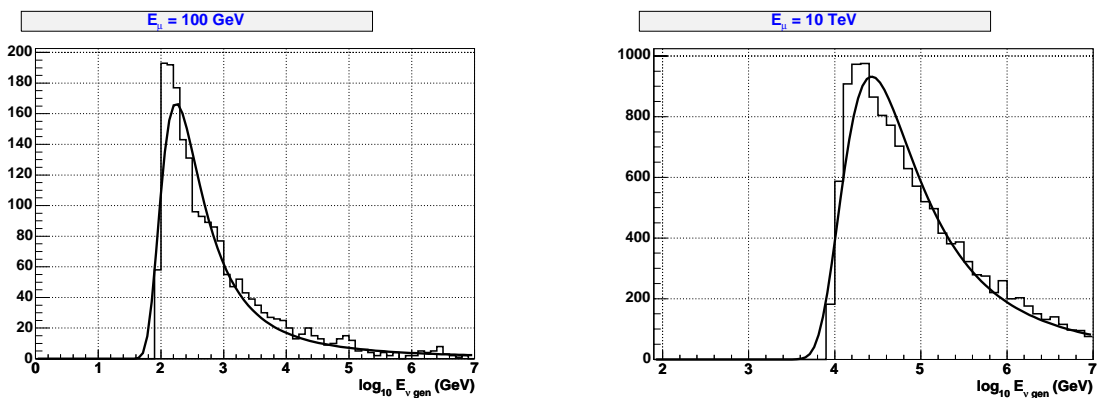
Figure 4.27: Distribution of $\log_{10} E_\nu^{gen}$ for two different muon energies.
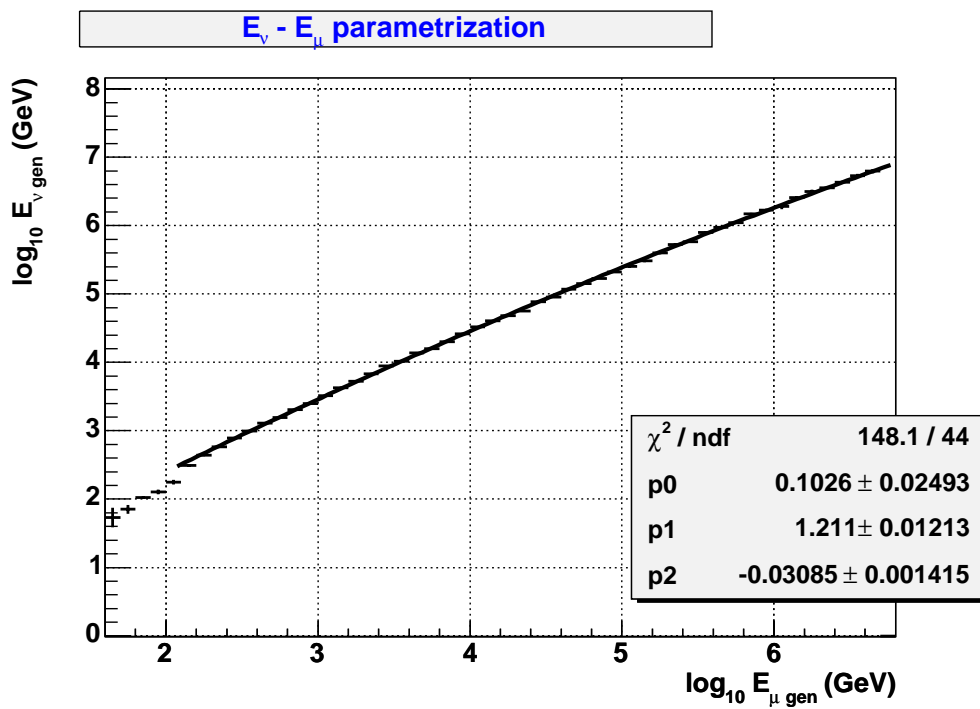
Figure 4.28: Parameterization of the relationship between the neutrino energy and the muon energy at the can.

From the curve shown in figure 4.28 we obtain the following parameterization:

$$\log_{10} E_\nu = 0.10 + 1.21 \cdot \log_{10} E_\mu - 0.0309 \cdot (\log_{10} E_\mu)^2 \tag{4.17}$$

Note that this parameterization will depend on the original neutrino spectrum, so a study of the influence of this effect has to be made. Figure 4.29 shows the parameterization curves for several spectral indexes. The systematic effect expected from this curves would be a shift of the order of $\sim 0.1 - 0.2$ in the logarithm of the reconstructed neutrino energy.
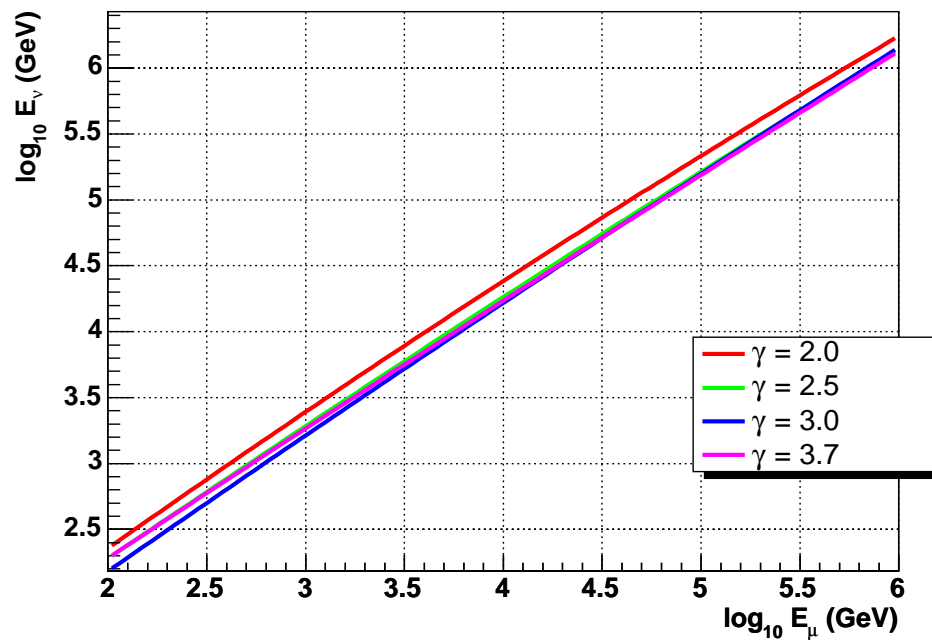
Figure 4.29: Comparison of the parameterization curves obtained for different spectral indexes.

Chapter 5

Sensitivity estimation

The sensitivity is a parameter related to the capability of the detector to constrain theoretical models. This parameter depends on the expected signal and background rates. Firstly, a set of quality cuts has to be established in order to remove the overwhelming flux of down-going events produced by cosmic rays in the atmosphere above the detector. In principle, this background should be rejected when the condition of being "up-going event" is imposed, but a fraction of these down-going atmospheric muons can be mis-reconstructed as up-going events. The tuning of the variables used to reject these fake events is explained in sections 5.1 and 5.2.

Once the atmospheric muon background has been removed, a last cut has to be applied to separate extraterrestrial diffuse neutrino fluxes from atmospheric neutrinos. This background is much more complicated to discriminate than the previous one, since they are up-going events and not mis-reconstructed tracks as in the case of atmospheric muons. For point-like source searches, the clustering of events is used to point out the presence of a signal. On the other hand, the detection of diffuse fluxes takes the advantage of integrating the flux over the whole sky, which increases the signal, but this also makes more difficult to reject the background. The only way to do such discrimination is to use a cut based on the energy spectrum of the detected muons. Theoretical models of astrophysical sources predict a harder spectrum, typically with $\sim E^{-2}$, than for atmospheric neutrinos, $\sim E^{-3.7}$. For this reason, an energy dependent variable is needed to do the discrimination. Since the neutrino rates predicted at high energies are very low, it is important to ensure the optimization of the variable and of its threshold. The analysis to perform such optimization in presented in section 5.3. In section 5.4, the results for several signal models are presented. Moreover, systematic effects are discussed in section 5.5. The main conclusions are summarized and compared with the former calculations [133] for the ANTARES detector in section 5.6.

Finally, the capability of the Pearson's and Kolmogorov-Smirnov tests to distinguish among the predictions of different models is studied in section 5.7.

5.1 Rejection of the atmospheric muon background

As previously said, the majority of the atmospheric down-going muons are rejected requiring the tracks to be up-going. The Earth filters out up-going muons produced by cosmic rays at the opposite hemisphere, so the remaining muon background is caused by the small fraction of down-going muons reconstructed as up-going events. Nevertheless, the flux of atmospheric down-going muons is so large ($\sim 10^6$ times the atmospheric neutrino flux at 2500 m deep) that even a small fraction of fake events must be considered as a dangerous source of background.

In this analysis we have used the Carmona strategy [118] for track reconstruction since, it has been specially optimized to reconstruct up-going events and, therefore its performance to reconstruct down-going events is very low. The quality cuts were chosen to reduce the muon atmospheric background as much as possible. Figure 5.1 shows the results of Carmona and Aart strategies when applied to the Bologna atmospheric muon sample (see section 3.2.2). As indicated in table 5.1, the Aart strategy is able to reconstruct many more down-going events than Carmona strategy. Moreover, only 11 events, equivalent to a rate of 1170 events/year, survive the Carmona quality cuts compared with the 24 events (2800 events/year) that pass Aart quality cuts.

	Carmona strategy		Aart strategy	
	MC Events	Rate (yr^{-1})	MC Events	Rate (yr^{-1})
Reconstructed	59849	7.8×10^6	1844105	2.9×10^8
Reconstructed as up-going	47202	6.1×10^6	213404	3.2×10^7
Quality	11	1170	24	2800

Table 5.1: Comparison of the number of reconstructed events of the atmospheric muon sample with the Carmona and the Aart strategies. "Quality" refers to the standard quality cuts of each strategy.

Figure 5.2 compares the true and reconstructed zenith angular distributions of the atmospheric muon sample. For the Carmona strategy, there are more events reconstructed as up-going than as down-going. This strategy tries to reconstruct all the events as up-going, and consequently, the quality of the fit when the true event is down-going is quite bad which makes the rejection of the muon atmospheric background easier.

The quality cuts as defined in the Carmona strategy [118] ("Carmona Quality") were adopted to reject all the mis-reconstructed atmospheric muons while keeping the greatest fraction of signal. However, they were constructed using a sample with lower statistics at high energies. When they are applied to the Bologna production, some events remain, as it can be seen in figures 5.1 and 5.2. In order to improve the muon rejection, a new set of selection criteria have been studied on the basis of the new and larger muon MC productions. These new cuts have also been applied to the MC
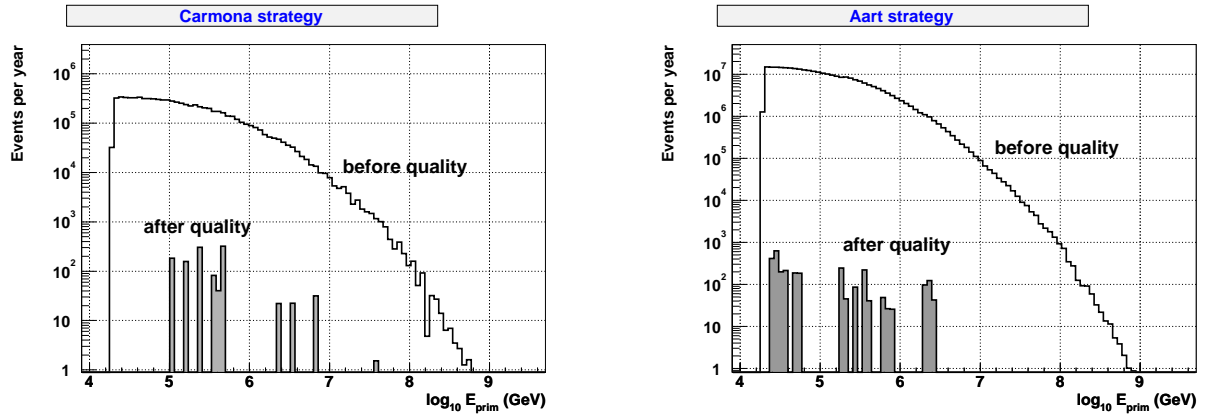
Figure 5.1: Comparison of the effect of the quality cuts in Carmona and Aart strategies. Only events reconstructed as up-going are included.
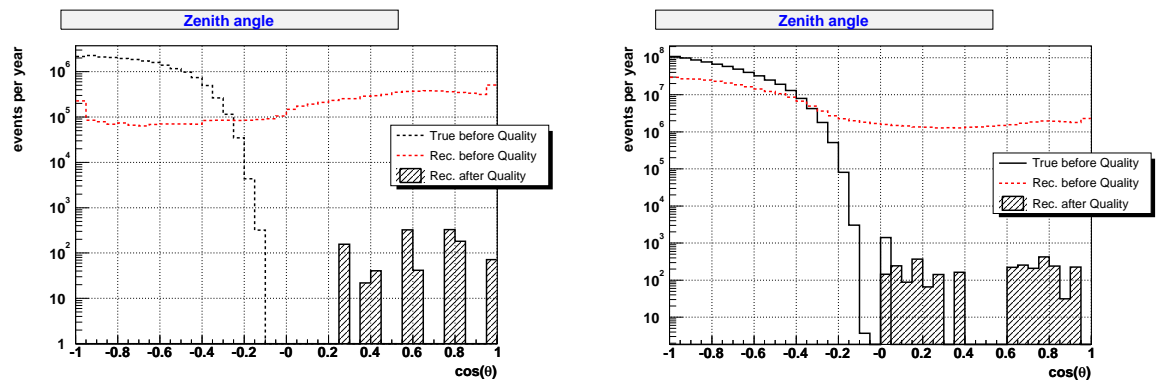

Figure 5.2: Distributions of the true and reconstructed zenith angle for Carmona (left) and Aart (right) strategies. The effect of the "Quality" cuts of each strategy can be seen.

samples of neutrino signal and atmospheric background described in chapter 3. The model used for atmospheric neutrinos is the Bartol calculation [43]. Concerning the cosmic neutrino signal, the upper bound limit calculated by Waxman and Bahcall has been used ($E^2\Phi_{WB} = 4.5 \times 10^{-8}$ GeVcm^{-2}s^{-1}sr^{-1}). In section 5.4, other models will be considered. The variables used to select the events are based on the selection criteria adopted in Carmona strategy but some of the cut values have changed and new conditions have been added to optimize muon background rejection. The final quality cuts, from now on called *Level* 2 cuts, are the following[1]:

- the angle between the fit and the prefit should be $\alpha < 25°$,

- the X parameter [2], defined to reject fake up-going events, should be $0.5 < X < 1$,

- the product of all the fit parameter errors should be: $d_1 \cdot d_2 \cdot d_3 \cdot d_4 \cdot d_5 < 10^{-3}$,

- the error in the fourth parameter, $d_4 < 1.5$ and

- the error in the fifth parameter, $d_5 < 6$.

Figure 5.3 shows the distributions of the variables used in this selection for all the reconstructed atmospheric muons as well as the effect of each cut. Also the signal neutrino model distributions are shown. Figure 5.4 shows the atmospheric muon and signal distributions when all the cuts but one are applied. The event rates for reconstructed events, up-going reconstructed events and selected by "Carmona Quality" and *Level* 2 cuts are given in table 5.2. With the *Level* 2 cuts we reject all the atmospheric muon background and reduce a 17% the atmospheric neutrino background whereas we loss only in 7% the signal. In figure 5.5 the muon energy spectra of the atmospheric muon background for the same selection cut levels are shown.

Since the quality cuts are based on the errors of the fitted parameters and not on likelihood, it is important to check that there is not relevant bias in the signal and atmospheric neutrino samples. Figure 5.6 shows the muon energy spectrum for reconstructed and selected events (at *Level* 2). As it can be seen, in the region where the neutrino signal can surpass the neutrino background (10 TeV - 1 PeV) the ratio of selected to reconstructed events is practically constant. The event distributions for the selected Carmona quality cuts are also shown.

Another way to see the effect of the *Level* 2 cuts is to compare the ratio between the number of events passing this selection with respect to the Carmona quality cuts. This is shown in figure 5.7. It is seen that the efficiency is near 90% in all the energy range. The effective area using this cut is also plotted.

---

[1]A small fraction of events show an abnormally low error in the first parameter of the fit. These events have been filtered for caution.

[2]The X parameter compares the number of selected hits for the fitted direction (θ, ϕ) and for a direction with the same ϕ but $\theta = 120°$. It has been proved to be very efficient for down-going muon rejection in the Carmona strategy [118].
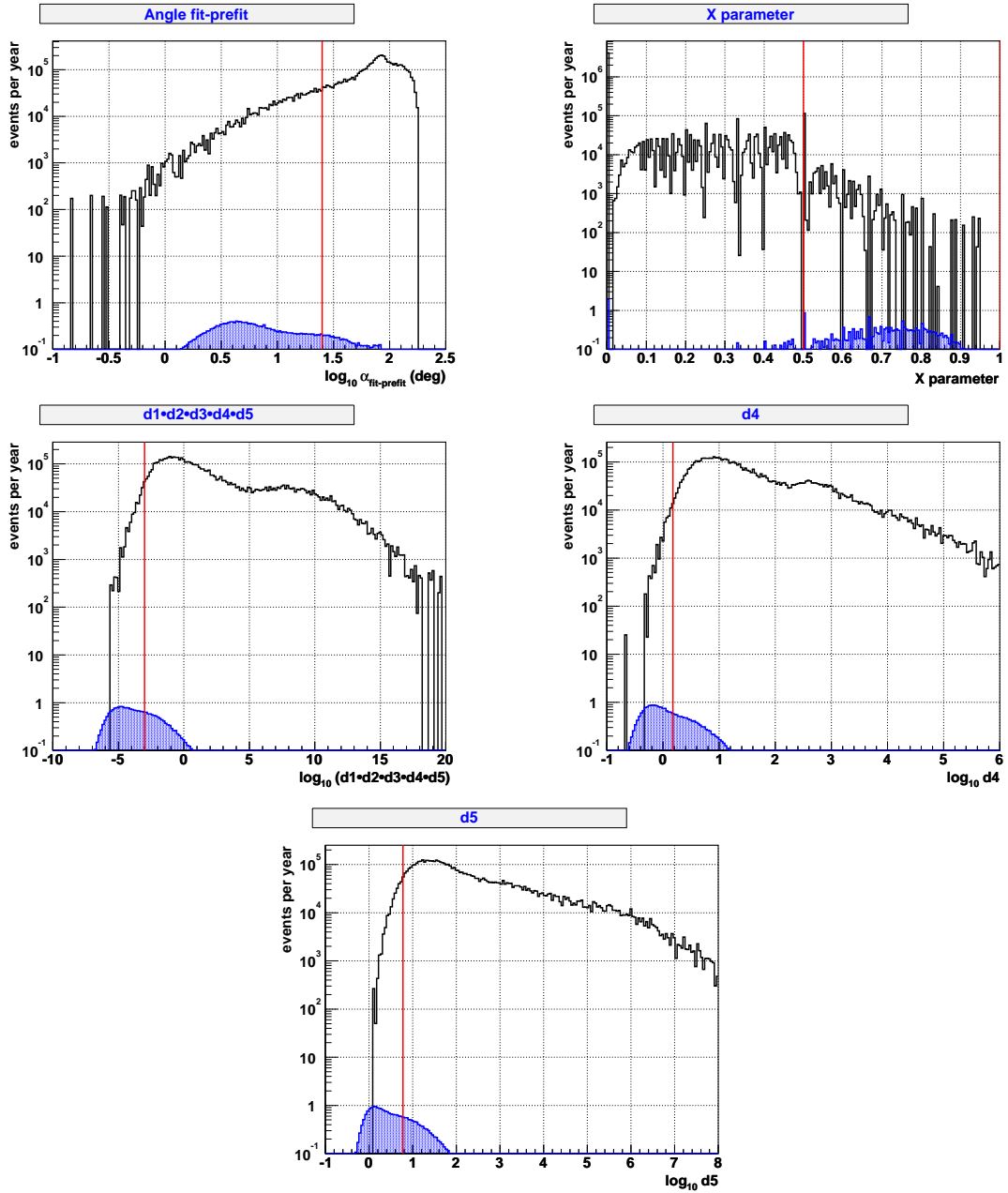
Figure 5.3: Cuts used to reject the atmospheric muon background. In reading-order, the plots correspond to the angle between the fit and the prefit α, the variable X, the product of the fit errors and the errors in the fourth and fifth parameters of the fit. The vertical lines correspond to the position of the cut (*Level* 2). The blank (solid) histogram is the atmospheric background (signal) rate per year.
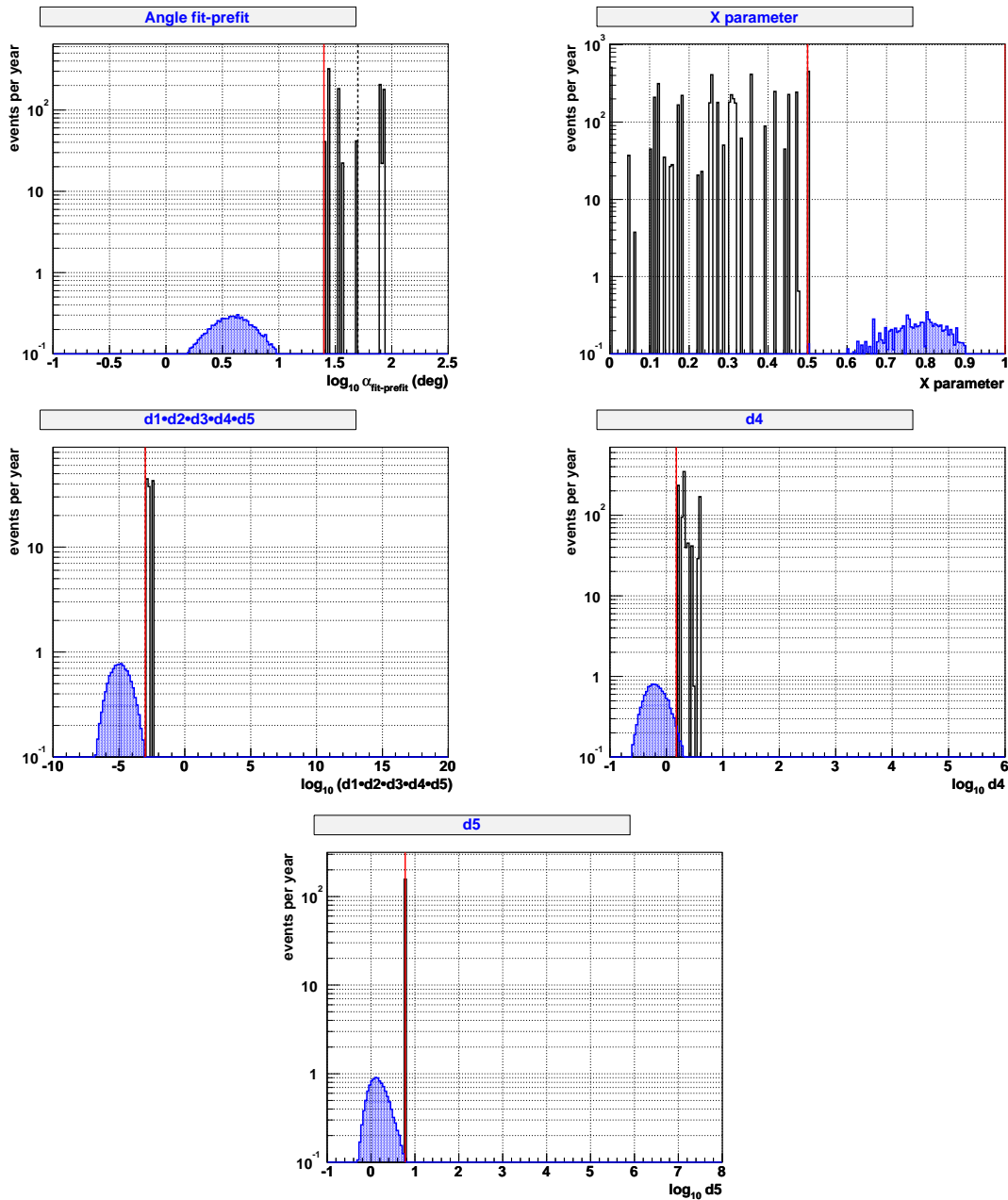
Figure 5.4: Distributions of background (blank) and signal (solid) when all the cuts of *Level* 2 are applied, except the one plotted. In reading-order, the plots correspond to the angle between the fit and the prefit α, the variable X, the product of the fit errors and the errors in the fourth and fifth parameters of the fit. The vertical lines correspond to the position of the cut (*Level* 2).

Level of selection	Atmospheric muons (yr^{-1})	Atmospheric neutrinos (yr^{-1})	Signal (yr^{-1})	MC Events
Reconstructed	7.8×10^6	6120	26	1682415
Reconstructed as up-going	6.1×10^6	6080	26	1673967
Carmona Quality	1170	1800	13	906269
Level 2	0	1510	12	796819

Table 5.2: Comparison of the rates per year at different levels of selection. The last column indicates the number of MC events at each level of cuts for the neutrino sample (atmospheric neutrinos and signal). The corresponding number of MC events for the atmospheric muon sample was given in table 5.1.
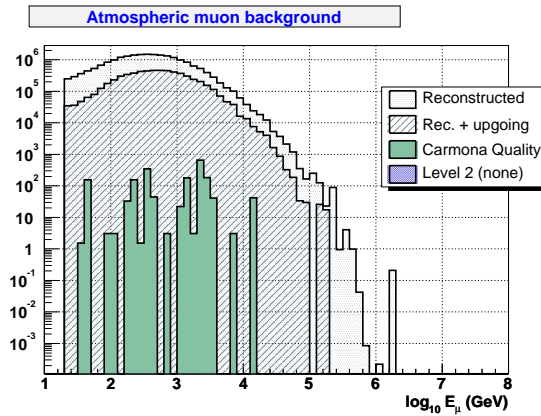
Figure 5.5: Atmospheric muon energy distributions (events/year) for the different selection cut levels. No event passes the *Level 2* set of cuts.
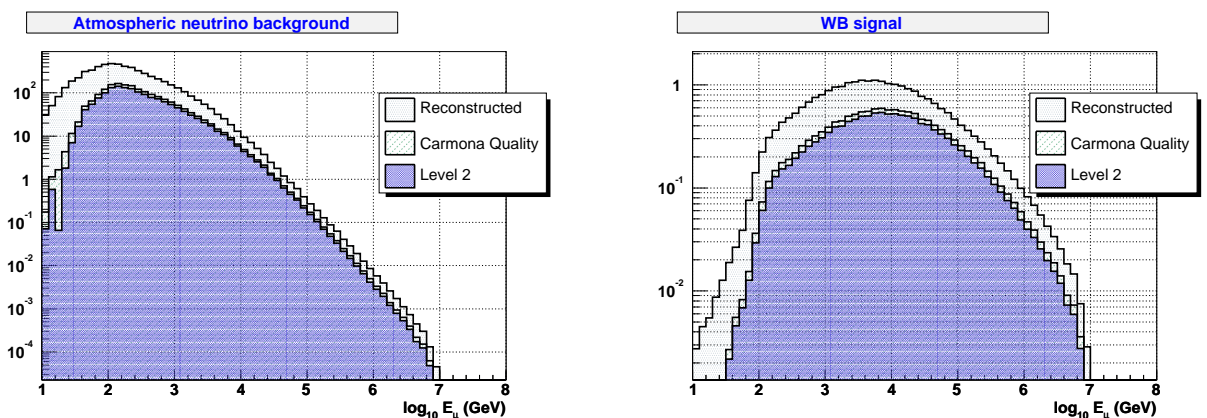
Figure 5.6: Reconstructed and selected event distributions (events/year) for signal and atmospheric neutrinos.
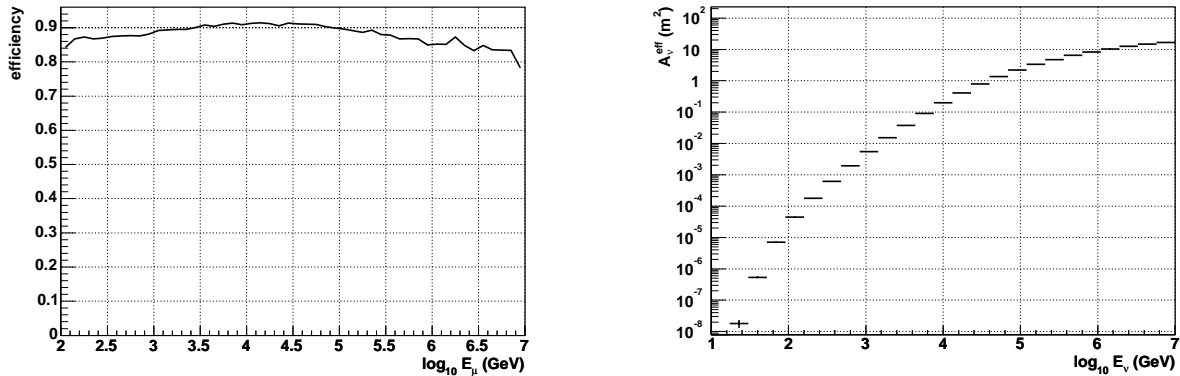
Figure 5.7: Left: Efficiency of the *Level* 2 cuts, calculated as the ratio between the number of events after the *Level* 2 set of cuts over the number of events after Quality. Right: Neutrino effective area using the *Level* 2 cuts.

The fact that there is no atmospheric muon event passing the cuts, does not allow us to conclude that this background is completely irrelevant. To be confident with the hypothesis of null background, the equivalent of at least several years of life-time MC samples for all primaries and energies would be needed. Nevertheless, there are some arguments that support the idea that this background is practically negligible for this analysis.

First of all, we can study how the energy muon spectrum changes as tighter selection criteria are applied. To do this, intermediate levels of selection criteria are defined in table 5.3. In figure 5.8 the effect of these different cuts is shown. There is no significant bias in the energy spectrum introduced by these selections so, in principle, we can assume that the spectral shape would be preserved as far as stringer selection criteria are applied. In fact, if we fit the distributions in the region of interest, the spectral indexes are quite similar (last column in table 5.3).

We have studied the hypothetical effect of some contamination from atmospheric muons. Although we have shown that no event of this kind is expected according to the Monte Carlo, we can estimate how many could pass the *Level* 2 cuts without a significant impact on the results. We have seen that even if 16 events pass the selection cuts, the background caused by atmospheric muons would represent only a 20% of the background due to atmospheric neutrinos above the energy-parameter threshold. It has been assumed that the selection cuts do not change the spectral shape, which is supported by the results presented in table 5.3.

Moreover, no atmospheric muon event survives either the *Level* 2 quality cuts in any of the additional MC samples mentioned in 3.2.2. Thus, for this analysis it is assumed that the contamination from atmospheric muon events is negligible in the high energy region.

Cut	$\alpha_{fit-prefit}$	X	d1· d2· d3· d4· d5	d4	slope
L0	-	-	-	-	-4.5
L1.1	$<90°$	>0.1	$<10^5$	<1000	-4.6
L1.2	$<80°$	>0.3	<100	<20	-4.8
L1.3	$<65°$	>0.4	<0.1	<5	-5.1
Carmona Quality	$<50°$	>0.5	<0.001	<1.5	-

Table 5.3: Definition of the different levels of intermediate selection cuts. All these cuts also include the condition of being reconstructed as up-going event. Last column shows the value of the slope of the exponential fit for different intermediate levels of cuts. The bias introduced by the cuts seems to be negligible.
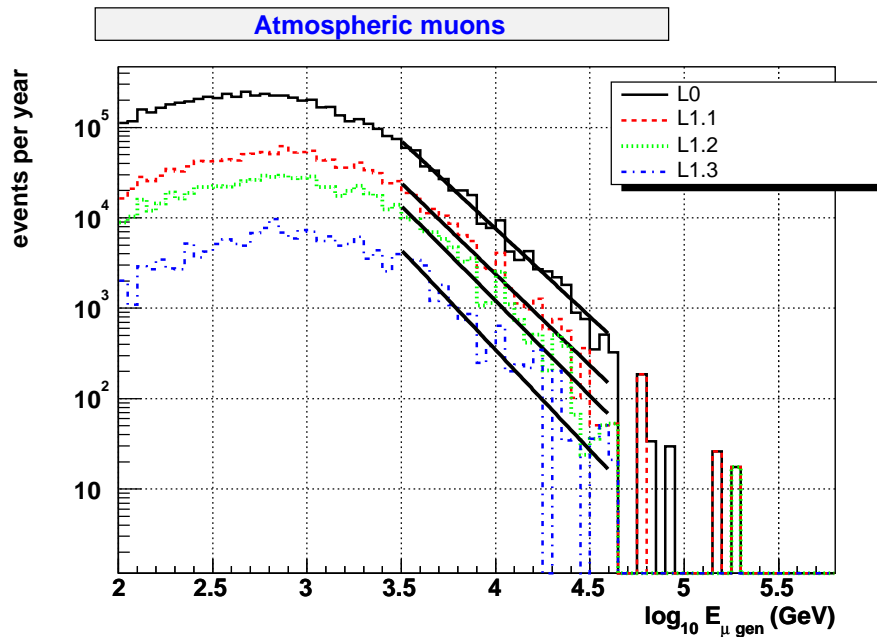
Figure 5.8: Energy spectra after different levels of intermediate cuts used to study the bias produced by the selection. The distributions do not show any obvious bias.

5.2   Effect of the *Level* 2 quality cuts

Once the new set of quality cuts, *Level* 2, has been defined, it is important to study the effect that these cuts produce on the distribution of the different track parameters. We study the muon and neutrino atmospheric backgrounds in sections 5.2.1 and 5.2.2, respectively, and the signal event distributions in section 5.2.3.

5.2.1   Atmospheric muon background

Although no atmospheric muon survives the *Level* 2 set of cuts, it is interesting to show the track parameter distributions at the different reconstruction levels, specially the Carmona quality cuts. Figures 5.9 and 5.11 show the distributions of several geometrical parameters of the track. It can be seen, for instance, that the events passing the Carmona quality cuts are mostly around $2\theta_C = 84°$ due to ghost solution tracks. These *ghost tracks* are produced by the symmetry of the Cherenkov effect (see figure 5.10).
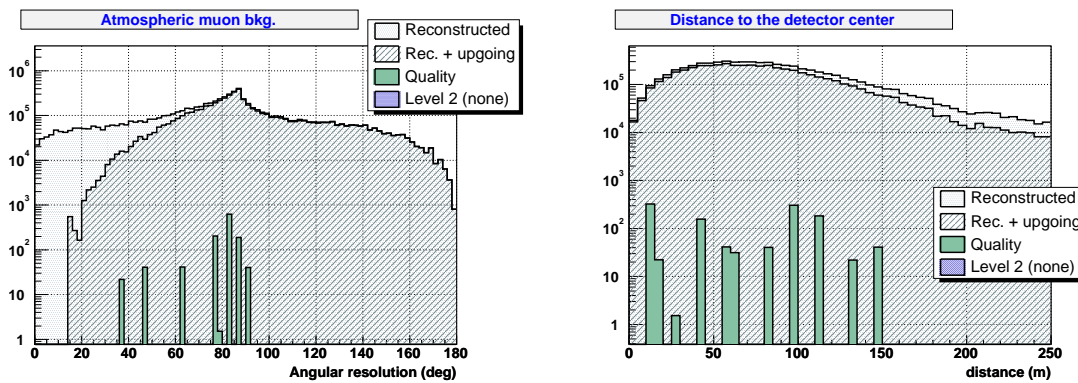
Figure 5.9: Distributions (events/year) of the angular resolution (left) and the distance to the detector centre (right) of the atmospheric muon background. The events passing the Carmona quality cuts are mostly at $2\theta_C = 84°$ (ghost solutions). After the *Level* 2 cuts, no event remains.

On the other hand, the tracks remaining after the Carmona quality cuts do not show any dependence on the minimum distance to the detector centre (figure 5.9, right).

The maximum of the true zenith angle distribution of tracks passing the up-going condition is around 130° (figure 5.11, left). These tracks are misreconstructed as nearly horizontal ghost tracks, as pointed out previously. There is no obvious effect of the selection on the azimuth angle distribution (figure 5.11, right), as expected.

Finally, figure 5.12 shows the effect of the selection cuts on the energy resolution. It can be seen that, since most of the events are low-energy events, the reconstructed energy is overestimated and the average energy resolution shifts to ∼0.5 being the distribution quite broad. This is also the case when only the events surviving the Carmona Quality cuts are considered.
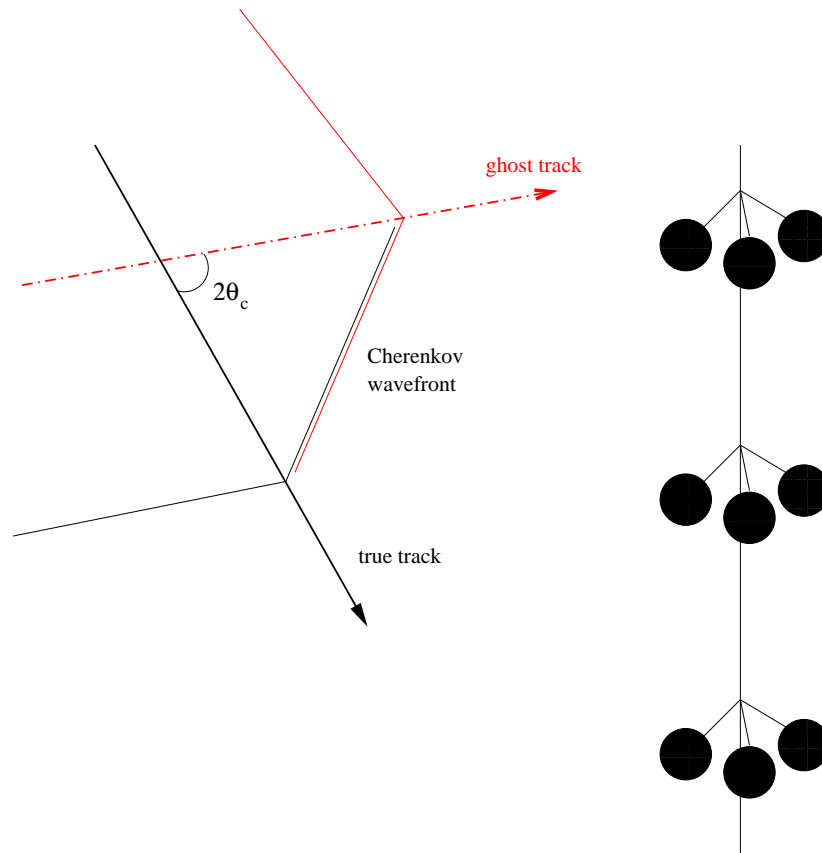
Figure 5.10: Most fake events are due to ghost tracks (dashed line) at $2\theta_C$ of the true track (solid line). These events are generally outside the detector and only half of the Cherenkov cone is detected.
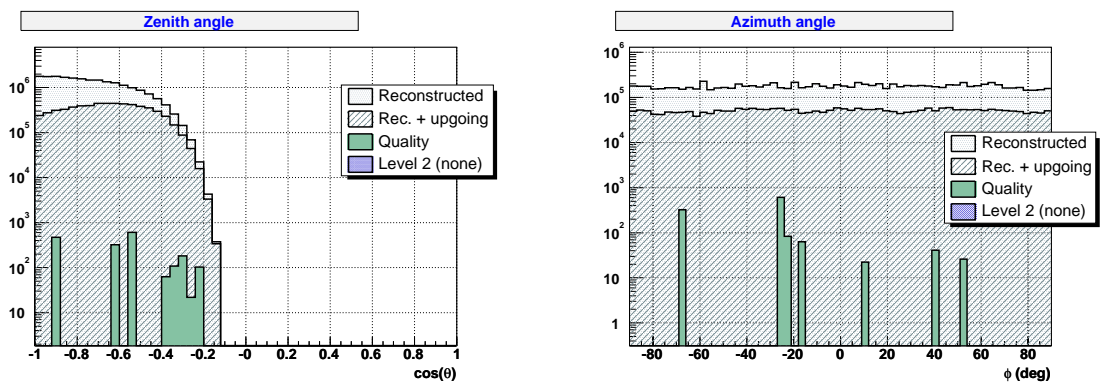
Figure 5.11: Cosine of zenith angle (left) and azimuth angle (right) distributions (events/year) of the atmospheric muon background.
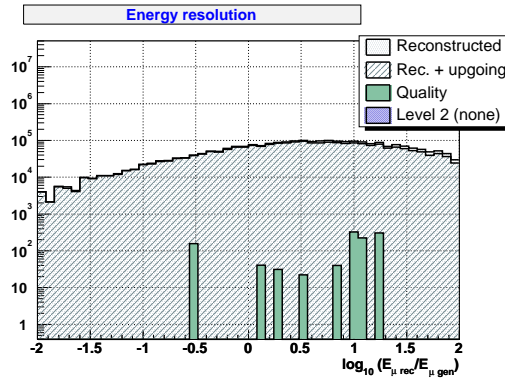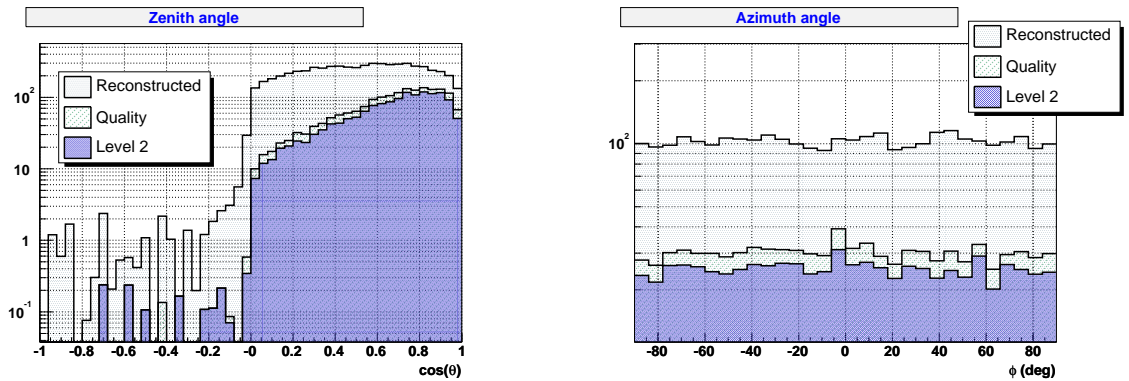
Figure 5.12: Energy resolution distribution (events/year) of the atmospheric muon background.

5.2.2   Atmospheric neutrino background

The relevant distributions for the atmospheric neutrinos are shown in figures 5.13-5.15. In this case, the angular resolution is much better, since these are up-going events. A small peak at 84° (ghost solution tracks) is still seen, but much lower. The distance distribution indicates that the selection cuts do not introduce any bias. Most of the selected events pass through the detector.
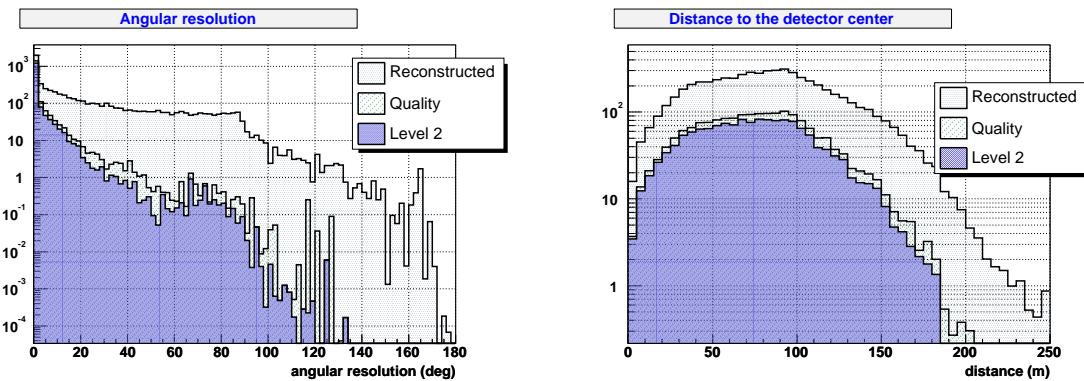
Figure 5.13: Distributions (events/year) of angular resolution (left) and distance to the detector centre (right) of the atmospheric neutrino background. The peak of ghost solutions in the angular resolution plot is now much lower.

Concerning the zenith angle distribution, two remarks can be made. Firstly, vertical events are most likely to pass the Carmona quality cuts (although no further bias is introduced by the *Level* 2 cut). Secondly, there is a small fraction of down-going muons which have been produced by almost horizontal up-going neutrinos. The azimuth angle distribution shows a nearly ϕ-independent behaviour as expected.

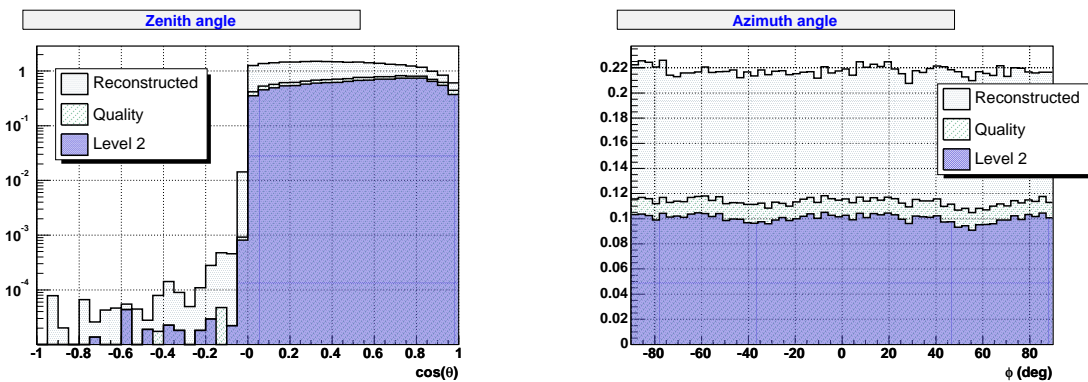**Figure 5.14:** Cosine of zenith angle (left) and azimuth angle (right) distributions (events/year) of the atmospheric neutrino background.

The effect of selection in the energy resolution (figure 5.15) demonstrates that the Quality cuts eliminate most of the tracks with wrongly reconstructed energy (low energy component). However, a shift of ~ 0.2 in the average value is still seen. The remaining distribution is not affected by the *Level* 2 set of cuts.
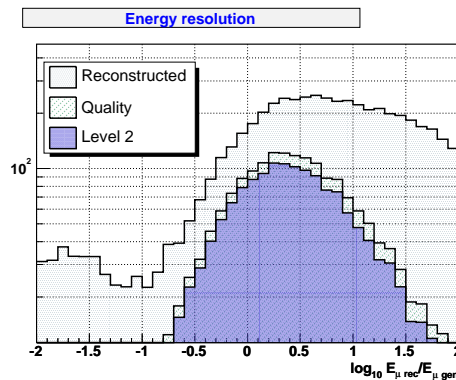
Figure 5.15: Energy resolution distribution (events/year) of the atmospheric neutrino background.

5.2.3 Cosmic neutrino signal

The distributions for the cosmic neutrino signal are shown in figures 5.16 and 5.17. Some of the conclusions are very similar to those of atmospheric neutrino background, since the only difference is the energy spectrum. This is the case of the angular resolution, distance to the centre of the detector and zenith and azimuth angle distributions.

On the other hand, the energy resolution distribution shows some differences. Firstly, the distribution of reconstructed events is more symmetric. The Carmona
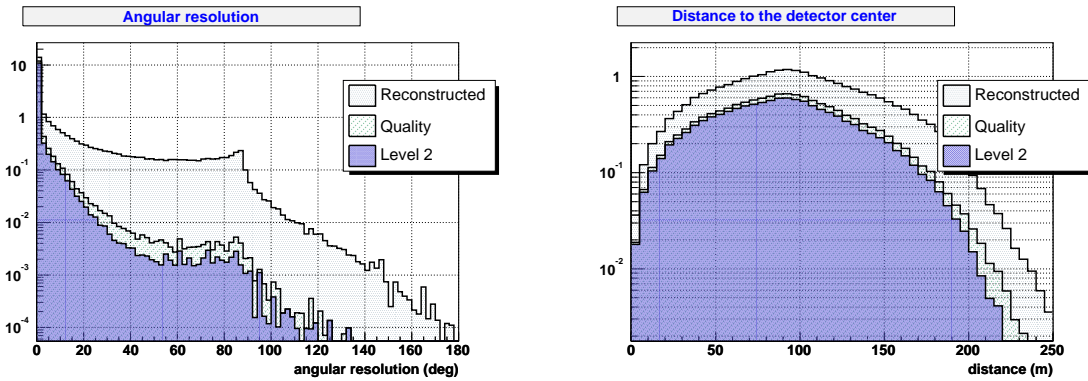
Figure 5.16: Angular resolution (left) and distance to the detector centre (right) distributions (events/year) of the cosmic neutrino signal. The peak at 84° is produced by ghost solution tracks.

Figure 5.17: Cosine of zenith angle (left) and azimuth angle (right) distributions (events/year) of the cosmic neutrino signal.

and *Level* 2 cuts do not produce any bias, and the average energy resolution is centered at zero, as desired. These differences with respect to the case of the atmospheric neutrinos are explained, as it has been mentioned by the different spectral indexes (the cosmic neutrino distribution is not dominated by low energy events, as it occurs with the atmospheric neutrinos).
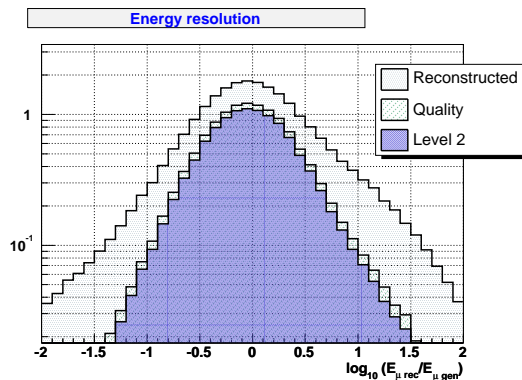
Figure 5.18: Energy resolution distribution (events/year) of the cosmic neutrino signal. The distribution is centered at zero, which means that the reconstructed energy is not biased.

5.3 Rejection of the atmospheric neutrino background

After removing all downward muon events, only upward atmospheric neutrinos induced by cosmic rays in the Earth's atmosphere remain as background. They have a origin different from the extraterrestrial neutrinos but, being also up-going events, their signatures in the detector are indistinguishable. The discrimination between cosmic and atmospheric neutrinos is based on statistical criteria. For the search of point-like sources, accumulations in declination and right ascension are looked for. However, for the diffuse neutrino flux, i.e. the integrated flux from unresolved sources, the event excess has to be found in the energy spectrum. Since atmospheric neutrinos follow a power law steeper than that of the cosmic neutrino spectrum, an excess of events at high energies would be an evidence of a cosmic diffuse flux. This can be seen in figure 5.19 where the integrated energy spectrum of the muon for the Bartol and Waxman-Bahcall rates are shown.

5.3.1 Energy Estimator

Unfortunately, in real conditions we will not have the true muon energy but an energy estimator distorted by the limited detector resolution. Several energy-dependent
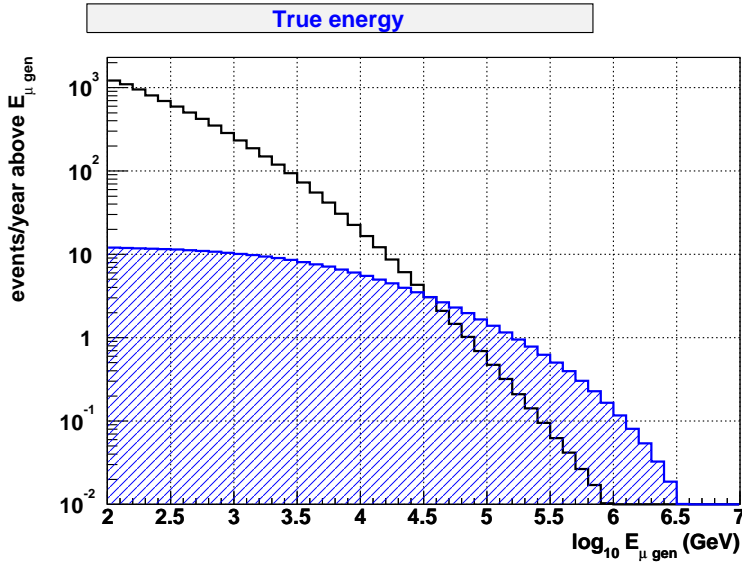
Figure 5.19: Integrated energy distribution of the true muon energy for signal (shaded) and atmospheric neutrino background (blank). At high energies, the background is expected to be much lower than the cosmic neutrino rate.

estimators can be considered to separate diffuse signal neutrinos from atmospheric neutrinos. We have investigated the two following possibilities[3]:

- Reconstructed energy based on the minimum ionising muon comparison method.

- The hit multiplicity.

In figure 5.20 (left) the dependence of the reconstructed muon energy on the true muon energy is shown together with the dispersion (RMS) in the $\log_{10} E_{\mu \text{ rec}}$. The reconstructed energy is obtained from the parameterization of the low energy estimator, as explained in chapter 4. In the plot on the right, the energy estimator dispersion is divided by the increase in the ordinate axis from $E_{\mu}^{gen} = 10^2$ GeV to $E_{\mu}^{gen} = 10^7$ GeV (Δy). This allows to compare the relative size of the dispersion for different variables.

Figure 5.21 shows the integrated spectrum for the reconstructed energy. As it can be seen, the spread of $\log_{10} E_{\mu \text{ rec}}$ combined with the sharp power-law of the atmospheric background deteriorates the separation power of the parameter used to make the discrimination. The larger the spread in the energy estimator, the greater the number of muon events whose energy will be overestimated and therefore, the higher the contamination in the high energy region.

We have also studied the performance of the total number of hits in the event, N_{hits}, as a possible variable for an energy estimator. Figure 5.22 shows that this variable

---

[3]Other possibilities, like the low or high energy estimator, are equivalent to use the reconstructed energy, since they are linearly related.
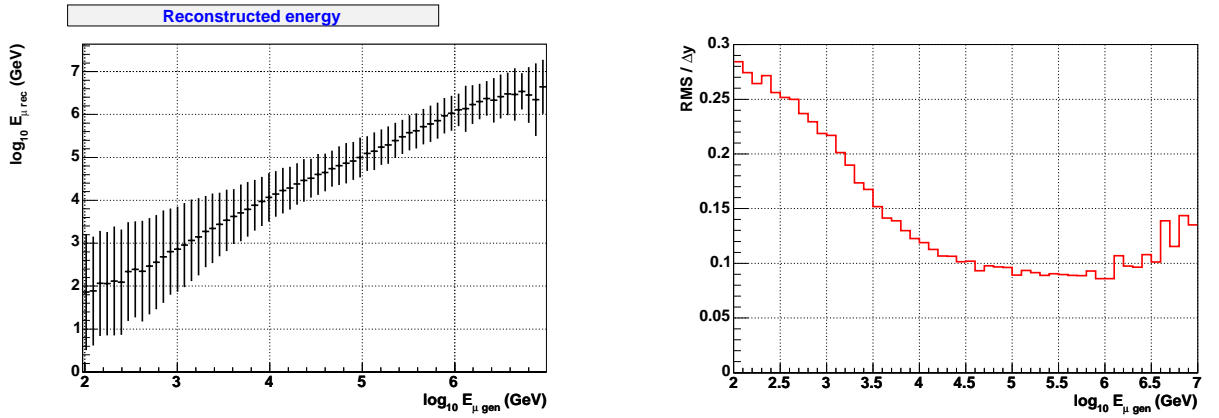
Figure 5.20: Left: Dependence of the reconstructed muon energy on the true muon energy. The bars indicate the spread (RMS) of the values of the reconstructed energy for each true muon energy bin. Right: The spread divided by the energy estimator increase as a function of the generated muon energy.
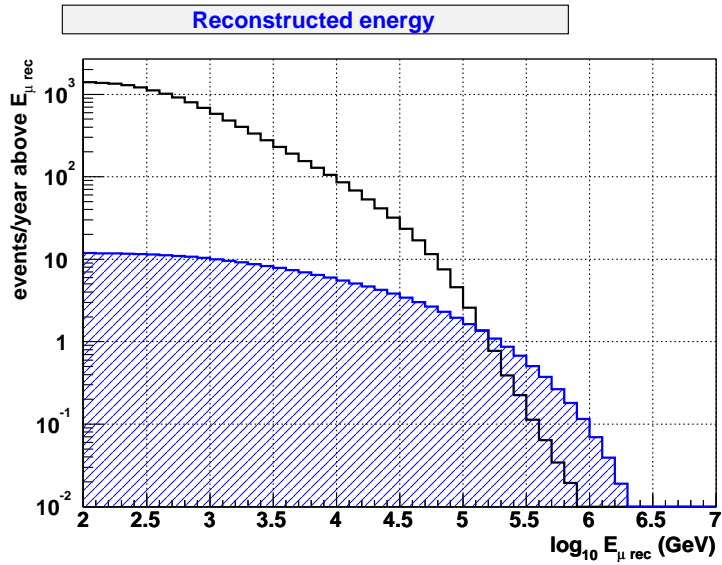

Figure 5.21: Integrated distribution of the reconstructed energy for signal (shaded) and atmospheric neutrino background (blank). The excess of signal over background is smaller than in the case of the true energy, due to the spread in the reconstructed energy.

offers a better compromise between spread in the region where the signal becomes larger than the background, and linearity in the high energy region. Only hits within a time window of ±4 ns around the direct time (i.e. the arrival time with respect to the expected non-scattered Cherenkov photons) are considered to avoid high fluctuations in the energy deposition. The comparison between signal and background using the number of hits as energy-dependent parameter can be seen in figure 5.23. This variable has a better performance for atmospheric neutrino discrimination, as it will be shown with the model rejection factor calculation (see section 5.3.3).
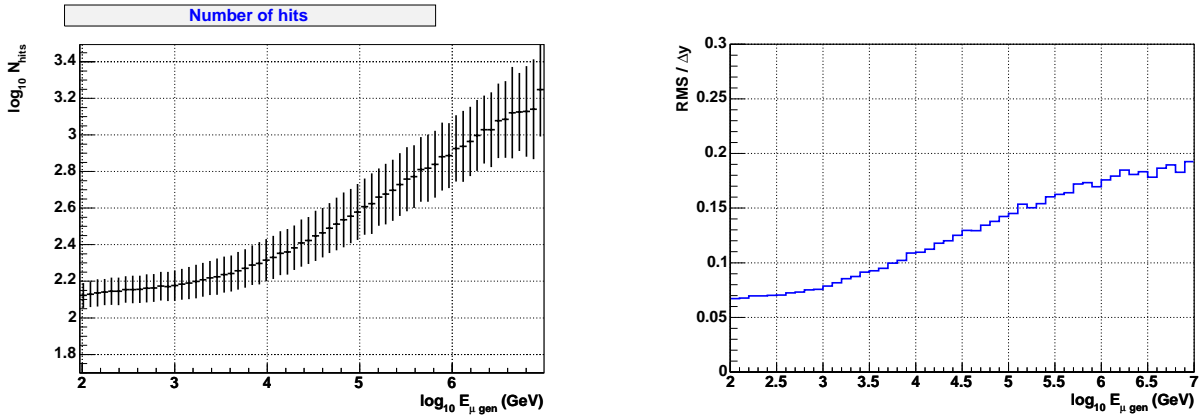
Figure 5.22: Left: Dependence of the number of selected hits on the true muon energy. The bars indicate the spread (RMS) of the logarithm of the number of hits for each true muon energy bin. Right: The spread divided by the energy estimator increase as a function of the generated muon energy.

5.3.2 Average upper limits

The method used to compute the sensitivity to a given flux model is the "Model Rejection Potential" technique described in [134]. Assuming that a predicted diffuse flux $\Phi(E)$ produces n_s signal events and that the observed number of events is compatible with background, the upper limit for the flux at a given confidence level CL is

$$\Phi(E)_{CL} = \Phi(E) \ \frac{\mu_{CL}(n_{obs}, n_{bg})}{n_s} \tag{5.1}$$

where n_{obs} is the observed number of events; n_{bg}, the expected background; n_s, the signal expectation, and $\mu_{CL}(n_{obs}, n_{bg})$, the Feldman-Cousins upper limit [135]. In this analysis we use the $CL=90\%$.

In order to avoid any bias when the best cut in the energy-dependent variable is established, the optimal cut has to be determined without observational information. We assume that no signal events are present and, by means of Monte Carlo predictions,
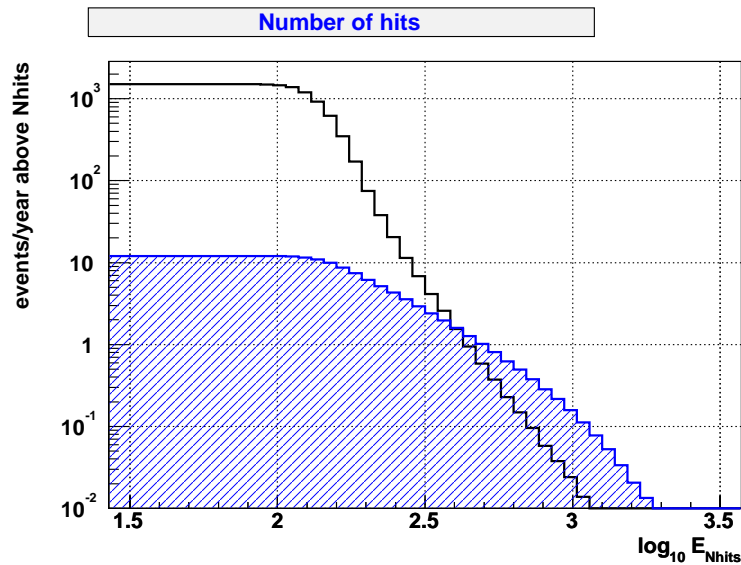
Figure 5.23: Integrated distribution of the number of hits for signal (shaded) and atmospheric neutrino background (blank). It shows a better rate of signal over background than the reconstructed energy.

we calculate an "average upper limit", $\bar{\mu}_{90}(n_{bg})$, taking into account all the possible numbers of observed events for the estimated background, weighed according to their Poisson probability:

$$\bar{\mu}_{90}(n_{bg}) = \sum_{n_{obs}=0}^{\infty} \mu_{90}(n_{obs}, n_{bg}) \frac{(n_{bg})^{n_{obs}} e^{-n_{bg}}}{n_{obs}!} \qquad (5.2)$$

This average upper limit (see figure 5.24) does not depend on the observed number of events, but only on the expected background.

The optimum threshold is the one that minimizes the so-called "model rejection factor" ($MRF = \bar{\mu}_{90}/n_s$) and hence, the average flux upper limit is given by:

$$\bar{\Phi}(E)_{90} = \Phi(E) \; \frac{\bar{\mu}_{90}(n_{obs}, n_{bg})}{n_s} \qquad (5.3)$$

5.3.3 Comparison between estimators

In order to choose the best energy-dependent variable we can compute the sensitivity for the estimators mentioned in section 5.3.1. As a reference value, we will first use the true muon energy to compute the sensitivity. This would correspond to an ideal detector with perfect energy resolution. In figure 5.25 (left) the integrated energy distributions for signal and background together with the average upper limit are shown. The same figure on the right side shows the model rejection factor ($\bar{\mu}_{90}/n_s$) as a function
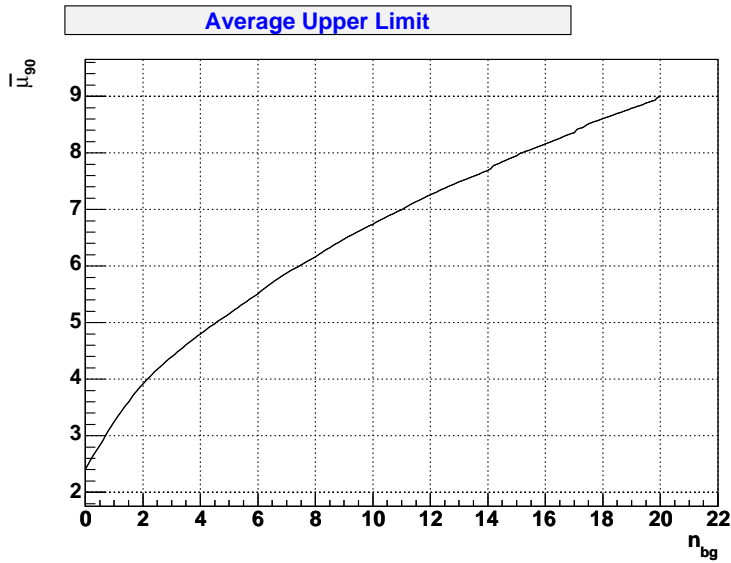
Figure 5.24: Average upper limit using the Feldman-Cousins method at the 90% CL, as a function of the number of background events. See text for details.

of the true muon energy. Following the frequentist approach, the average upper limit computed with "classical" standard confidence intervals [136] is also shown. Analogous distributions are shown in figures 5.26 and 5.27 using the reconstructed energy, E_μ^{rec} and the number of hits, N_{hits}, respectively.

A comparison of the results obtained for the different energy estimators is shown in table 5.4. The model rejection factors calculated with the classical standard method are systematically lower than the Feldman-Cousins values, but the latter are considered to be more appropriate, since it unifies the two-sided confidence levels and the upper limits [135].

The variable having the lowest MRF is the number of hits. The value using the true energy is only ~30 % better. The reason is that this estimator has a lower dispersion at low energies and a better linearity at high energies. In the next section, the influence of these two factors on the calculation of the average upper limit is studied in more detail.

Spread

Firstly, we have simplified the energy reconstruction by smearing the logarithm of the true muon energy according to a Gaussian distribution $G(\log_{10} E_\mu, \sigma)$. As a first approximation, we assume that the value of σ is independent of the muon energy. In figure 5.28 the average flux upper limit for different values of the real detector energy resolution are compared. The prompt neutrino contribution (RQPM model [137]) is included in the background. Two conclusions can be made from figure 5.28. The higher
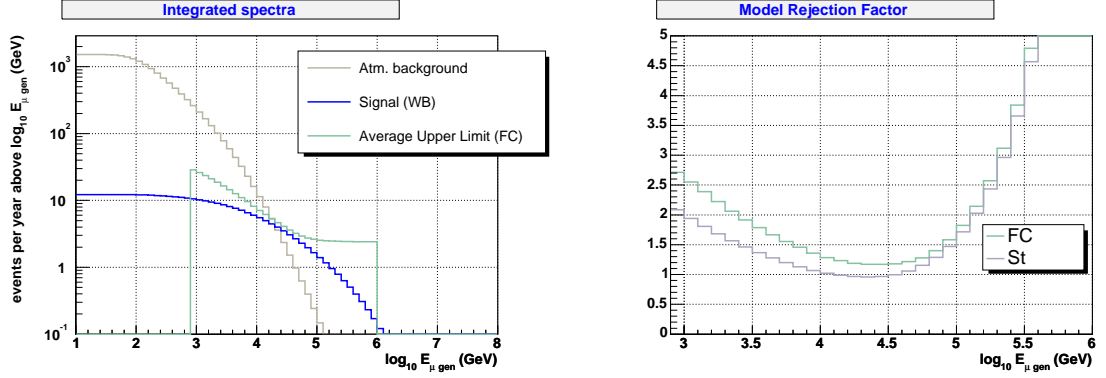
Figure 5.25: Left: Integrated distributions of the true muon energy for signal and atmospheric background. The average upper limit assuming that only atmospheric neutrino background is observed is also shown. Right: Model rejection factor for the Feldman-Cousins (FC) and classical (St) approach.
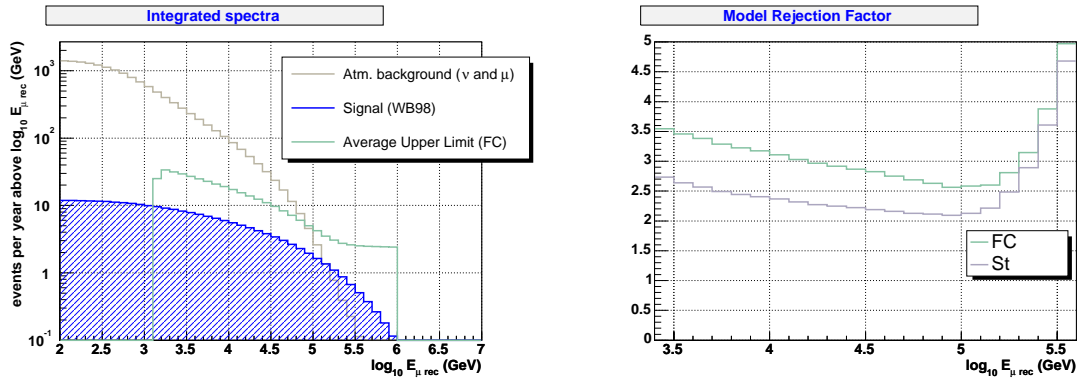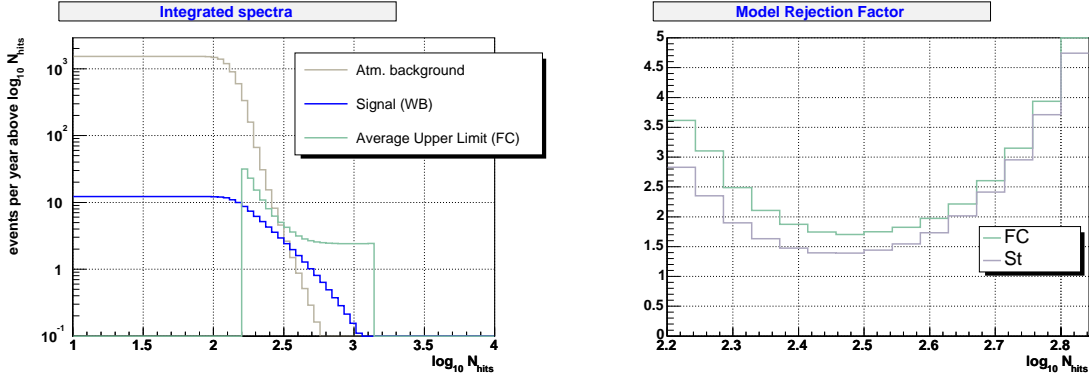

Figure 5.26: Left: Integrated distributions of the reconstructed muon energy for signal and atmospheric background. The average upper limit assuming that only atmospheric neutrino background is observed is also shown. Right: Model rejection factor for the Feldman-Cousins (FC) and classical (St) approach.

Figure 5.27: Left: Integrated distributions of the number of hits for signal and atmospheric background. The average upper limit assuming that only atmospheric neutrino background is observed is also shown. Right: Model rejection factor for the Feldman-Cousins (FC) and classical (St) approach.

1 year					
Variable	MRF (FC)	MRF (st)	Best cut	Background	Signal
True energy	1.17	0.96	2.2×10^4 (GeV)	3.6	4.0
Reconstructed energy	2.56	2.09	7.9×10^4 (GeV)	4.6	2.0
Number of hits	1.72	1.40	287	4.6	2.9

3 years					
Variable	MRF (FC)	MRF (st)	Best cut	Background	Signal
True energy	0.54	0.44	3.2×10^4 (GeV)	4.6	9.2
Reconstructed energy	1.20	0.98	1.3×10^5 (GeV)	4.1	4.0
Number of hits	0.84	0.67	316	7.6	7.2

Table 5.4: Model rejection factor obtained for the different energy estimators. The values shown in the "Best cut" column correspond to the optimum threshold obtained with the Feldman-Cousins approach. The number of signal and background events above the best cut are also indicated.

the value of σ, the higher the average flux upper limit and the higher the threshold cut. The value of the energy resolution is typically around 0.4-0.5, which produces, according to the plot, an increase of $\sim 40\%$ in the average flux upper limit. A shift in the mean would produce an additional increase in the limit.
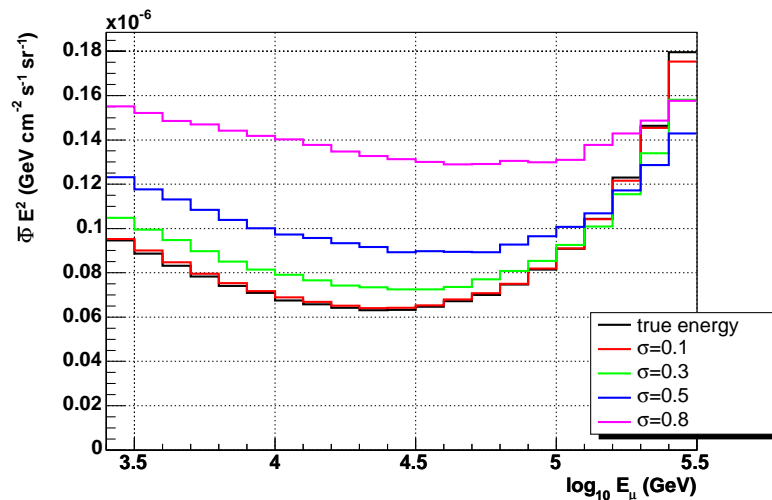

Figure 5.28: Average flux upper limit for several values of the energy resolution as a function of the muon energy. This reconstructed energy is simulated by a Gaussian smearing (of width σ) of the true muon energy distribution $\log_{10} E_\mu$.

As shown in the previous chapter, the value of the energy resolution is not constant with the energy. Therefore, we have also considered this possibility. This dependence is parameterized by means of a straight line with slope s. The results are plotted in figure 5.29. We see in these plots that a large value of σ at low energies has a strong effect in the average upper limit, even if the resolution at high energies does not change much, due to the migration of many low-energy events to the high energy region.

Linearity

As we have indicated, the effect of saturation, in particular at high energies is also important. We have fitted the distribution of the low energy estimator to a cubic polynomial and have changed the coefficient of the cubic term to simulate different degrees of saturation.

For the low energy estimator, the value of the cubic term a (in the polynomial parameterization $y = ax^3 + cx + d$) is 0.05. In the results shown in figure 5.30, the dispersion in the estimator value is $\sigma = 0.4$. The neutrino background also contains prompt neutrinos according to the RQPM model. From these plots, we conclude that small values of the saturation (a<0.05) do not affect very much the average flux upper limit. However, for larger values (a>0.05) the degradation becomes important.
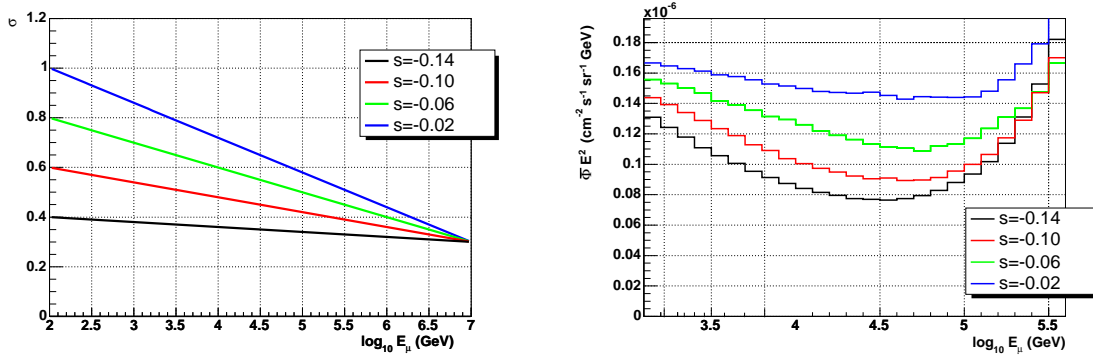
Figure 5.29: Simulated dependence of the energy resolution on the true muon energy (left) and the corresponding average flux upper limit for the flux (right). The value of s indicates the slope of the straight line which parameterizes this dependence.
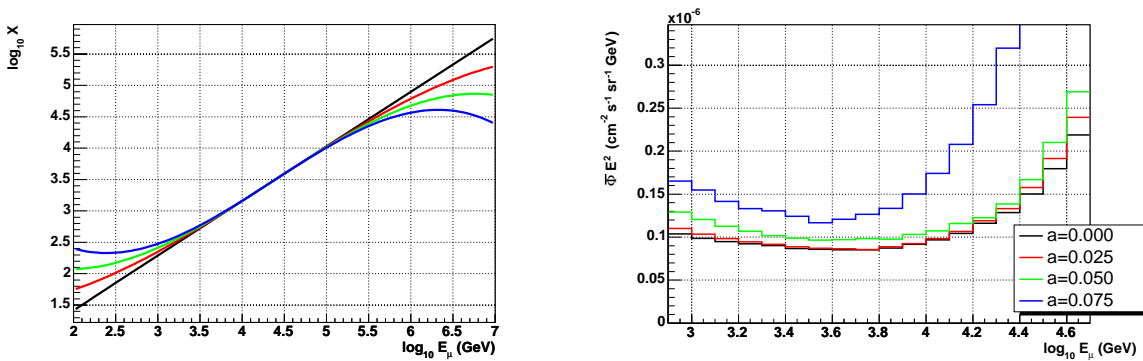

Figure 5.30: Dependence of the simulated estimator on the true muon energy (left) and average flux upper limit (right) for different degrees of saturation, given by a, the coefficient of the cubic term in the polynomial parameterization $y = ax^3 + cx + d$.

5.4   Sensitivity results

The computed model rejection factor can be applied to some theoretical models in order to calculate the corresponding average flux upper limit. In particular, the average upper limit for a flux in the limit of the Waxman-Bahcall bound would be:

$$E^2 \Phi_{90} < 7.7 \times 10^{-8} \text{ GeV cm}^{-2} \text{ s}^{-1} \text{ sr}^{-1} \quad \text{(after 1 year)} \tag{5.4}$$

Figure 5.31 shows the $N_{hits} - E_\nu$ distributions for background and signal. The threshold used in the sensitivity calculation $N_{hits} > 287$ is shown. It can be seen that in order to reject the bulk of the atmospheric neutrino background, an important fraction of the cosmic neutrino signal is discarded. The effect of the cut on the muon and neutrino spectrum can be seen in figures 5.32 and 5.33. In these plots, it can be also seen that most of the signal is overlapped by the atmospheric neutrino background, so the discrimination is very difficult. Despite this limitation most of the background is rejected. As in the case of the cut *Level* 2, we can plot the efficiency when the cut in the number of hits is applied (figure 5.34). As desired, the effect of the cut is an important decrease of the efficiency in the low energy region, while it remains almost the same at high energies.

After three years of data taking, the model rejection factor decreases approximately by a factor two, so the sensitivity for the Waxman-Bahcall upper bound is

$$E^2 \Phi_{90} < 3.8 \times 10^{-8} \text{ GeV cm}^{-2} \text{ s}^{-1} \text{ sr}^{-1} \quad \text{(after 3 years)} \tag{5.5}$$

In figure 5.35, the evolution of the model rejection factor with the number of years of data taking is shown.

5.4.1   Other models for the cosmic neutrino signal

We have studied the ANTARES sensitivity to other signal predictions and upper bounds described in chapter 1. Figure 5.36 shows the integrated rates predicted for each of these models compared with the Bartol atmospheric flux. In table 5.5 the corresponding model rejection factors are shown.

5.5   Systematic errors

In this section we review the main sources of systematics uncertainties and estimate how they affect to the sensitivity calculation. We take into account two different kinds of systematic errors:
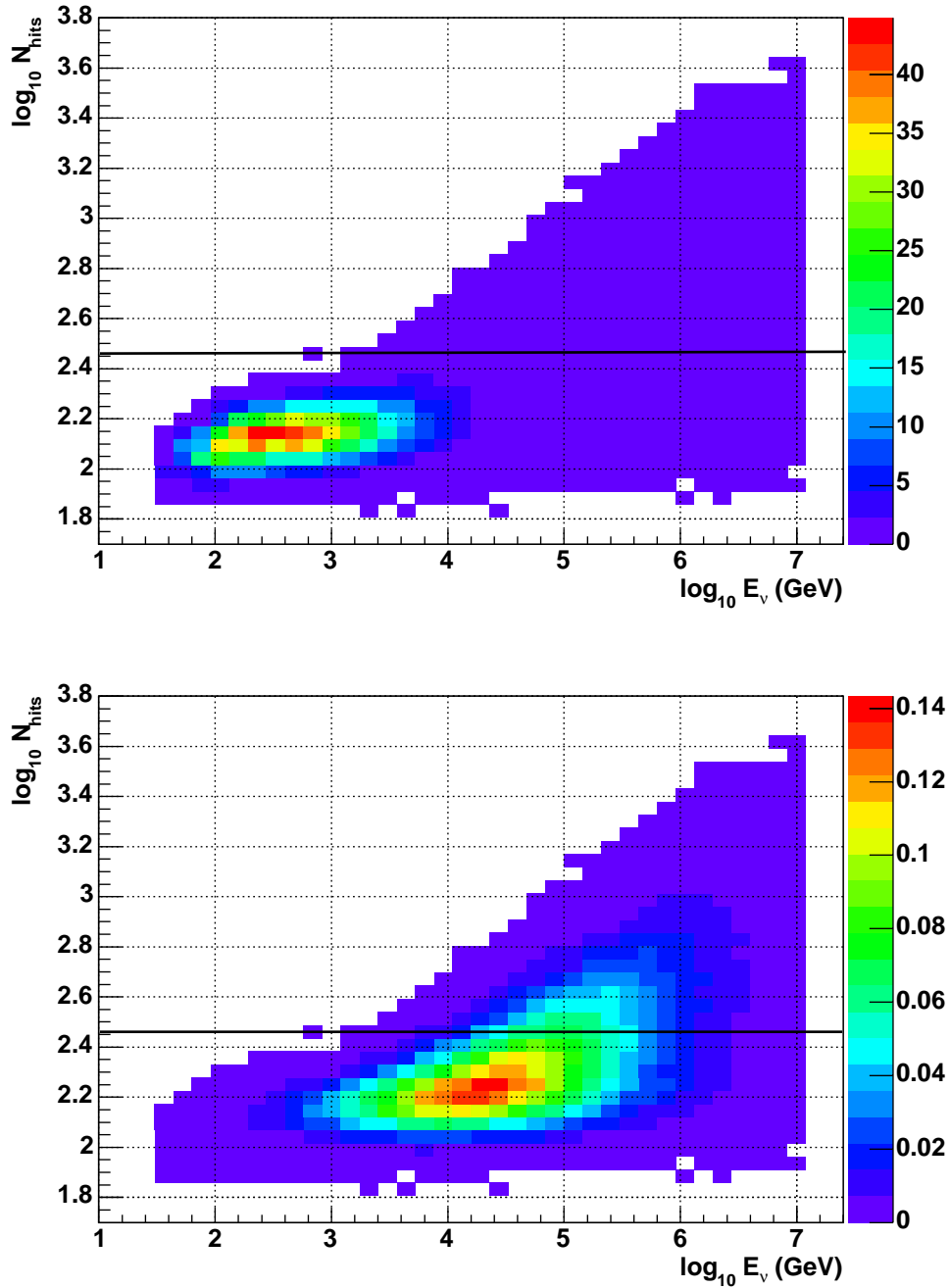
Figure 5.31: $N_{hits} - E_\nu$ distribution for atmospheric neutrino background (top) and cosmic neutrino signal (bottom). The horizontal line indicates the N_{hits} threshold used to reject the atmospheric neutrino background.
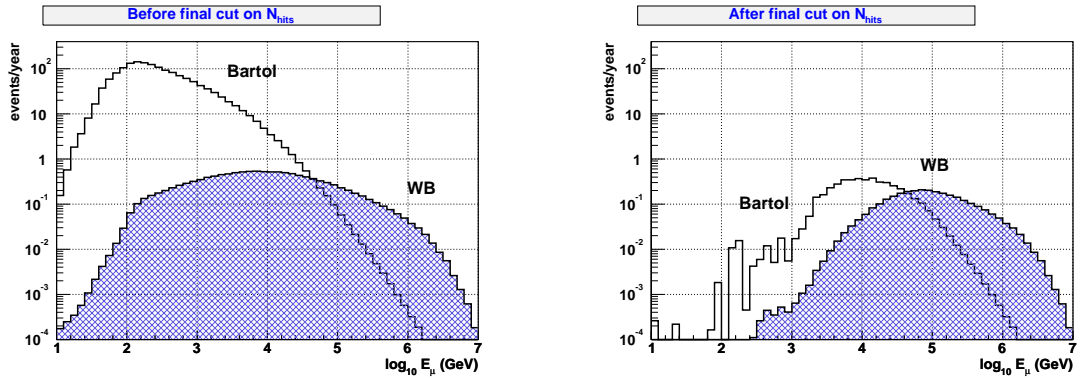
Figure 5.32: Muon energy spectrum before and after applying the $N_{hits} > 287$ cut.
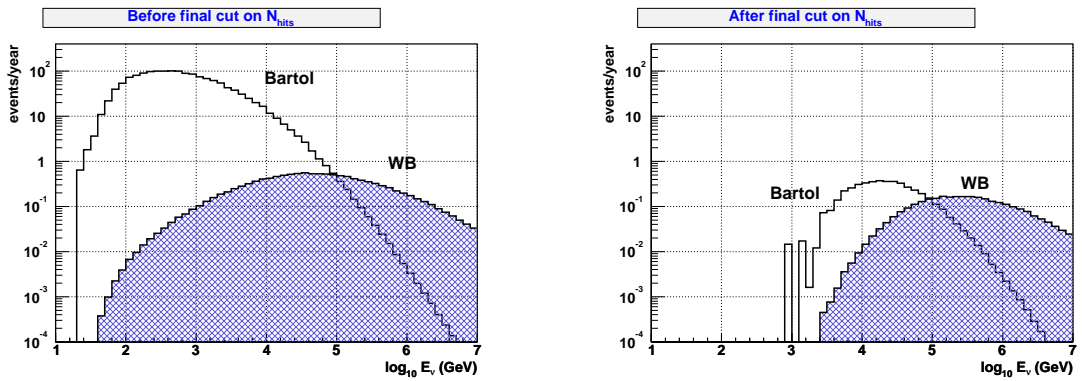

Figure 5.33: Neutrino energy spectrum before and after applying the $N_{hits} > 287$ cut.
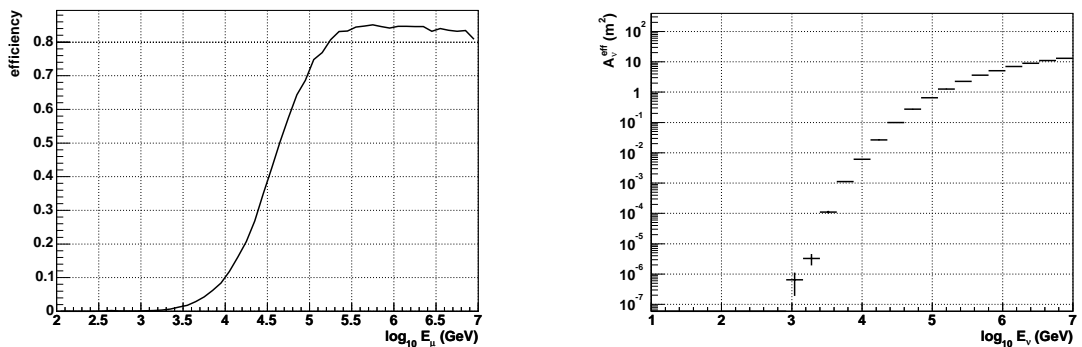

Figure 5.34: Left: Efficiency of the cut in the number of hits, calculated as the ratio between the number of events after this cut over the number of events after Carmona quality cuts. Right: Neutrino effective area using the N_{hits} cut.
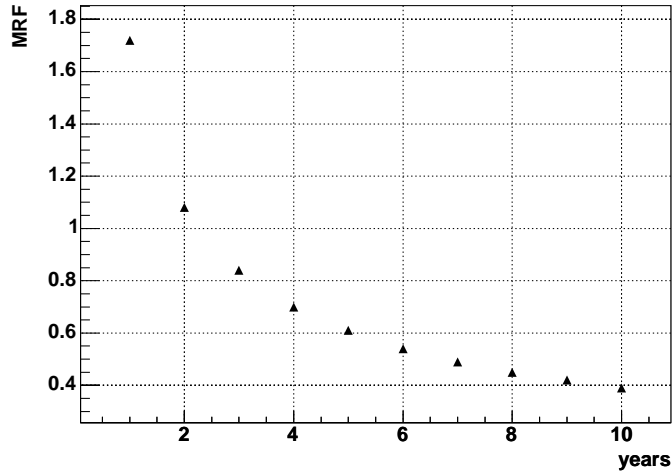
Figure 5.35: Model rejection factor evolution with the number of years of data taking.
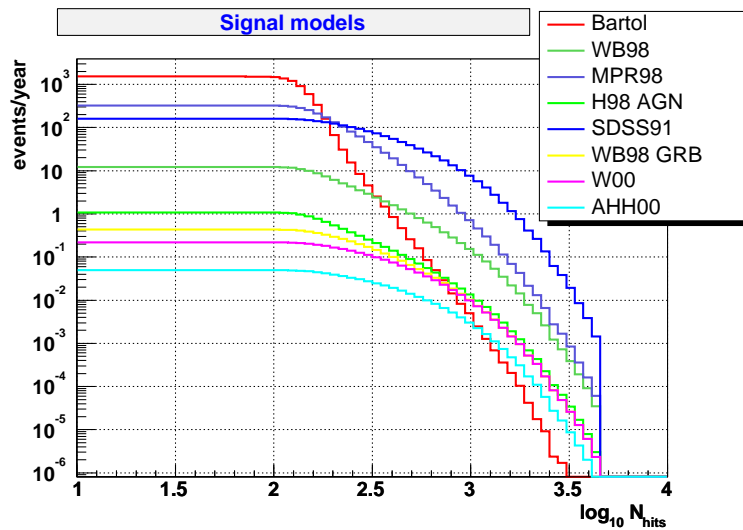

Figure 5.36: Integrated distributions of the number of hits, N_{hits}, for several cosmic neutrino signal models. The Bartol prediction for the background neutrinos is also plotted as a reference.

Model	MRF (FC)	MRF (St)	Best cut (N_{hits})	Background	Signal
WB98 [76]	1.7	1.4	287	4.6	2.9
MPR98 [77]	0.1	0.078	235	15	81
H98 AGN [138]	19.6	16	287	4.6	0.26
SDSS91 [139]	0.056	0.047	349	15	64
WB98 GRB [140]	29	24	316	2.6	0.15
W00 [141]	42	35	349	1.48	0.086
AHH00 [142]	163	139	385	0.48	0.02

Table 5.5: Comparison of the model rejection factor for several cosmic neutrino signal models after one year of data taking. Models with MRF$\lesssim$1 can be tested by the experiment.

- **Prediction of the background:** Concerning the atmospheric neutrino background, we consider the following systematic uncertainties: the conventional atmospheric neutrino model, the uncertainty in the absolute value and the contribution of the prompt neutrinos.

- **Efficiency:** In principle, the uncertainty in the detection efficiency can be different for atmospheric background and signal, but as a first approximation they can be considered the same. The two main sources of systematic errors in the efficiency are the water model and the propagation simulation. Other factors which could alter the efficiency are the ^{40}K background, long periods of very high bioluminiscence or the failure of some number of photomultipliers, but these factors will be known, so their effect can be taken into account when measured *in situ* and should not contribute sizeably to the uncertainty.

The way to include systematic uncertainties is the following. We assume that systematic errors follow a Gaussian distribution and calculate the new probability distribution q as the convolution of the initial Poisson distribution p (see [143] for details) with these Gaussian distributions:

$$q(n)_{s+b} = \frac{1}{2\pi\sigma_b\sigma_\epsilon} \times \int_0^\infty \int_0^\infty p(n)_{b'+\epsilon's} \exp\left(-\frac{(b-b')^2}{2\sigma_b^2}\right) \exp\left(-\frac{(1-\epsilon')^2}{2\sigma_\epsilon^2}\right) db'd\epsilon'$$

(5.6)

where σ_b is the uncertainty in the background estimation level b and σ_ϵ is the uncertainty in the detection efficiency ϵ expressed in relative terms with respect to the nominal efficiency.

5.5.1   Atmospheric models

Figure 5.37 shows the integrated N_{hits} distributions for three different theoretical predictions of the atmospheric neutrino background. The models Bartol [43],

Honda [144] and Fluka [145] are considered. The Bartol and Honda calculations agrees at the level of 10%. However, it has been pointed out that this comes from the compensation of two systematic errors: on the one hand, the Honda model assumes a higher primary spectrum normalization than the one used in the Bartol model. The spectrum used by Honda is based on Webber et al. measurements [146] and is in contradiction with the results of other experiments [147, 148]. On the other hand, the interaction model used by Bartol produces a much higher pion multiplicity. Concerning Fluka, the most relevant feature is that the calculation is tridimensional. Moreover, the interaction model also presents some differences with respect to the previous calculations.
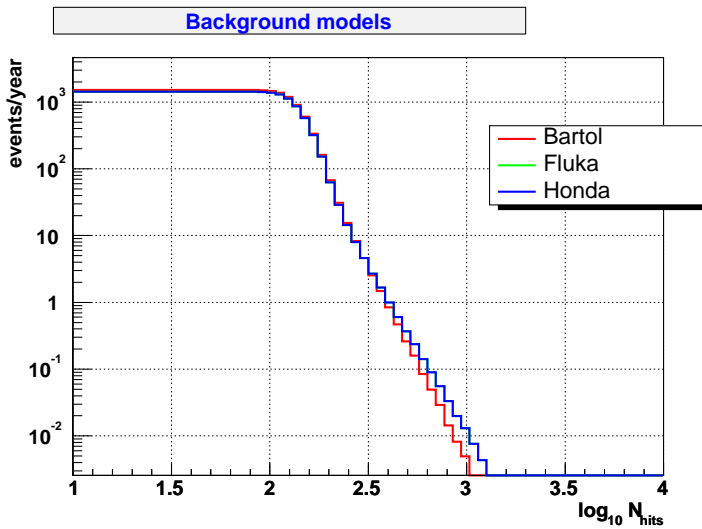

Figure 5.37: The N_{hits} integrated distribution for three conventional atmospheric neutrino models.

Model	MRF (FC)	MRF (St)	Best cut (N_{hits})	Background	Signal
Bartol	1.72	1.40	287	4.6	2.9
Fluka	1.72	1.39	287	4.6	2.9
Honda	1.72	1.39	287	4.6	2.9

Table 5.6: Comparison of the model rejection factor for several atmospheric neutrino background models. The differences in the prediction are too small to have a significant effect at the energies of interest.

The differences between Bartol and Fluka are small (see table 5.6), since they predict very similar spectra, so they are not considered a relevant contribution to the uncertainty. This implies that the best cut in the number of hits does not depend on the model.

5.5.2   Normalization of the atmospheric background

As it has been mentioned previously, the uncertainty in the normalization of the atmospheric neutrino flux has been estimated to be of the order of 25-30%. This is the dominant source of uncertainty at low energies (<1 TeV), which comes basically from the hadronic interaction model and the cosmic primary spectrum uncertainties. Table 5.7 compares the results using different normalizations. The change in the sensitivity is lower than 10% in the expected uncertainty range ($\pm 30\%$). Moreover, new experiments and simulations are being carried out to improve the knowledge of the primary spectrum and the interaction cross-sections, so these uncertainties will be reduced in the future.

Model	MRF (FC)	MRF (St)	Best cut (N_{hits})	Background	Signal
Bartol	1.72	1.40	287	4.6	2.9
Bartol+30%	1.87	1.51	287	5.9	2.9
Bartol-30%	1.52	1.23	260	5.7	3.6
Bartol+50%	1.97	1.59	316	3.9	2.4
Bartol-50%	1.36	1.11	260	4.1	3.6

Table 5.7: Analysis of the effect of the uncertainty in the neutrino flux normalization on the sensitivity.

5.5.3   Prompt neutrinos

The influence of the prompt neutrino component is difficult to evaluate, since there is a wide range of theoretical predictions (see figure 5.38). Moreover, prompt neutrinos are critical in this analysis since they become important at the same energies than the astrophysical sources. Indeed this is the dominant source of uncertainty in the background prediction at the energies of interest. We have considered four models (see [149] for a review):

- **QGSM [150]** (Quark Gluon String Model): a semi-empirical model of charm production based on the non-perturbative QCD calculations, normalized to accelerator data and applied to the prompt neutrino calculation by Volkova [151].

- **RQPM [137]**: (Recombination Quark Parton Model): a phenomenological non-perturbative model, taking into account the intrinsic charm contribution, in which a $c\bar{c}$ is coupled to more than one constituent of the projectile hadron.

- **pQCD [152]** (perturbative QCD) and **TIG [153]** (Thunman-Ingelman-Gondolo): Two predictions which use the perturbative QCD approach to calculate the charm production cross-section, with differences in the quark masses and the factorization and renormalization scale dependence.
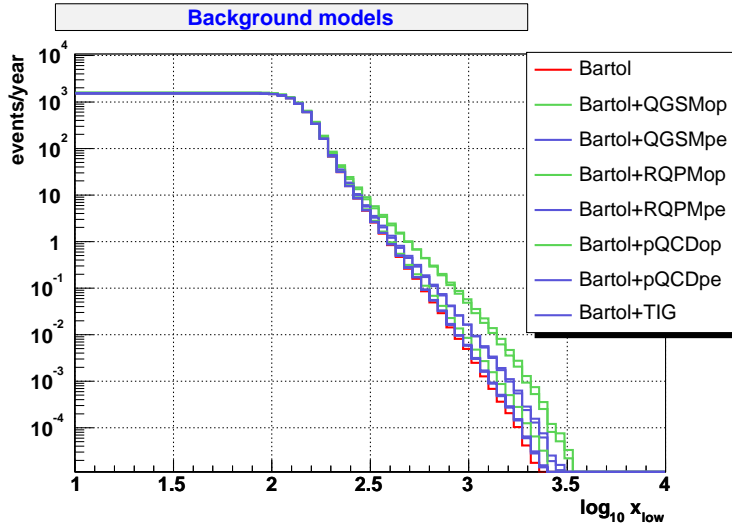
Figure 5.38: Integrated N_{hits} distributions for different prompt neutrino calculations. The subscripts *op* and *pe* stand for "optimistic" or "pessimistic", in the sense that the predicted rate is maximum or minimum, respectively, depending on the used parameters.

Model	MRF (FC)	MRF (St)	Best cut (N_{hits})	Background	Signal
Bartol	1.72	1.40	287	4.6	2.9
Bartol+QGSM op	2.21	1.74	260	14.6	3.6
Bartol+QGSM pe	1.90	1.53	287	6.1	3.6
Bartol+RQPM op	2.12	1.68	260	13	3.6
Bartol+RQPM pe	1.84	1.49	287	5.6	2.9
Bartol+pQCD op	1.76	1.44	287	4.9	2.9
Bartol+pQCD pe	1.73	1.41	287	4.7	2.9

Table 5.8: Comparison of the model rejection factor for several prompt neutrino models. The model used for conventional atmospheric neutrinos is Bartol.

The MRF and the optimum N_{hits} cut values are indicated in table 5.8. If we consider the number of events predicted by the different models of prompt neutrinos above the optimum N_{hits} threshold calculated in the previous section[4], we see that the RMS of these values is 25%, so we will consider this as the uncertainty from the prompt neutrinos.

---

[4]Note that the values indicated in table 5.8 are calculated with the optimum threshold for each case, not with the threshold calculated in the previous section, which is 287 hits.

5.5.4   Water model

We have considered several water models (see section 3.1.3) to estimate the corre-spondig contribution to the systematic errors. Table 5.9 shows the parameters of the different models used in this analysis. We have also studied a model without scattering (*nwater*), as a reference for comparison. The sensitivity calculation results are shown in table 5.10.

Model Name	λ_{scatt} (m)	$< \cos\theta >$	λ_{eff} (m)	Parameters
partic-0.01	40.8	0.77	177.4	$\eta = 0.17$
partic-0.0075	52.0	0.77	226.0	$\eta = 0.17$
n2	22.3	0.90	223.0	$\alpha = 1.0\ g_1 = 0.9\ g_2 = 0$
medsea-0.01	41.5	0.90	415.0	$\alpha = 0.985\ g_1 = 0.92\ g_2 = -0.6$
medsea-0.0075	52.8	0.90	528.0	$\alpha = 0.985\ g_1 = 0.92\ g_2 = -0.6$
nwater	∞	-	-	-

Table 5.9: Water model parameters used in this analysis. The model *nwater*. The parameter η tunes the effect of Rayleigh scattering. The coefficient α gives the relative weight of the two HG phase functions, which are characterized by the average cosine of the scattering angle g.

Model	MRF (FC)	MRF (St)	Best cut (N_{hits})	Background	Signal
partic-0.0075	1.73	1.42	260	4.1	2.8
partic-0.01	1.69	1.38	260	4.5	3.0
medsea-0.0075	1.65	1.34	235	4.7	3.1
medsea-0.01	1.59	1.30	235	4.1	3.0
n2	1.68	1.38	235	4.6	3.0
nwater	1.71	1.40	213	4.0	2.8

Table 5.10: Comparison of the model rejection factor for several water models. The result given with the partic-0.0075 model is not directly comparable with results given in the previous section since the hadronic cascade simulation is not included, due to CPU time limitations.

If we calculate the detection efficiency uncertainty due to the water model as the RMS of the number of events above the partic-0.0075 threshold (260 hits), we obtain a $\sim$25% error. This is quite conservative, since experimental data seem to support the partic-0.0075 model.

5.6   Conclusions on Sensitivity

Once the main sources of uncertainty have been estimated, we can use equation 5.6 to calculate the new value of the sensitivity taking into account systematic errors. We have used the program POLE++ [154] to make such a calculation. As input, we have assumed an uncertainty of 30% in the background prediction (including errors from the normalization and from the prompt neutrinos) and 30% in the detection efficiency[5]. Using the Feldman-Cousins method, the average flux upper limit including systematics is

$$E^2\Phi_{90} < 9.0 \times 10^{-8} \text{ GeVcm}^{-2}\text{s}^{-1}\text{sr}^{-1} \quad \text{(after 1 year)} \tag{5.7}$$

$$E^2\Phi_{90} < 4.3 \times 10^{-8} \text{ GeVcm}^{-2}\text{s}^{-1}\text{sr}^{-1} \quad \text{(after 3 years)} \tag{5.8}$$

This shows that the degradation of the sensitivity due to systematic uncertainties is about 15%.

The calculated sensitivity of ANTARES to a E^{-2} cosmic neutrino diffuse flux is around a 20% better than the previous calculation [133]. Part of this improvement is expected due to the fact that the new geometry of the ANTARES layout has been used, with 12 lines instead of 10 (although the number of photomultipliers is the same). Other updates are the inclusion of the hadronic shower in the MC simulation, the upgrading of the parton distribution functions and, the most important one, the use of a new larger sample of atmospheric muon background. Moreover, there are also some other differences in the approach followed: the Carmona strategy has been used in the track reconstruction and the energy-related variable used in order to reject the atmospheric neutrino background is the number of hits.

In figure 5.39, the sensitivity to $\nu_\mu + \bar{\nu}_\mu$ diffuse fluxes with spectral shape E^{-2} is compared with other experimental limits, as well as with some predicted fluxes. This plot shows that ANTARES will be an important advance in the constraint of the theoretical models. Compared with the last results published by AMANDA [91], it means almost a factor ~ 3 of improvement after one effective year of data taking.

5.7   Model comparison

In the previous sections we have studied the sensitivity of ANTARES to detect astrophysical signals over the atmospheric neutrino background. An alternative approach to look for cosmic neutrino diffuse fluxes can be based on the comparison of the expected x_{low}-estimator distributions assuming different models either for the atmospheric neutrino background and the cosmic neutrino signal. For instance, a clear

---

[5]As we have said, the 25% of uncertainty seems to be quite conservative, since large differences from partic-0.0075 are unlikely. Nevertheless, we prefer to increase this value up to a 30% to take into account other sources of efficiency uncertainty as the MC propagation, the Optical Module sensitivity or the ^{40}K rate.
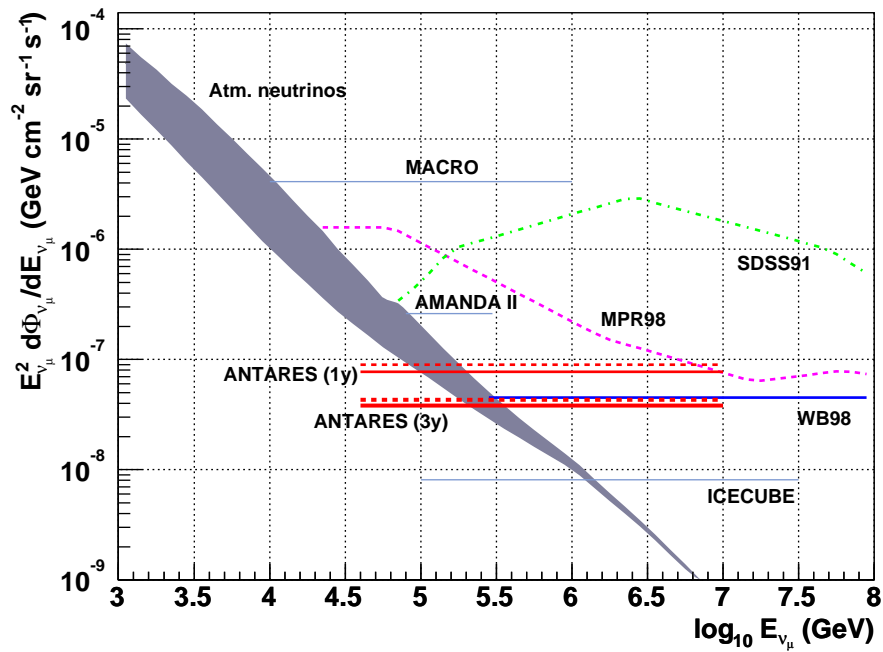
Figure 5.39: Expected sensitivity of ANTARES to $\nu_\mu + \bar{\nu}_\mu$ diffuse E^{-2} fluxes, compared with different theoretical models. The atmospheric neutrino background includes the contribution of prompt neutrinos (QGSM model). Dashed lines indicate the sensitivity including systematic uncertainties. Some other experimental limits are also shown.

excess of high energy events would not be compatible with the expected distribution from the atmospheric neutrino hypothesis so a goodness-of-fit test can be used to prove that the experimental data comes from a different distribution. Two statistical tests have been used to determine the detector capability to distinguish between different theoretical predictions: the Pearson's test and the Kolmogorov-Smirnov test. Concerning the theoretical models, the following possibilities have been considered:

- Conventional atmospheric neutrinos: Bartol and Fluka models.

- Prompt neutrinos: Optimistic and pessimistic prediction of the QGSM model.

- Astrophysical signal: Waxman-Bachcall and Mannheim-Protheroe-Rachen upper limits.

The analysis method is as follows:

1. We assume as initial hypothesis a combination of the predictions mentioned above: conventional neutrinos only, coventional and prompt neutrinos and conventional and cosmic signal neutrinos.

2. Given a hypothetical prediction we generate the distribution of the energy estimator, x_{low}, taking into account statistical fluctuations in the histogram bins.

3. Since Poissonian fluctuations will make the results to change for different runs, we generate 1000 one-year (and three-years) distributions of the x_{low} estimator for the assumed hypothesis.

4. Each simulated experimental distribution is compared with its parent distribution and with the Bartol atmospheric neutrino prediction (which will be used as a reference) by means of a Pearson's test and a Kolmogorov-Smirnov test. If simulated experimental data are drawn from the parent distribution, the test statistic probability distributions must be compatible with a flat distribution. On the contrary, if the assumed hypothesis is quite different from the parent distribution, a large deviation from flatness at low probability values should appear.

5.7.1   Goodness-of-fit tests

Before presenting the results of this analysis we will describe very briefly the main characteristics of the statistical tests used.

Pearson's test

We assume that the observations of our variable can be classified in N different groups (in our case, the bins of the histogram). The number of events n_i in each bin will follow a distribution which is unknown. The Pearson's test compares the number of observed events with the number events h_i predicted by the hypothesis under study:

$$X^2 = \sum_{i=1}^{N} \frac{(n_i - h_i)^2}{h_i} \tag{5.9}$$

If the hypothesis is true, X^2 follows approximately a χ^2 distribution with N-1 degrees of freedom. It is important to note that the highest the number of events in each bin, the best the χ^2 approximation works, which suggests to work with a low number of bins (we use five bins).

Kolmogorov-Smirnov test

The Kolmogorov-Smirnov test is an alternative method applicable to unbinned distributions of a single independent variable. It is based on the comparison of the cumulative functions $S(x)$ and $F(x)$ of the measured and the hypothesis distributions, respectively. If we define $z = \sqrt{n}|D_{max}|$, where D_{max} is the maximum vertical separation between S and F, the probability is given by:

$$P(z) = 2 \sum_{j=1}^{\infty} (-1)^{j-1} \exp(-2j^2 z^2) \tag{5.10}$$

In figure 5.40 we show the distribution of the values of χ^2/ndf obtained for the Pearson's test, together with the χ^2-probability distribution. Figure 5.41 shows the distribution of values of z, the statistic used in the Kolmogorov-Smirnov test (left) and its probability distribution (right).

Figures 5.42-5.47 show some examples of the test probability distributions for different model comparison. A more extensive and detailed comparison between models is reviewed in appendix B.

- **Conventional atmospheric neutrinos**

  In figure 5.42 the conventional neutrino models Fluka and Bartol are compared. Experimental data are generated according to the Fluka model and compared either with Fluka and Bartol predictions. As it is seen, both models are compatible with the measured distributions. Even after three years (see figure 5.43), the results are very similar.

- **Prompt neutrinos**

  Concerning the prompt neutrinos, figure 5.44, shows the results assuming as initial hypothesis the prediction given by Bartol+QGSM models. The comparison is made for the optimistic version of the prompt neutrino model. Only events having $x_{low} > 100$ are included. As expected, the probability distribution corresponding to the parent distribution is flat. However, the probability distribution corresponding to the Bartol distribution shows a peak at low probabilities which means that a significant fraction of the experiments are not compatible with the
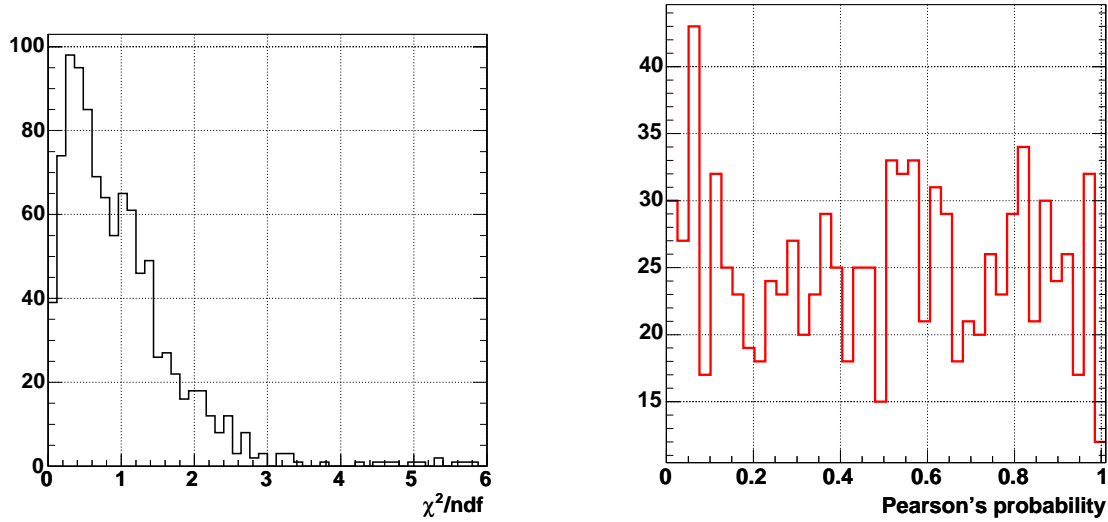
Figure 5.40: Pearson's test. Left: Distribution of χ^2/ndf for 1000 one-year experiments, using the Bartol model. Right: The corresponding probability distribution.
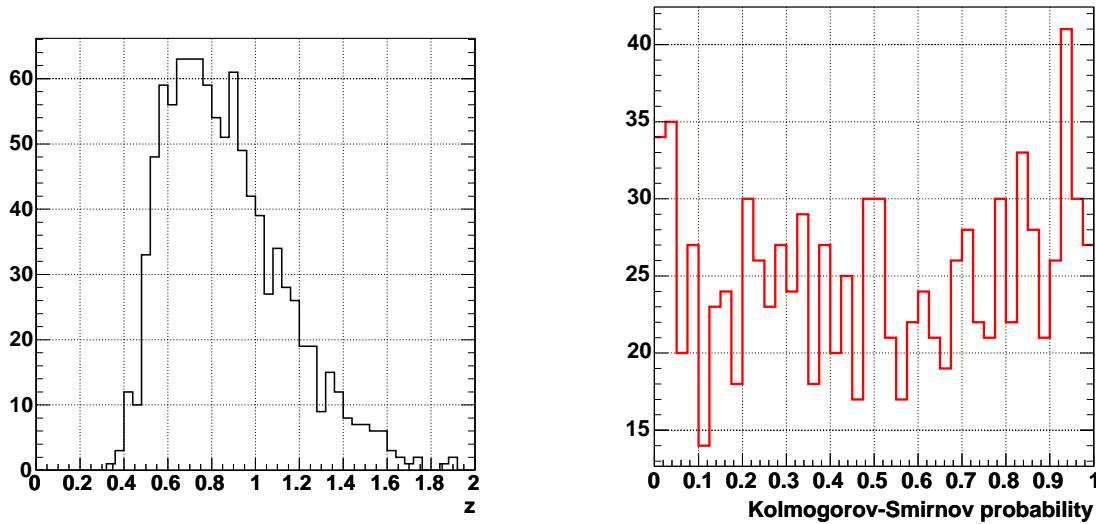

Figure 5.41: Kolmogorov-Smirnov test. Left: Distribution of z for 1000 one-year experiments, using the Bartol model. Right: The corresponding probability distribution.
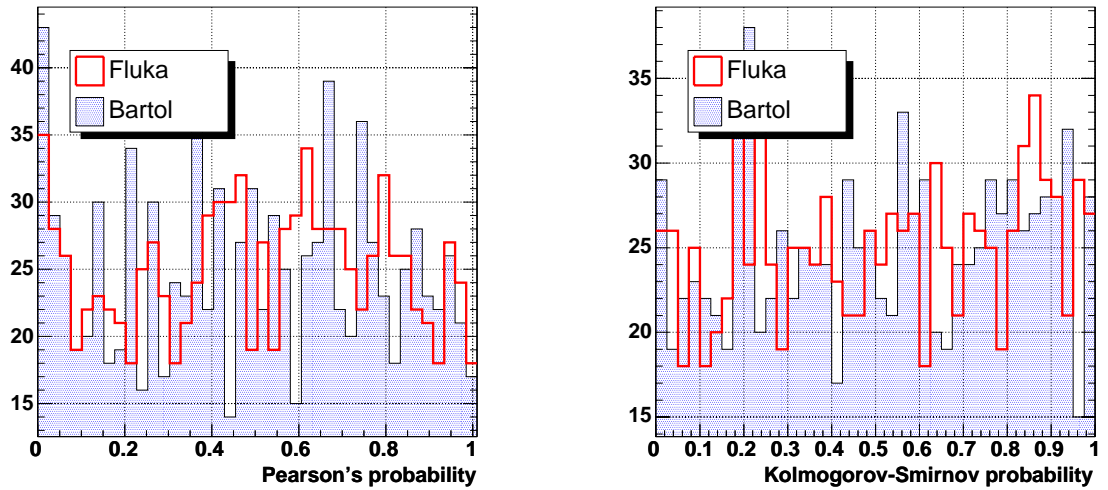
Figure 5.42: Probability distribution of the Pearson's (left) and Kolmogorov-Smirnov (right) tests for 1000 one-year experiments. The data distributions have been generated according to Fluka, and are compared either with Fluka and with Bartol predictions.
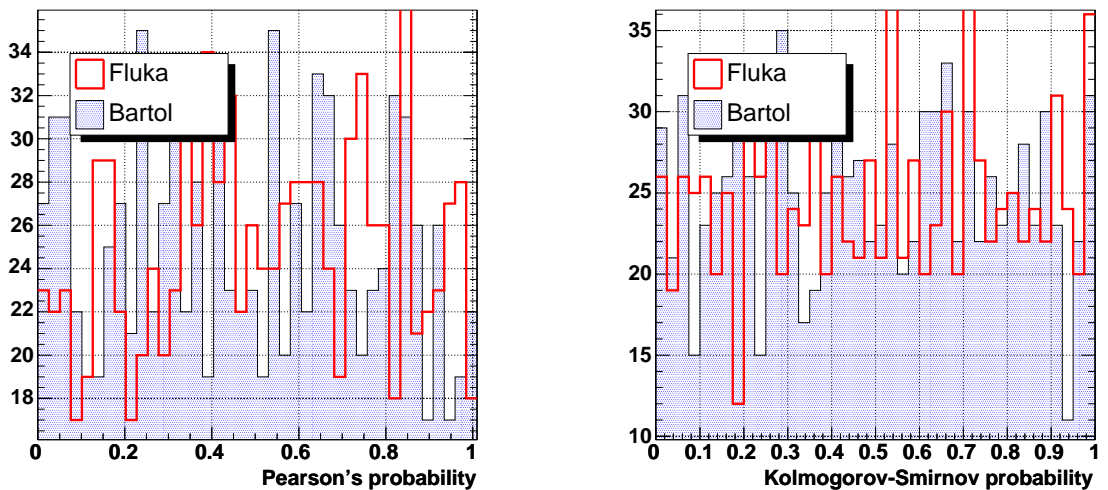
Figure 5.43: Probability distribution of the Pearson's (left) and Kolmogorov-Smirnov (right) tests for 1000 three-year experiments. The data distributions have been generated according to Fluka, and are compared either with Fluka and with Bartol predictions.
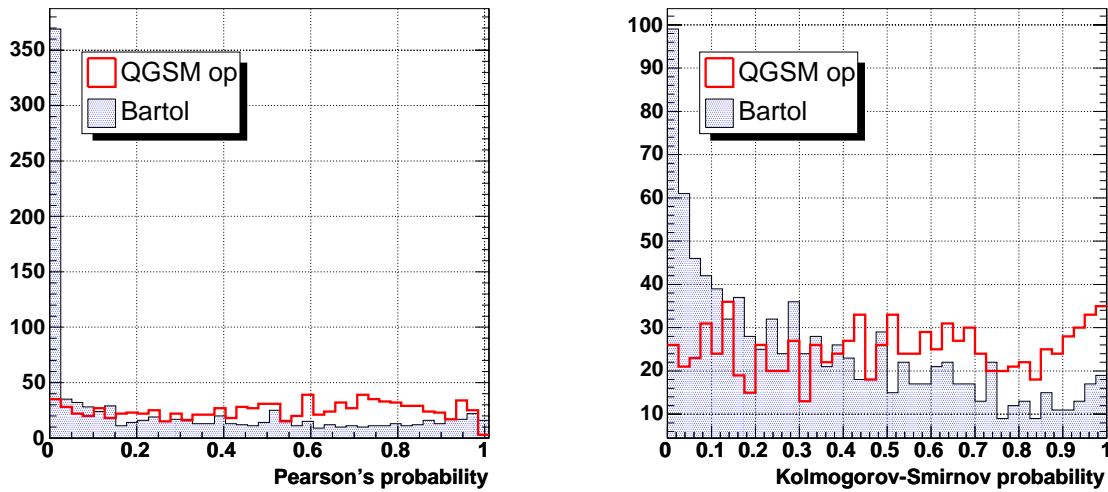
Figure 5.44: Probability distribution of the Pearson's (left) and Kolmogorov-Smirnov (right) tests for 1000 one-year experiments. The distributions have been generated assuming Bartol+QGSM$_{op}$, and are compared with Bartol+QGSM$_{op}$ and with Bartol predictions. Only events with $x_{low} > 100$ are used.

latter prediction. For a set of 1000 three-years experiments, the results improve as shown in figure 5.45.

- **Cosmic neutrinos**

  We can also study the performance of these tests when the presence of a cosmic neutrino signal is included to generate the experimental distributions. Figures 5.46 and 5.47 show the results when a signal in the Waxman-Bahcall limit is used, for one year and three years, respectively. It can be seen that after three years, the hypothesis of only conventional neutrinos begins to be incompatible with the experimental data.

Tables 5.11 and 5.12 show the percentage of experiments giving a probability larger than 0.05 (top) and 0.5 (bottom) when the measured x_{low} distribution is compared with its parent distribution and with the Bartol prediction. The pessimistic version of the QGSM prompt neutrino model as well as different version of the MPR upper limit are included. As a general conclusion, it can be said that this kind of tests begin to be conclusive after at least three years of data taking. Models predicting small signal or few prompt neutrinos are difficult to discriminate from the hypothesis of only conventional atmospheric neutrinos, but if the signal or prompt neutrino rates are larger, some evidence would be expected.

P>0.05				
	Pearson		**Kolmogorov-Smirnov**	
	Parent (%)	Bartol (%)	Parent (%)	Bartol (%)
Bartol	94	94	95	95
Fluka	94	91	96	96
QGSM$_{op}$	93	60	95	84
QGSM$_{pe}$	94	82	95	94
WB	93	48	95	95
MPR	95	0	95	0
0.1·MPR	95	51	95	87

P>0.50				
	Pearson		**Kolmogorov-Smirnov**	
	Parent (%)	Bartol (%)	Parent (%)	Bartol (%)
Bartol	51	51	50	50
Fluka	51	49	54	51
QGSM$_{op}$	52	28	51	30
QGSM$_{pe}$	52	49	50	47
WB	49	27	48	45
MPR	48	0	90	0
0.1·MPR	50	24	50	36

Table 5.11: Percentage of one-year experiments giving a probability larger than 0.05 (top) and 0.50 (bottom) in a Kolmogorov-Smirnov and Pearson's test when the measured $\log_{10} X_{low}$ distribution is compared with its parent distribution and with the Bartol prediction.

P>0.05				
	Pearson		**Kolmogorov-Smirnov**	
	Parent (%)	Bartol (%)	Parent (%)	Bartol (%)
Bartol	95	95	95	95
Fluka	94	90	96	95
QGSM$_{op}$	92	32	93	58
QGSM$_{pe}$	93	85	95	90
WB	95	30	94	90
MPR	94	0	95	0
0.1·MPR	95	29	94	71

P>0.50				
	Pearson		**Kolmogorov-Smirnov**	
	Parent (%)	Bartol (%)	Parent (%)	Bartol (%)
Bartol	50	50	51	51
Fluka	51	45	51	48
QGSM$_{op}$	49	6	50	11
QGSM$_{pe}$	54	32	50	42
WB	50	6	51	42
MPR	48	0	51	0
0.1·MPR	48	4	48	19

Table 5.12: Percentage of three-year experiments giving a probability larger than 0.05 (top) and 0.50 (bottom) in a Kolmogorov-Smirnov and Pearson's test when the measured $\log_{10} X_{low}$ distribution is compared with its parent distribution and with the Bartol prediction.
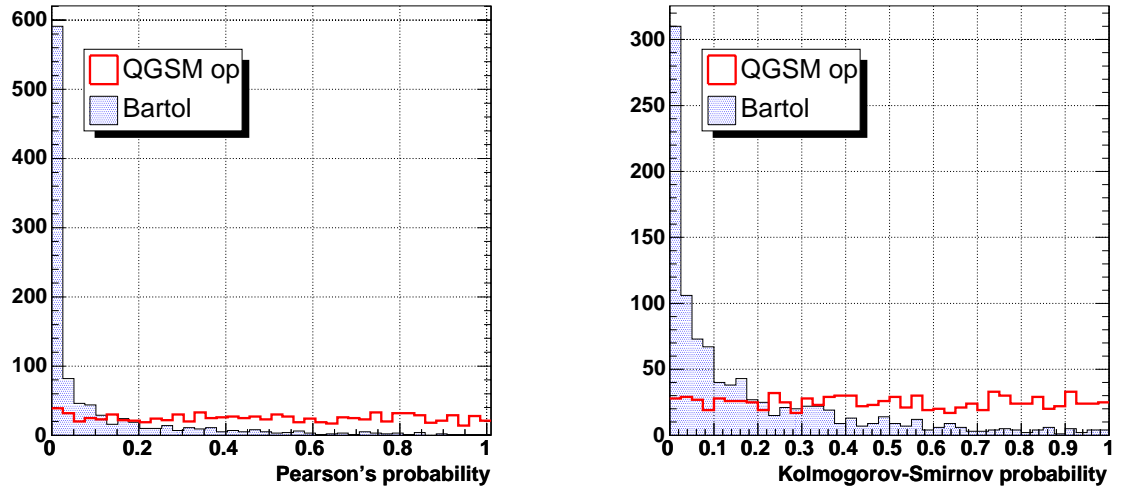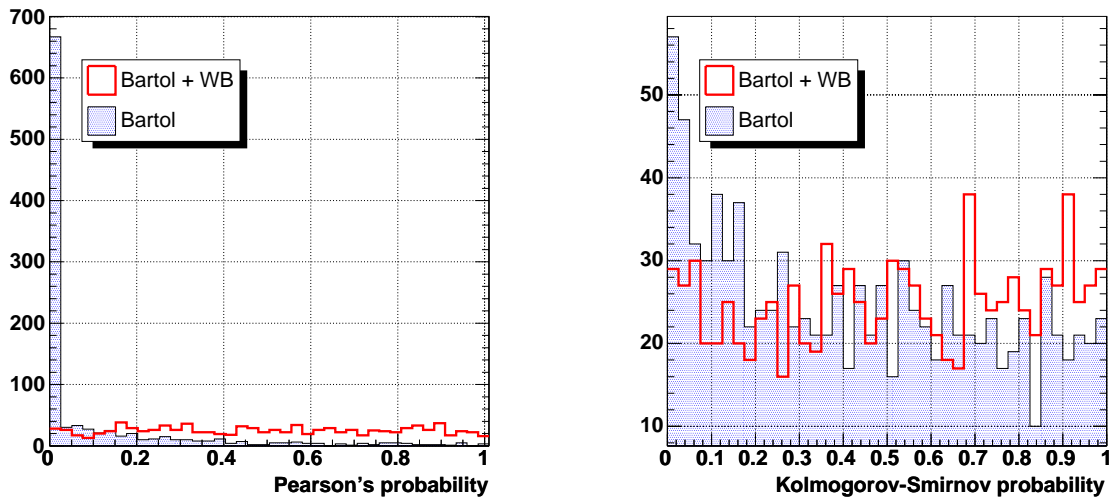
Figure 5.45: Probability distribution of the Pearson's (left) and Kolmogorov-Smirnov (right) tests for 1000 three-year experiments. The data distributions have been generated assuming Bartol+QGSM$_{op}$, and are compared with Bartol+QGSM$_{op}$ and with Bartol predictions. Only events with $x_{low} > 100$ are used.
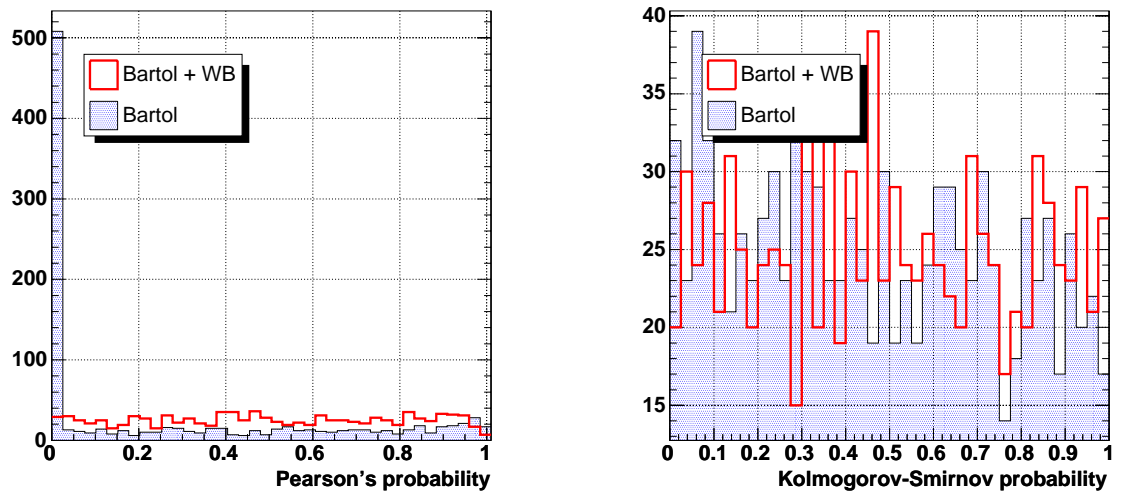
Figure 5.46: Probability distribution of the Pearson's (left) and Kolmogorov-Smirnov (right) tests for 1000 one-year experiments. The data distributions have been generated assuming Bartol+WB, and are compared with Bartol+WB and with Bartol predictions.

Figure 5.47: Probability distribution of the Pearson's (left) and Kolmogorov-Smirnov (right) tests for 1000 three-year experiments. The data distributions have been generated assuming Bartol+WB, and are compared with Bartol+WB and with Bartol prediction.

Chapter 6

Energy spectrum deconvolution

The reconstruction of energy spectra is a major point in the analysis of neutrino telescopes. In principle, spectra can be obtained using the reconstructed energy of each event. However, this approach is not the most efficient in our case. On the one hand, the atmospheric neutrino spectrum follows a power law, with a fast decrease in the number of events with the energy. On the other hand, the dispersion in the energy deposited in the detector is large, due to the stochastic nature of the processes involved in the muon energy loss. The combination of both factors can be seen in Figure 6.1. The number of events in the right side of the spectrum is overestimated. This is particularly dangerous if we want to detect the presence of an astrophysical signal or the prompt neutrino contribution, but it also produces poor results when the atmospheric spectrum is reconstructed.

The right approach to obtain the spectrum should be based on the unfolding (also called deconvoluting) techniques. This means to make a transformation of the measured distribution (which can be the reconstructed energy or other energy-related parameter) into the true spectrum. In order to do this, the matrix relating both distributions has to be calculated. A general introduction to the problem of the spectrum deconvolution is explained in section 6.1 [155]. In section 6.2 we describe in detail the two methods we have used in this analysis: the Single Value Decomposition algorithm [156] and the iterative method based on the Bayes' theorem [157]. The performance of both methods are presented in sections 6.3 and 6.4, respectively. In section 6.5 these methods are compared. We obtain the atmospheric neutrino flux in section 6.6. Finally, the atmospheric down-going muon spectrum is reconstructed is section 6.7.

6.1   Spectrum deconvolution

The deconvolution of spectra is a very common issue in physics. The problem can be described as follows. We are going to measure a physical variable y which follows a probability density function $f_{true}(y)$. However y is not always directly measurable. Instead of that, a measured quantity b, following a different pdf $f_{meas}(b)$, is obtained in each observation. The relationship between the corresponding probability density
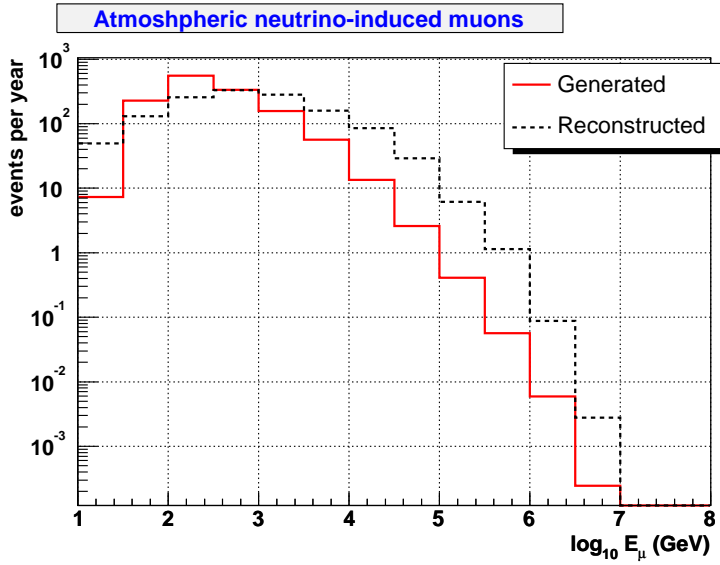
Figure 6.1: Comparison between the true energy spectrum of the neutrino-induced muons (according to the Bartol model) and the spectrum obtained using the reconstructed energy of each event individually. The effect of a large dispersion in a steepen power-law spectra limits severely the quality of the result.

functions is given by the so-called Fredholm integral equation of first kind:

$$f_{meas}(b) = \int R(b|y) f_{true}(y) dy \tag{6.1}$$

where $R(b|y)$ is the response function[1]. In practice, we are going to histogram the variables, so previous equation can be rewritten, using matrix notation, as follows:

$$\hat{A}\mathbf{y} = \mathbf{b} \tag{6.2}$$

where $\mathbf{b}$ ($\mathbf{y}$) is a vector of dimension n_b (n_y) which contains the measured (true) distribution and the $n_b \times n_y$ matrix $\hat{A}$ is the probability matrix, generated by Monte Carlo, where each term $\hat{A}_{ij}$ means the probability to observe an event in bin i when the true value is bin j. In this study, since there is no data available, we have also to simulate the measured distributions.

This response matrix has to take into account three factors:

- **Limited acceptance:** Not all the events are going to produce a detectable signal, so the probability to observe an event can be lower than 1.

- **Transformation:** The measured quantity $\mathbf{b}$ is not the true quantity whose spectrum we want to reconstruct but a related one. Of course, in order to get the

---

[1]Also called kernel.

optimum results, we should use a quantity highly correlated with the true quantity. An example would be to use the number of hits as measured quantity to determine the true energy spectrum.

- **Finite resolution:** The measured quantity **b** is smeared out due to the finite resolution of the detector. In experiments with good resolution, the effect of migrations to adjacent bins is small and the reconstruction can be easily done by a bin-by-bin correction. Unfortunately, this is not our case. As mentioned before, there is a large dispersion in the signal produced by equal energy events due to the large fluctuations in the muon energy loss.

Once the probability matrix $\hat{A}$ and the measured distribution **b** are established, the standard method to solve the system 6.2 would be inverting the response matrix:

$$\mathbf{y} = \hat{A}^{-1}\mathbf{b} \tag{6.3}$$

Although strictly speaking, this method provides the exact solution, it is completely useless because the unavoidable statistical fluctuations in the measured distribution **b** lead to large oscillations in the unfolded result **y**. In fact, the unfolding problem is a typical example of ill-posed problems where small changes in the data yield large changes in the result[2].

In principle, there are no physical reasons supporting the idea of a wildly oscillating solution so, one way to avoid the instability of the matrix inversion method is to impose some *a priori* condition based on the degree of smoothness of the true solution. This procedure is known as Tikhonov regularization and can be expressed transforming the linear system 6.2 into the minimization problem:

$$||\hat{A}\mathbf{y} - \mathbf{b}||^2 + \tau||C\mathbf{y}||^2 = min \tag{6.4}$$

The basic idea consists in the addition of a regularization term (C matrix), representing the smoothness of the true distribution, which will damp the spurious oscillating components coming from data errors. The regularization parameter τ controls the relative importance of the regularization term. For $\tau = 0$ the exact spiky solution is obtained. Intermediate τ values give smoother solutions approaching observed data,

---

[2]This can be seen in a simple example [158], the case of two bins, with a matrix response like:

$$A = \begin{pmatrix} 1 - \epsilon & \epsilon \\ \epsilon & 1 - \epsilon \end{pmatrix}$$

The corresponding inverse matrix has the form

$$A^{-1} = \frac{1}{1 - 2\epsilon} \begin{pmatrix} 1 - \epsilon & -\epsilon \\ -\epsilon & 1 - \epsilon \end{pmatrix}$$

If the measured vector is (10, 10) and the resolution ϵ is 0.4, the unfolded distribution would be (10, 10), but unfolding (11, 9) gives (15, 5), from (12, 8) one obtains (20, 0) and (13, 7) gives (25, -5). This simple example illustrates the bad performance of the inverse matrix when the migrations from bin to bin are important.

and huge τ values leads to a perfect smooth solution. Therefore, the problem has been translated to the proper choice of the regularization parameter τ.

A different unfolding approach is taken in the iterative method proposed in [157]. Starting from an initial guess for the true distribution, the Bayes' theorem is used to update the estimation at each iteration. The procedure is iterated until some convergence criterion is achieved. In principle, good results are obtained in a few iterations. However, if the number of iterations increases continuously, large variances in the estimation can arise and the oscillating solution from matrix inversion is obtained. This effect can be reduced if the result is smoothed before entering a new iteration. Otherwise, the number of iterations should be controlled with Monte Carlo.

6.2   Unfolded methods used in this analysis

In order to study the performance of the ANTARES detector for energy spectrum deconvolution, two unfolding methods have been used. The first one is a regularization method based on the Singular Value Decomposition of the matrix response [156]. The second one is the iterative method based on the Bayes' theorem [157]. They are explained in more detail in this section.

6.2.1   Single Value Decomposition

This unfolding procedure, proposed by Höcker and Kartvelishvili [156], is based on the Single Value Decomposition of the response matrix $\hat{A}$:

$$\hat{A} = USV^T \tag{6.5}$$

where U is an $m \times m$ orthogonal matrix, V is a $n \times n$ orthogonal matrix and S is an $m \times n$ diagonal matrix with non-negative diagonal elements. The diagonal elements of S are called the singular values, s_i, of the SVD decomposition of $\hat{A}$. This approach makes easier to identify large oscillating terms of the vector solution $\mathbf{y}$ since it can be expressed as a linear combination of the V matrix columns, $\mathbf{v_i}$:

$$\mathbf{y} = \sum_i \frac{\mathbf{u_i^T b}}{s_i} \mathbf{v_i} \tag{6.6}$$

Small s_i values give rise to high and meaningless fluctuations. These oscillating components should be removed by adding a regularization term to the system to be minimized but, before doing so, it is convenient to rescale the equations and normalize the unknowns. Equation 6.2 can be regarded as a least square problem:

$$(\hat{A}\mathbf{y} - \mathbf{b})^T B^{-1} (\hat{A}\mathbf{y} - \mathbf{b}) = min \tag{6.7}$$

being B the covariance matrix of the measured vector $\mathbf{b}$. One way to smooth the vector solution is defining a new unknown vector:

$$w_j = y_j/y_j^{ini} \tag{6.8}$$

where y_j^{ini} is the initial Monte Carlo estimation used to compute the probability matrix $\hat{A}_{ij}$. A new equivalent linear system is then proposed:

$$\sum_{j=1}^{n_y} A_{ij} w_j = b_i \tag{6.9}$$

where now, A_{ij} is the actual number of events generated in bin j and ended up in bin i. Finally, after rotating the covariance matrix B:

$$B = QRQ^T \tag{6.10}$$

the system 6.7 becomes straightforward:

$$(\tilde{A}\mathbf{w} - \tilde{\mathbf{b}})^T (\tilde{A}\mathbf{w} - \tilde{\mathbf{b}}) = min \tag{6.11}$$

where

$$\tilde{A}_{ij} = \frac{1}{r_i} \sum_m Q_{im} A_{mj}, \quad \tilde{b}_i = \frac{1}{r_i} \sum_m Q_{im} b_m. \tag{6.12}$$

Covariance matrix is now proportional to the identity matrix and all the equations have the same statistical significance. On the other hand, the new unknown vector $\mathbf{w}$ has lower bin-to-bin variations so less terms in the orthogonal decomposition are needed. However, the large fluctuations of the exact solution are still there. Some kind of regularization term has to be added in order to obtain the unfolded solution. Using as *a priori* condition the minimum curvature (sum of the squares of the second derivatives) the system to solve reads:

$$(\tilde{A}\mathbf{w} - \tilde{\mathbf{b}})^T (\tilde{A}\mathbf{w} - \tilde{\mathbf{b}}) + \tau (C\mathbf{w})^T C\mathbf{w} = min \tag{6.13}$$

where the matrix C represents the total curvature of the solution. Since C is a singular matrix, a small diagonal component, ξ, has been added to make inversion possible:

$$\begin{pmatrix} -1+\xi & 1 & 0 & 0 & \dots & \\ 1 & -2+\xi & 1 & 0 & \dots & \\ 0 & 1 & -2+\xi & 1 & \dots & \\ & \dots & & & \dots & \\ & \dots & & 1 & -2+\xi & 1 \\ & \dots & & & 1 & -1+\xi \end{pmatrix} \tag{6.14}$$

Introducing the following definitions:

$$A' = \tilde{A}C^{-1}, \qquad \mathbf{w}' = C\mathbf{w} \tag{6.15}$$

the system 6.13 becomes:

$$(A'\mathbf{w}' - \tilde{\mathbf{b}})^T (A'\mathbf{w}' - \tilde{\mathbf{b}}) + \tau (\mathbf{w}')^T \mathbf{w}' = min \tag{6.16}$$

and inserting the SVD for the matrix $A' = USV^T$, it can be shown that the solution is given by:

$$\mathbf{w}' = \sum_{i=1}^{n_y} f_i \frac{d_i}{s_i} \mathbf{v_i} \tag{6.17}$$

where the vector $\mathbf{d}$ is defined as:

$$\mathbf{d} \equiv U^T \tilde{\mathbf{b}} \tag{6.18}$$

and the factors f_i, called Tikhonov filter factors, regularize the components with low s_i values analogously to a cutoff for a low-pass filter:

$$f_i = \frac{s_i^2}{s_i^2 + \tau} \simeq \begin{cases} 1 & \text{if } s_i \gg \tau \\ s_i^2/\tau & \text{if } s_i \ll \tau \end{cases} \tag{6.19}$$

The true unfolded distribution $\mathbf{y}$ can be recovered from 6.8 and 6.15, multiplying by the initial Monte Carlo distribution y_{ini}:

$$y_j = y_j^{ini} w_j = y_j^{ini} \sum_i C_{ji}^{-1} w_i' \tag{6.20}$$

We are now ready to calculate the solution for any given value of the regularization parameter τ. The following question is how to choose the optimum value of τ. There are several possibilities, which we will describe in this section and whose results will be compared latter.

The choice suggested by Höcker and Kartvelishvili [156] is based on the values of the components of the vector $\mathbf{d}$. According to equation 6.18, d_i can be interpreted as the ith component of the decomposition of the measured and rescaled histogram $\tilde{\mathbf{b}}$ in the new orthogonal basis defined by the columns of the matrix U. Furthermore, it gives the significance of the ith component in the decomposition. For small i, $|d_i|$ values are expected to be much larger than zero since they correspond to the statistically significant components. After a critical point k, d_i values follow a Gaussian distribution with variance equal to one and mean close to zero meaning that contributions of quickly oscillating basis vectors are compatible with zero. Therefore, the recommended value of τ should be put equal to the square of the kth singular value s_k:

$$\tau = s_k^2 \tag{6.21}$$

A different approach suggested also in [156] is based on a Monte Carlo initial distribution close to the true expected one. The best choice of τ is the one yielding the smallest χ^2 between the true and the unfolded distributions. However, we do not know the true spectrum, so this approach depends on the initial Monte Carlo distribution.

Finally, another way to choose the best value of τ is by means of the so-called L-curve [159]. The regularized solution of the system 6.13 can be written as:

$$\mathbf{w}_{reg} = \text{argmin}\{||\tilde{\mathbf{A}}\mathbf{w} - \tilde{\mathbf{b}}||^2 + \tau||\mathbf{C}\mathbf{w}||^2\} \tag{6.22}$$

The L-curve is defined as the log-log plot of the norm of the regularized solution $||C\mathbf{w}||$ versus the norm of the corresponding residual $||\tilde{A}\mathbf{w} - \tilde{\mathbf{b}}||$ (Figure 6.2 shows a typical example of L-curve). If too much regularization is imposed on the solution, the residual $||\tilde{A}\mathbf{w} - \tilde{\mathbf{b}}||$ will be too large. On the other hand, if too little regularization is imposed, the solution will be dominated by oscillating contributions and therefore, $||C\mathbf{w}||$ will be too large. Figure 6.2 shows a typical example of L-curve illustrating this feature. Each point in this curve has been calculated using a different value of τ. The value which offers a best trade-off between both contributions corresponds to the vertex of the curve. Therefore, the L-curve criterion for choosing the regularization parameter is based on looking for the τ giving the maximum curvature.
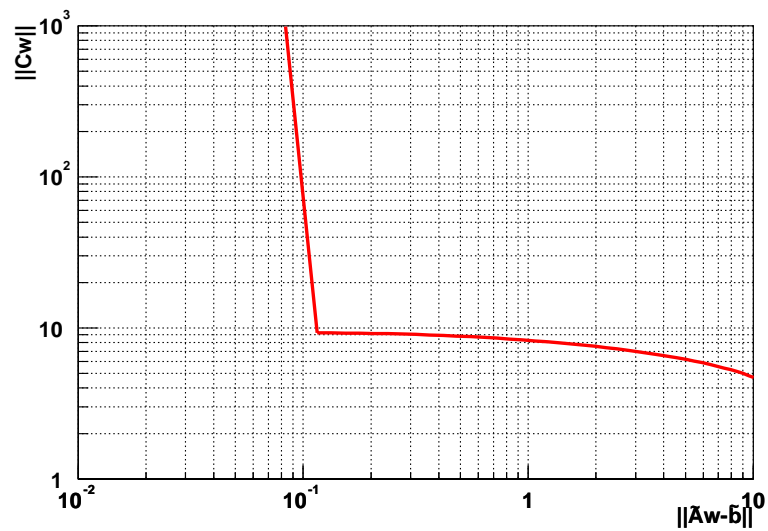
Figure 6.2: Typical L-curve. Each point has been calculated with a different τ. The optimum value is the one in the vertex of this curve.

The solution and residual norms can be expressed in terms of the SVD as:

$$\eta = ||C\mathbf{w}||^2 = \sum_{i=1}^{n_y} \left(f_i \frac{u_i^T \tilde{\mathbf{b}}}{s_i} \right)^2 \tag{6.23}$$

$$\rho = ||\tilde{A}\mathbf{w} - \tilde{\mathbf{b}}||^2 = \sum_{i=1}^{n_b} ((1 - f_i) u_i^T \tilde{\mathbf{b}})^2 \tag{6.24}$$

and the curvature can be expressed as:

$$\kappa = 2 \frac{\eta \rho}{\eta'} \frac{\tau \eta' \rho + 2\tau^{1/2} \eta \rho + \tau^2 \eta \eta'}{(\tau \eta^2 + \rho^2)^{3/2}} \tag{6.25}$$

6.2.2   Iterative method based on Bayes' theorem

The second method analyzed to unfold the experiment distribution uses the Bayes' theorem, which can be stated as follows. Let's be a set of several independent causes, which in our case will be the bin energies (E_i, $i = 1, 2, \ldots, n_E$). These energies can produce measurable effects or energy estimators (X_j, $j = 1, 2, \ldots, n_X$). If we know the *a priori* probability of the energies $P_o(E_i)$ and the conditional probability $P(X_j|E_i)$ of the energy E_i to produce the effect X_j, according to the Bayes' theorem, the probability $P(E_i|X_j)$ of the true energy to be E_i if the effect X_j has been measured is given by:

$$P(E_i|X_j) = \frac{P(X_j|E_i)P_o(E_i)}{\sum_{l=1}^{n_E} P(X_j|E_l)P_o(E_l)}. \tag{6.26}$$

So the probability $P(E_i|X_j)$ depends basically on:

- **The response matrix** $P(X_j|E_i)$: this probability has to be calculated by Monte Carlo simulation and takes into account the bin-to-bin migration.

- **The initial guess** $P_o(E_i)$: The need of an initial distribution can give the impression that the equation 6.26 is useless but this can be overcome by an iterative method. In principle, the final result should not be sensitive to this initial guess.

If $\mathbf{n}(X) \equiv \{n(X_1), n(X_2), \ldots, n(X_{n_X})\}$ gives the distribution of the measured estimator (effects), the energy distribution (causes) can be written as:

$$\hat{n}(E_i) = \frac{1}{\epsilon} \sum_{j=1}^{n_X} n(X_j) P(E_i|X_j) \tag{6.27}$$

where ϵ is the efficiency taking into account the possibility that a cause does not always produce an effect in the range we are considering. This expected number of events with energy E_i can be used to calculate a new $P(E_i)$ distribution:

$$\hat{P}(E_i) = \frac{\hat{n}(E_i)}{\sum_{i=1}^{n_E} \hat{n}(E_i)} \tag{6.28}$$

The obtained distribution is somewhere between the initial guess, $P_o(E_i)$, and the true distribution. This brings out the idea of an iterative process which should be independent on the initial guess and that, after each iteration, should provide a closer distribution to the true one. The procedure must contemplate the following steps:

1. Choose the initial distribution $P_o(E_i)$. For instance, the theoretical predictions of the atmospheric neutrino flux.

2. Calculate $\hat{n}(E_i)$ and $\hat{P}(E_i)$ according to 6.27 and 6.28.

3. Compare $\hat{n}(E_i)$ with the previous result (χ^2 test, for instance).

4. Replace $P_0(E_i)$ by $\hat{P}(E_i)$ and $n_0(E)$ by $\hat{n}(E_i)$

5. Go to step 2 until convergence is attained in step 3.

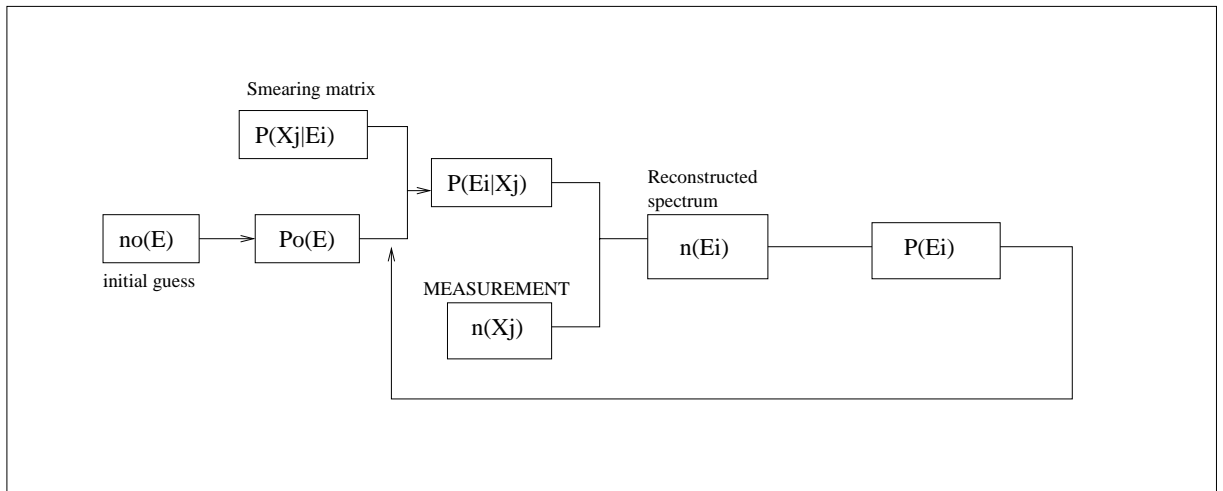In Figure 6.3 a scheme of this process is shown.

Figure 6.3: Scheme of the iterative algorithm based on the Bayes' theorem. The initial ingredients are the response matrix (generated by Monte Carlo) and a prior guess of the true spectrum. This prior guess is normalized to obtain the probability density function, which combined with the response matrix allows to calculate the probability of being E_i if X_j. When the observation is made (which in this analysis is also simulated by MC) the spectrum can be reconstructed. This spectrum can be compared with the previous result to decide if convergence has been attained. If not, the process continues, using the new spectrum as input guess.

As already mentioned, after several iterations the obtained distribution is quite similar to the true one, but if iteration continues, the convergence is toward the wildly oscillating distribution of matrix inversion. In order to avoid this undesirable solution, a smoothing of the results after each step of the iterative process should be performed. The assumption underling this hypothesis is that wild oscillations do not appear in most of the physical distributions. Note that this is also the hypothesis, quite reasonable, made supporting the regularized unfolding.

6.3 Performance of SVD method

In this section, we evaluate the performance of the SVD method in the energy spectrum reconstruction of the detected up-going muons. The true distribution is defined by the logarithm of the true energy of the muon when it enters the can, $\mathbf{y} = \log_{10} E_{\mu\,\text{gen}}$. As energy related variable, the logarithm of the low energy estimator is

used to define the measured distribution: $\mathbf{b} = \log_{10} X_{low}$. This estimator offers the best trade-off between linearity and low spread in the region of interest (see chapter 5). The detector behaviour is taken into account by a number-of-event matrix A_{ij}, obtained by Monte Carlo simulation. This matrix is shown in figure 6.4 together with the probability response matrix $\hat{A}_{ij}$.

The measured distribution ($\mathbf{b}$) is computed with a different Monte Carlo sample. Starting from a "true" muon energy distribution, $\mathbf{y}^{true} = \log_{10} E^{true}_{\mu \, gen}$, the events are simulated through the detector and the corresponding $\log_{10} X_{low}$ distribution is obtained. Statistical fluctuations are taken into account by a Poissonian smearing of the content of each bin. In figure 6.5 the $\log_{10} X_{low}$ distribution is shown for one year of data taking.

In order to test the algorithm, we try to unfold the same simulated data distribution (generated with the Bartol model) with three different response matrices, each of them generated with a different muon energy distribution (see figure 6.6). In the first case ($fun0$), we also use the Bartol model to generate the response matrix. This is to test that the algorithm can overcome the Poissonian fluctuations in the real sample. However, it is also necessary to check that even if we do not know exactly the true distribution, we can reconstruct it. So in order to verify the robustness of the results, we use two other distributions to generate the response matrix. The first test distribution, $fun1$ (red dashed line in figure 6.6) exhibits an important deficit at high energies and some excess at lower energies. For the second test function, $fun2$ (blue dotted line in figure 6.6), we have moved the maximum of the distribution and we have set an excess at high energies.

Using the simulated distribution shown in figure 6.5 as data, we unfold the spectra with the SVD method. The vectors of singular values are shown in figure 6.7. It is seen that singular values fall gradually to zero.

As explained in section 6.3, an estimation of the regularization parameter τ can be obtained by looking at the components of the vector $\mathbf{d}$, which are shown in figure 6.8. In the case of $fun0$, the distribution is dominated by the first component. This is because we have used the same assumption to create the response matrix and the measured distribution. On the other hand, for $fun1$ and $fun2$ we see a first region of exponential fall in the values of $|d_i|$ followed by a flat behaviour. As a first approach, we use $\tau = s_k^2$, where s_k is the singular value of the last significant equation. This criterion can be checked using a χ^2 test. Figure 6.9, shows the χ^2 values obtained when comparing the true and the unfolded distributions for different values of τ ($fun0$). From this plot, it is seen that the best τ corresponds to $i = 2$, in agreement with the estimation from the $|d_i|$ plot.

The χ^2 criterion can be used to set bounds for a more precise determination of the τ value using the curvature of the L-curve. As an example, figure 6.10 shows the L-curve corresponding to $fun0$. According to the L-curve criteria, the optimal τ is 3.4×10^5. Finally, we use this value to reconstruct the spectrum, which is shown in figure 6.11. The differences between the true and the unfolded distributions are shown in the same figure. The agreement between the true and the unfolded spectrum is very good. It
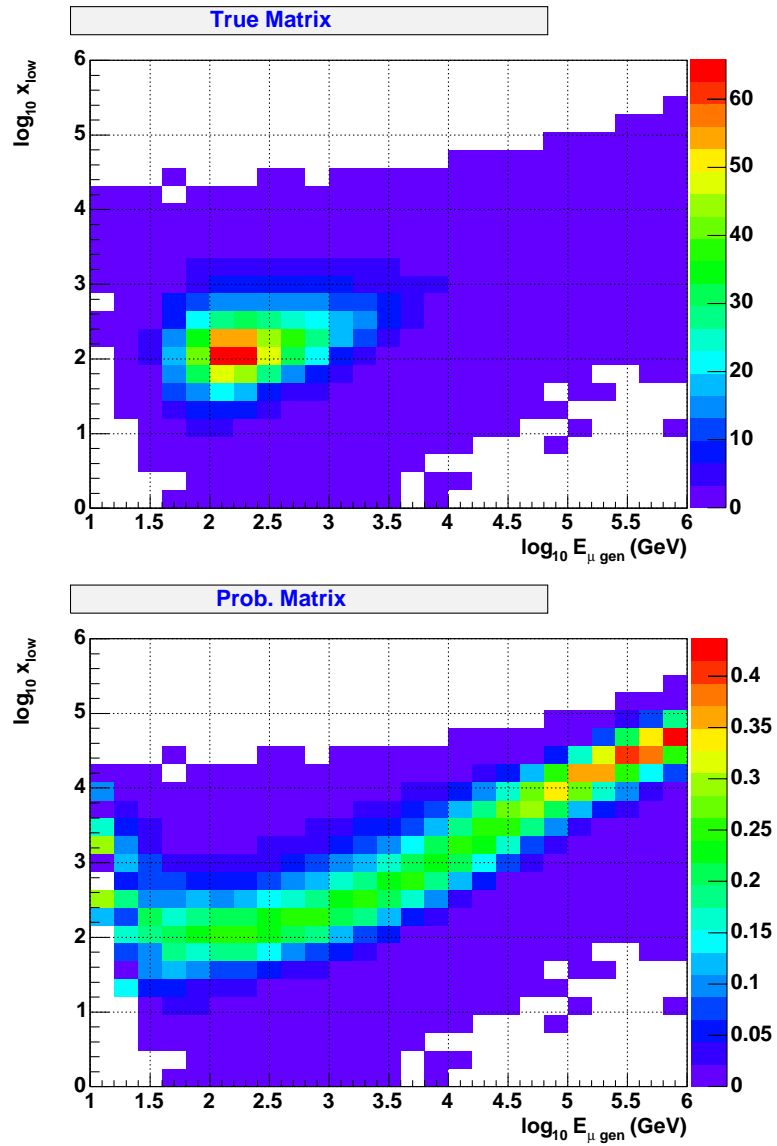
Figure 6.4: Top: Monte Carlo simulated number-of-event matrix A_{ij}, generated assuming the Bartol distribution. Bottom: The response matrix $\hat{A}_{ij}$, obtained after normalizing each $\log_{10} E_{\mu\,\text{gen}}$ slice of A_{ij}.
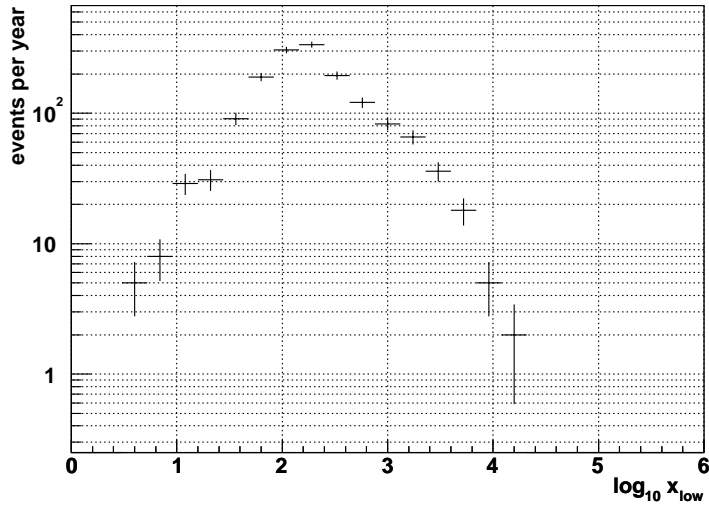
Figure 6.5: Distribution of the low energy estimator X_{low} for one year of data taking. The content of each bin is obtained after a Poissonian randomization of the expected rate in that bin, calculated assuming the Bartol model.
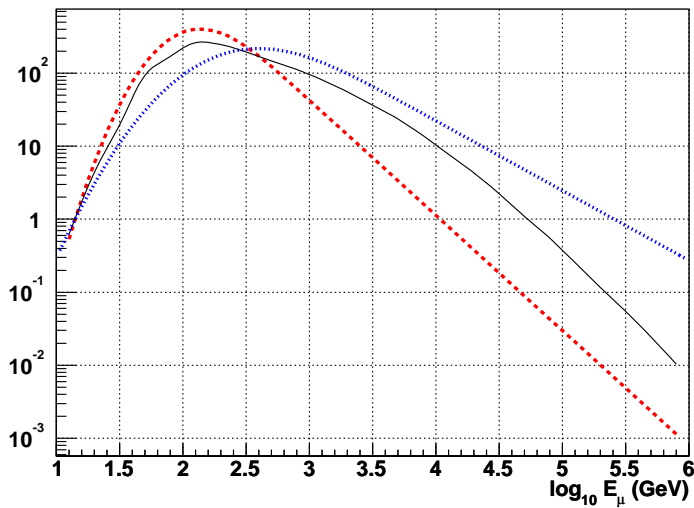

Figure 6.6: The three distributions (events/year) used to generate three different response matrices. The black solid line corresponds to the Bartol model ($fun0$), which is also used to generate the observed spectrum. Red dashed and blue dotted lines correspond to $fun1$ and $fun2$, two modifications used to check that the algorithm is not too sensitive to the hypothesis made to build the response matrix.
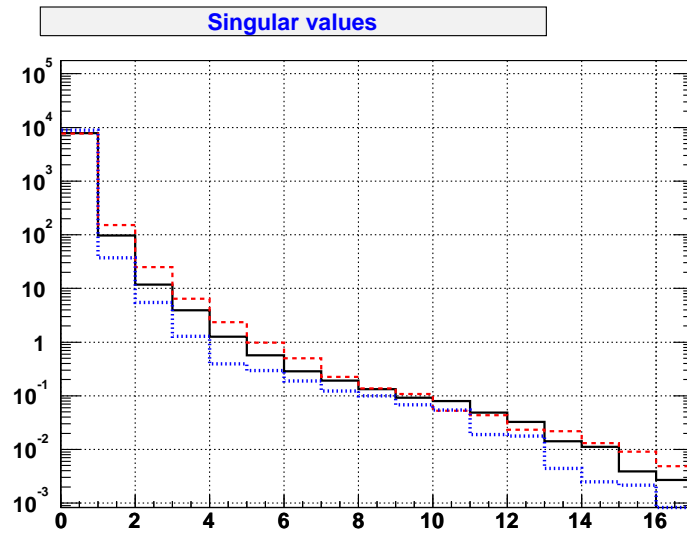
Figure 6.7: Singular values obtained for the different distributions. Black solid, red dashed and blue dotted lines correspond to $fun0$, $fun1$ and $fun2$ respectively (see text for explanation).
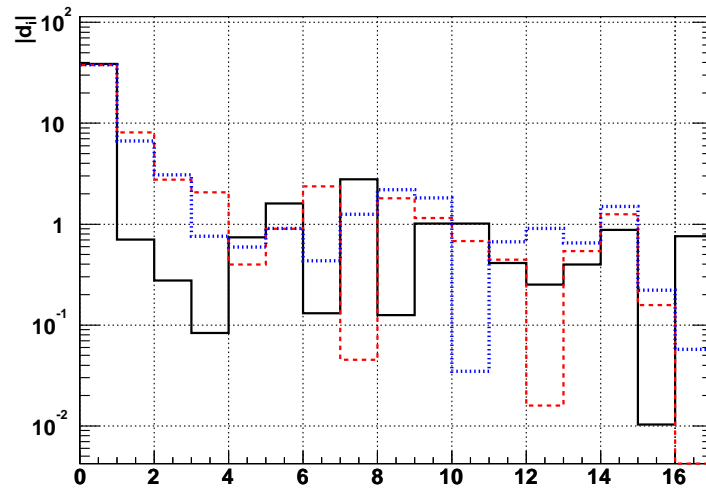
Figure 6.8: Absolute values of d_i. After a fast fall in the very first components, the values of $|d_i|$ become stable. This gives a hint about the optimal value of the regularization parameter τ $(= s_k^2)$.
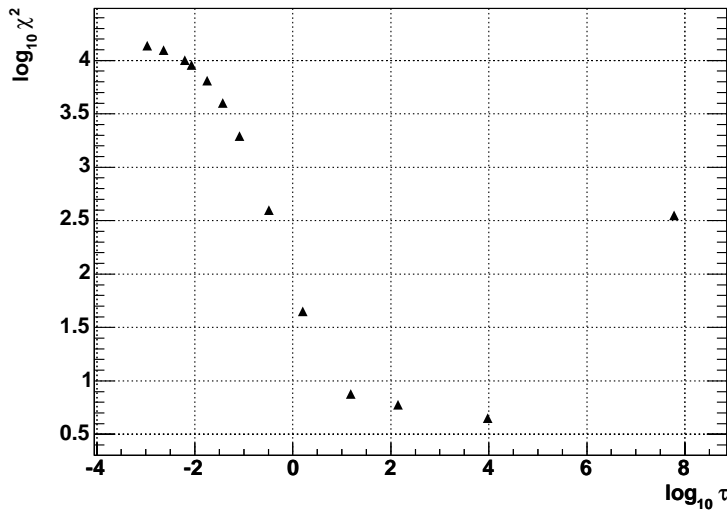
Figure 6.9: χ^2 values obtained when comparing the true and the unfolded distributions for different values of τ, calculated as $\tau = s_i^2$, where s_i are the singular values. In the $fun0$ example of figure 6.8, the exponential fall ends in the second bin. This is also the best value according to the χ-test (i grows from right to left).

can be seen that the fluctuations are within the calculated errors.

The unfolded spectra obtained when the $fun1$ and $fun2$ distributions are used to generate the kernel are shown in figures 6.12 and 6.13. In the first case, the quality of the reconstruction is good. The case of $fun2$ is a bit more complicated to reconstruct since the differences with respect to the $fun0$ are more pronounced. However, the results still remain within the calculated errors.

6.4   Performance of the iterative method

The second unfolding approach is an iterative method based on the Bayes' theorem (see section 6.2.2 for details). As in the SVD approach, the true energy distribution (simulated data) is obtained with Monte Carlo assuming the Bartol model. For the initial energy distribution, needed to start the iterative process, $fun1$ and $fun2$ are used. The iterative process is stopped after three iterations, which according to the Monte Carlo is a good election. Other finishing criteria, as a χ^2 comparison between consecutive iterations does not work properly, because of the low statistics in the high energy region. Figures 6.14 and 6.15 show the true and unfolded distribution when using $fun1$ and $fun2$ as initial guess respectively.

In the first case, the quality of the reconstructed spectrum presents a deficit at intermediate energies, whereas in the second case, there is a significant deficit at very low energies and an excess at intermediate energies. At high energies, both examples
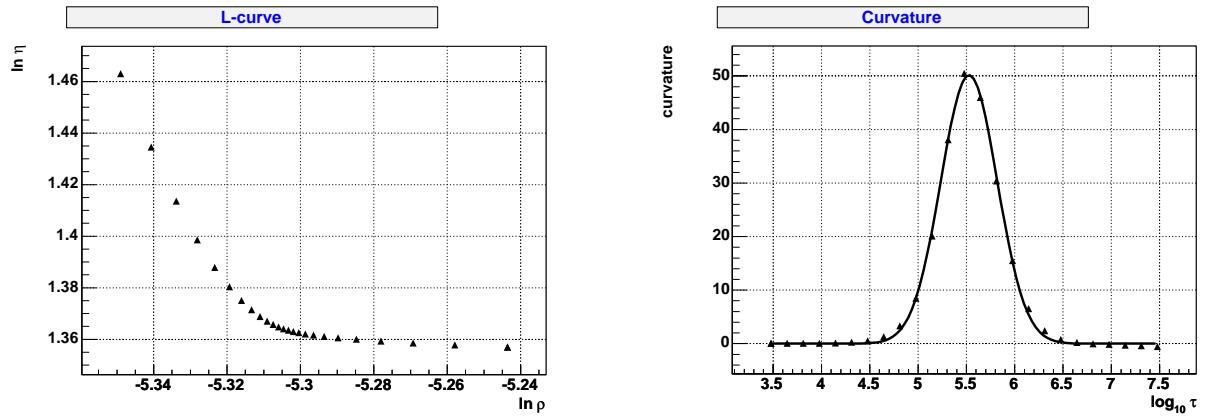
Figure 6.10: Left: The L-curve obtained for the $fun0$ case. Each point corresponds to a different τ value. Right: Curvature of the L-curve as a function of τ. The optimal τ is given for the point of maximum curvature.
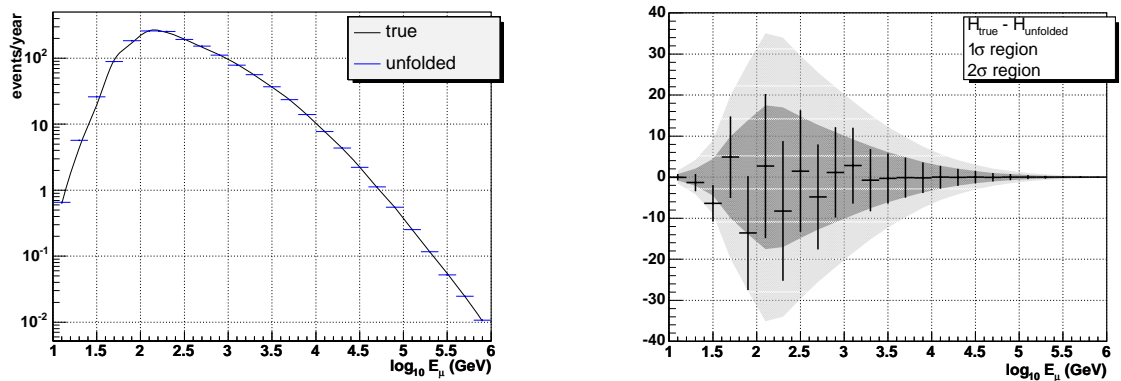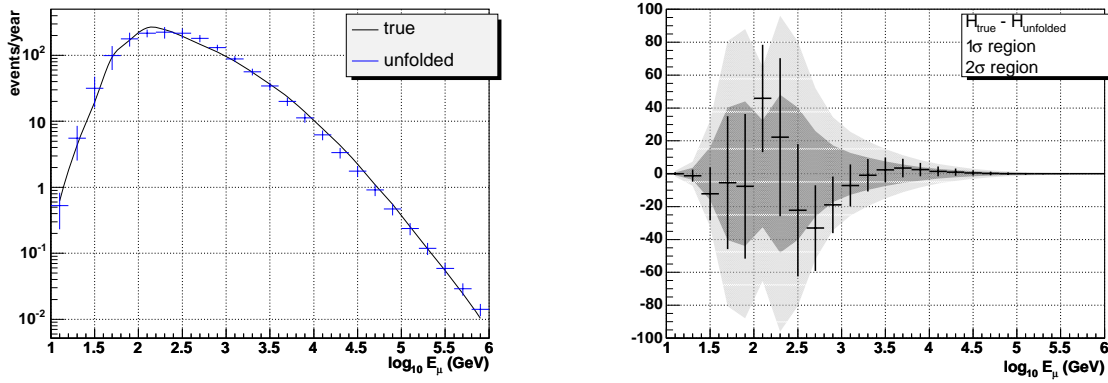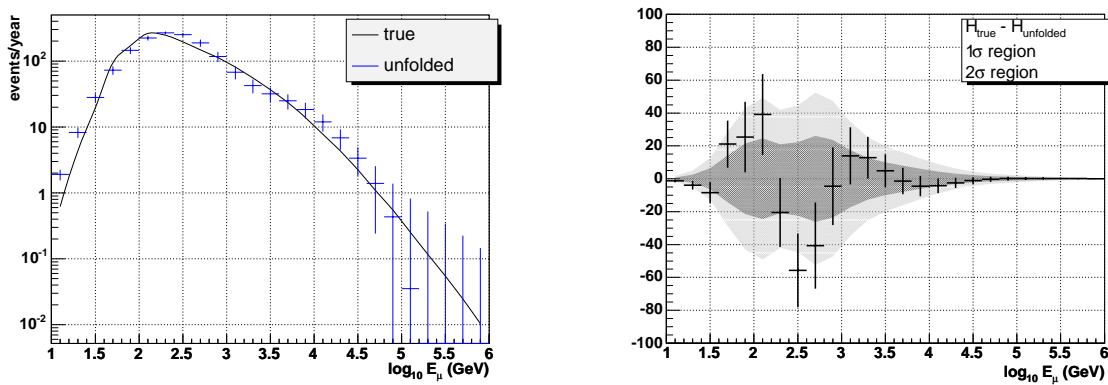

Figure 6.11: Left: Neutrino-induced muon energy distribution obtained with the response matrix generated with $fun0$: the solid black (blue bars) line represents the true (unfolded) spectrum. The excellent agreement is due to the fact that the true distribution is also $fun0$, so the algorithm has only to cope with the statistical fluctuations. Right: Difference between the true and the unfolded spectra. The 1σ and 2σ regions are also shown as a reference.

Figure 6.12: Left: Neutrino-induced muon energy distribution obtained with the response matrix generated with $fun1$: the solid black (blue bars) line represents the true (unfolded) spectrum. Right: Difference between the true and the unfolded spectra. The 1σ and 2σ regions are also shown as a reference.

Figure 6.13: Left: Neutrino-induced muon energy distribution obtained with the response matrix generated with $fun2$: the solid black (blue bars) line represents the true (unfolded) spectrum. Right: Difference between the true and the unfolded spectra. The 1σ and 2σ regions are also shown as a reference.
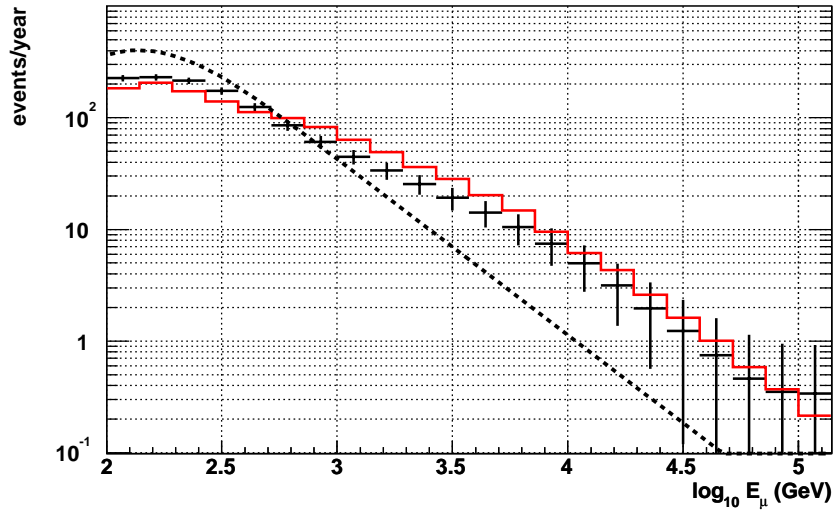
Figure 6.14: True (red line) and unfolded (black bars) muon energy distribution obtained for the iterative method. The initial guess is the $fun1$ distribution (dashed line).
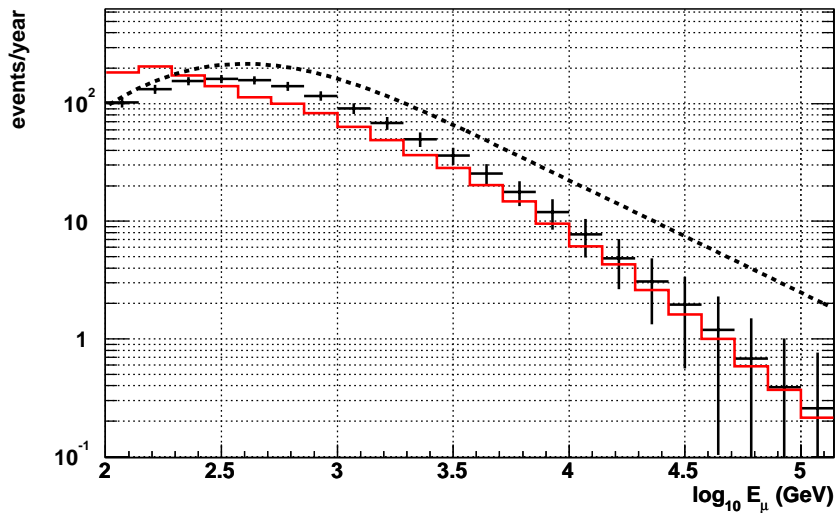
Figure 6.15: True (red line) and unfolded (black bars) muon energy distribution obtained for the iterative method. The initial guess is the $fun2$ distribution (dashed line).

work well.

It is also interesting to note that the performance of this method improve largely when there is no limitation in statistics. In the example of figure 6.16, a distribution according to the Bartol flux has been used as initial guess. When the data are simulated, a signal like the Waxman-Bahcall upper bound is added. After just four iterations, the algorithm reconstructs the presence of such a signal. Unfortunately, the simulated statistics is equivalent to 1000 years of data taking.
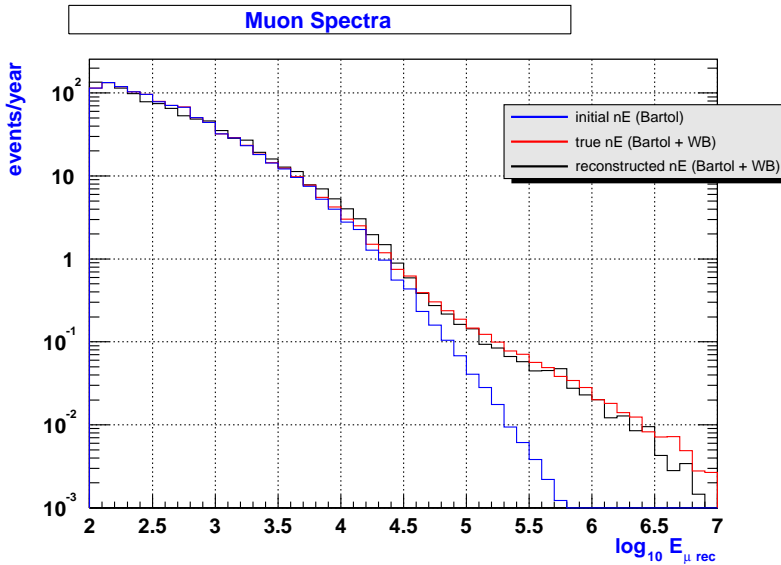
Figure 6.16: Unfolded spectrum using unlimited statistics. The blue line shows the initial guess, generated according to the Bartol flux. In the simulation of the data we have included the presence of a signal (WB upper bound). The algorithm success to detect such a signal.

6.5   Comparison between the SVD and the iterative method

Figures 6.17 and 6.18 show the unfolded spectra for different theoretical models using the SVD and the iterative approach, respectively. We make the unfolding using different models for the measured spectrum and using always the prediction of Bartol to generate the response matrix in the SVD approach and as initial hypothesis in the iterative method. In order to make a comparison of both methods, a Pearson's test between the true and the unfolded distributions is performed.

Table 6.1 shows the results of this comparison. From the previous table we conclude that both algorithms show good performance, in general. Nevertheless, we choose the SVD method for two reasons. Firstly, the values of the X^2 statistic for this method show that the differences between the true and the unfolded distributions are lower. Secondly, we avoid to choose the optimum number of iterations, which could be unstable in extreme cases.

	X^2	
Model	SVD	Iterative
Bartol	0.10	1.0
Fluka	0.78	1.6
QGSM op	1.2	1.7
QGSM pe	0.20	0.73
WB98	0.83	0.52
MPR98	49	42

Table 6.1: Value of the statistic X^2 for a Pearson's test which compares the unfolded and the true spectrum using different models. For the cases other than the conventional neutrinos, only the high energy region (E>1 TeV) is compared.

6.6 Atmospheric neutrino flux

In the previous sections we have seen that good results can be obtained with the studied unfolding algorithms, specially with the SVD method, when reconstructing the muon energy spectrum of the selected events. Once we have tested the peformance of the unfolding algorithm in the reconstruction of the muon energy at the can level, we can go further and try to reconstruct the atmospheric neutrino flux.

The muon energy spectrum deconvolution is made using the SVD algorithm where the kernel matrix is generated with the $fun1$ distribution and the measured data follows the Bartol prediction. The unfolded muon energy spectrum corresponds to the detector level. We transformate it into the atmospheric neutrino flux in two steps. First, we convert the muon energy spectrum into a neutrino energy spectrum by means of a Monte Carlo matrix where each element represents the probability that a muon of energy E_μ at the detector were produced by a neutrino of energy E_ν, for the *Level* 2 selection criteria and assuming the Bartol model for the atmospheric neutrino flux (see figure 6.19). The energy neutrino spectrum obtained in this way is not the true atmospheric neutrino spectrum, since it only corresponds to those interacting neutrinos having produced a selected muon. To obtain the true atmospheric neutrino flux, we apply a bin-by-bin efficiency correction which is given by the ratio of the atmospheric

neutrino flux to the number of events per year passing the *Level* 2 quality cuts. This is called "filtering function" (see figure 6.20).

After applying this filtering function, we obtain the atmospheric neutrino spectrum which is shown in Figure 6.21. As expected, the reconstructed distribution is an almost power-law spectrum. The slope of this function above 1 TeV is

$$\gamma_{int} = 2.72 \pm 0.04 \tag{6.29}$$

This is the integral spectral index, which is a unit lower than the differential spectral index[3]

$$\gamma = 3.72 \pm 0.04 \tag{6.30}$$

In this energy region, the predicted value (see chapter 1) is $\gamma \simeq 3.7$. This is a simulation of the result that we would obtain according to the Monte Carlo. As expected, a good agreement in the spectrum reconstruction leads to the expected value in the fitted flux slope.

The difference between the zenith angle θ^* at production and the zenith angle θ at detector (see section 1.5) has been taken into account when the average flux is calculated. The parameterization of the relationship between $\cos\theta$ and $\cos\theta^*$ is shown in figure 6.22.

6.7 Atmospheric down-going muon spectrum

Analogously to the case of the neutrino spectrum, we can also reconstruct the atmospheric down-going muon spectrum at the can level. In this analysis it is convenient to use the Aart strategy for track reconstruction since, as we have seen in chapter 5, the quality of the Carmona strategy, which is optimized for neutrino events, is poor for down-going muons.

Unlike the neutrino spectrum, the statistics of the down-going muon spectrum is high. The true (simulated) atmospheric down-going muon spectrum at the level of the detector is shown in figure 6.23. This figure also shows the spectrum used to compute the response matrix in the SVD unfolding approach. Again, it has been chosen to be clearly different from the simulated data spectrum.

As in the case of neutrino events, we use the L-curve criterion in order to choose the best value of τ, the one with the maximum curvature (see figure 6.24). Figure 6.25 shows the true muon energy distribution together with the unfolded one.

---

[3]For a differential flux $d\phi(E)/dE = \phi_\circ E^{-\gamma}$, the number of events in each bin of a logarithmic histogram is $n_i = \int_{E_i}^{kE_i} \phi_\circ E^{-\gamma} dE = \phi_\circ \frac{k^{1-\gamma}-1}{1-\gamma} E_i^{-\gamma+1}$.
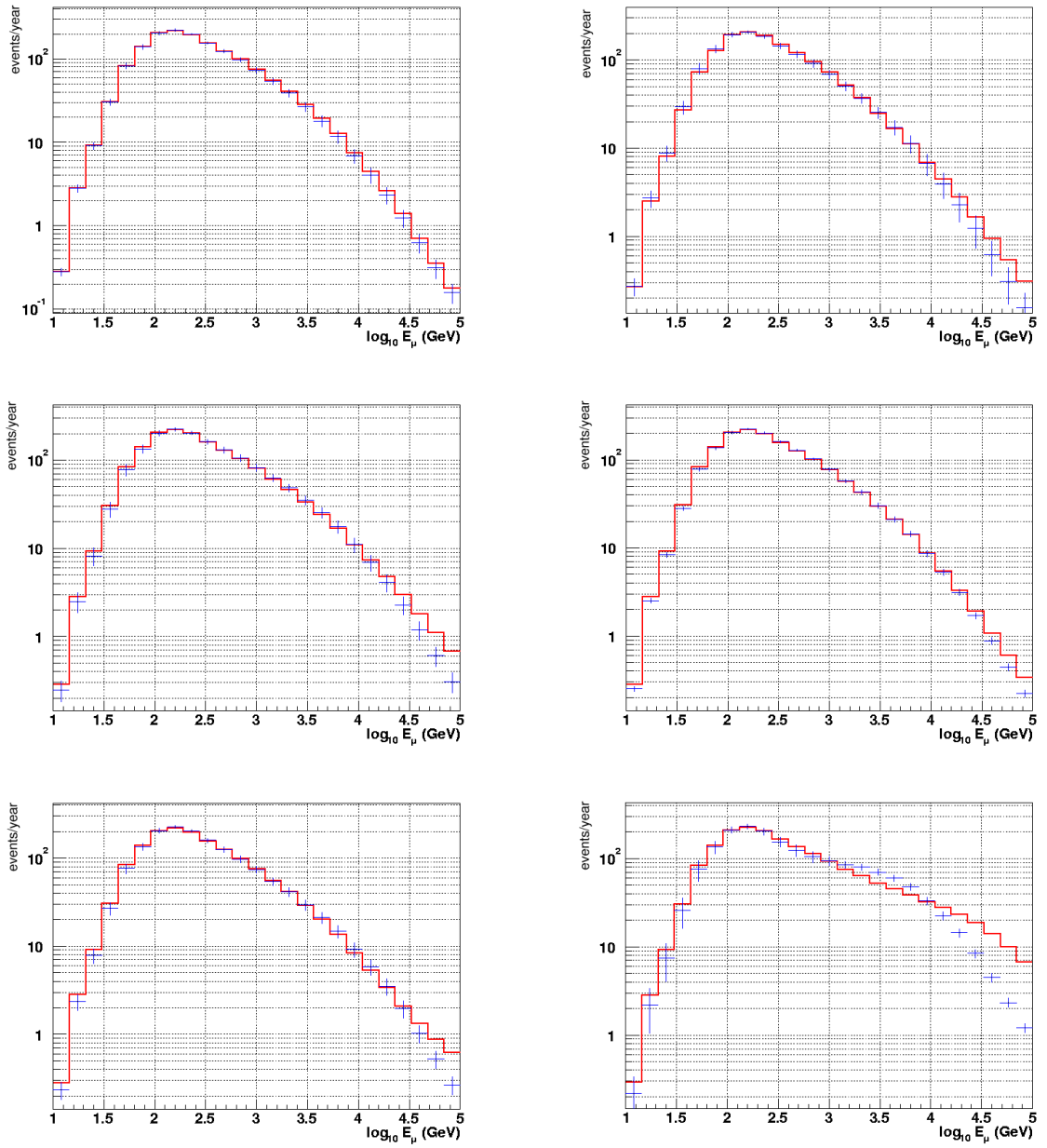
Figure 6.17: SVD algorithm. Unfolded spectrum (blue bars) compared to the true distribution (red line) for different models. In reading order, Bartol, Fluka, QGSM$_{op}$, QGSM$_{pe}$, WB98 and MPR98. In all the cases, the response matrix has been generated with the Bartol model prediction.
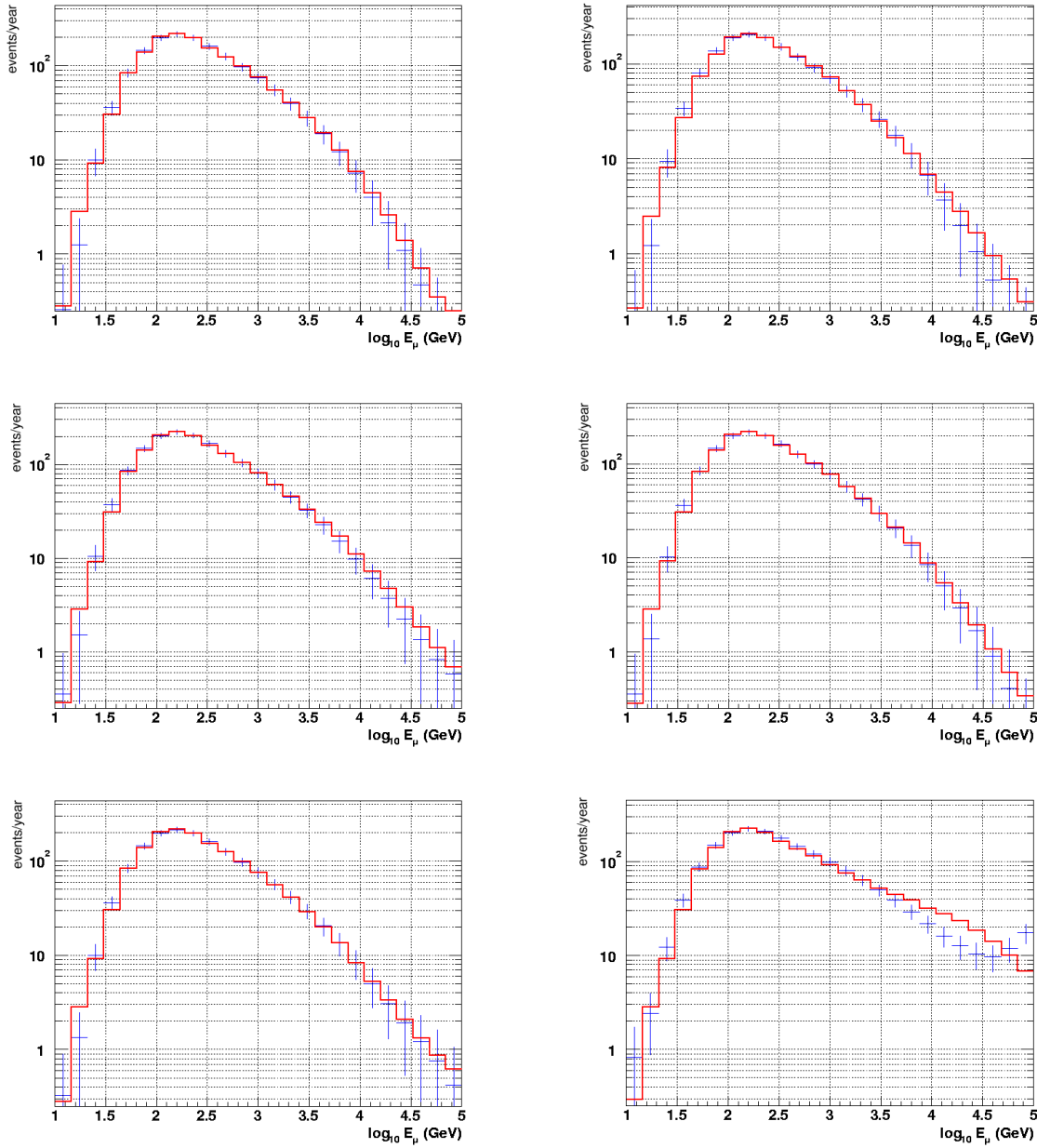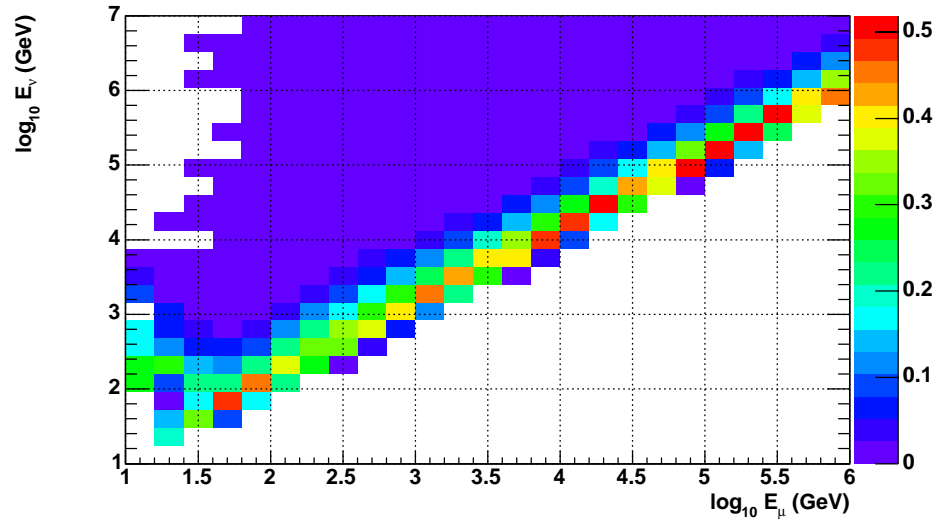
Figure 6.18: Iterative algorithm. Unfolded spectra (blue bars) compared with the true distribution (red line) for different models. In reading order, Bartol, Fluka, $QGSM_{op}$, $QGSM_{pe}$, WB98 and MPR98. In all the cases, the initial guess is the Bartol prediction.

Figure 6.19: Probability of a muon of energy E_μ of having being produced by a neutrino of energy E_ν, assuming the Bartol atmospheric neutrino flux.
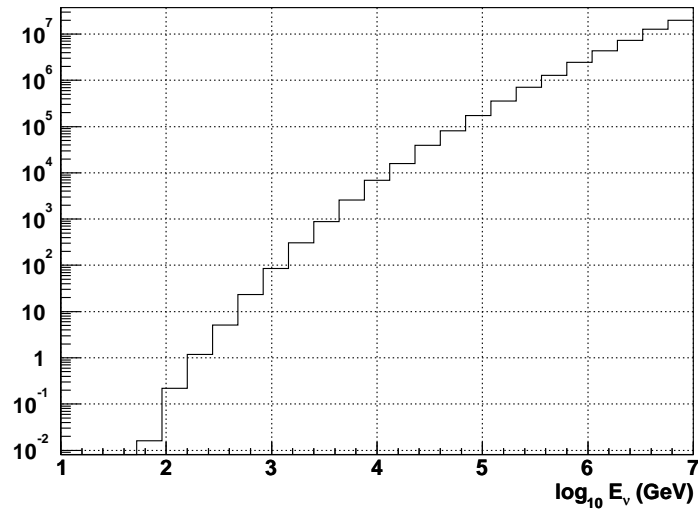
Figure 6.20: Filtering function of the detector calculated as the ratio between the flux $(\mathrm{cm}^{-2}\mathrm{s}^{-1})$ of atmospheric neutrinos and the number of events/year which pass the quality cuts in the detector, according to the MC.
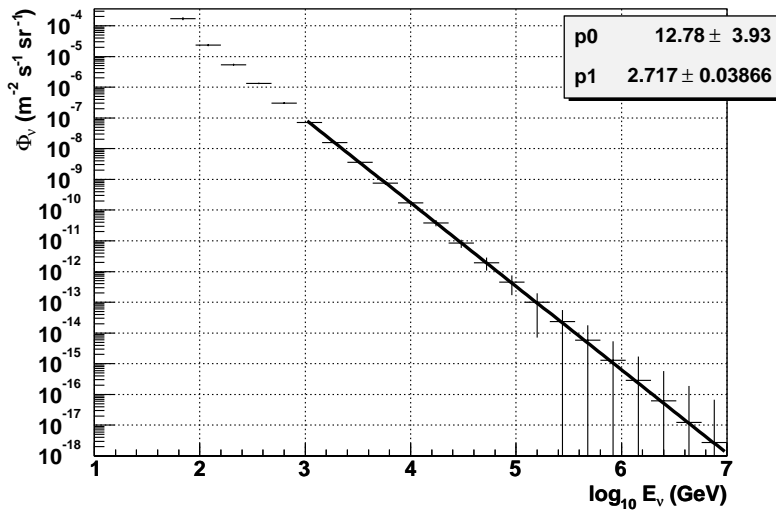
Figure 6.21: Reconstructed flux of atmospheric neutrinos. The slope of the integrated spectrum agrees with the theoretical value ($\gamma_{int} \simeq 2.7$), as expected since the muon spectrum was well reconstructed. The spectrum is averaged in cos θ^*.
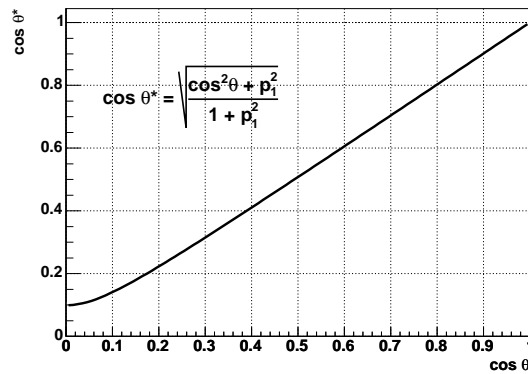
Figure 6.22: Parameterization of the relationship between the zenith angle at production (θ^*) and at the detector (θ). The value used for p_1 is 0.099755, which comes from a simplification of the parametrization used in [160].
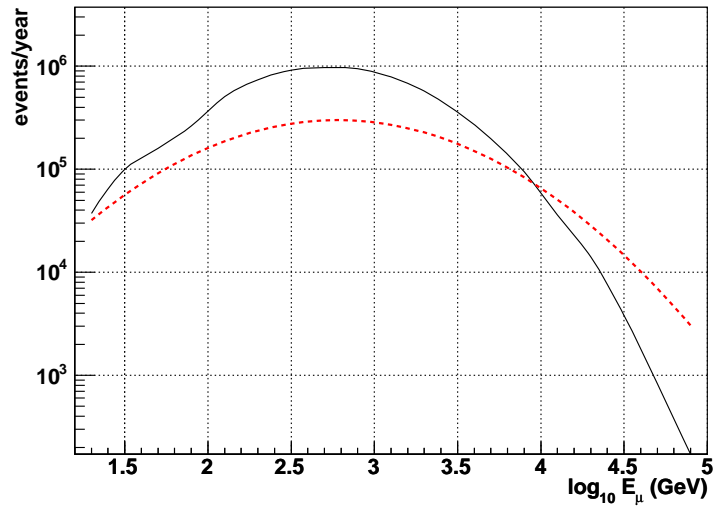
Figure 6.23: Comparison between the true energy spectra of the atmospheric down-going muons (black solid line) and the spectrum used to generate the kernel (red dashed line). The latter has been chosen to be quite different from the true one to show the robustness against model uncertainties.
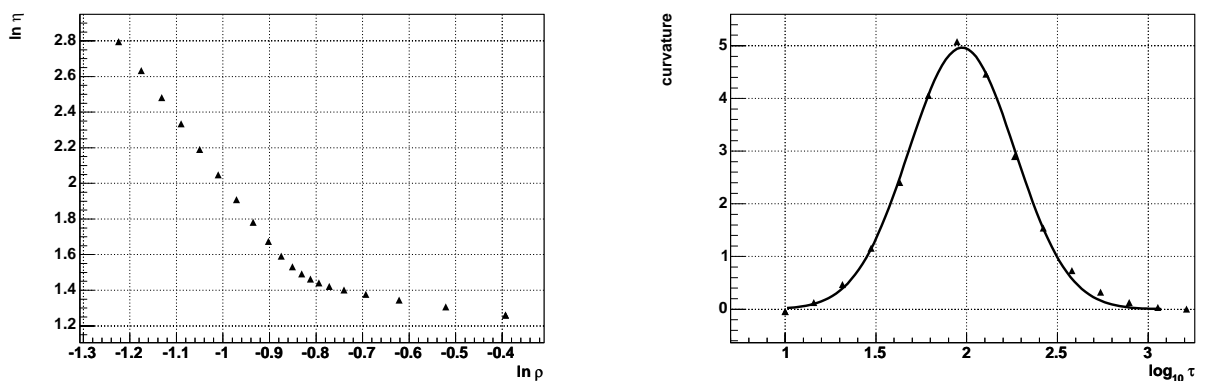
Figure 6.24: L-curve (left) and curvature (right) plot used to choose the optimum τ in the down-going atmospheric neutrino spectrum.
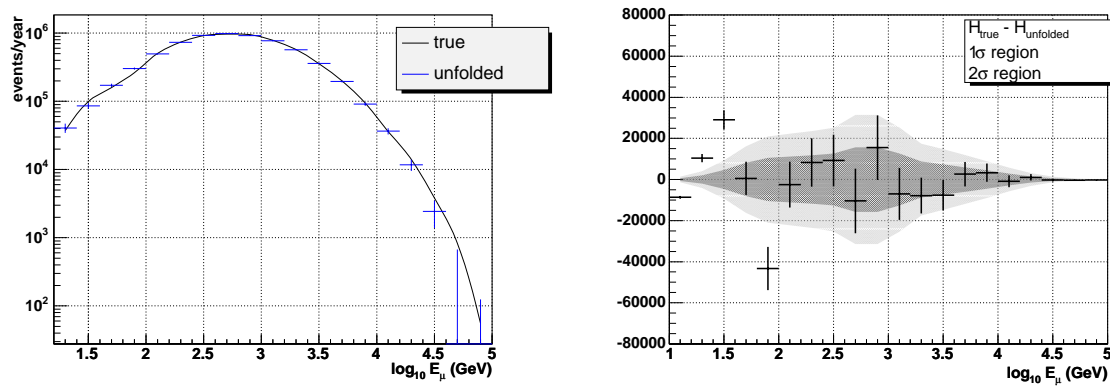
Figure 6.25: Left: True (black solid) and unfolded (blue bars) spectra of down-going muons at the detector level. Right: Difference between the true and the unfolded spectra. The 1σ and 2σ regions are also shown as a reference.

Conclusions

The ANTARES telescope will open the neutrino window to the Southern sky. Many of the most challenging astrophysical objects (active galactic nuclei, gamma ray bursts, microquasars...) are expected to emit high energy neutrinos, so this kind of detectors will play an important role in the next years. Other scientific issues in the ANTARES scope are the nature of dark matter and the neutrino oscillations. After intense years of studies on the technical aspects of the project, the environmental parameters of the site and the performances of the detector, data taking will start in 2005. The aim of the thesis has been focused in different issues related to the telescope "calorimetry": the energy reconstruction, the detector sensitivity to diffuse fluxes of high energy cosmic neutrinos and the energy spectrum unfolding.

Energy reconstruction

The muon energy can be estimated from the light output in the detector, since above the critical energy (~ 600 GeV in water), the average energy loss of the muon (due to pair production, *bremsstrahlung*, and photo-nuclear interactions) is proportional to the muon energy. Two estimators have been used (for the low and high energy regime) which compare the signal produced by the muon in the PMTs with the signal that a minimum ionizing muon along the same track would have produced. The main conclusions are:

- Several parameterizations of the relationship of the estimators with the true muon energy have been studied. The best performance is obtained when a fit to a straight line is used.

- With other functions like parabolic or cubic fits, a fraction of events cannot be reconstructed, since they are below the minimum (low energies) or above the maximum (high energies) of the parabola or cubic function.

- At intermediate energies, a good relationship between reconstructed and generated energy is obtained. Using the low energy estimator, the mean value of the $\log_{10} E_\mu^{rec}/E_\mu^{gen}$ distribution is around zero (within 0.2), for energies ranging from 500 GeV to 1 PeV.

177

- The value of the sigma of the $\log_{10} E_\mu^{rec}/E_\mu^{gen}$ distribution decreases with energy from 0.45 (at 500 GeV) to 0.25 (at 1 PeV). This implies a knowledge of the muon energy within a factor 2-3.

- At energies below the critical energy, the relation between the estimator and the muon energy deviates from a straight line because of the flatness in the energy loss function, so a shift in the average value of the reconstructed energy is observed ($\sim$0.2). At high energies, the estimator saturates, as expected from its definition, so there is a shift (0.25 at 1 PeV) in the reconstructed energy.

- The dependence on geometrical factors of these results have been also studied. Among other conclusions, it has been found a slight tendency to overestimate (underestimate) the energy of the nearest (farest) tracks. Moreover, the energy of vertical ($\cos\theta > 0.8$) tracks is also overestimated (~ 0.1) in average.

Sensitivity to cosmic neutrino diffuse fluxes

The sensitivity is a parameter which describes the capability of the detector to separate signal from background. Quality cuts aim to eliminate the background produced by atmospheric muons. An additional cut on a neutrino energy dependent variable is needed to discriminate the cosmic neutrino signal from the atmospheric neutrino background (since the latter follows a softer energy spectrum). The study presented in this work on the ANTARES sensitivity to high energy neutrino diffuse fluxes concludes that:

- At the level of the simulated statistics, all the atmospheric muon background is rejected with the proper quality cuts based on the fit-prefit angle, the track reconstruction errors and a variable used to eliminate ghost tracks.

- The loss of signal events with respect to the standard quality cuts of the Carmona track reconstruction strategy is lower than 7%, while the improvement in the atmospheric neutrino background rejection is $\sim 17\%$.

- Two neutrino-energy dependent variables have been studied to make the final cut which tries to separate the cosmic neutrino signal from the atmospheric neutrino background: the reconstructed energy and the total number of hits of the event. These options are compared by minimising the model rejection factor (MRF).

- The best MRF using the reconstructed energy is 2.56 (FC method), with a cut threshold at 7.9×10^4 GeV. The total number of hits has been found to be a better option. The optimum cut at $N_{hits} > 287$ provides a MRF of 1.72, to be compared with the best possible value (using the true energy) which is 1.17.

- The resulting limit for a signal in the Waxman-Bahcall limit using the Bartol model for the atmospheric neutrino signal is $E^2\Phi_{90} < 7.7\times10^{-8}$ GeV cm^{-2} s^{-1} sr^{-1}

after one year of data taking (FC method). The limit after three years is $E^2\Phi_{90} < 3.8 \times 10^{-8}$ GeV cm^{-2} s^{-1} sr^{-1}.

- When systematic errors due to the uncertainty in the normalization of the conventional atmospheric neutrino flux, the prompt neutrino models or the water optical properties are included, the average upper limit of the Waxman-Bahcall flux is $E^2\Phi_{90} < 9.0 \times 10^{-8}$ GeV cm^{-2} s^{-1} sr^{-1}, after one year of data taking. The limit after three years is $E^2\Phi_{90} < 4.3 \times 10^{-8}$ GeV cm^{-2} s^{-1} sr^{-1}.

- This represents an improvement $\sim 20\%$ with respect to previous results in the ANTARES collaboration. This difference can be partially explained by the new detector layout, which has 12 lines instead of 10 (although with the same number of PMTs). Another relevant difference, apart from the fact that a new energy dependent variable has been used to discriminate the atmospheric neutrinos, is the new sample of atmospheric muons, much more significant statistically. There are also other updates like the parton distribution function or the inclusion of the hadronic cascade in the simulation.

- The calculated value for the ANTARES sensitiviy after one year of data taking is a factor three better than the present limit set by AMANDA (see 6.26).
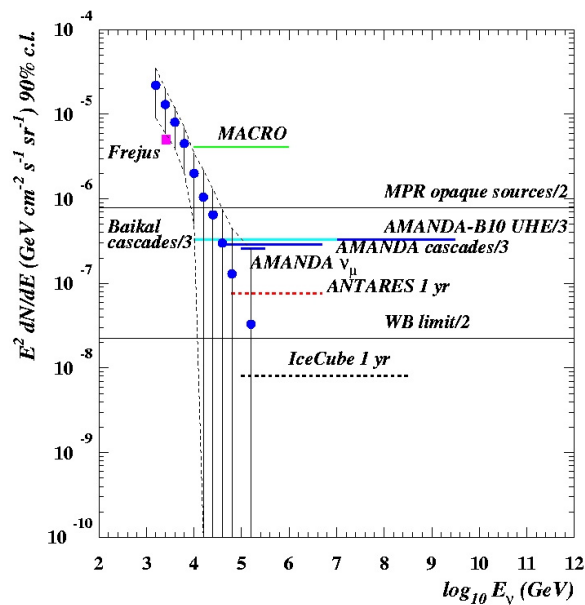

Figure 6.26: Expected sensitivity of ANTARES (90% C.L.) to $\nu_\mu + \bar{\nu}_\mu$ diffuse E^{-2} fluxes compared with other experiments and different theoretical upper bounds. The WB and MPR limits are divided by 2 to take into account neutrino oscillations.

The distributions of the low energy estimator x_{low} assuming different models of the atmospheric neutrino spectra, the prompt neutrino component and the extraterrestrial signal have been compared by means of statistical tests. The differences in the spectra after one year of data taking will not be very conclusive, except for very optimistic models. After three years of data taking, the discrimination power of these tests is much better.

Spectrum deconvolution

Since the spectra involved in this analysis follow a fast decreasing power law and the energy deposition is very stochastic, the energy spectra cannot be reconstructed event by event, but unfolding techniques have to be used. The study carried out on the spectrum deconvolution shows the following conclusions:

- Two unfolding algorithms have been studied. The first one is based on the Singular Value Decomposition (SVD) of the response matrix. The second one is an iterative method based on the Bayes's theorem.

- The SVD algorithm presents a better performance in the energy spectrum deconvolution. Even if the distribution used to generate the kernel is different from the one used to generate the simulated data, the spectrum can be reconstructed.

- The iterative algorithm based on Bayes' theorem is more sensitive to uncerntainties in the initial distribution shape.

- By means of the SVD algorithm, a first attempt to reconstruct the atmospheric neutrino flux has been made in a simplified way. The agreement between the true and reconstructed spectral indexes is promising.

Bibliography

[1] A. M. Markov. In *Proceedings of the Rochester Conference*, New York, 1960.

[2] T. K. Gaisser, F. Halzen, and T. Stanev. *Phys. Rep. 258*, 258:173, 1995. Erratum-ibid: 271, 355-356 (1996).

[3] The AMANDA Collaboration. *Nucl. Phys. B (Proc. Suppl.)*, 91:423, 2000.

[4] The Baikal Collaboration. *Nucl. Phys. B (Proc. Suppl.)*, 91:438, 2000.

[5] C. L. Cowan et al. *Science*, 124:103, 1956.

[6] R. Davis, D. S. Harmer, and K.C. Hoffman. *Phys. Rev. Lett.*, 1968.

[7] B. Pontecorvo. *J.Exptl.Theort.Phys.*, 549, 1957.

[8] IMB Collaboration J.C. Van Der Velde et al. *Nucl. Instrum. Meth.*, A264:28–31, 1988.

[9] The Super-Kamiokande Collaboration. *Nucl. Phys. B (Proc. Suppl.)*, 91:127, 2001.

[10] Q. R. Ahmad et al. *Phys. Rev. Lett.*, 89:011301, 2002. nucl-ex/0204008.

[11] K. Eguchi. *Phys. Rev. Lett.*, 90:021802, 2003.

[12] I. Kato. The results of oscillation analysis in K2K experiment and an overview of JHF-nu experiment. 2003. hep-ex/0306043.

[13] D. Michael et al. *Nucl. Phys. B (Proc. Suppl.)*, 118:189, 2003.

[14] S. Navas-Concha. *AIP Conf. Proc.*, 698:298–302, 2004.

[15] M. Ambrosio et al. *IEEE Trans. Nucl. Sci.*, 51:975–979, 2004. physics/0409137.

[16] V. F. Hess. *Phys. Zeitschr.*, 13:1084, 1913.

[17] T. Maeno et al., BESS Collab. *Astropart. Phys.*, 16:121, 2001.

[18] P. Biermann and G. Sigl. *Lect. Notes Phys.*, 576:1–26, 2001. astro-ph/0202425.

[19] K. Greisen. *Phys. Rev. Lett.*, 16:748, 1966.

[20] G. Zatsepin and V. A. Kuzmin. *JETP Lett.*, 4:78, 1966.

[21] R. U. Abbasi et al. *Phys. Rev. Lett.*, 92:151101, 2004. astro-ph/0208243.

[22] AGASA Collaboration M. Takeda et al. *Phys. Rev. Lett.*, 81:1163, 1998.

[23] E. Fermi. *Phys. Rev.*, 75:1169, 1949.

[24] R. D. Blanford and D. Eichler. *Phys. Rep.*, 154:1, 1987.

[25] T. K. Gaisser. *Cosmic Rays and Particle Physics*. Cambridge University Press, 1992.

[26] E. Leer W. I. Axelford and G. Skadron. In *Proceedings of the 15th International Cosmic Ray Conference*, volume 11, 1977.

[27] G.F. Krymsky. *Dok. Acad. Nauk. USSR*, 234:1306, 1977.

[28] R. Battistoni. Astroparticle Physics with AMS on the International Space Station. *Nucl.Part.Phys.*, 29:891–902, 2003.

[29] A. Giuliani S. Mereghetti M. Tavani A. Pellizzoni, A. Chen and S. Vercellone. Agile sky exposure and sensitivity maps. In *AIP Conference Proceedings*, volume 587 (1), pages 759–763, 2001.

[30] I.V. Moskalenko J.E. McEnery and J.F. Ormes. GLAST: Understanding the High Energy Gamma-Ray Sky. 2004. astro-ph/0406250.

[31] S.D. Biller et al. J.A. Zweerink, C.W. Akerlof. *Astrophys. J.*, L141:490, 1997.

[32] F. Aharonian, HEGRA Collaboration. *Astron. Astrophys.*, 349:11, 1999.

[33] T.Kifune. *Adv. Space Res.*, 25:641, 2000.

[34] F. Piron, CAT Collaboration. Observations of the gamma-Ray Emission Above 250 GeV from the Blazars Markarian 501 and Markarian 421 by the CAT Cherenkov Atmospheric Imaging Telescope. In *Proceedings of the XIth rencontres de Blois*, 1999.

[35] P.M. Chadwick et al. *Eur.Phys.J.*, C 33, 2004.

[36] T.C. Weekes. TeV Gamma-ray Observations and the Origin of Cosmic Rays. In *Proceedings of the 28th International Cosmic Ray Conference*, volume 3, Tsukuba, Japan, 2003. Universal Academic Press. ISBN 4-946443-80-0.

[37] M. Mori et al. *Proc. 27th ICRC (Hamburg)*, OG231, 2001.

[38] J. A. Barrio et al. The MAGIC Telescope. *MPI-PhE/98-5*, 1998.

[39] T. Naito et al. R. Enomoto, T. Tanimori. *Nature*, 416:823, 2002.

[40] O. Reimer and M. Pohl. *Astron. Astrophys.*, L43:390, 2002.

[41] F. Aharonian et al. Very high energy gamma rays from the direction of Sagittarius A*, 2004. astro-ph/0408145.

[42] L.V. Volkova. *Sov. J. Nucl. Phys*, 31:784, 1980.

[43] P. Lipari V. Agrawal, T.K. Gaisser and T. Stanev. *Phys.Rev.*, D53:1314, 1996.

[44] T.K. Gaisser and M. Honda. *Annu. Rev. Nucl. Part. Sci.*, 52:153, 2002.

[45] G. Ingelman and M. Thunman. *Phys. Rev.*, D54:4385, 1996.

[46] W. Bednarek, G. Fiorella Burgio, and T. Montaruli. Galactic discrete sources of high energy neutrinos. 2004. astro-ph/0404534.

[47] E. Waxman and A. Loeb. *Phys. Rev. Lett.*, 87:071101, 2001.

[48] D.R. Lorimer. The galactic population and birth rate of radio pulsars. In *Proceedings of the Young neutrons stars and their enviroments IAU Symp, (2003)*. astro-ph/0308501.

[49] G. B. Hobbs et al. N. Vranesevic, R. N Manchester. Pulsar birthrate from parkes multi-beam survey. In *Proceedings of the Young neutrons stars and their enviroments IAU Symp, (2003)*. astro-ph/0310201.

[50] W. Bednarek R.J. Protheroe and Q. Luo. *APh*, 9:1, 1998.

[51] W. Bednarek J.H. Beall. *Astrophys. J.*, 569:343, 2002.

[52] S. Nagataki. *Astrophys. J.*, 600:883–904, 2004. astro-ph/0309715.

[53] W. Bednarek. *Astron. Astrophys.*, 407:1, 2003.

[54] D. Guetta E. Amato and P. Blasi. *Astron. Astrophys.*, 402:827–836, 2003. astro-ph/0302121.

[55] F. Halzen J. Alvarez-Muniz. *Astrophys. J.*, L33:576, 2002.

[56] W. Bednarek. *MNRAS*, 331:483, 2002.

[57] R. Fender and T. Maccarone. 2003. astro-ph/0310538.

[58] A. Levinson and E. Waxman. *Phys Rev Lett.*, 87:17, 2001.

[59] E. Waxman A. Levinson C. Distefano, D. Guetta. *Astrophys. J.*, 575:378, 2002.

[60] D.F. Torres, G.E. Romero and F. Mirabel. Neutrinos from microquasars. In *5th Microquasar Workshop: Microquasars and Related Astrophysics*, Beijing (China), 2004. astro-ph/0407494.

[61] G.F. Burgio, ANTARES Collaboration. Detecting high-energy neutrinos from microquasars with the ANTARES telescope. In *5th Microquasar Workshop: Microquasars and Related Astrophysics*, Beijing (China), 2004. astro-ph/0407339.

[62] P. Meszaros E. Waxman A.K. Harding B. Zhang, Z.G. Dai. *Astrophys. J.*, 595:346, 2003.

[63] M. Metzger et al. *Nature*, 387:878, 1997.

[64] A. MacFadyen and S.E. Woosley. *Astrophys. J.*, 524:262, 1999.

[65] B. Paczynski. *Acta Astronomica*, 41:257, 1991.

[66] K.S.Cheng and Z.G. Dai. *Phys.Rev.Lett.*, 77:1210, 1996.

[67] M. Bottcher. *Astrophys. J.*, 21:L515, 1999.

[68] A. Muecke and R.J. Protheroe. *Astropart. Phys.*, 15:121, 2001.

[69] K. Mannheim. *Space Sci. Rev.*, 75:331, 1996.

[70] F. Halzen and D. Hooper. *Rept. Prog. Phys.*, 65:1025–1078, 2002. astro-ph/0204527.

[71] T. Weiler. *Phys.Rev.Lett.*, 49:234, 1982.

[72] P. Gondolo and J. Silk. *Nucl. Phys. B Proc. Suppl.*, 87:87, 2000.

[73] P. Sreekumar et al., EGRET Collaboration. *Ap. J.*, 494:523, 1998.

[74] A. Muecke et al. *Comput. Phys. Commun.*, 124:290, 2000.

[75] R.J. Protheroe P. Rachen and K. Mannheim. The relation of extragalactic cosmic ray and neutrino fluxes: The logic of the upper bound debate. 1998. astro-ph/9908031.

[76] E. Waxman and J. Bahcall. *Phys. Rev.*, D59:023002, 1999.

[77] R.J. Protheroe K. Mannheim and J.P Rachen. *Phys. Rev.*, D63:023003, 2001.

[78] E. Waxman and K. Manheimm. *Europhys. News.*, 32:6, 2001.

[79] M.H. Reno R. Gandhi, C. Quigg and I. Sarcevic. *Phys. Rev.*, D58:093009, 1998. hep-ph/9807264.

[80] K. Hagiwara et al. (Particle Data Group). *Phys. Rev.*, D66:010001, 2002.

[81] J. Pumplin et al. *JHEP*, 07:012, 2002. hep-ph/0201195.

[82] F. Bernard. *Caractérisation des performances d'un télescope sous-marin à neutrinos pour la détection de cascades contenues dans le cadre du projet ANTARES*. PhD thesis, Université de la Méditerranée, Aix-Marseille II, Marseille, France, 2000.

[83] P. Amram et al. The ANTARES optical module. *Nucl. Instr. and Methods*, A484:369, 2002.

[84] J.D. Zornoza. Study of photomultiplier tubes for the antares neutrino telescope. In *Proceedings of the 28th International Cosmic Ray Conference*, volume 3, Tsukuba, Japan, 2003. Universal Academic Press. ISBN 4-946443-80-0.

[85] J. J. Hernández-Rey. Timing callibration of the antares neutrino telescope. In *Proceedings of the 28th International Cosmic Ray Conference*, volume 3, pages 1537–1540, Tsukuba, Japan, 2003. Universal Academic Press. ISBN 4-946443-80-0.

[86] J. A. Aguilar et al. *Astropart. Phys.*, 23:131–155, 2005. astro-ph/0412126.

[87] P. Amram et al. *Astropart. Phys.*, 13:127–136, 2000. astro-ph/9910170.

[88] P. Amram et al. *Astropart. Phys.*, 19:253, 2003.

[89] The Dumand Collaboration. Proposal to construct a 148000 m^{2}sr Deep Ocean Lab for the study of High Energy Neutrino Astrophysics and Particle Physics. Technical report, University of Hawaii, 1988. HCD-2-88.

[90] C. Spiering et al. The Baikal neutrino telescope: Results, plans, lessons. 2004. astro-ph/0404096.

[91] K. Woschnagg for the AMANDA collaboration. New results from the antarctic muon and neutrino detector array. *Submitted to Nucl. Phys. B Proc. Suppl.*

[92] The NESTOR Collaboration. *Nucl. Phys. B (Proc. Suppl.)*, 85:153, 2000.

[93] A. Capone. Site characterization for a km^3 scale deep underwater astrophysical neutrino observatory in the mediterranean sea. Prepared for 26th International Cosmic Ray Conference (ICRC 99), Salt Lake City, Utah, 17-25 Aug 1999.

[94] J. G. Learned and K. Manheim. *Ann. Rev. Nucl. Part. Sci.*, 50:679, 2000.

[95] D. J. L. Bailey. Genhen v5r1: Software documentation. ANTARES internal note. ANTARES-Software/2002-004.

[96] A. Edin G. Ingelman and J. Rathsman. *Comput. Phys. Commun.*, 101:108, 1997.

[97] T. Sjostrand. PYTHIA 5.7 and JETSET 7.4. *hep-ph/9508391*, 1995.

[98] S. Jadach, Z. Was, R. Decker, and Johann H. Kuhn.

[99] P. Antonioli, C. Ghetti, E. V. Korolkova, V. A. Kudryavtsev, and G. Sartorelli. A three-dimensional code for muon propagation through the rock: MUSIC. *Astropart. Phys.*, 7:357–368, 1997.

[100] I.A. Sokalski, E.V. Bugaev, and S.I. Klimushin. *Phys. Rev.*, D64:074015, 2001.

[101] D. Heck et al. Report FZKA 6097, 1998.

[102] E. Scapparone. HEMAS: a Monte Carlo code for hadronic, electromagnetic and TeV muon components in air shower. In *Proceedings of the International Workshop on Simulation and analysis methods for large neutrino detectors, Desy Zeuthen (1998)*, pages 238–246. (physics/9902043).

[103] S. S. Ostapchenko N. N. Kakmykov and A. I. Pavlov. *Nucl. Phys. B (Proc. Suppl.)*, 52B:17.

[104] J. Ranft. *Phys. Rev.*, D51:64.

[105] S. Navas and L. Thompson. KM3: User guide and reference manual. ANTARES Internal Note, 1999. ANTARES-Software/1999-011.

[106] J. Brunner. GEASIM: User manual. ANTARES Internal documentation. http://antares.in2p3.fr/internal/software/geasim.html.

[107] L.C. Henyey and J.L. Greenstein. *Astrophys. J.*, 93:70–83, 1941.

[108] C. D. Mobley. *Appl. Optics*, 32:7484, 1993.

[109] N. Palanque-Delabrouille. Light transmission in the ANTARES site. Measurement in blue light. ANTARES internal note. ANTARES-Site/1999-003.

[110] A. Morel and H. Loisel. *Applied Optics*, 21, 1998.

[111] T.J. Petzold. Volume scattering functions for selected ocean waters. SIO Ref. 72-78, Scripps Institute of Oceanography, 1972.

[112] J.D. Zornoza. Characterization of two Photomultiplier Models and Study by Monte Carlo Simulation of several Calibration Systems based on Optical Beacons for the ANTARES Detector. Research Work, Universitat de València, 2001.

[113] F. Cassol. GENDET 1.0: a program to generate detector files. ANTARES Internal Note. ANTARES-Soft/1999-007.

[114] F. Cassol Brunner. GENDET 1.2: Cards and tags. ANTARES Internal Note. ANTARES-Soft/2000-8.

[115] F. Cassol. Reconstruction re-organisation: RECO version 2.0. ANTARES internal note. ANTARES-Soft/1999-004.

[116] F. Cassol. RECO version 2.1: code and scripts. ANTARES internal note. ANTARES-Soft/1999-005.

[117] A. Romeyer and Th. Stolarczyk. Reconstruction algorithms: a handbook for developers. ANTARES internal note. ANTARES-Soft/2001-001.

[118] E. Carmona. *Study of the event reconstruction and expected performances for the point-like sources of the future ANTARES neutrino telescope.* PhD thesis, Universitat de València, 2003.

[119] E. Carmona and J. J. Hernández. A new reconstruction technique for ANTARES. ANTARES internal note. ANTARES-Soft/2000-11.

[120] E. Carmona. Update of the new pre-fit for reconstruction. ANTARES internal note. ANTARES-Soft/2001-006.

[121] A. Heijboer. *Track Reconstruction and Point Source Searches with ANTARES.* PhD thesis, NIKHEF, Amsterdam, 2004.

[122] A. Romeyer and T. Montaruli. Conventional and prompt atmospheric neutrino fluxes. ANTARES Internal Note. ANTARES-Phys/2001-015.

[123] A. Margiotta. Simulation of muons from atmospheric showers in the antares detector using hemas. ANTARES internal note. ANTARES-Software/2004-002.

[124] J. Hörandel. *Astrop. Phys.*, 19:193.

[125] E. Bugaev S. Klimushin and I. Sokalski. *Proc. 27th ICRC (Hamburg)*, 2001. hep-ph/0106010.

[126] C. Cârloganu. Simulation of muons from atmospheric showers in the antares detector using hemas. ANTARES internal note. ANTARES-Software/2004-002.

[127] R. Kopp W. Lohmann and R. Voss. Energy loss of muons in the range 1-10000 gev. *CERN Yellow Report*, 85-03, 1985.

[128] P. Lipari and T. Stanev. *Phys. Rev.*, D44:3543–3554, 1991.

[129] I. A. Sokalski, E. V. Bugaev, and S. I. Klimushin. Mum: Flexible precise algorithm for the muon propagation. 2001. hep-ph/0106011.

[130] I. Sokalski, Private communication.

[131] F. Hubaut. *Optimisation et caractérisation des performances d'un télescope sousmarin a neutrinos pour le projet ANTARES.* PhD thesis, CPPM - Marseille, 1999.

[132] A. Oppelt. *Étude de la résolution angulaire du télescope à neutrinos ANTARES*. PhD thesis, CPPM - Marseille, 2001.

[133] A. Romeyer. *Étude de la sensibilité du détecteur ANTARES à un flux diffus de neutrinos cosmiques de haute énergie*. PhD thesis, Université Denis Diderot - Paris VII, 2003.

[134] Gary C. Hill and Katherine Rawlins. *Astropart. Phys.*, 19:393–402, 2003. astro-ph/0209350.

[135] G. J. Feldman and R. D. Cousins. *Phys. Rev.*, D57:3873, 1998.

[136] J. Neyman. *Phil. Trans. Royal Soc. London*, A, 1937.

[137] V.A. Naumov T.S. Sinegovskaya S.I. Sinegovsky E.V. Bugaev, A. Misaki and N. Takahashi. *Phys. Rev.*, D58:054001, 1998.

[138] F. Halzen. Lecture on neutrino astronomy: theory and experiment. 1999. astro-ph/9810368.

[139] M.H. Salamon P. Sommers F.W. Stecker, C. Done. *Phys. Rev. Lett.*, 66, 1991. Errata, Phys.Rev.Lett. 69 738 (1992).

[140] E. Waxman and J. Bahcall. *Phys. Rev. Lett.*, 78:2292, 1997.

[141] E. Waxman. *Nucl. Phys. Proc. Suppl.*, 87, 2000.

[142] J. Alvarez-Muniz, F. Halzen, and D. W. Hooper. *Phys. Rev.*, D62:093015, 2000. astro-ph/0006027.

[143] A. Hallgren C. Pérez de los Heros J. Conrad, O. Botner. *Phys. Rev.*, D67:012002, 2003. hep-ex/0202013.

[144] M. Honda et al. *Phys. Rev.*, D52:4985, 1995.

[145] P. Lipari T. Montaruli P.R. Sala T. Rancati G. Battistoni, A. Ferrari. *Astropart. Phys.*, 12:315–333, 2000.

[146] W.R. Webber et al. *Proc. 20th ICRC (Moscow)*, 1, 1987.

[147] T. Sanuki et al. *Astrophys. J.*, 545:1135, 2000.

[148] J. Alcaraz et al. *Phys. Lett.*, B490:27, 2000.

[149] C. G. S. Costa. *Astropart. Phys.*, 16:193, 2001.

[150] A. Kaidalov and O.I. Piskunova. *Z. Phys.*, C30:145, 1986.

[151] P.Galeotti L.V. Volkova, W. Fulgione and O. Saavedra. *Nuovo Cimento*, C10:465, 1987.

[152] P. Gondolo G. Gelmini and G. Varieschi. *Phys. Rev.*, D61:036005, 2000.

[153] G. Ingelman M. Thunman and P. Gondolo. *Astropart. Phys.*, 5:309, 1996.

[154] J. Conrad et al. *Phys. Rev.*, D67, 2003.

[155] G. Cowan. A survey of unfolding methods for particle physics. Prepared for Conference on Advanced Statistical Techniques in Particle Physics, Durham, England, 18-22 Mar 2002.

[156] A. Hoecker. *Nucl. Inst. & Meth. in Phys. Res.*, A 372:469–481, 1996.

[157] G. D'Agostini. *Nucl. Inst. & Meth. in Phys. Res.*, A 362:487–498, 1995.

[158] V. Blobel. Regularised unfolding, the *run* program. LEP wide WG on 2-photon Physics, 2000.

[159] *The L-curve and its use in the numerical treatment of inverse problems.* WIT Press, 2001.

[160] D. Chirkin. Fluxes of atmospheric leptons at 600 GeV - 60 TeV. *hep-ph/0407078*, 2004.

Appendix A

Systematic effect due to ARS saturation

This appendix shows the results of the study of the systematic effect of the ARS saturation in the energy reconstruction. The ANTARES detector is foreseen to have two modes to gather the PMT signal information. On the one hand, in the so-called single photo-electron (SPE) mode, just the total charge and time are recorded. The saturation level in this case is assumed to be 8 photoelectrons. In order to extend the dynamic range of the charge integration, the waveform (WF) mode can be used. In this case, 128 samples of the analog signal (activated above a threshold of 2-10 pe) are taken, giving a saturation level of 200 pe.

During the ANTARES design stage, it was suggested to remove the WF mode. For this reason it was necessary to carry out a study on the impact of this possibility on the detector performances, including the energy resolution. As explained, the energy reconstruction algorithm is based on the comparison between the charge collected by each PMT and the charge that would be collected if the muon was a MIP. In order to perform this study, three cases have been considered:

- no saturation,

- saturation at 200 pe (WF mode implemented) and

- saturation at 8 pe (WF mode not implemented).

This analysis has been performed with the Monte Carlo sample I described in chapter 3 and, therefore, the detector geometry corresponds to the 10-string layout (see figure A.1).

Saturation is simulated assigning a charge of 8 (200) pe to those hits with charge greater than 8 (200) pe. In Figure A.2 (left), the charge distribution of the hits is shown. Table A.1 gives the number of hits with charge above 8 and 200 pe compared to the total number of hits. The total charge of these hits is also shown. The percentage of hits with charge greater than 8 (200) pe is only 6% (0.5%). However, this percentage
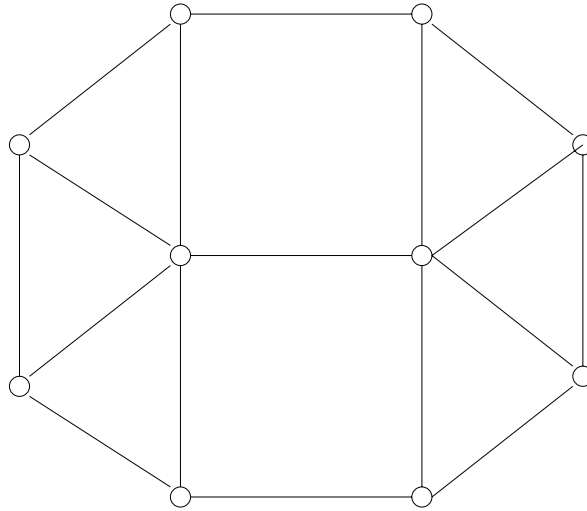
Figure A.1: Layout of the 10-line detector.

represents the 88% (66%) of the total collected charge. This can be better seen in figure A.2 (right), where each hit is weighed by its own charge.
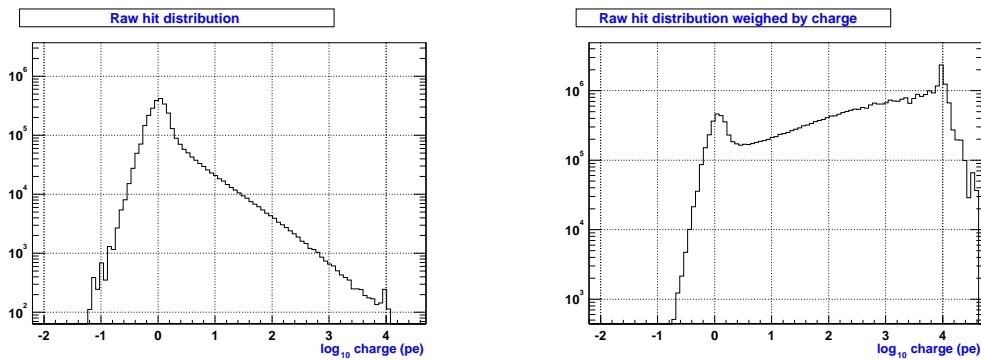

Figure A.2: Left: Charge distribution of the hits. Right: Charge distribution of the hits where each entry is weighed by the charge of the hit.

Figure A.3 shows the number of tracks having at least one saturated hit, as a function of the energy, either for 8 pe or 200 pe saturation level. At high energies, almost all the tracks have some saturated hit.

In figure A.4 the selected tracks are classified according to the percentage of saturated hits and the muon energy. As expected the percentage of saturated hits increases with the energy.

Figure A.5 shows the percentage of charge lost by the effect of saturation. There are tracks where a large percentage of the charge is lost and it can be seen, as expected,

	Number of hits	Total charge (pe)
all hits	3.6×10^6	3.3×10^7
hits >8 pe	2.2×10^5	2.9×10^7
hits >200 pe	1.9×10^4	2.2×10^7

Table A.1: Number of hits above a given saturation threshold compared to the total number of hits, in a sample of 10^{10} neutrinos. The corresponding charge is also indicated.
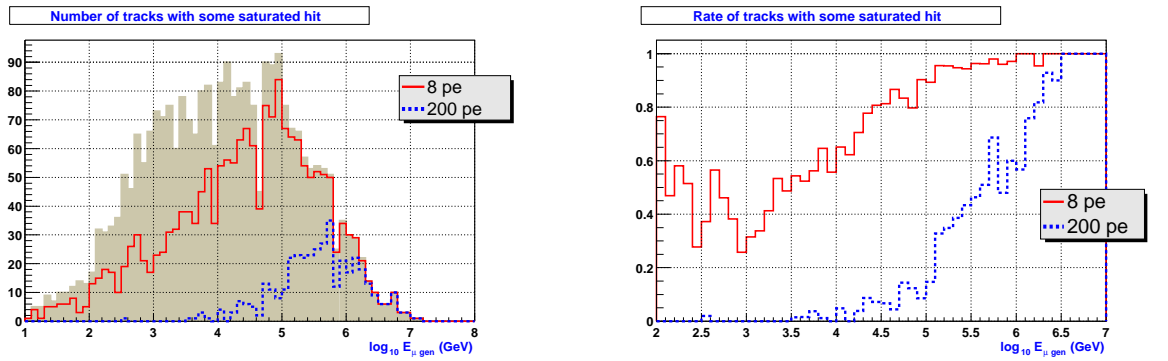
Figure A.3: Left: Number of tracks with at least one saturated hit. The filled histogram shows all the reconstructed tracks. Right: Ratio of tracks with at least one saturated hit.
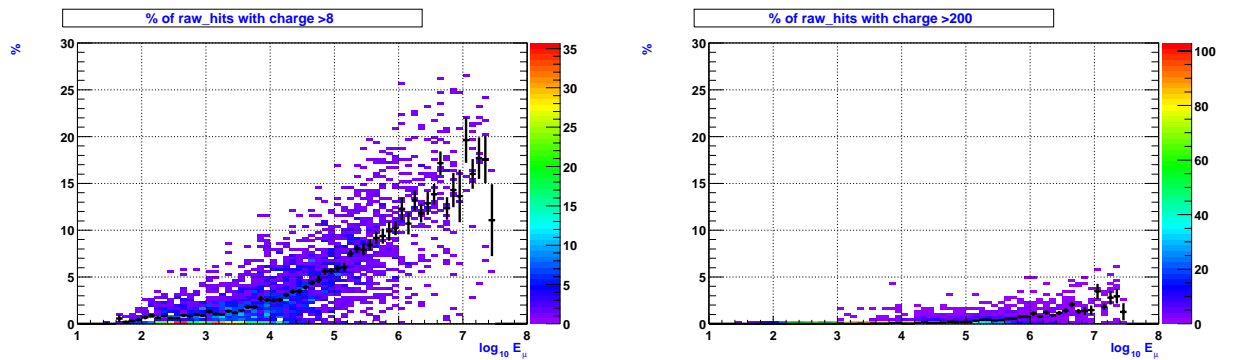
Figure A.4: Percentage of hits above 8 pe (left) and 200 pe (right) as a function of the energy.

that the effect increases with the muon energy. It can be seen that the difference between no saturation and saturation at 200 pe is small. In the case of sautrarion at 8 pe, the dependence is similar on E_{gen} although less steep.
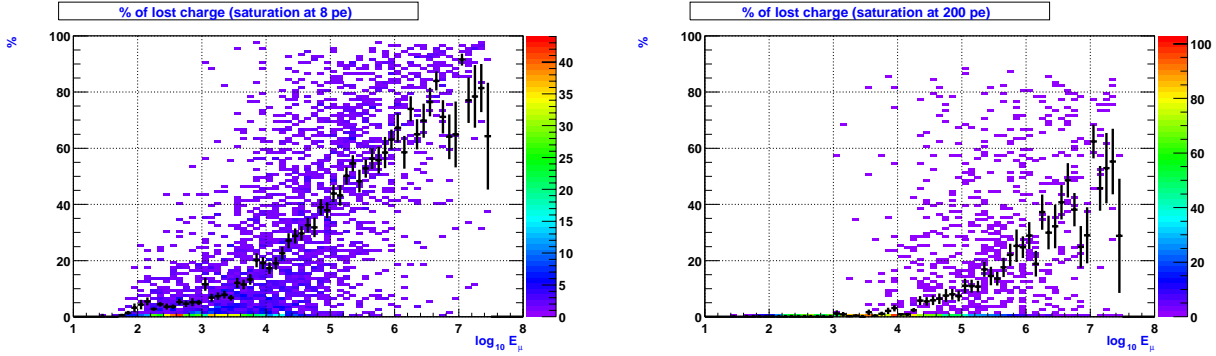
Figure A.5: Percentage of charge lost when saturation occurs at 8 pe (left) or at 200 pe (right) as a function of the energy.

As mentioned, the effect of saturation on the energy resolution comes from the definition of the estimator used in the algorithm. Figure A.6 shows the modification in the relationship between the generated muon energy and the energy estimator.
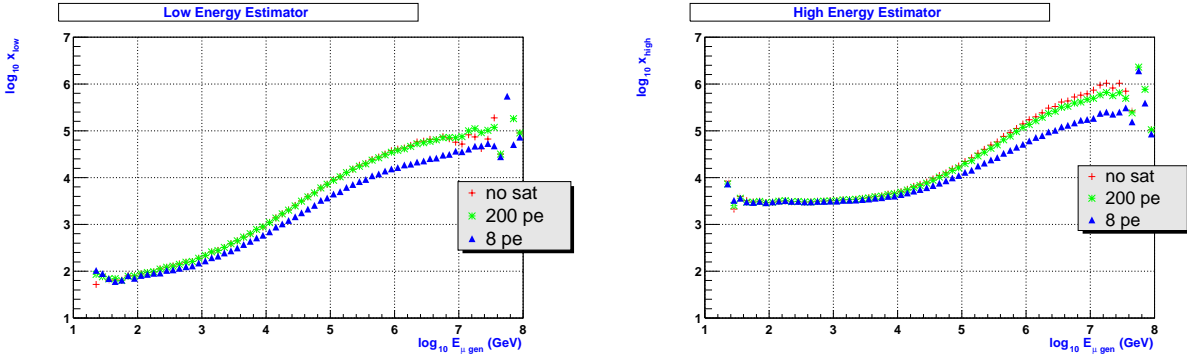
Figure A.6: Low energy (left) and high energy (right) estimator as a function of the energy, for the three cases under study.

Since the relationship between the energy estimator and the muon energy is modified, a new set of parameters for each saturation level has to be calculated. Using the proper parameters in each case, we obtain that the $\log_{10} E_{rec}/E_{gen}$ distributions are similar, both in the mean and the sigma, so no important effect is expected from ARS saturation.

Appendix B

Model comparison with statistical tests

In section 5.7, the results of a comparison with statistical test between different neutrino models have been presented. In this appendix, we extend this study to other models.

If we use the pessimistic version of QGSM to generate the experiments, the results are much less conclusive than when using the optimistic version, since the fraction of prompt neutrinos is much smaller[1] (see figures B.1 and B.2). There is still a visible peak at zero in the probability distributions when the estimator distribution is compared with the Bartol prediction, but there are a large fraction of experiments with intermediate or high probability values.

In section 5.7, a signal in the Waxman-Bahcall limit was used. With a larger signal, the comparison would be more conclusive. Using the MPR limit, the experimental distribution will not be compatible with the hypothesis of only Bartol spectrum (see figures B.3 and B.4).

A version reduced by a factor ten in this limit has been also tried (see figures B.5 and B.6. As in the case of the WB limit, almost 70% of the experiments with the hypothesis are rejected, losing only less than 5% of the experiments with the true hypothesis.

In order to see better these results, we can also plot the number of experiments above a given threshold of probability (see figures B.7-B.11). These plots also show the ratio between these two histrograms.

---

[1]On the other hand, this also means that it is easier to distinguish between the optimistic and the pessimistic cases.
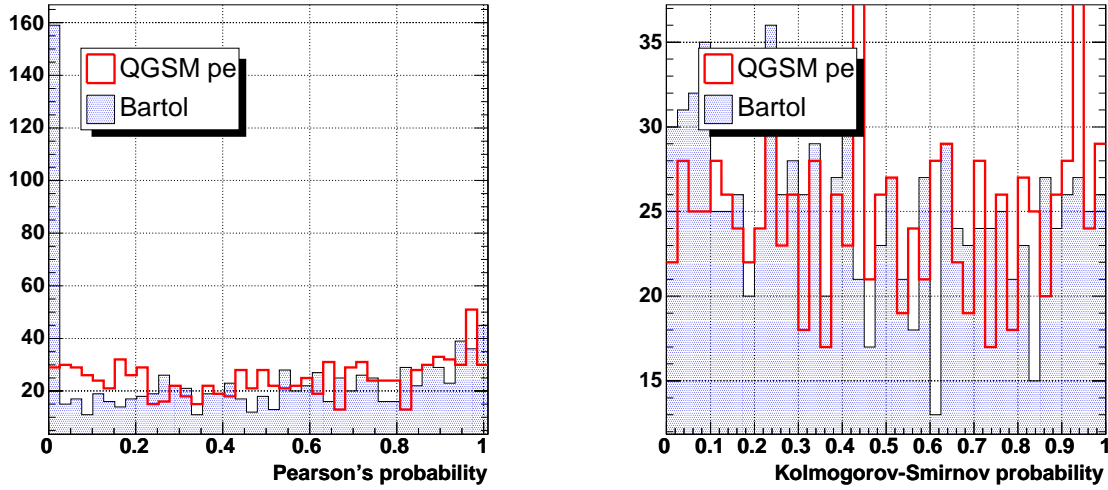
Figure B.1: Probability distribution of the Pearson's (left) and Kolmogorov-Smirnov (right) tests after 1000 one-year experiments. The distributions have been generated with $QGSM_{pe}$, and are compared with $Bartol+QGSM_{pe}$ and with Bartol.
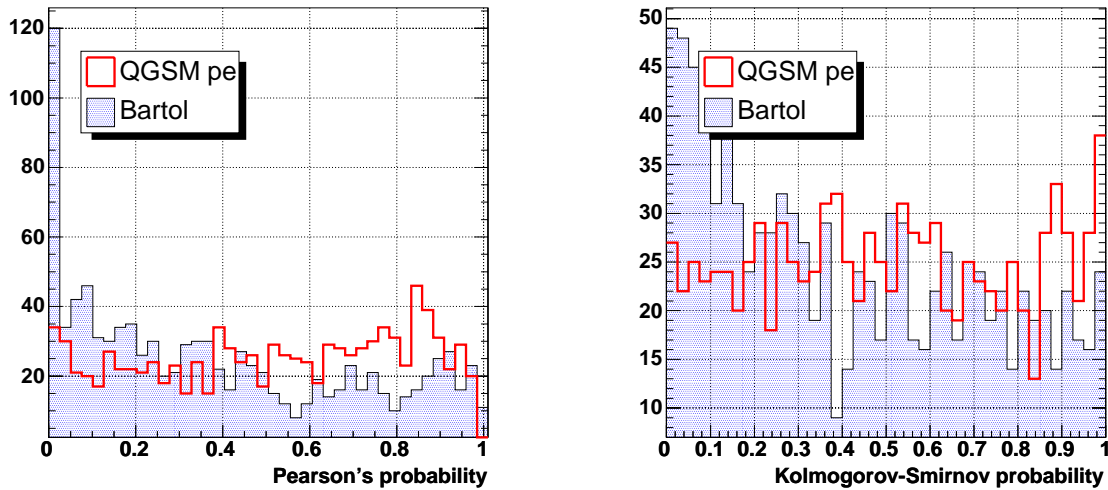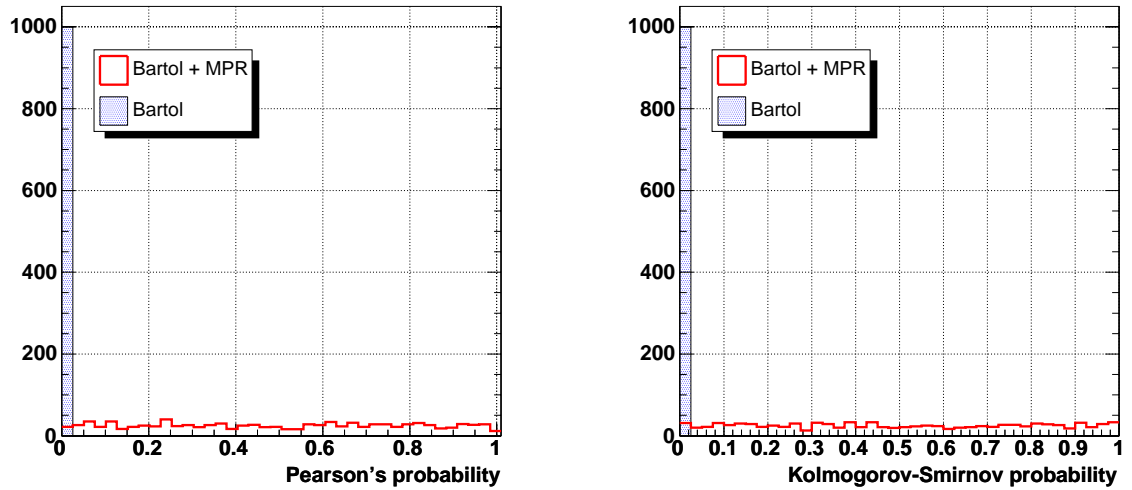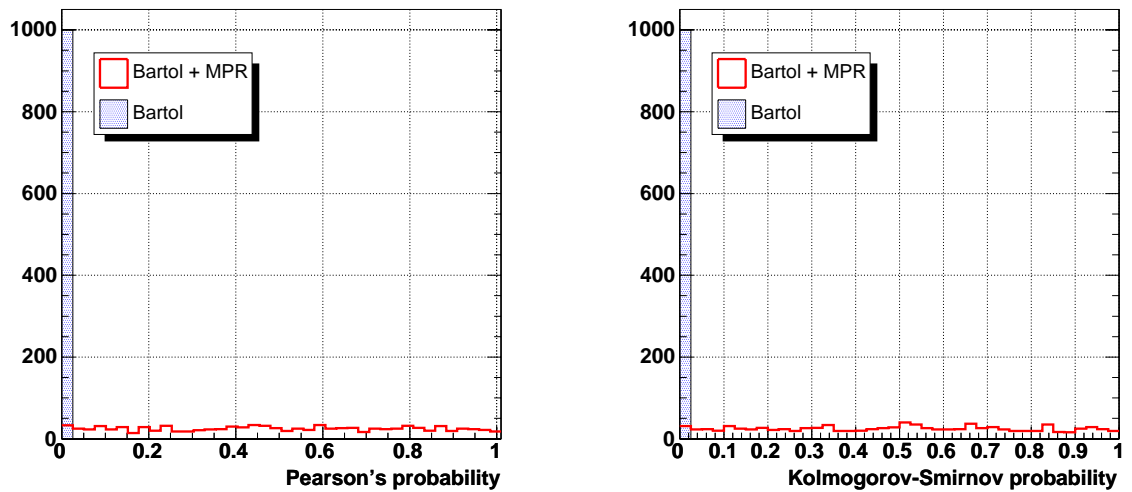

Figure B.2: Probability distribution of the Pearson's (left) and Kolmogorov-Smirnov (right) tests after 1000 three-year experiments. The distributions have been generated with $Bartol+QGSM_{pe}$, and are compared with $Bartol+QGSM_{pe}$ and with Bartol.

Figure B.3: Probability distribution of the Pearson's (left) and Kolmogorov-Smirnov (right) tests after 1000 three-year experiments. The distributions have been generated with Bartol+MPR, and are compared with Bartol+MPR and with Bartol.
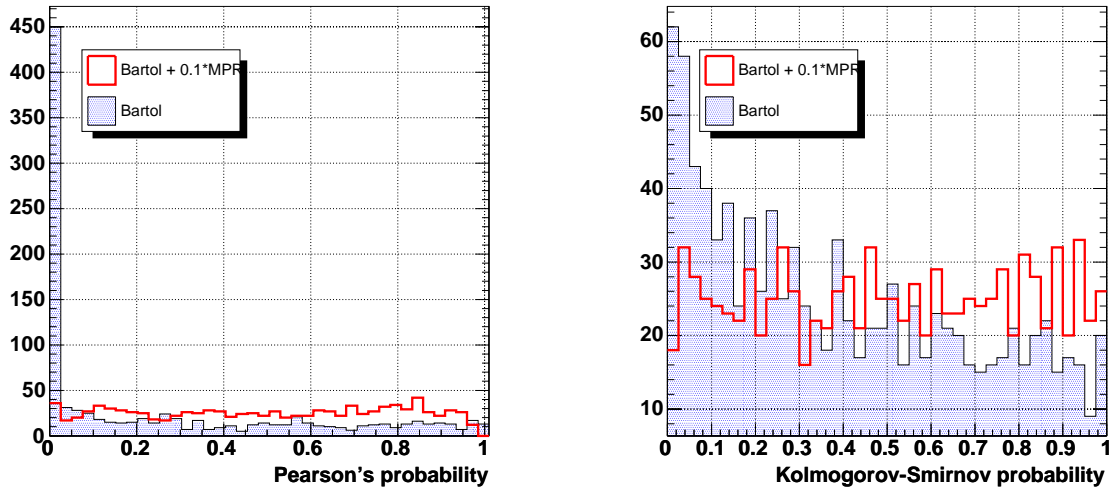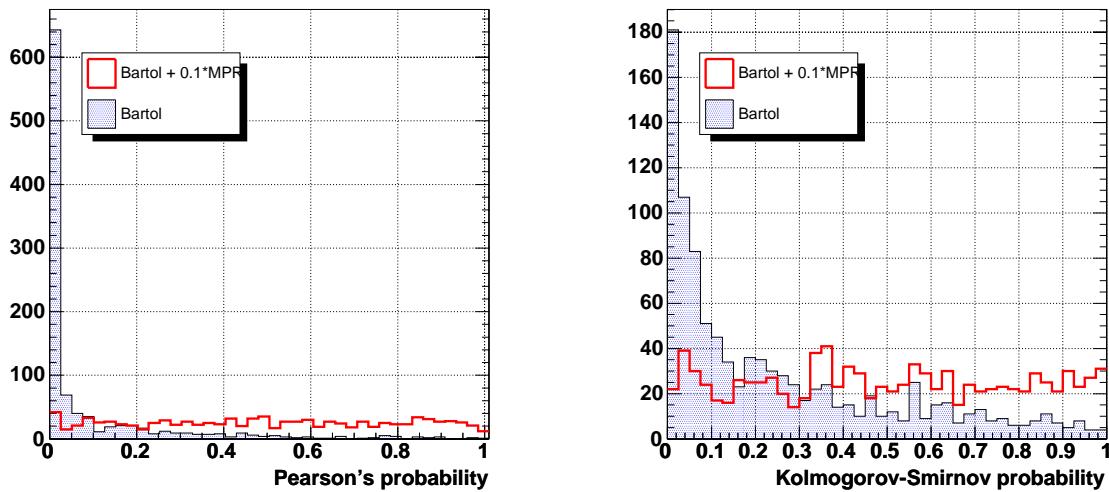

Figure B.4: Probability distribution of the Pearson's (left) and Kolmogorov-Smirnov (right) tests after 1000 three-year experiments. The distributions have been generated with Bartol+MPR, and are compared with Bartol+MPR and wtih Bartol.

Figure B.5: Probability distribution of the Pearson's (left) and Kolmogorov-Smirnov (right) tests after 1000 one-year experiments. The distributions have been generated with Bartol+0.1·MPR, and are compared with Bartol+0.1·MPR and with Bartol.
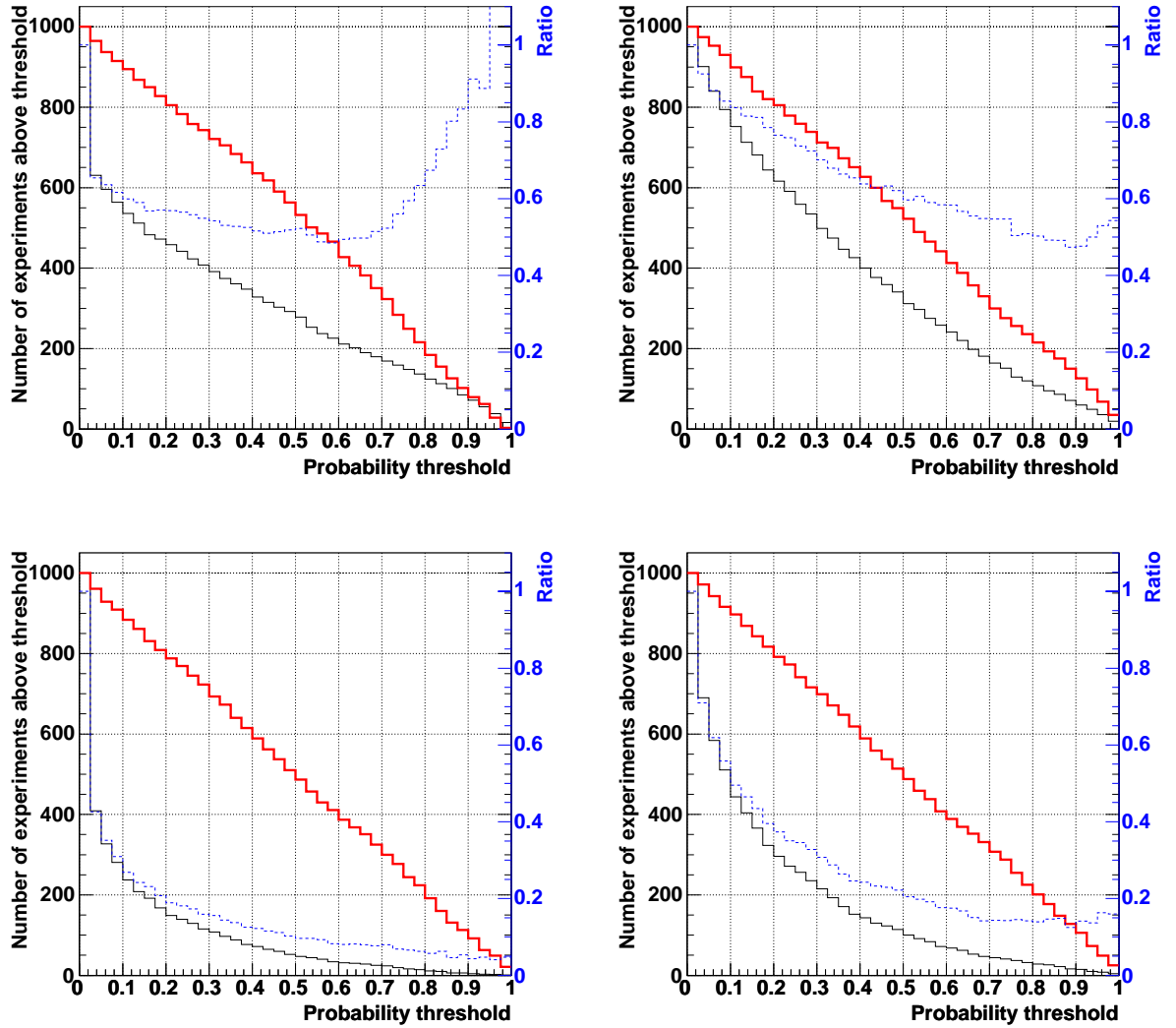

Figure B.6: Probability distribution of the Pearson's (left) and Kolmogorov-Smirnov (right) tests after 1000 three-year experiments. The distributions have been generated with Bartol+0.1·MPR, and are compared with Bartol+0.1·MPR and with Bartol.

Figure B.7: Number of one-year (top) and three-years (bottom) experiments above a given probability threshold for the Pearson's (left) and Kolmogorov-Smirnov (right) tests. Red, thick (black, thin) line corresponds to the comparison with the Bartol+QGSM$_{op}$ (Bartol) model. The blue, dashed line indicates the ratio between both histograms (the scale is indicated on the right axis).
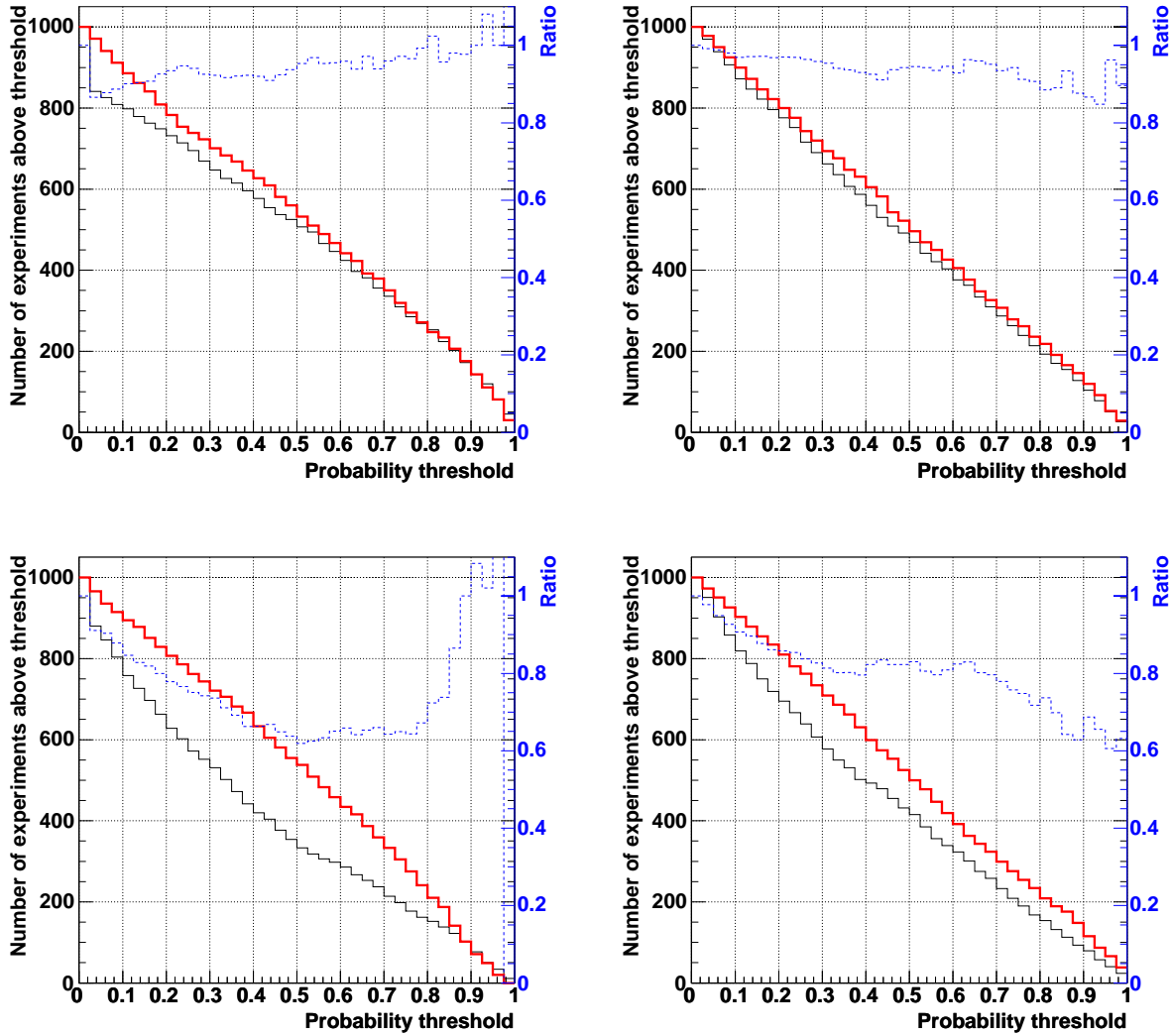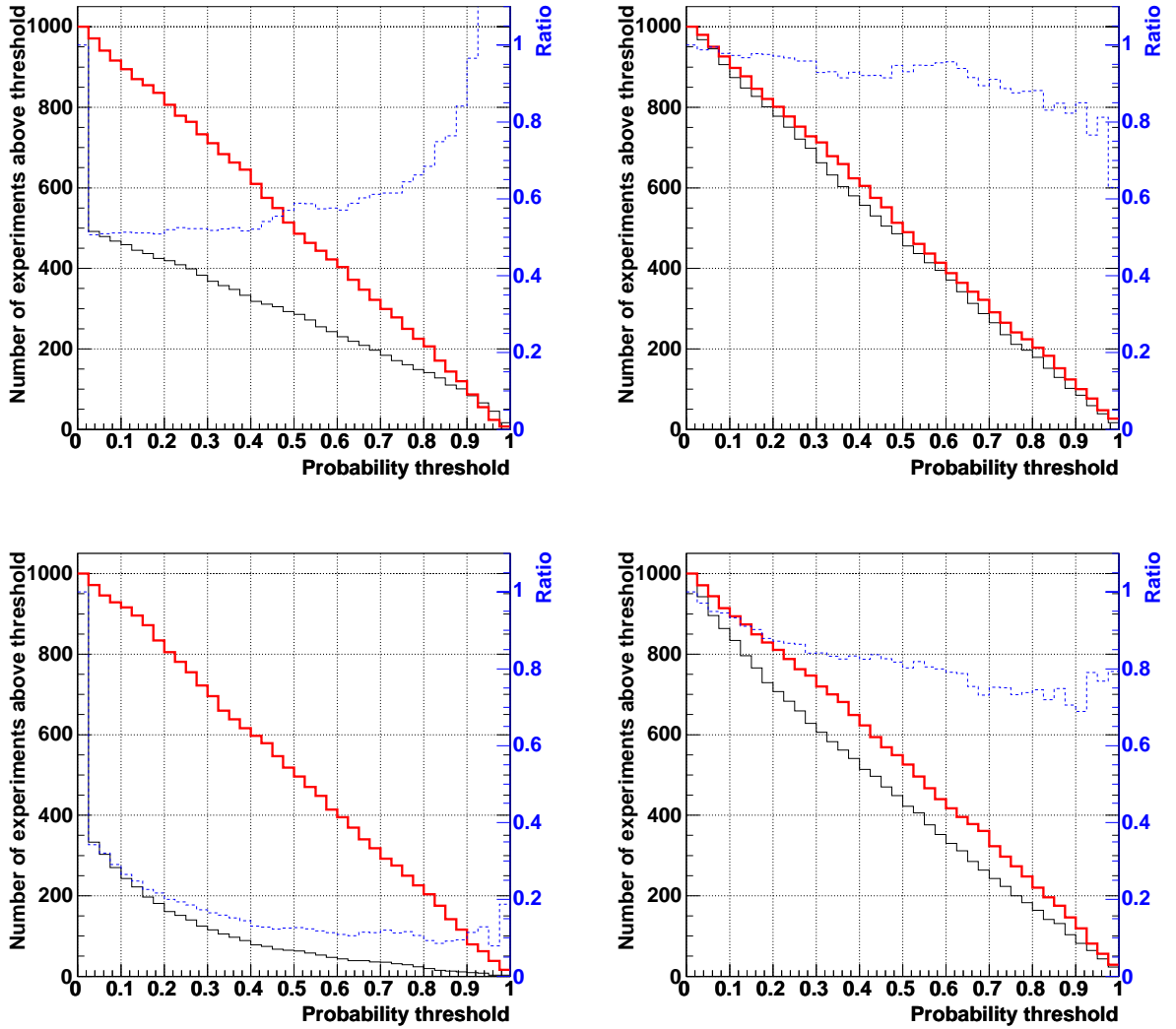
Figure B.8: Number of one-year (top) and three-years (bottom) experiments above a given probability threshold for the Pearson's (left) and Kolmogorov-Smirnov (right) tests. Red, thick (black, thin) line corresponds to the comparison with the Bartol+QGSM$_{pe}$ (Bartol) model. The blue, dashed line indicates the ratio between both histograms (the scale is indicated on the right axis).

Figure B.9: Number of one-year (top) and three-years (bottom) experiments above a given probability threshold for the Pearson's (left) and Kolmogorov-Smirnov (right) tests. Red, thick (black, thin) line corresponds to the comparison with the Bartol+WB (Bartol) model. The blue, dashed line indicates the ratio between both histograms (the scale is indicated on the right axis).
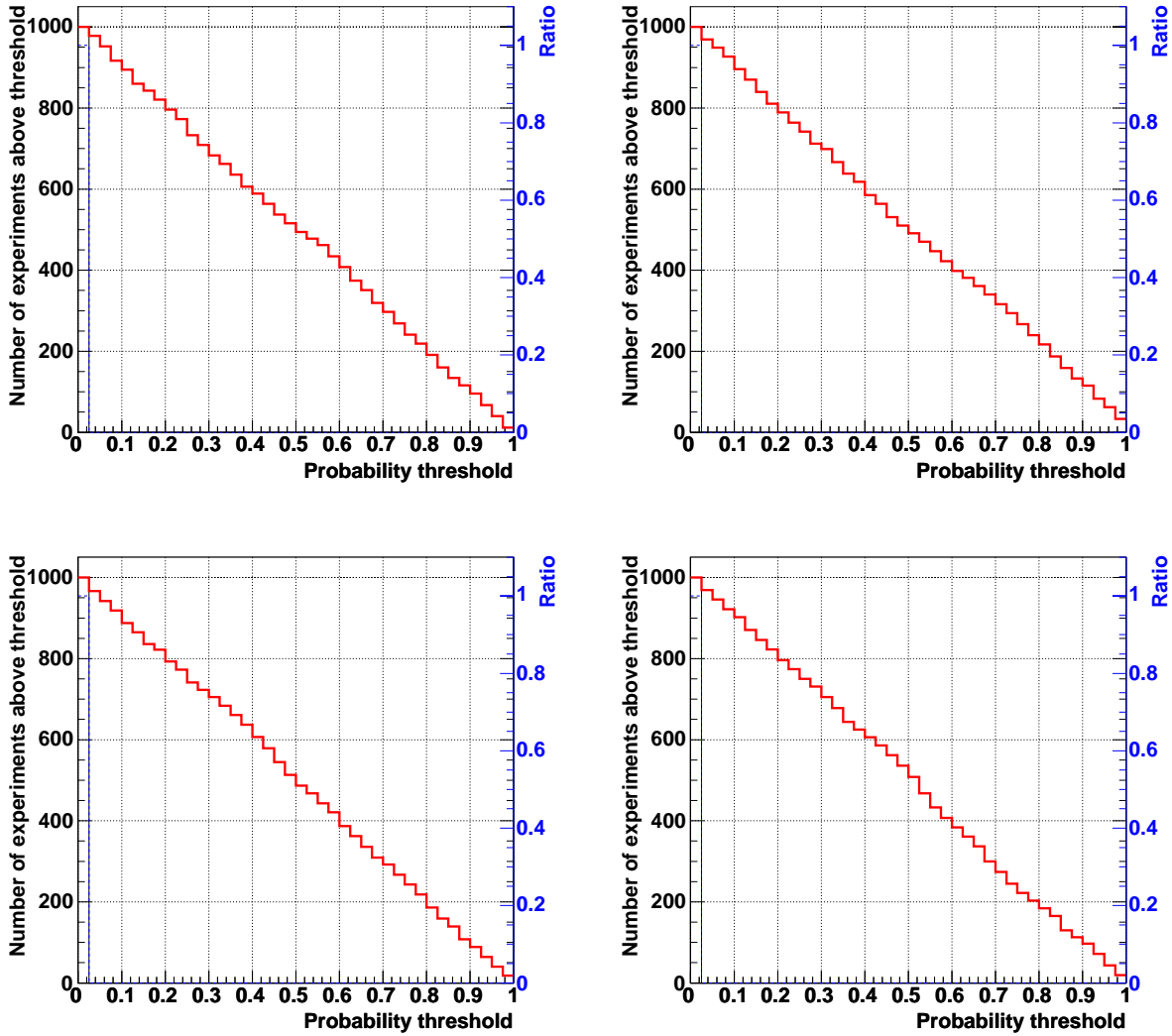
Figure B.10: Number of one-year (top) and three-years (bottom) experiments above a given probability threshold for the Pearson's (left) and Kolmogorov-Smirnov (right) tests. Red, thick (black, thin) line corresponds to the comparison with the Bartol+MPR (Bartol) model. The blue, dashed line indicates the ratio between both histograms (the scale is indicated on the right axis).
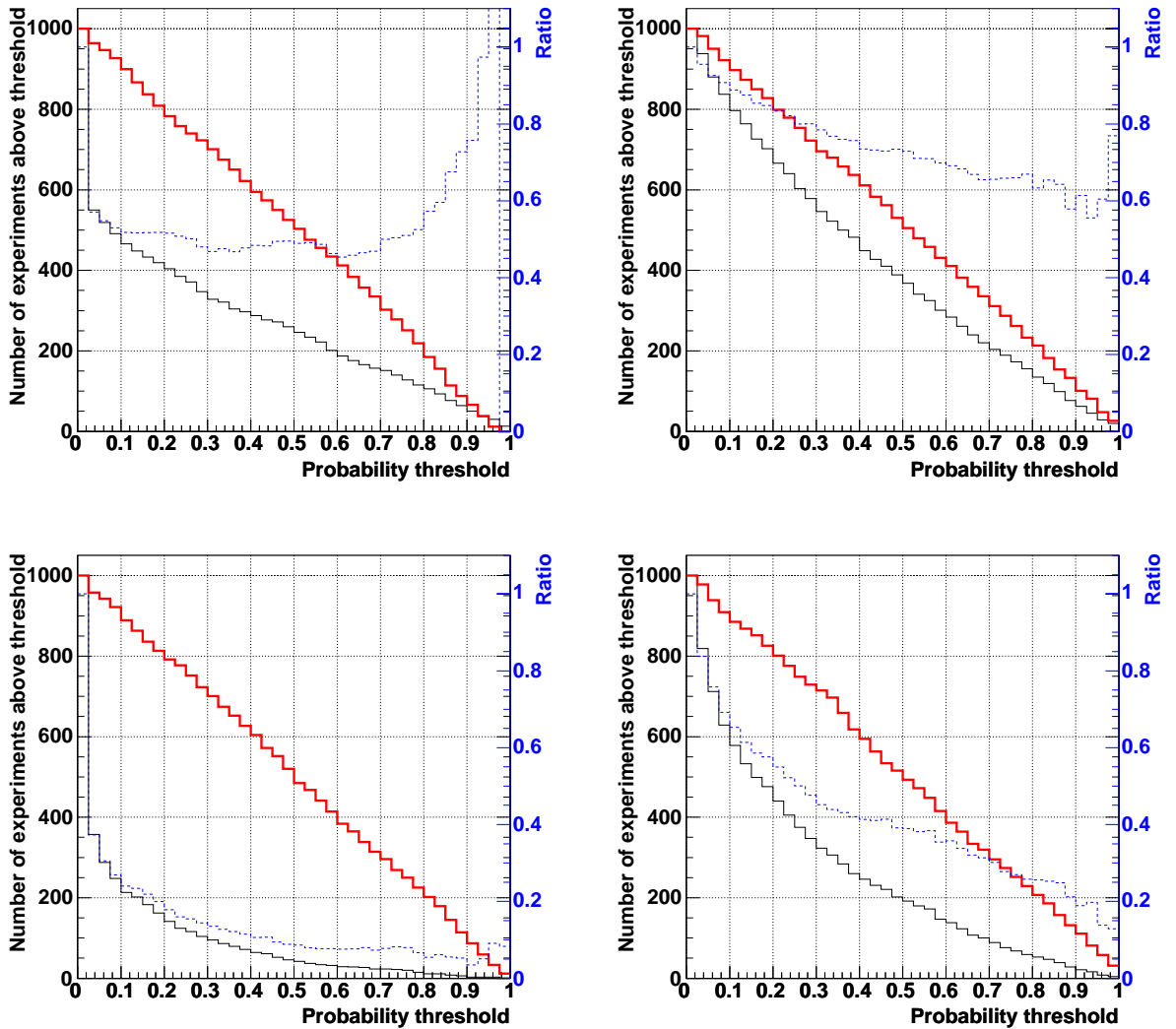
Figure B.11: Number of one-year (top) and three-years (bottom) experiments above a given probability threshold for the Pearson's (left) and Kolmogorov-Smirnov (right) tests. Red, thick (black, thin) line corresponds to the comparison with the Bartol+0.1·MPR (Bartol) model. The blue, dashed line indicates the ratio between both histograms (the scale is indicated on the right axis).